Control of Rydberg atoms for quantum technologies

DISSERTATION

zur Erlangung des akademischen Grades

DOCTOR RERUM NATURALIUM

(Dr. rer. nat.)

am Fachbereich Physik

der Freien Universität Berlin

vorgelegt von

M.SC. SABRINA PATSCH

Berlin, 08. Oktober 2021

Erstgutachterin: PROF. DR. CHRISTIANE P. KOCH
Freie Universität Berlin
Fachbereich Physik

Zweitgutachter: DR. SÉBASTIEN GLEYZES
Laboratoire Kastler Brossel
Collège de France
Paris, Frankreich

Tag der Disputation: 08. April 2022

The beautiful is always bizarre.

— CHARLES BAUDELAIRE

CONTENTS

Acknowledgments **v**

Abstract **vii**

Zusammenfassung **ix**

List of Publications **xi**

1 Introduction **1**

2 Rydberg atoms **5**
2.1 Field-free description . . . 6
2.1.1 Hydrogen-like atoms . . . 6
2.1.2 Alkali atoms . . . 7
2.1.3 Matrix elements . . . 9
2.2 Stark effect . . . 11
2.2.1 Hydrogen-like atoms . . . 11
2.2.2 Alkali atoms . . . 15
2.3 Dynamics in the generalised Bloch sphere . . . 17
2.3.1 n-level Rabi oscillation and the generalised Bloch sphere . . . 18
2.3.2 Spin coherent states . . . 21

3 Fast Navigation in the Stark manifold **25**
3.1 Methods for quantum dynamics and control . . . 26
3.1.1 Implementation of the rubidium Hamiltonian . . . 26
3.1.2 Propagation . . . 29
3.1.3 Optimisation . . . 31
3.2 Fast and accurate circularisation . . . 34
3.2.1 Circularisation using π-pulses . . . 35
3.2.2 Optimisation of an improved guess pulse . . . 37
3.2.3 Robustness analysis . . . 41

3.2.4 Quantum speed limit . . . 43
3.2.5 Experimental implementation . . . 46
3.3 Electrometric cat states . . . 51
3.3.1 Choosing the target state . . . 51
3.3.2 Cat state preparation . . . 56
3.4 Summary . . . 60

4 Improved modelling of alkaline-earth atoms **63**
4.1 Methods for modelling alkaline-earth atoms . . . 64
4.1.1 Single-active-electron (SAE) model . . . 65
4.1.2 Angular momentum coupling . . . 66
4.1.3 Fine-structure corrections . . . 70
4.1.4 Implementation of the strontium Hamiltonian . . . 71
4.2 Optimising the Stark map of strontium . . . 73
4.2.1 Benchmark and modification of the SAE model . . . 73
4.2.2 Optimisation of the model parameters . . . 78
4.2.3 Optimised Stark maps . . . 85
4.3 Circularisation of strontium . . . 87
4.4 Summary . . . 90

5 Quantum simulation of open quantum systems **91**
5.1 Methods for open quantum systems . . . 92
5.1.1 Dynamics of open quantum systems . . . 94
5.1.2 Quantum measurements . . . 96
5.1.3 The Lindblad master equation . . . 98
5.1.4 Non-Markovian dynamics . . . 100
5.2 Exploring the parameter landscape of the quantum simulator . . . 103
5.2.1 The model . . . 103
5.2.2 Calculation of the non-Markovianity measure . . . 107
5.2.3 Tuning dissipation or non-Markovianity . . . 111
5.2.4 Realising the Markovian limit . . . 113
5.3 Independent tunability of non-Markovianity and dissipation . . . 119
5.4 Summary . . . 123

6 Scattering of Rydberg atoms and polar molecules **125**
6.1 Theory of polar molecules . . . 126
6.1.1 The molecular Hamiltonian . . . 126
6.1.2 Symmetric top molecules . . . 129
6.1.3 Inversion of ammonia . . . 132
6.2 Modelling the scattering between polar molecules and Rydberg atoms . . . 135
6.2.1 Multipole expansion of the interaction potential . . . 136
6.2.2 Scattering process . . . 140
6.2.3 Calculation of the cross-section . . . 142
6.3 Electric field control of the scattering cross-sections . . . 147
6.3.1 State-selected molecules . . . 147
6.3.2 Thermal ensemble of molecular states . . . 150
6.4 Summary . . . 153

7 Multipolar character of Förster resonance energy transfer **155**
7.1 Dipole-dipole interaction of two-level systems . . . 157
7.1.1 Flip-flop transitions . . . 158
7.1.2 Criss-cross transitions . . . 161
7.2 Cross-section line shapes for different order multipole contributions . . . 162
7.2.1 Dipole-dipole transitions . . . 163
7.2.2 Dipole-quadrupole transitions . . . 168
7.2.3 Dipole-octupole transition . . . 171
7.2.4 Velocity-dependence of multipole transition line shapes . . . 173
7.3 Electric field control of a quadrupole transition . . . 176
7.4 Summary . . . 181

8 Summary and Outlook **183**

Appendix A Parameters of the simulation **I**
A.1 Rubidium . . . I
A.2 Strontium . . . II
A.2.1 Quantum defects . . . II
A.2.2 SAE parameters . . . III
A.2.3 Experimental data at zero field . . . III
A.2.4 Summary of the optimised model parameters . . . V
A.3 Scattering . . . V

Appendix B Spherical tensors **VII**
B.1 Dipole . . . VII
B.2 Quadrupole . . . IX
B.3 Octupole . . . X

Appendix C Technical details regarding strontium **XIII**
C.1 Calculating the matrix elements of $\hat{l}_1 \cdot \hat{s}_1$ . . . XIII
C.2 Optimisation of the radial part . . . XV
C.3 Stark map around 50f triplets . . . XIX

References **XXI**

Declaration of Authorship **XXXIII**

ACKNOWLEDGMENTS

First and foremost I would like to thank my supervisor CHRISTIANE KOCH for giving me the opportunity to write this thesis in her group, for supporting me over the last seven years of my life, and for making it possible for me to gain so many valuable professional and private experiences during my many travels around the world. She proved that a good supervisor always takes the time for her students. For this, I gladly followed her $350\,\mathrm{km}$ to the Freie Universität Berlin. Thank you for everything.

Furthermore, I thank SÉBASTIEN GLEYZES for his never-ending enthusiasm, and his ability to explain science in one thousand and one entertaining ways, be it through dancing, with the help of croissants, balloons or bouzoukis. I also thank ARTHUR LARROUY – my experimental counterpart, without whom a great part of this thesis would not have been possible – for making my stays in Paris so enjoyable, also on a personal level. I am grateful for having had the opportunity to work with such outstanding experimentalists and I thank the whole team at Collège de France for making Paris a second home for me.

I would also like to thank SABRINA MANISCALCO and her group in Turku for welcoming me so many times and showing me the beauty of Finnish nature (and the Finnish sauna). Furthermore, I thank MARTIN ZEPPENFELD for insightful discussions and for introducing me to the world of molecules.

I am also grateful to the STUDIENSTIFTUNG DES DEUTSCHEN VOLKES for financial support and the unique opportunities to polish my English, French and Spanish skills.

On a personal level, I would like to thank all the members of the AG Koch in Berlin and Kassel for making the university a friendly place with relaxing coffee and entertaining lunch breaks. In particular, I want to thank DANIEL BASILEWITSCH for being the best travel buddy – be it in the roasting sun or between walls of snow –, and for being there for me in difficult times.

Finally, my special thanks goes to MANEL MONDELO who grounded me, kept me sane in times of lockdowns and home office, and supplied me with comfort, coffee and camomile tea.

ABSTRACT

Rydberg atoms are the "giants" in the world of atomic physics. Their highly excited valence electron gives them remarkable properties, such as a long lifetime, large dipole moments and great sensitivity to external fields rendering them ideal tools for the study of quantum effects and quantum technology applications. Quantum technologies promise to outperform their classical counterparts in terms of speed, security, accuracy and performance while presenting us with new challenges. This thesis explores different applications of Rydberg atoms for quantum technologies from a quantum control perspective with a special focus on quantum measurements.

Many quantum technologies require the fast and accurate engineering of quantum states to achieve peak performance and avoid decoherence. I tackle this requirement by employing quantum optimal control theory (OCT) and demonstrate fast and accurate navigation in the high-dimensional Stark manifold of rubidium Rydberg atoms. This is illustrated by means of two examples: the circularisation of Rydberg atoms and the preparation of a Schrödinger-cat-like state which promises quantum sensing of electric fields at the fundamental limit using alkali atoms.

While Rydberg physics has focused for a long time on alkali atoms, it is worth to extend the study to alkaline-earth atoms, as their second valence electron promises new opportunities for quantum technology. However, modelling alkaline-earth atoms is challenging due to electronic interactions. I therefore develop an improved single-active-electron model and optimise the parameters to maximise the agreement with spectroscopic data. This enables OCT applications of strontium which require a precise model for the quantum system under consideration.

Fast protocols are an important tool to avoid decoherence. However, quantum technologies rely on accessing the system for information processing and read-out. The study of open quantum systems is thus crucial for realising quantum technology in presence of decoherence. I therefore propose a quantum simulator for open quantum systems which enables the systematic study of dissipation, memory effects and their interplay for quantum control. The simulator is based on frequent measurements of a system by a meter which can be realised, for instance, by a photonic mode of a cavity and a Rydberg atom, respectively.

The strong interaction of composite systems involving Rydberg atoms lends itself not only for quantum simulation but also for spectroscopy. Many standard detection methods for quantum objects are based on their destruction, e.g. by absorption or ionisation. Förster resonance energy transfer (FRET), on the other hand, is a popular spectroscopic tool and promising candidate for the non-destructive detection of polar molecules. The large size of Rydberg atoms, however, suggests a breakdown of the commonly employed dipole-dipole approximation. To enable the study of FRET, I simulate the collision between a Rydberg atom and a polar molecule considering dipole-dipole, -quadrupole and -octupole interactions. The computed scattering cross-sections allow for studying of the multipolar character of FRET and its spectroscopic potential.

ZUSAMMENFASSUNG

Rydberg-Atome sind die "Riesen" in der Welt der Atomphysik. Ihr hoch angeregtes Valenzelektron verleiht ihnen bemerkenswerte Eigenschaften wie eine lange Lebensdauer, große Dipolmomente und eine große Empfindlichkeit gegenüber äußeren Feldern, was sie zu idealen Werkzeugen für die Untersuchung von Quanteneffekten und Quantentechnologie macht. Quantentechnologien versprechen ihre klassischen Vorläufer in Bezug auf Geschwindigkeit, Sicherheit, Genauigkeit und Leistung zu übertreffen, stellen uns aber auch vor neue Herausforderungen. In dieser Arbeit untersuche ich verschiedene Anwendungen von Rydberg-Atomen für Quantentechnologien unter Verwendung von Quantenkontrolle, wobei ein besonderer Schwerpunkt auf dem quantenmechanischen Messprozess liegt.

Viele Quantentechnologien erfordern die schnelle und genaue Präparation von Quantenzuständen, um beste Ergebnisse zu erzielen und Dekohärenz zu vermeiden. Ich bearbeite diese Anforderung mit Hilfe der Theorie optimaler Quantenkontrolle (OCT) und demonstriere eine schnelle und genaue Navigation in der hochdimensionalen Stark-Mannigfaltigkeit von Rubidium-Rydberg-Atomen. Dies wird anhand von zwei Beispielen veranschaulicht: der Zirkularisierung von Rydberg-Atomen und der Präparation eines Schrödinger-Katzen-Zustands, der Quantensensorik von elektrischen Feldern an der fundamentalen Grenze unter Verwendung von Alkaliatomen verspricht.

Während sich die Rydberg-Physik lange Zeit auf Alkaliatome konzentriert hat, lohnt es sich, die Forschung auf Erdalkaliatome auszudehnen, da deren zweites Valenzelektron neue Möglichkeiten für die Quantentechnologie verspricht. Die Modellierung von Erdalkaliatomen ist jedoch aufgrund der elektronischen Wechselwirkungen eine Herausforderung. Ich entwickle daher ein verbessertes effektives Einelektronmodell und optimiere die Parameter, um die Übereinstimmung mit den spektroskopischen Daten zu maximieren. Dies ermöglicht OCT-Anwendungen von Strontium, die ein präzises Modell für das betrachtete Quantensystem erfordern.

Schnelle Protokolle sind ein wichtiges Instrument zur Vermeidung von Dekohärenz. Quantentechnologien sind jedoch auf den Zugang zum System angewiesen, um Informationen zu verarbeiten und auszulesen. Die Untersuchung offener Quantensysteme ist daher von entscheidender Bedeutung für die Verwirklichung von Quantentechnologie in Gegenwart von Dekohärenz. Ich präsentiere daher einen Quantensimulator für offene Quantensysteme, der die systematische Untersuchung von Dissipation, Gedächtniseffekten und deren Zusammenspiel für die Quantenkontrolle ermöglicht. Der Simulator basiert auf wiederholten Messungen eines Systems durch ein Mess-System, die z.B. als photonische Mode einer Kavität bzw. ein Rydberg-Atom realisiert werden können.

Die starke Wechselwirkung von zusammengesetzten Systemen, die Rydberg-Atomen beinhalten, eignet sich nicht nur für die Quantensimulation, sondern auch für die Spektroskopie. Viele Standardnachweisverfahren für Quantenobjekte beruhen auf deren Zerstörung, z.B. durch Absorption oder Ionisation. Der Förster-Resonanz-Energie-Transfer (FRET) hingegen ist ein beliebtes spektroskopisches Werkzeug und ein vielversprechender Kandidat für den zerstörungsfreien Nachweis polarer Moleküle. Die große Ausdehnung von Rydberg-Orbitalen lässt jedoch darauf schließen, dass die üblicherweise verwendete Dipol-Dipol-Näherung nicht ausreichend ist. Um die Untersuchung von FRET zu ermöglichen, simuliere ich den Zusammenstoß zwischen einem Rydberg-Atom mit einem polaren Molekül unter Berücksichtigung von Dipol-Dipol-, Quadrupol- und Oktupol-Wechselwirkungen. Die berechneten Streuquerschnitte ermöglichen die Untersuchung des multipolaren Charakters von FRET und seines spektroskopischen Potenzials.

LIST OF PUBLICATIONS

Two of the five main chapters are based on the following publications. The author contributions are indicated below.

- S. PATSCH, D. M. Reich, J.-M. Raimond, M. Brune, S. Gleyzes, and C. P. Koch.
  Fast and accurate circularization of a Rydberg atom.
  Physical Review A, **97**, 053418 (2018)
  DOI: 10.1103/PhysRevA.97.053418
  Basis for Chapter 3 and follow-up project to my Master's thesis [1]. SP conducted all the simulations and wrote the code based on prior work of DMR. SP, DMR and CPK developed the theoretical ideas. SP and CPK wrote the manuscript. JMR, MB and SB contributed to the development of the project and provided input on the experimental details.

- S. PATSCH, S. Maniscalco, and C. P. Koch
  Quantum simulation of non-Markovianity using the quantum Zeno effect
  Physical Review Research, **2**, 023133 (2020)
  DOI: 10.1103/10.1103/PhysRevResearch.2.023133
  Basis for Chapter 5 and follow-up project to my Bachelor's thesis [2]. SP carried out the calculations and simulations. All authors contributed to developing the theoretical ideas and to writing the manuscript.

- A. Larrouy*, S. PATSCH*, R. Richaud, J.-M. Raimond, M. Brune, C. P. Koch, and S. Gleyzes
  * *These authors contributed equally to this work.*
  Fast Navigation in a Large Hilbert Space Using Quantum Optimal Control.
  Physical Review X, **10**, 021058 (2020)
  DOI: 10.1103/PhysRevX.10.021058
  Basis for Chapter 3 and follow-up project to [PRA 97, 053418 (2018)]. SP carried out the theoretical investigations of the project, AL and RR conducted the experiments. SP and CPK developed the theoretical ideas. JMR, MB and SB supervised the experiments. All authors contributed to the writing of the manuscript. The experimental part of the project was published in the doctoral thesis of AL [3].

Manuscripts for the remaining Chapters 4, 6 and 7 are in preparation. The Bachelor theses [4, 5], conducted under my co-supervision, contributed to the results presented in Chapters 6 and 7.

1 Introduction

In the circus, tamers make animals sit, jump, roll over, or act in other peculiar ways. In quantum physics, we are doing the same with the smallest building blocks of nature. Since the dawn of quantum physics, we have been fascinated – and not rarely puzzled – by the strange nature of the quantum world. For decades, researchers were being limited to exploring nature in thought, as it seemed impossible to observe or control single quanta. Today, we are able to make the quantum world our own; tame molecules, atoms or even single particles of light, understand and predict their behaviour and even exploit them for the development of cutting edge technology.

One famous example for the remarkable control of single quanta is the observation of the birth and death of a single photon [6] which, amongst others, was awarded the Nobel prize in 2012 [7]. Key to this experiment was the strong interaction between light and highly excited atoms, so-called Rydberg atoms [8, 9]. Other experiments showed that these atoms can be used for observing the progressive decoherence of a superposition [10], measuring photons without destroying them [11], making photons talk to each other [12], generating single photons [13], or – in other words – watching quantum physics at work.

Leveraged by experimental advances in the last decades, the study of quantum physics has passed the point of fundamental research. In fact, many established technologies, such as lasers, MRI or microchips, rely in one way or another on the principles of quantum physics. But there is more to come. High-level control of quantum systems, such as demonstrated by the groundbreaking experiments listed above, enables new technologies which exploit the quantum nature of their building blocks [14]. In the so-called second quantum revolution, we envision technologies that outperform their classical counterparts in terms of speed, security, accuracy, or performance [15]. The idea of simulating physics with computers built of quantum particles was first formulated by Richard Feynman [16] which is commonly considered the spark that ignited the field of quantum technology. Today, quantum computing is just one of four main pillars of quantum technology, next to quantum simulation, quantum communication and quantum sensing/metrology.

Rydberg atoms have proven to be excellent tools for studying quantum effects and are thus a natural choice for the construction of quantum technologies [17]; current research interests revolve especially around quantum computing, quantum simulation, quantum optics and quantum sensing [18]. Rydberg states are commonly prepared in alkali atoms by exciting their single valence electron to a very high principal quantum number n [9]. This turns the atoms into huge objects, as the size of the valence electron's orbital scales as n^2. For $n \sim 100$, they measure a micron in diameter – about the size of a bacterium. As the electron is, on average, very distant from the ionic core, it is only weakly bounded and thus very sensitive to external fields. Moreover, the overlap of the electron's wavefunction with low lying states is minimal, leading to a long lifetime on the scale of $100\,\mu\text{s}$. By exciting the angular momentum quantum number ℓ to maximal values, i.e. $\ell = n - 1$, the lifetime can even be increased to tens of milliseconds. The orbital of these atoms is shaped like a hula hoop giving rise to the name circular Rydberg atoms [19]. In addition to their long lifetime, Rydberg atoms possess extremely large dipole moments which scale as n^2, rendering them ideal for usage in many-body or composite systems. For instance, Rydberg atoms interact strongly with light, polar objects, or each other [20]. In the latter case, two Rydberg atoms can not only interact via dipole-dipole but also via van-der-Waals interaction, thus rendering their interaction tunable and Rydberg systems ideal for quantum simulation [21]. In addition to that, their strong interaction with light allows for trapping the atoms in impressive, essentially arbitrary geometries in space [22].

In this thesis, I contribute to the study of Rydberg atoms for quantum technologies. For this reason, I provide a thorough introduction to Rydberg physics in Chapter 2. A special emphasis of this thesis lies on the field of quantum metrology. The general idea of quantum metrology, or often synonymously called quantum sensing, is to measure a physical quantity with enhanced sensitivity beyond what is classically possible by means of quantum strategies [23]. In fact, the measurement process itself is a central thread than runs through this thesis. According to the Copenhagen interpretation of quantum mechanics, the quantum mechanical wave function does not possess any reality but is only a means to the end of determining the outcome of a measurement. In this sense, measurements are the crucial link that connects the abstract quantum world with our tangible classical world; the translator from quantum to classical physics; the enabler from concepts to technologies.

The high sensitivity of Rydberg atoms to electric or magnetic fields makes them ideal sensors for their measurement. Quantum enhanced measurement protocols typically rely on preparing the quantum sensors in entangled or other highly non-classical states which are highly sensitive to the quantity that is to be measured [24, 25, 26]. The preparation of these intricate sensing states is often challenging and the main obstacle for achieving accuracies at the fundamental limit. Our approach to this problem is optimal control – another focus of this thesis. Quantum optimal control theory (OCT) [27] is based on defining a figure of merit and treating it as a functional of the external controls, such as electromagnetic pulses driving the system from one state to another. The functional is then minimised using variational calculus under dynamical constraints. The

control problem is often solved numerically, as an analytical treatment is rarely possible. While originally envisioned for controlling molecular processes [28], OCT is an ideal tool whenever high fidelities or fast protocols [29] are desired.

Fast protocols are useful when time is a decisive factor – i.e. when it is playing against you. The high sensitivity of quantum systems to external fields is one of their major assets for quantum technologies, but also their greatest weakness. They do not only react to deliberate controls but also to undesired sources of noise which, over time, destroy coherence and erase information. This process is called decoherence and a major adversary in engineering quantum technologies [30]. One approach to beat decoherence is to perform protocols faster than decoherence can destroy them. In Chapter 3, I investigate on how OCT can help to speed-up and improve the state preparation in Rydberg atoms at the example of circular and Schrödinger-cat-like states for quantum metrology applications.

One premise for the application of OCT is the existence of an accurate model to describe the quantum system that is to be controlled. If the employed model is inadequate, the optimised controls will not be effective in experimental applications. Alkali Rydberg atoms are thus ideal for this purpose, as they can be described by comparatively easy models with high accuracy due to their similarity to the hydrogen atom. However, there are reasons to move forward and consider Rydberg states in alkaline-earth atoms, which possess two valence electrons [31]. These atoms promise to be true experts of multi-tasking: While one electron can be used for trapping, cooling or imaging the atom, the other one is available for quantum technology applications. Modelling alkaline-earth atoms is, however, a challenging task due to electronic interactions. The single-active-electron (SAE) model [32] incorporates the influence of the inner, ground state electron on the outer, Rydberg electron into an effective core potential. While showing qualitatively good results in some areas of Hilbert space, the model fails to predict the outcome of experiments in others. In Chapter 4, I take on the task of improving the SAE model by optimising newly introduced model parameters on the basis of experimental data, thus paving the way for optimal control of alkaline-earth atoms.

Unfortunately, it is not always possible to speed-up protocols with OCT sufficiently to overcome decoherence. Moreover, perfect isolation of the quantum system is neither possible in reality nor constructive, as quantum technologies rely on the system being accessible for processing and read-out of information. The study of open quantum systems [33] is thus crucial for the realisation of quantum technology in presence of decoherence [30]. In Chapter 5, I employ an approach to studying open quantum systems that can be summarised as "To know your enemy, you must become your enemy"[1]. Specifically, I employ quantum simulation [34] to study the influence of an environment on the open system's dynamics. The idea of quantum simulation is to mimic the dynamics of a complex system in a simpler, controllable one. Here, I exploit this idea and deliberately induce dissipation in a photonic mode of a cavity by performing repeated, indirect measurements of the system's state using Rydberg atoms. When tuning the parameters

[1] Sun Tzu, *The Art of War*

of the measurement carefully, it is possible to mimic dissipation and memory effects, i.e. non-Markovian dynamics [35], and study their role for the control of open quantum systems.

The key property of measurements for quantum simulation is that they destroy information – similarly to the environment of an open quantum system. In many areas of physics, this property is highly detrimental. In the worst case, a measurement destroys the quantum system of interest, for instance when photons are measured via absorption. A viable route to circumvent this problem is by measuring the system of interest indirectly using a meter [36]. For instance, the detection of polar molecules [37, 38, 39] is still a challenging task, as existing methods often require specific properties of the molecule [40]. In Chapter 6 and 7, I study the interaction between polar molecules and Rydberg atoms, which promises to serve as a new detection scheme for polar molecules [40]. More specifically, I model the scattering process between polar molecules and Rydberg atoms *ab initio* in Chapter 6 and provide predictions for the outcome of realistic experiments. During the collision, the particles interact via Förster resonant energy transfer (FRET) [41], a process which is typically described by means of the dipole-dipole interaction between them. However, since Rydberg atoms can take macroscopic dimensions, approximating their charge distribution as a dipole seems questionable. This is why in the presented model, I go beyond this approximation and study the multipolar character of the interactions. In Chapter 7, I selectively study the role of higher order multipole elements for FRET and formulate a condition for the breakdown of the dipole approximation.

This thesis is structured in 8 chapters. Chapter 2 summarises the necessary foundations of Rydberg physics. The following five chapters each present the results of one project as outlined above. Each of these chapter (except for Chapter 7 which forms a unit with Chapter 6) starts with one section on the theoretical concepts from literature required for the subsequent chapter, and ends with an individual summary. The findings of the complete thesis are summarised and embedded into the current state of research on quantum technology in Chapter 8. As emphasised before, quantum technology is about more than abstract concepts. It is about real-life applications and the development of cutting edge technology. Experimental feasibility is therefore a mandatory requirement for all research that aims to bring quantum technology forward. In this thesis, I therefore put a special emphasis on realistic models for the proposed concepts. This perspective was enriched by fruitful experimental collaborations which contributed to Chapters 3, 4, 6 and 7. I thus provide in this thesis the full range from theoretical modelling, over numerical simulations, to experimental predictions, reproduction of experimental data, and the successful comparison of theory and experiment, in order to open up new areas of quantum technologies with Rydberg atoms.

2

RYDBERG ATOMS

As this work focuses on the usage of Rydberg atoms in quantum technologies, we dedicate a full chapter on the theoretical foundations of these atoms. The term "Rydberg atom" relates to the Rydberg formula [8]

$$\Delta E = R_H \left(\frac{1}{m^2} - \frac{1}{n^2} \right) \tag{2.1}$$

which was first formulated by Johannes Rydberg in 1890. It gives the energy difference between the n-th and m-th level of hydrogen where the natural constant R_H is known as the Rydberg constant. Any system with a somewhat localised positively charged core and a more strongly delocalised electron shows some degree of hydrogenic behaviour. This is particularly true for systems with a highly-excited valence electron and therefore, atoms whose valence electron is in a state with a high principal quantum number n are known as Rydberg atoms. Rydberg states can also be found in molecules or semiconductors but due to the natural resemblance of alkali atoms with hydrogen, these are a popular choice in the field of Rydberg physics [18]. In this chapter, we consider both hydrogen-like atoms, which are constituted of a single electron and an arbitrary number of protons and neutrons in the core; and alkali atoms, with one valence electron and an ionic core which consists of the atomic core and multiple inner shell electrons.

We start by describing Rydberg atoms without external perturbations in Sec. 2.1 and show that only small adjustments of the hydrogen-like model are necessary to adequately describe also alkali atoms. Afterwards, in Sec. 2.2, we discuss the influence of a static electric field on Rydberg atoms and the properties of the emerging Stark manifold. Finally, in Sec. 2.3, we describe the dynamics in the Stark manifold when the atoms are under the influence of time-dependent pulses.

2.1 Field-free description

For the largest part of this thesis, we consider experiments with rubidium Rydberg atoms with a special focus on circular states. However, alkali atoms in high-angular-momentum states, such as the circular state, behave similar to hydrogen, as the overlap between the valence electron and the ionic core is negligible. Therefore, we start by recapitulating the properties of free hydrogen-like atoms in Sec. 2.1.1. Only for low-angular-momentum states does the valence electron dive into the ionic core which slightly changes the properties of alkali atoms in comparison to hydrogen as we discuss in Sec. 2.1.2. In order to describe interactions of Rydberg atoms with external field or other particles, we present the matrix elements of the position operator in Sec. 2.1.3.

2.1.1 Hydrogen-like atoms

We consider an electron in the field of an atomic core with charge Ze, where e is the elementary charge and Z an integer. In the centre of mass frame and atomic units, which will be employed throughout the thesis, the Hamiltonian takes the form [8]

$$\hat{H}_0 = \hat{T} + \hat{V}_\mathrm{C}(\hat{r}) = -\frac{\nabla^2}{2m_r} - \frac{Z}{\hat{r}}, \tag{2.2}$$

where r is the distance between electron and core, and $m_r = \frac{m_e m_c}{m_c+m_e}$ is the reduced mass of the electron with mass m_e and the core with mass m_c. We neglect fine-structure contributions due to spin-orbit coupling, as they are of the order of a few hundred hertz which is six orders of magnitude smaller than the transition frequencies we consider in this work. The hyperfine structure is a further three orders of magnitude smaller [9].

The potential $\hat{V}_\mathrm{C}(\hat{r}) = -Z/\hat{r}$ is a central potential, as it only depends on the distance r between the electron and the core. Therefore, the angular momentum $\hat{\boldsymbol{L}} = \hat{\boldsymbol{r}} \times \hat{\boldsymbol{p}}$ of the electron is conserved. By expressing the Laplace operator ∇^2 in spherical coordinates and introducing a product ansatz for the wavefunction, $\psi(\boldsymbol{r}) = R(r)Y(\vartheta,\varphi)$, the Schrödinger equation $\hat{H}_0\psi(\boldsymbol{r}) = E\psi(\boldsymbol{r})$ can be separated into a radial and angular part [8]. The solution of the angular part is given by spherical harmonics $Y_\ell^m(\vartheta,\varphi)$ where ℓ can take non-negative integer values and m takes values between $-\ell$ and ℓ. The spherical harmonics are eigenfunctions of the angular momentum operator, satisfying

$$\hat{\boldsymbol{L}}^2 Y_\ell^m(\vartheta,\varphi) = \ell(\ell+1)\, Y_\ell^m(\vartheta,\varphi), \tag{2.3a}$$

$$\hat{L}_z Y_\ell^m(\vartheta,\varphi) = m\, Y_\ell^m(\vartheta,\varphi). \tag{2.3b}$$

ℓ and m are called the angular momentum and magnetic quantum number, respectively.

Introducing the substitution $R(r) = \rho(r)/r$ yields the radial Schrödinger equation [8]

$$\left(-\frac{1}{2m_r}\frac{\partial^2}{\partial r^2} + \frac{\ell(\ell+1)}{2m_r r^2} - \frac{Z}{r}\right)\rho(r) = E\,\rho(r). \tag{2.4}$$

In the following, we restrict ourselves to bound solutions with $E < 0$. Eq. (2.4) can be solved analytically and the radial wavefunctions, $R_{n\ell}(r)$, which depend on n and ℓ, can be expressed using generalized Laguerre polynomials [42]. n is a positive, non-zero integer and called the principal quantum number, and ℓ is the angular quantum number which can take values between 0 and $n-1$. The resulting eigenvalues are

$$E_n = -\frac{m_r Z^2}{2n^2} = -\frac{R\,Z^2}{n^2}, \tag{2.5}$$

where $R = m_r/2$ is the Rydberg constant. Note that the energy E_n only depends on n and not on ℓ or m. Each energy level is thus n^2-fold degenerate as a result of the symmetry of the Coulomb problem [43]. The state of the atom can be fully described by the complete set of commuting observables $\{\hat{H}_0, \hat{\boldsymbol{L}}^2, \hat{L}_z\}$ and their corresponding quantum numbers n, ℓ and m. In short, the eigenstates of hydrogen-like atoms can be labelled by $|n, \ell, m\rangle$.

2.1.2 Alkali atoms

The crucial difference between hydrogen-like and alkali atoms is their ionic core. While the former have only one electron, heavier atoms possess several electrons constituting one or multiple closed inner shells in addition to their single valence electron. If the valence electron of an alkali atom is highly excited, the overlap of its orbital with the ionic core is negligible. In this case, the electrons in the ionic core shield the charge of the atomic core and the valence electron effectively only "feels" one positive charge in the centre [8]. High-angular-momentum Rydberg states can thus be described equivalently to hydrogen atoms. As the ionic core has a finite size, however, the probability of the valence electron to be located inside the ionic core becomes significantly larger as the angular momentum decreases. The screening effect subsides and the valence electron starts to be affected by the inner structure of the ionic core. The positive charge inside the ionic core deepens the effective core potential with respect to the hydrogenic one. As a result, states with low angular momenta experience a tighter bonding which breaks the ℓ-degeneracy of the n-manifolds as shown in Fig. 2.1.

Beyond the lifted ℓ-degeneracy, accurate Rydberg spectroscopy reveals a j-dependence of the energy levels, where j is the quantum number corresponding to the total angular momentum operator $\hat{\boldsymbol{J}} = \hat{\boldsymbol{L}} + \hat{\boldsymbol{S}}$ with $\hat{S}$ being the spin-operator [8]. In general, j ranges from $|\ell - s|$ to $\ell + s$. For (effective) one electron systems with spin $s = \frac{1}{2}$, j takes only two values, $\ell \pm \frac{1}{2}$ (except for $\ell = 0$ where $j = \frac{1}{2}$). The lifted degeneracy is due to spin-orbit coupling and can be incorporated

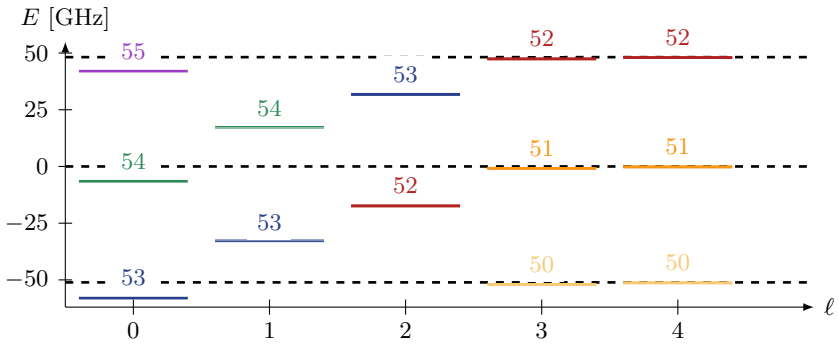

Figure 2.1: Quantitative spectrum of rubidium around the $n = 51$-manifold. The numbers above the levels denote their n value and states from the same n-manifold are depicted in the same colour. The vertical dashed lines present the energy levels of hydrogen. States with $\ell > 4$ coincide with the dashed lines on this scale. The origin of the energy scale is set to the hydrogenic state $n = 51$. The p-state ($\ell = 1$) splits up due to spin-orbit coupling; the upper state has $j = \frac{3}{2}$, the lower one $j = \frac{1}{2}$. The spin-orbit coupling of the other states is not visible on this scale.

in the Rydberg formula of Eq. (2.5) by modifying the principal quantum number n as [8],

$$E_{n\ell j} = -\frac{m_r Z^2}{2(n - \delta_{n\ell j})^2} = -\frac{R\, Z^2}{(n - \delta_{n\ell j})^2}, \tag{2.6}$$

where $\delta_{n\ell j}$ is called the quantum defect. Note that for alkali atoms, $Z = 1$, due to the shielding effect. The quantum defect is often parametrised via a modified Rydberg-Ritz expression [8] as

$$\delta_{n\ell j} = \delta_{\ell j,0} + \frac{\delta_{\ell j,2}}{(n - \delta_{\ell j,0})^2} + \ldots, \tag{2.7}$$

where the $\delta_{lj,i}$ on the right-hand side are empirical constants that describe the i-th order correction with i being an even number.

To calculate the wave function of the valence electron of an alkali atom, two modifications have to be considered with respect to the Coulomb potential $\hat{V}_{\mathrm{C}}(\hat{r})$. Firstly, the spin-orbit coupling is described by the additional term [43]

$$\hat{V}_{\mathrm{so}}(\hat{r}) = \frac{\alpha^2}{4\hat{r}^3}\Big(j(j+1) - \ell(\ell+1) - s(s+1)\Big), \tag{2.8}$$

where α is the fine structure constant. Spin-orbit coupling also occurs for hydrogen and hydrogen-like atoms but can usually be neglected. Secondly, the valence electron polarises the ionic core, a process that can be described as [8]

$$\hat{V}_{\mathrm{pol}}(\hat{r}) = -\frac{\alpha_c^2}{2\hat{r}^4}, \tag{2.9}$$

where α_c is the static dipole polarisability. It can be shown [8] that the expectation value $\langle r^{-4} \rangle$

scales as $n^{-3}\ell^{-5}$. The effect of both the spin-orbit coupling and the polarisability can be included in the quantum defect, as they are diagonal in the spherical basis and vanish as ℓ increases. Nevertheless, the modified potential plays a role if the wave functions are to be calculated, for instance for the calculation of matrix elements. Since the overall potential of the alkali atom,

$$\hat{V}_{\text{alkali}}(\hat{\boldsymbol{r}}) = \hat{V}_{\text{C}}(\hat{r}) + \hat{V}_{\text{so}}(\hat{\boldsymbol{r}}) + \hat{V}_{\text{pol}}(\hat{\boldsymbol{r}}), \tag{2.10}$$

is still spherically symmetric, the Schrödinger equation stays separable and the solution of the angular part is unchanged. The radial wave function, however, differs from the hydrogenic case, as the potential is no longer of Coulomb type. In this case, the radial Schrödinger equation cannot be solved analytically. Instead, we solve it numerically using Numerov's method [44] as explained in more detail in Sec. 3.1.1.

2.1.3 Matrix elements

Atoms can couple to, for instance, external electric fields or polar particles via their dipole moment, $\hat{\boldsymbol{d}} = q\hat{\boldsymbol{r}}$. In order to determine the interaction strength between Rydberg atoms and such objects later, we require the matrix elements of the position operator $\hat{\boldsymbol{r}}$. Using the product ansatz for the wave function, the matrix elements can be split into a spherical and a radial part,

$$\left\langle n\ell m \,\middle|\, \hat{\boldsymbol{r}} \,\middle|\, n'\ell'm' \right\rangle = \left\langle \ell m \left| \frac{\hat{\boldsymbol{r}}}{r} \right| \ell'm' \right\rangle \int dr\, r^2 R_{n\ell}(r)\, r\, R_{n'\ell'}(r), \tag{2.11}$$

which can be computed separately. The radial integral is solved either by numerical integration using the wavefunction previously obtained analytically for hydrogen-like atoms, or by using Numerov's method for alkali atoms as explained in Sec. 3.1.1. The angular term is identical for hydrogen-like and alkali atoms and can be solved analytically. Instead of calculating the matrix elements of each Cartesian components, $\hat{x}, \hat{y}$ and $\hat{z}$, directly, it is more convenient to move to the spherical basis given by $\hat{x} \pm i\hat{y}$ and $\hat{z}$. The matrix elements can be calculated using the properties of Legendre polynomials. The only non-vanishing elements are [43] $\langle \ell m|\hat{z}/r|\ell \pm 1, m\rangle$, $\langle \ell m|(\hat{x} \pm i\hat{y})/r|\ell + 1, m \pm 1\rangle$, and $\langle \ell m|(\hat{x} \pm i\hat{y})/r|\ell - 1, m \pm 1\rangle$, from which the well-known dipole transition selection rules $\Delta\ell = \pm 1$ and $\Delta m = 0, \pm 1$ can be derived. The analytic formulas for these matrix elements are given in Appendix B.1.

Higher order matrix elements,

$$\left\langle n\ell m \left| \prod_i^k \hat{x}_i \right| n'\ell'm' \right\rangle = \left\langle \ell m \left| \frac{\prod_i^k \hat{x}_i}{r^k} \right| \ell'm' \right\rangle \int dr\, r^2 R_{n\ell}(r)\, r^k\, R_{n'\ell'}(r), \tag{2.12}$$

can be calculated similarly. The radial part requires the evaluation of the radial integral of r^k, which can be done numerically. The angular part can be calculated using so-called spherical tensors $T_q^{(k)}$, where k is called the rank of the tensor and $q = -k, \ldots, k$. Above, we have already

used a spherical tensor of rank $k = 1$ with components defined as[1] [45]

$$T_0^{(1)} = z, \tag{2.13a}$$

$$T_{\pm 1}^{(1)} = \mp \frac{1}{\sqrt{2}}(x \pm iy). \tag{2.13b}$$

Spherical tensors are proportional to spherical harmonics. For example, the rank-1 tensor satisfies

$$T_q^{(1)} = \sqrt{\frac{4\pi}{3}} r Y_1^m. \tag{2.14}$$

As a result, spherical tensors of rank k transform like angular momentum eigenstates with $\ell = k$ under rotations. They are called irreducible tensors as they cannot be decomposed further without losing their transformation properties. Given two spherical tensors of rank k_1 and k_2, tensors of rank k can be constructed as [45]

$$T_q^{(k)} = \sum_{q_1} \sum_{q_2} \langle k_1, k_2; q_1 q_2 | k_1 k_2; kq \rangle \, T_{q_1}^{(k_2)} T_{q_2}^{(k_2)}, \tag{2.15}$$

where $\langle k_1, k_2; q_1 q_2 | k_1 k_2; kq \rangle$ are Clebsch-Gordan coefficients. When setting $k_1 = k_2 = 1$ and employing the tensors from Eq. (2.13), we obtain spherical tensors of rank 2 and 0 as shown explicitly in Appendix B.2. In more general terms, every (reducible) rank-2 tensor $(T_{ij})_{ij}$ can then be decomposed into three parts [45],

$$\boldsymbol{T} = \boldsymbol{T}^{(0)} + \boldsymbol{T}^{(1)} + \boldsymbol{T}^{(2)}, \tag{2.16}$$

where $\boldsymbol{T}^{(0)}$ is a rank-0 tensor (scalar) equal to the trace of the matrix; $\boldsymbol{T}^{(1)}$ is an antisymmetric rank-1 tensor; and $\boldsymbol{T}^{(2)}$ is a symmetric, traceless rank-2 tensor. Each of these three tensors is irreducible and has $2k + 1$ components. When employing the spherical basis, $\boldsymbol{T}^{(1)}$ is given by Eq. (2.13) and the other two terms can be derived using Eq. (2.15). As an example, we consider the next higher order of the multipole expansion, the quadrupole moment. While the dipole moment is a vector, the quadrupole moment takes the form of a 3×3 matrix, $\boldsymbol{Q} = (x_i x_j)_{x_i, x_j = x,y,z}$. However, not all of its elements are independent, as the matrix is symmetric, $x_i x_j = x_j x_i$. This reducible tensor can be expressed in terms of spherical tensors, namely rank-2 tensors and the rank-0 tensor which gives the trace of the matrix. Since the matrix is symmetric, no rank-1 tensor is involved. In Appendix B.2, we show explicitly the relations between the Cartesian and spherical tensor of rank 2 following [46].

When using the proportionality between spherical tensors and spherical harmonics, we can evaluate matrix elements of higher rank tensors easily. We exploit the well-known relation for

[1] The back transformation from spherical to Cartesian coordinates follows directly from inverting these equations and is explicitly given in Appendix B.1.

spherical harmonics [45]

$$\int_0^{2\pi}\int_0^{\pi} Y_{\ell_1}^{m_1} Y_{\ell_2}^{m_2} Y_{\ell_3}^{m_3} \sin\vartheta \, d\vartheta \, d\varphi = \sqrt{\frac{(2\ell_1+1)(2\ell_2+1)(2\ell_3+1)}{4\pi}} \begin{pmatrix} \ell_1 & \ell_2 & \ell_3 \\ 0 & 0 & 0 \end{pmatrix} \begin{pmatrix} \ell_1 & \ell_2 & \ell_3 \\ m_1 & m_2 & m_3 \end{pmatrix} \tag{2.17}$$

where the expressions in the brackets are Wigner 3j symbols [45]. Together with the property $Y_\ell^m = (-1)^m Y_\ell^{-m}$, we arrive at the expression

$$\langle \ell m | \, Y_k^q \, | \ell' m' \rangle = (-1)^m \sqrt{\frac{(2\ell+1)(2q+1)(2\ell'+1)}{4\pi}} \begin{pmatrix} \ell & q & \ell' \\ 0 & 0 & 0 \end{pmatrix} \begin{pmatrix} \ell & q & \ell' \\ -m & k & m' \end{pmatrix}, \tag{2.18}$$

for angular matrix elements into which we can insert Eq. (2.14) or tensors of higher rank.

The selection rules for the matrix elements follow from the properties of the Wigner 3j symbols. From the condition $m_1 + m_2 + m_3 = 0$ follows $\Delta m = m - m' = k$ and from $|\ell_1 - \ell_2| \leq \ell_3 \leq \ell_1 + \ell_2$ follows $|\ell - q| \leq \ell' \leq \ell + q$. In addition, $\ell_1 + \ell_2 + \ell_3$ must be an even number which means that for even (odd) q, $\Delta\ell = \ell - \ell'$ must be even (odd). For instance, for the dipole moment involving rank-1 tensors with $k = 1$ and $q = 0, \pm 1$, we obtain the well-known selection rules $\Delta m = 0, \pm 1$ and $\Delta\ell = \pm 1$. For the quadrupole moments, the selection rules are $\Delta m = 0, \pm 1, \pm 2$ and $\Delta\ell = 0, \pm 2$. The above formalism can be generalised to higher order tensors using Eq. (2.15). In Appendix B.3, we have derived the corresponding relations for the octupole moment with $k = 3$. The selection rules for the octupole are $\Delta m = 0, \ldots, \pm 3$ and $\Delta\ell = \pm 1, \pm 3$.

2.2 Stark effect

In a free, hydrogen-like atom, no quantisation axis is preferred due to the spherical symmetry of the Coulomb potential. As a result, each energy level has a n^2-fold degeneracy. An external electric field, however, can break the spherical symmetry and the total angular momentum is not a constant of motion any more. In this work, the splitting of the energy levels resulting from a coupling of the atom to an electric field, known as the Stark effect, plays a crucial role. We start by describing the Stark effect in hydrogen-like atoms in Sec. 2.2.1, to later on discuss the differences in alkali atoms in Sec. 2.2.2.

2.2.1 Hydrogen-like atoms

We consider a homogeneous, static (DC) electric field pointing in z-direction. The problem then becomes cylindrically symmetric, thus conserving the angular momentum along the z-axis and m stays a "good" quantum number. Good, in this context, means that the quantum number

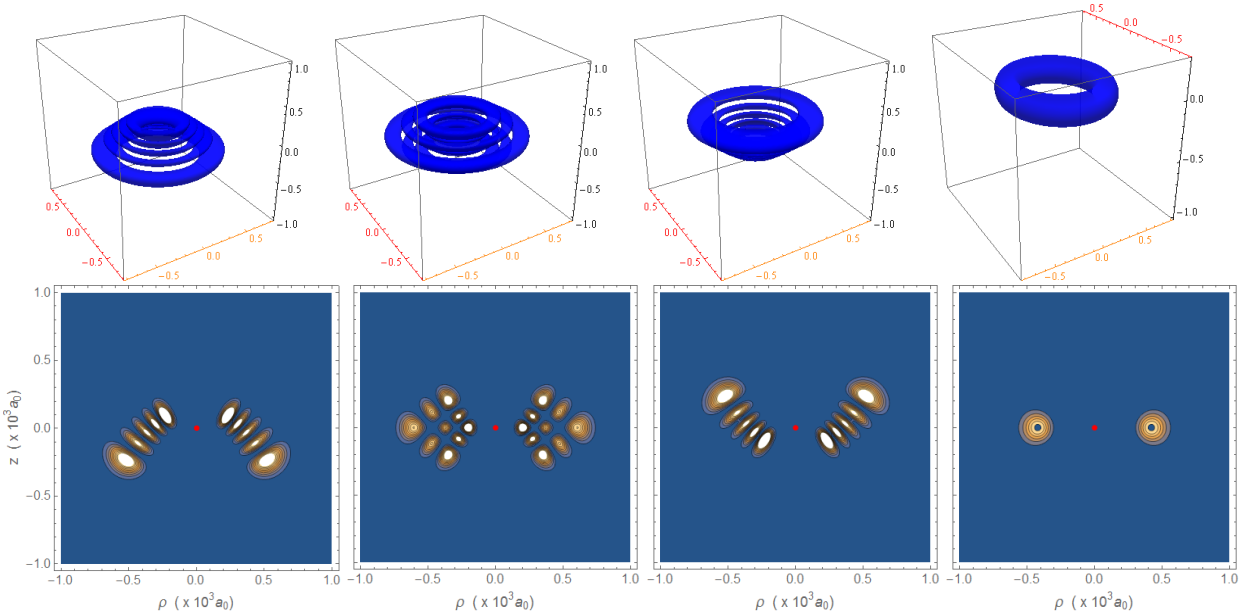

Figure 2.2: Wavefunctions for four different parabolic states in the hydrogen atom without DC field (from left to right): $|n = 21, m = 16, \mu = -4\rangle$, $|21, 16, 0\rangle$, $|21, 16, 4\rangle$, $|21, 20, 0\rangle$. The red dot marks the centre of mass. In the first row, the orbitals are shown in three dimensions with the vertical axis being the quantisation axis (z) with units of the $1000a_0$. The surfaces show areas with a probability density of $1.5 \cdot 10^{-9} a_0^{-3}$. The second row shows the projection onto the $z\rho$-plane. The colour map ranges from 0 (blue) to $1.5 \cdot 10^{-9} a_0^{-3}$ (white). Figure taken from [47].

corresponds to a conserved observable. The potential of the DC field is given by

$$\hat{V}_{\mathrm{DC}} = -\hat{\boldsymbol{d}} \cdot \boldsymbol{F}_{\mathrm{DC}} = \hat{z} F_{\mathrm{DC}} \tag{2.19}$$

with the dipole operator $\hat{\boldsymbol{d}} = q\hat{\boldsymbol{r}}$ and the amplitude of the DC field F_{DC}. The influence of the DC field on the eigenenergies of the hydrogen-like atoms can be calculated using perturbation theory. The spherical basis, however, is not practical for this task, as the DC field breaks spherical symmetry and ℓ is thus not a good quantum number any more. In the spherical basis, the matrix elements of the dipole operator vanish [43],

$$\langle n, \ell, m | \, q\hat{\boldsymbol{r}} \, | n, \ell, m \rangle = 0, \tag{2.20}$$

and hence the first order correction to the energy eigenvalues using degenerate perturbation theory vanish. Instead, another basis is utilised which reflects the symmetry of the problem more accurately.

In general, any problem involving a central force, such as the field-free hydrogen atom, can be separated in spherical coordinates. However, if the central force is of Coulomb type, $V(r) = -\kappa/r$, the separation can also be carried out in parabolic coordinates which turns out to be particularly useful for perturbation problems where one direction in space is distinguished [43],

such as in our case by the DC field. This alternative approach is connected to the "accidental degeneracy" of the Coulomb problem which can be understood more intuitively by comparing the free hydrogen atom to the classical Kepler problem. During the motion of a planet in the gravitational field of its star, three quantities are conserved: the energy, the angular momentum and the Lenz-Runge vector. The latter lies in the plane of motion and points from the focus to the perihelion, i.e. the nearest point of the orbit to its focus. It turns out [48] that its quantum mechanical analogue, the Lenz-Runge operator,

$$\hat{\boldsymbol{A}} = \frac{1}{2}\left(\hat{\boldsymbol{p}} \times \hat{\boldsymbol{L}} - \hat{\boldsymbol{L}} \times \hat{\boldsymbol{p}}\right) - m_r \kappa \frac{\hat{\boldsymbol{r}}}{r}, \tag{2.21}$$

is a constant of motion in hydrogen-like atoms resulting in the accidental degeneracy of states with the same n but different ℓ values. It can be shown [48] that its z-component commutes both with $\hat{H}_0$ and $\hat{L}_z$. When normalised within each eigenspace of $\hat{H}_0$, $\hat{\boldsymbol{a}} = \frac{1}{\sqrt{-2m_r E_n}}\hat{\boldsymbol{A}}$, it has the same dimension as an angular momentum. The eigenstates of a hydrogen-like atom can then be characterised by the complete set of commuting observables $\{\hat{H}_0, \hat{L}_z, -\hat{a}_z\}$ and their eigenvalues, $|n, m, \mu\rangle$. μ is the eigenvalue of the negative, normalised Lenz-Runge operator. It is called the eccentricity quantum number because it determines the eccentricity of the electronic orbital equivalently to the classical Lenz-Runge vector whose absolute value equals the eccentricity of the Kepler orbit. The corresponding wave functions can be obtained from solving the field-free Schrödinger equation in parabolic rather than spherical coordinates[1]. We accordingly refer to the basis $|n, m, \mu\rangle$ as the parabolic basis. Fig. 2.2 shows some exemplary orbitals. If $\mu < 0$ (first column), the electronic orbital is mainly located in the area with $z < 0$, and conversely for $\mu > 0$ (third column). Due to the shape of the orbitals, states with large values of $|\mu|$ are also called elliptic states. If $\mu = 0$, the orbital is symmetric with respect to the $z = 0$-plane (second and fourth column). It is apparent that the parabolic wave functions are in general asymmetric with respect to the $z = 0$ plane as opposed to the wave functions in the spherical basis. As a result, this basis is more suitable when considering problems with cylindrical symmetry.

Different from spherical coordinates, the Schrödinger equation of hydrogen-like atoms remains separable in the DC potential when using parabolic coordinates [8]. Although its solution cannot be calculated analytically, the corrections of the energy eigenvalues can be determined to arbitrary order using perturbation theory [50]. The first order correction is given by the diagonal elements of the potential $\hat{V}_{\mathrm{DC}}$ in Eq. (2.19). While the matrix elements of the potential, and hence the $\hat{z}$ operator, vanish in the spherical basis (cf. Eq. (2.20)), they can be evaluated in the parabolic basis as [49]

$$\langle n, m, \mu | \, \hat{z} \, | n, m, \mu \rangle = -\frac{3n}{2Z} \langle n, m, \mu | \, \hat{a}_z \, | n, m, \mu \rangle = \frac{3n}{2Z}\mu. \tag{2.22}$$

[1] Details on the solution of the hydrogenic Schrödinger equation using parabolic coordinates can be found for instance in [8, 43, 49].

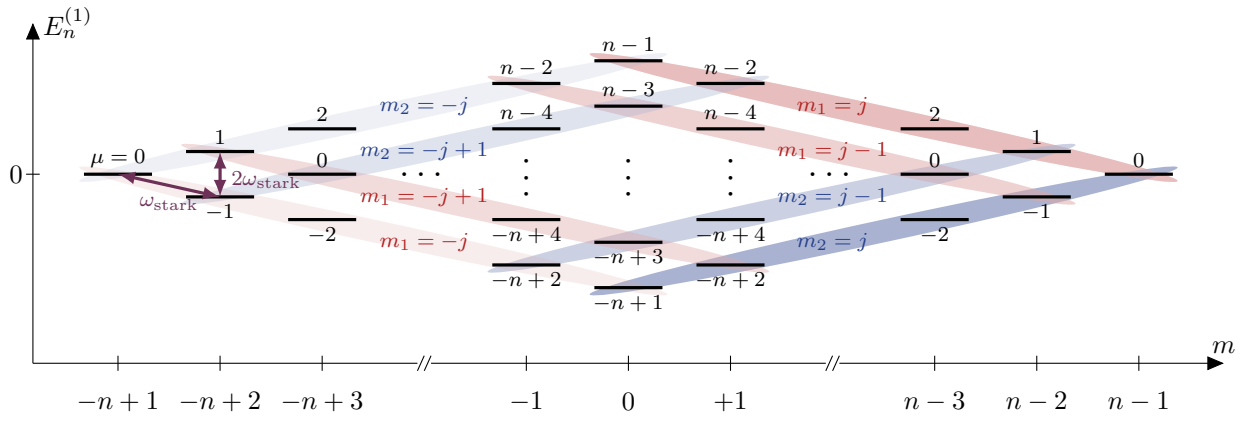

Figure 2.3: First order Stark shift for the states of one n-manifold. The energy levels are separated in ladders with constant values of m. The quantum number $\mu = m_1 - m_2$ is denoted next to each level. States with equal m_1 (m_2) quantum numbers are connected by red (blue) ellipses. The operators $\hat{J}_1^{\pm}$ ($\hat{J}_2^{\pm}$), and hence σ^+ (σ^-)-polarised light, couple states within each blue (red) area.

From this, the first order energy correction can be calculated to [43]

$$E_n^{(1)} = \frac{3}{2Z} F_{\text{DC}} n \mu, \tag{2.23}$$

which gives rise to the linear Stark effect, as the energy correction is linear in the DC field strength. For $n = 50$ and $F_{\text{DC}} = 1\,\frac{\text{V}}{\text{cm}}$, which is the parameter range we are interested in, the linear Stark effect is of the order of $100\,\text{MHz}$. The spectrum of one particular n-manifold, called the Stark manifold, is shown in Fig. 2.3. The energy shift does not depend on m and therefore, the degeneracy of one n-manifold is not entirely lifted. We can divide the manifold into vertical, harmonic m-ladders with an energy spacing of $2\omega_{\text{stark}}$ where

$$\omega_{\text{stark}} = \frac{3}{2Z} F_{\text{DC}} n, \tag{2.24}$$

such that $E_n^{(1)} = \omega_{\text{stark}}\,\mu$. Each ladder has $n - |m|$ steps and is symmetric with respect to the energy of the unperturbed energy E_n. Diagonal ladders, where m changes by one, have an energy spacing of ω_{stark}. The energy shift $E_n^{(1)}$ is proportional to μ which can be understood intuitively by considering the eccentricity of the orbital. As the DC field points in the z-direction, states with a $\mu > 0$ ($\mu < 0$) have a higher probability density in areas with high (low) electric potential which leads to an increase (decrease) in energy. Orbitals with $\mu = 0$, on the other hand, are symmetric with respect to the z-plane and their energy levels are unaffected by the DC field.

It can be shown that the second order correction, or the quadratic Stark effect, is given by [8]

$$E_n^{(2)} = -\frac{1}{16}\left(\frac{n}{Z}\right)^4 \left(17n^2 - 3\mu^2 - 9m^2 + 19\right) F_{\text{DC}}^2. \tag{2.25}$$

The energy shift is always negative and lifts the degeneracy between states with different $|m|$ but keeps the symmetry of states with opposite m values. The energy shift is a result of a mixing of parabolic states with different principal quantum numbers. We refer to the atomic eigenstates in presence of a DC field as the DC dressed eigenstates. For the considered field strengths, the second order Stark effect is two orders smaller than the first and can usually be neglected.

We close this section with a remark on the basis $|n, m, \mu\rangle$. Both $\hat{L}$ and $\hat{a}$ have the unit of angular momenta and commute with $\hat{H}_0$. However, $\hat{a}$ does not fulfil the commutation relations of angular momenta, and $\hat{\boldsymbol{L}}$ and $\hat{\boldsymbol{a}}$ do not commute with each other [49]. It is possible to recover two three-dimensional, commuting angular momentum operators by defining [49, 51, 48]

$$\hat{\boldsymbol{J}}_1 = \tfrac{1}{2}\left(\hat{\boldsymbol{L}} - \hat{\boldsymbol{a}}\right), \tag{2.26a}$$

$$\hat{\boldsymbol{J}}_2 = \tfrac{1}{2}\left(\hat{\boldsymbol{L}} + \hat{\boldsymbol{a}}\right). \tag{2.26b}$$

Each component of $\hat{\boldsymbol{J}}_1$ commutes with each component of $\hat{\boldsymbol{J}}_2$ and with $\hat{H}_0$ (and vice versa). We can denote the eigenvalues of $\hat{\boldsymbol{J}}_\alpha^2$ as $j_\alpha(j_\alpha + 1)$ with $\alpha = 1, 2$ and write

$$j_\alpha = \frac{n-1}{2} \equiv j \tag{2.27}$$

from which follows that j is either an integer or half-integer. $\hat{\boldsymbol{J}}_1$ and $\hat{\boldsymbol{J}}_2$ define two independent angular momenta with a fixed absolute value in a subspace of constant n. Within each subspace, we can characterise the states by their projections $\hat{J}_{\alpha z}$ on the z-axis; their eigenvalues m_α take the n integer values between $\pm j$. Hence, the parabolic states can also be written as $|n, m_1, m_2\rangle$. In fact, the two notations $|n, m_1, m_2\rangle$ and $|n, m, \mu\rangle$ are equivalent: by construction (cf. Eq. (2.26)), $|n, m_1, m_2\rangle$ are eigenstates of $\hat{a}_z$ and $\hat{L}_z$,

$$\hat{a}_z |n, m_1, m_2\rangle = (m_2 - m_1) |n, m_1, m_2\rangle, \tag{2.28}$$

$$\hat{L}_z |n, m_1, m_2\rangle = (m_1 + m_2) |n, m_1, m_2\rangle. \tag{2.29}$$

Since we denote the eigenvalues of $\hat{L}_z$ and $\hat{a}_z$ by m and $-\mu$, it follows that $m = m_1 + m_2$ and $\mu = m_1 - m_2$. From this and the possible values of m_i, we can conclude that for a fixed n and m, μ can take the values between $-(n - |m| - 1)$ and $(n - |m| - 1)$ in steps of two. The red and blue ellipses in Fig. 2.3 mark states with identical values of m_1 and m_2, respectively.

2.2.2 Alkali atoms

In alkali atoms, the n^2-fold degeneracy of each energy level is partly lifted even in absence of an external DC field due to the penetration of the valence electron into the ionic core. As a result, the analytic calculations shown above strictly apply only to hydrogen-like atoms. However, as we discuss in the following section, the hydrogenic model constitutes an excellent approximation for alkali atoms under certain conditions.

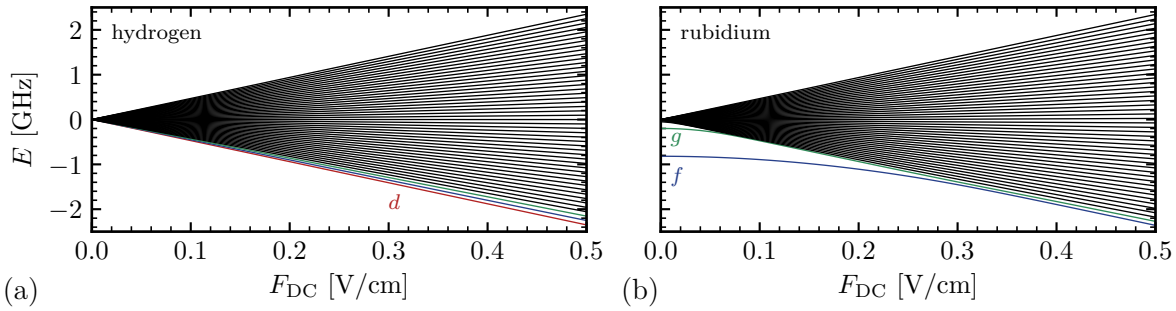

Figure 2.4: Stark map for the $n = 51$, $m = 2$-manifold for hydrogen (a) and rubidium (b). The data was obtained by numerically diagonalising the full Hamiltonian. The states which have $\ell = 2$ (d, red), 3 (f, blue) and 4 (g, green) at zero field are highlighted in different colours.

Without a DC field, states with small values of ℓ are displaced from the centre of each n-manifold due to the penetration of the orbitals into the ionic core (cf. Fig. 2.1). The quantum defect $\delta_{n\ell j}$ therefore determines the spectrum of alkali atoms as given by Eq. (2.6) in the absence of a DC field, where the potential is spherically symmetric. As the quantum defect is ℓ-dependent, the spherical basis is the most suitable to label the energy levels. We use the notation $|n\ell, m\rangle$ to characterise quantum defect states with ℓ being represented by the standard spectroscopic notations ($s, p, d, f, \ldots$; e.g. $|51f, 2\rangle$ for $n = 51$, $\ell = 3$, $m = 2$).

Fig. 2.4 shows the Stark map, i.e. the energy of the DC dressed eigenstates as a function of the DC field strength, of hydrogen and rubidium for $n = 51$ and $m = 2$ in comparison. Since hydrogen, shown in Fig. 2.4 (a), does not have a quantum defect, the energy splitting increases linearly with the DC field. For rubidium, shown in panel (b), low-angular-momentum states are displaced from the manifold due to the quantum defect. As the DC field is gradually switched on, the Stark effect eventually becomes larger than the energy shift by the quantum defect and the previously displaced states join the Stark manifold. States with high angular momenta, $\ell > 4$, have such a weak quantum defect that they join the Stark manifold for very weak fields, $F_{\mathrm{DC}} < 0.03\,\frac{\mathrm{V}}{\mathrm{cm}}$. The g-state ($\ell = 4$) joins around $0.08\,\frac{\mathrm{V}}{\mathrm{cm}}$, followed by the f-state ($\ell = 3$) at $0.3\,\frac{\mathrm{V}}{\mathrm{cm}}$. For the states within the Stark manifold, the cylindrical potential induced by the DC field is dominating and the parabolic basis is the most suitable to describe the states. The quantum defect of states with $\ell < 3$, on the other hand, is too big for the states to join their respective manifold. The d-state ($\ell = 2$), for instance, is shifted down by $\sim 70\,\mathrm{GHz}$ such that it is located below the adjacent $n = 50$ manifold (cf. Fig. 2.1). The $n = 51$ and 50 manifolds collide around $5.5\,\frac{\mathrm{V}}{\mathrm{cm}}$ – before the $51d$-state could join its corresponding manifold. Instead, the $52d$ state join the $n = 51$ manifold around $4.4\,\frac{\mathrm{V}}{\mathrm{cm}}$.

The absence of some states from the Stark manifold modifies the energy splitting of the corresponding m-ladder as illustrated in Fig. 2.5 (a). For $m = 0, 1$ and 2, there are three (s, p and d), two (p and d) and one (d) states missing from the vertical ladders, respectively. Ladders with $m \geq 3$, on the other hand, behave hydrogenically for fields higher than $0.3\,\frac{\mathrm{V}}{\mathrm{cm}}$ (cf. Fig. 2.4 (b)).

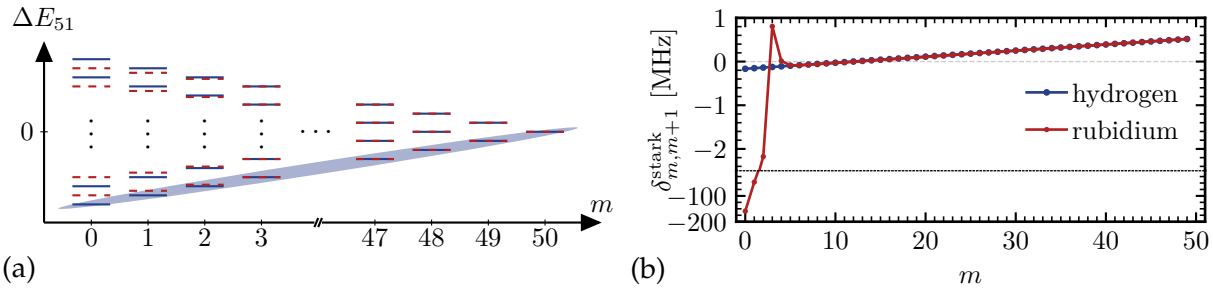

Figure 2.5: (a) Schematic Stark manifold for $m \geq 0$ and $n = 51$ for hydrogen (solid blue) and rubidium (dashed red) for a moderate DC field. The zero of energy was set to the field-free energy of hydrogen. The states of rubidium with $|m| \leq 2$ are significantly affected by the quantum defect. (b) Numerically calculated detuning, $\delta^{\text{stark}}_{m,m+1} = (E_{m+1} - E_m) - \omega_{\text{stark}}$ of the lowest diagonal ladder (blue ellipse in a) of hydrogen and rubidium for $n = 51$ and $F_{\text{DC}} = 2.346\,\frac{\text{V}}{\text{cm}}$ with respect to $\omega_{\text{stark}} = 229.64\,\text{MHz}$. Notice the different scaling of the y-axis above the black dashed line.

The modification affects most importantly the transition frequencies of the diagonal ladders, as shown in Fig. 2.5 (b). The linear slope for $m > 4$ is due to the second order Stark effect and occurs also for hydrogen. The harmonicity of the diagonal ladder is broken significantly for $m < 2$ due to the missing quantum defect states.

2.3 Dynamics in the generalised Bloch sphere

In the previous section, we have reviewed the time-independent problem of a Rydberg atom in a static electric field. We now introduce time-dependent pulses which drive transitions between the DC dressed eigenstates. The potential induced by a time-dependent electric field (the "drive") can be described similarly to a DC field (cf. Eq. (2.19)) as

$$\hat{V}_{\text{AC}}(t) = \hat{\boldsymbol{r}} \cdot \boldsymbol{F}_{\text{AC}}(t). \tag{2.30}$$

If the driving field is linearly polarised in z-direction, i.e. $\boldsymbol{F}_{\text{AC}}(t) = F_{\text{AC}}(t)\boldsymbol{e_z}$, it is called π-polarised. Due to the selection rule of the $\hat{z}$-operator (cf. Eq. (B.5)), a π-polarised pulse drives transitions with $\Delta m = 0$ and $\Delta l = \pm 1$. If the pulse is left or right circularly polarised with the electric field vector rotating in the xy-plane, it is called $\sigma^{\pm}$-polarised and it drives transitions with $|\Delta m| = 1$ and $|\Delta \ell| = 1$ as we show in detail in Sec. 2.3.1. For $n \sim 50$, transitions between adjacent n-manifolds are of the order of $50\,\text{GHz}$ and can be induced by microwave (MW) pulses. The transition frequencies between states within the same Stark manifold are determined by the Stark effect and are the ones we will be most interested in. For $n \sim 50$ and moderate DC fields around $1\,\frac{\text{V}}{\text{cm}}$, they are of the order of $100\,\text{MHz}$ and hence in the radio frequency (RF) regime. In Sec. 2.3.1, we thoroughly discuss the coupling of parabolic states by an RF pulse which gives rise to n-level Rabi oscillation in the generalised Bloch sphere spanned by diagonal ladders within the

Stark manifold. Afterwards, in Sec. 2.3.2, we present a special class of states, called spin coherent states, which arise naturally when Rydberg atoms are driven by RF pulses. Note that a similarly concise summary of the topic can be found in Refs. [52, 47, 1].

2.3.1 n-level Rabi oscillation and the generalised Bloch sphere

A $\sigma^{\pm}$-polarised drive can be written as

$$\begin{aligned}\boldsymbol{F}^{\pm}_{\mathrm{RF}}(t) &= 2F_{\mathrm{RF}}\big(\cos(\omega_{\mathrm{RF}}t+\phi_{\mathrm{RF}})\boldsymbol{e}_x \pm \sin(\omega_{\mathrm{RF}}t+\phi_{\mathrm{RF}})\boldsymbol{e}_y\big)\\ &= F_{\mathrm{RF}}\left(e^{\mp i(\omega_{\mathrm{RF}}t+\phi_{\mathrm{RF}})}(\boldsymbol{e}_x+i\boldsymbol{e}_y)+e^{\pm i(\omega_{\mathrm{RF}}t+\phi_{\mathrm{RF}})}(\boldsymbol{e}_x-i\boldsymbol{e}_y)\right)\end{aligned} \tag{2.31}$$

where F_{RF} is the field strength, ω_{RF} the frequency and ϕ_{RF} the phase of the driving field. The potential in Eq. (2.30) then takes the form

$$\hat{V}^{\pm}_{\mathrm{AC}}(t) = F_{\mathrm{RF}}\left(e^{\mp i(\omega_{\mathrm{RF}}t+\phi_{\mathrm{RF}})}(\hat{x}+i\hat{y})+e^{\pm i(\omega_{\mathrm{RF}}t+\phi_{\mathrm{RF}})}(\hat{x}-i\hat{y})\right). \tag{2.32}$$

The operators $\hat{x}\pm i\hat{y}$ couple the state $|nm_1m_2\rangle$ to $|nm_1\pm 1m_2\rangle$ and to $|nm_1m_2\pm 1\rangle$ (cf. matrix elements of Eq. (B.6) in Appendix B.1). It is possible to decouple the two ladders m_1 and m_2 by utilising the two angular momenta $\hat{\boldsymbol{J}}_\alpha$ with $\alpha = 1,2$ introduced in Eq. (2.26). To this end, the corresponding ladder operators are introduced as

$$\hat{J}^{\pm}_{\alpha} = \hat{J}_{\alpha,x} \pm i\hat{J}_{\alpha,y} \tag{2.33}$$

with matrix elements

$$\hat{J}^{\pm}_1|n,m_1,m_2\rangle = \sqrt{j(j+1)-m_1(m_1\pm 1)}\,|n,m_1\pm 1,m_2\rangle\,, \tag{2.34a}$$

$$\hat{J}^{\pm}_2|n,m_1,m_2\rangle = \sqrt{j(j+1)-m_2(m_2\pm 1)}\,|n,m_1,m_2\pm 1\rangle\,. \tag{2.34b}$$

The Cartesian components can be recovered by the transformation

$$\hat{J}_{\alpha,x} = \frac{1}{2}(\hat{J}^{+}_{\alpha}+\hat{J}^{-}_{\alpha}),\quad \hat{J}_{\alpha,y} = \frac{1}{2i}(\hat{J}^{+}_{\alpha}-\hat{J}^{-}_{\alpha}),\quad \hat{J}_{\alpha,z} = \frac{1}{2}(\hat{J}^{+}_{\alpha}\hat{J}^{-}_{\alpha}-\hat{J}^{-}_{\alpha}\hat{J}^{+}_{\alpha}). \tag{2.35}$$

When comparing the matrix elements of the ladder operators in Eq. (2.34) with the matrix elements of $\hat{x}\pm i\hat{y}$, it is possible to deduce the relation,

$$\hat{x}\pm i\hat{y} = \frac{3n}{Z}\left(\hat{J}^{\pm}_1\otimes\hat{\mathbb{1}}_2-\hat{\mathbb{1}}_1\otimes\hat{J}^{\pm}_2\right). \tag{2.36}$$

Inserting this into the potential leads to

$$\hat{V}^{\pm}_{\mathrm{AC}}(t) = V\left(e^{\mp i(\omega_{\mathrm{RF}}t+\phi_{\mathrm{RF}})}\left(\hat{J}^{+}_1\otimes\hat{\mathbb{1}}_2-\hat{\mathbb{1}}_1\otimes\hat{J}^{+}_2\right)+e^{\pm i(\omega_{\mathrm{RF}}t+\phi_{\mathrm{RF}})}\left(\hat{J}^{-}_1\otimes\hat{\mathbb{1}}_2-\hat{\mathbb{1}}_1\otimes\hat{J}^{-}_2\right)\right), \tag{2.37}$$

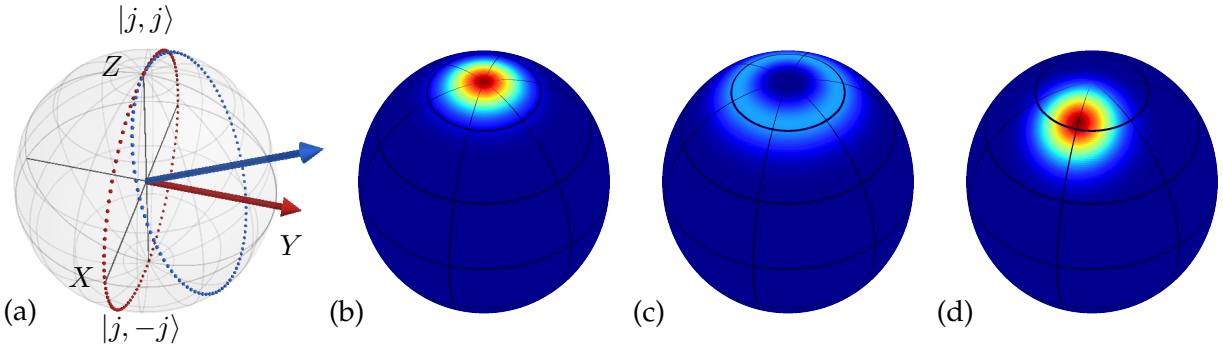

Figure 2.6: (a) Axes of the generalised Bloch sphere and two exemplary rotation axes. The dots display the thereby induced trajectories of the initial state $|j,j\rangle$. The red arrow depicts the rotation axis of a resonant drive with $\varphi = 0$, the drive leading to the blue arrow is slightly detuned. (b-d) Q-functions of four different states on the generalised Bloch sphere with $n = 51 \Rightarrow j = 25$. (b) Parabolic state $|j,j\rangle$ or SCS $|\vartheta = 0, \varphi\rangle$ with arbitrary φ. (c) Parabolic state $|j, m_1 = 23\rangle$. (d) SCS $|\vartheta = 0.4, \varphi = 0\rangle$ with $\langle \hat{J}_{1,z}\rangle = 23$ (cf. Eq. (2.44)). This state is the result of rotating state (b) by $\vartheta = 0.4$ around the red axis in (a).

where $V = \frac{3n}{Z} F_{\mathrm{RF}}$ is the coupling strength. This expression can be simplified by removing off-resonant terms. When considering, for example, a σ^+-polarised pulse, the first term in the sum creates an excitation in m_1 via the operator $\hat{\boldsymbol{J}}_1^+$, which increase the energy, while absorbing one RF photon. The third term in the sum annihilates an excitation in m_1 via the operator $\hat{\boldsymbol{J}}_1^-$, which decrease the energy, while emitting one RF photon. The remaining two terms, on the other hand, are off-resonant and can thus be removed in the rotating wave approximation. The reasoning is equivalent for σ^--polarised pulse when considering the m_2 ladder, instead. In summary, the potential of the two possible polarisations can be written as

$$\hat{V}_{\mathrm{RF}}^+(t) = V\left[\left(\hat{J}_1^+ \otimes \hat{\mathbb{1}}_2\right) e^{-i(\omega_{\mathrm{RF}} t + \phi_{\mathrm{RF}})} + \left(\hat{J}_1^- \otimes \hat{\mathbb{1}}_2\right) e^{+i(\omega_{\mathrm{RF}} t + \phi_{\mathrm{RF}})}\right] \tag{2.38a}$$

$$\hat{V}_{\mathrm{RF}}^-(t) = -V\left[\left(\hat{\mathbb{1}}_1 \otimes \hat{J}_2^-\right) e^{-i(\omega_{\mathrm{RF}} t + \phi_{\mathrm{RF}})} + \left(\hat{\mathbb{1}}_1 \otimes \hat{J}_2^+\right) e^{+i(\omega_{\mathrm{RF}} t + \phi_{\mathrm{RF}})}\right] \tag{2.38b}$$

Eq. (2.38a) shows that a σ^+-polarised pulse induces transitions in $\hat{\boldsymbol{J}}_1$ with $\Delta m_1 = \pm 1$ while leaving $\hat{\boldsymbol{J}}_2$ unchanged. It couples states within diagonal ladders, marked by the blue ellipses in Fig. 2.3. From the figure we also see that, in other words, a σ^+-polarised pulse drives transitions between states with $\Delta m = +1$ (-1) whilst increasing (decreasing) the energy. The opposite rules apply for σ^--polarised pulses (red ellipses).

It is now possible to restrict the dynamics to one of the diagonal ladders within the Stark manifold if a purely σ^+ or σ^--polarised pulse is employed. In the following, we review how these dynamics can be interpreted as rotations on a generalised, n-dimensional Bloch sphere. For simplicity, we henceforth assume a σ^+-polarised pulse which allows us to decompose the Hilbert space into independent diagonal ladders with constant values of m_2. If the initial state is located on one of these ladders, i.e. it can be written as $|\Psi(t=0)\rangle = \sum_{m_1} c_{m_1} |n, m_1, m_2\rangle$ with fixed n

and m_2, it is possible to reduce the Hilbert space to just one diagonal ladder[1], i.e. any one blue ellipse in Fig. 2.3. Each diagonal ladder can be interpreted as an n-level, or spin-j, system with $n = 2j+1$ where n is the principal quantum number and m_1 takes all the values from $-j$ to j. We therefore denote the basis states in the standard notation for angular momenta, $|j, m_1\rangle_{n,m_2}$. Up to first order in the electric field and by using Eq. (2.38a), the Hamiltonian of the driven n-level system, $\hat{H}^+ = \hat{H}_0 + \hat{V}_{\text{DC}} + \hat{V}^+_{\text{RF}}$, of a hydrogen-like atom can be written as a tridiagonal matrix

$$\hat{H}^+ = \begin{pmatrix} -j\omega_{\text{stark}} & V_{-j}e^{+i(\omega_{\text{RF}}t+\phi_{\text{RF}})} & 0 & \dots & 0 \\ V_{-j}e^{-i(\omega_{\text{RF}}t+\phi_{\text{RF}})} & (-j+1)\omega_{\text{stark}} & V_{-j+1}e^{+i(\omega_{\text{RF}}t+\phi_{\text{RF}})} & & \vdots \\ 0 & V_{-j+1}e^{-i(\omega_{\text{RF}}t+\phi_{\text{RF}})} & \ddots & & 0 \\ \vdots & & & \ddots & V_{j-1}e^{+i(\omega_{\text{RF}}t+\phi_{\text{RF}})} \\ 0 & \dots & 0 & V_{j-1}e^{-i(\omega_{\text{RF}}t+\phi_{\text{RF}})} & j\omega_{\text{stark}} \end{pmatrix},$$

with ω_{stark} as given in Eq. (2.24), and the matrix elements $V_{m_1} = V\sqrt{j(j+1) - m_1(m_1+1)}$. By going to a frame of reference rotating with the driving field frequency ω_{RF}, the Hamiltonian becomes time-independent,

$$\hat{H}^+_{\text{RF}} = \begin{pmatrix} -j\delta & V_{-j}e^{i\phi_{\text{RF}}} & 0 & \dots & 0 \\ V_{-j}e^{-i\phi_{\text{RF}}} & (-j+1)\delta & V_{-j+1}e^{i\phi_{\text{RF}}} & & \vdots \\ 0 & V_{-j+1}e^{-i\phi_{\text{RF}}} & \ddots & & 0 \\ \vdots & & & \ddots & V_{j-1}e^{i\phi_{\text{RF}}} \\ 0 & \dots & 0 & V_{j-1}e^{-i\phi_{\text{RF}}} & j\delta \end{pmatrix}$$

with the detuning $\delta = \omega_{\text{stark}} - \omega_{\text{RF}}$. Finally, by defining the Rabi frequency,

$$\Omega_{\text{RF}} = 2V = 6F_{\text{RF}}n, \tag{2.39}$$

and utilising the definition of the components of $\hat{\boldsymbol{J}}_1$ in Eq. (2.35), the Hamiltonian can be written in the simple form

$$\hat{H}^+_{\text{RF}} = \boldsymbol{\Omega} \cdot \hat{\boldsymbol{J}}_1, \quad \text{with} \quad \boldsymbol{\Omega} = (\Omega_{\text{RF}} \cos\phi_{\text{RF}},\, \Omega_{\text{RF}} \sin\phi_{\text{RF}},\, \delta)\,, \tag{2.40}$$

with the generalised Rabi frequency $\Omega = |\boldsymbol{\Omega}| = \sqrt{\Omega^2_{\text{RF}} + \delta^2}$. Since the Hamiltonian is time-independent, the solution of the Schrödinger equation is simply given by

$$|\Psi(t)\rangle = e^{-i\boldsymbol{\Omega}\cdot\hat{\boldsymbol{J}}_1 t}\,|\Psi(t=0)\rangle\,. \tag{2.41}$$

The dynamics can be interpreted as the rotation of a Bloch vector on a generalised Bloch sphere. The coordinates (X, Y, Z) on this sphere are defined as the expectation values of the three angular momenta $\langle \hat{J}_{1,x_i}\rangle_{\Psi(t)}$ with $x_i = x, y, z$. The Z component is equal to the expectation value of m_1,

[1] The following discussion can be generalised to σ^--polarised pulses or mixtures, and arbitrary initial states straightforwardly by linear combination

i.e. $\langle \hat{J}_{1,z} \rangle_{\Psi(t)} = \langle m_1 \rangle_{\Psi(t)}$. Fig. 2.6 (a) depicts two exemplary trajectories on the Bloch sphere. The dotted lines indicate the precession of the state's Bloch vector around the rotation axis $\mathbf{\Omega}$ (red or blue arrow) with the angular frequency Ω. In resonance, $\delta = 0$ (red), the Bloch vector rotates between the north and south pole of the sphere. In the presence of a detuning, the direction of the rotation axis changes such that the Bloch vector does not reach the south pole any more.

Before discussing some special states on the generalised Bloch sphere, some limits to this representation shall be pointed out. Firstly, the n-level system was assumed to be harmonic. As shown in Fig. 2.5 (b), even hydrogen-like atoms are slightly anharmonic due to the second order Stark effect. Alkali atoms show an even stronger anharmonicity towards small $|m|$ due to the quantum defect. To account for this, we have to consider a state-dependent detuning $\delta^{\text{RF}}_{m_1,m_1+1} = (E_{m_1+1} - E_{m_1}) - \omega_{\text{RF}}$ with respect to the frequency ω_{RF} of the driving field. Hereby, the Z-component of the generalised Rabi frequency (i.e. replacing δ in Eq. (2.40) by $\delta^{\text{RF}}_{m_1,m_1+1}$) becomes state-dependent. This results in a state-dependent rotation around the Z-axis and thus an azimuthal drift of the Bloch vector. Secondly, the Hilbert space has been restricted to one diagonal ladder with a fixed value of m_2. However, even if the initial state is perfectly located on one m_2 ladder, some population might get excited to states with $m_2' = m_2 \pm 1$, i.e. one of the adjacent blue ellipses in Fig. 2.3. This might happen due to two reasons. On the one hand, impurely polarised light in a realistic experiment with fractions of σ^--polarisation induces transitions in m_2 with constant m_1 values (i.e. drive the population along the red ellipses in Fig. 2.3). On the other hand, higher order Stark effects induce mixing of the parabolic states which allows previously forbidden transitions. Since this mixing is weak and the transitions highly off-resonant with a frequency of $3\omega_{\text{stark}}$, they only play a role if the drive is very strong. However, if these assumptions do not hold, it is not possible to reduce the Hilbert space to just one diagonal ladder. The picture of the generalised Bloch sphere is thus no longer sufficient, as the system is not an n-level system any more.

2.3.2 Spin coherent states

In Eq. (2.41), we have written the dynamics in the generalised Bloch sphere in form of a rotation of the angular momentum $\hat{\boldsymbol{J}}_1$ around the axis defined by Ω. Even though the generalised Bloch sphere describes a large spin-j system, we show in the following that for a particular class of states, two coordinates are sufficient for a complete characterisation. We set $\varphi = \phi_{\text{RF}} - \pi/2$ such that φ describes the angle between the rotation axis and the Y-axis. For simplicity, we further assume a resonant drive, $\delta = 0$, while the following results can also be generalised to the off-resonant case. In resonance, $\mathbf{\Omega}$ lies in the XY-plane of the Bloch sphere (see e.g. red arrow in Fig. 2.6 (a)) and the time evolution operator can be written as,

$$\mathcal{R}(\vartheta, \varphi) = e^{-i\vartheta(J_{1,x}\sin\varphi - J_{1,y}\cos\varphi)}, \tag{2.42}$$

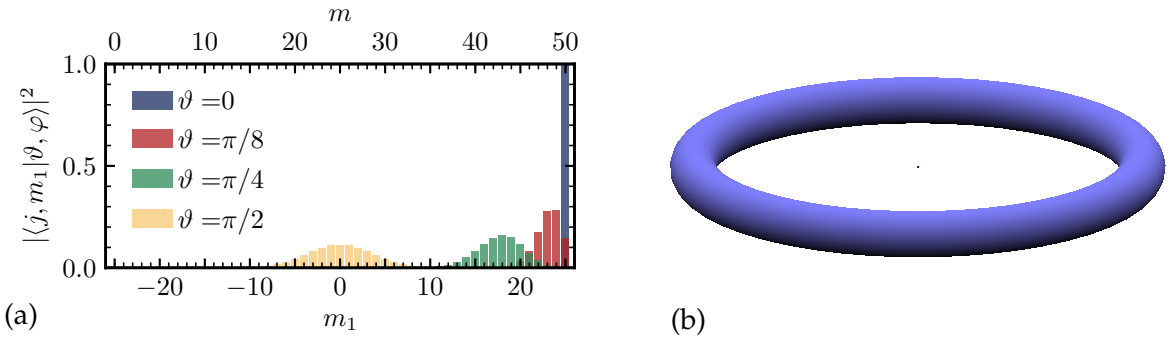

Figure 2.7: (a) Overlap of four different SCS with the parabolic states of one diagonal ladder for $n = 51$. The overlap is independent of φ and m_2. The m-values on top refer to the case where $m_2 = j$, i.e. the lowest diagonal ladder of the Stark manifold. (b) Orbital of the circular state, $|j, j\rangle_{n=51,m_2=j} = |\vartheta = 0, \varphi\rangle$. The red dot in the centre depicts the ionic core.

with the Rabi angle $\vartheta = \Omega_{\mathrm{RF}} t$. The angles ϑ and φ can be interpreted as the canonical angles of the spherical coordinates[1]. By applying $\mathcal{R}(\vartheta, \varphi)$ to the state $|j, m_1 = j\rangle_{n,m_2}$, which is the highest of the diagonal ladder, we can generate a so-called spin coherent state (SCS). The explicit expression of a SCS in the parabolic basis is given by [53]

$$|\vartheta, \varphi\rangle = \mathcal{R}(\vartheta, \varphi)\,|j, j\rangle_{n,m_2} = \sum_{m_1=-j}^{j} \binom{2j}{j+m_1}^{1/2} \left(\cos\frac{\vartheta}{2}\right)^{j+m_1} \left(\sin\frac{\vartheta}{2}\right)^{j-m_1} e^{i(j-m_1)\varphi}\,|j, m_1\rangle_{n,m_2}\,. \tag{2.43}$$

As shown in Fig. 2.7 (a), the overlap of a SCS with the parabolic states follows a binomial distribution while being independent of φ, n and m_2. For $\vartheta = 0$ (π), which corresponds to the north (south) pole of the sphere, the sine (cosine) term becomes zero except for $m_1 = j$ ($-j$). This entails the special cases $|\vartheta = 0, \varphi\rangle = |j, j\rangle_{n,m_2}$ (by construction) and $|\vartheta = \pi, \varphi\rangle \propto |j, -j\rangle_{n,m_2}$. For $\vartheta \sim \frac{\pi}{2}$, on the other hand, the distribution is very similar to a Gaussian and spreads across many parabolic states. The angle ϑ is connected to the Z-component of the Bloch vector of a SCS via

$$\cos\vartheta = \frac{\langle m_1\rangle}{j} = \frac{\langle \hat{J}_{1,z}\rangle}{j}. \tag{2.44}$$

SCS are the analogue to coherent states $|\alpha\rangle$ in harmonic oscillators which are prominently employed in quantum optics [9]. In particular, it can be shown [53] that SCS are minimum-uncertainty states and thus as close an approach to classical localisation as is possible.

[1]Note that φ denotes the angle between X axis and the projection of the Bloch vector on the XY plane, thus justifying this interpretation. For $\phi = 0$, the state rotates in the XZ plane such that the angle between the Bloch vector and the X axis is 0. The rotation vector Ω, on the other hand, is orthogonal to this plane and thus points in Y direction.

SCS are the only states which can be characterised completely by a single point (ϑ, φ) on the generalised Bloch sphere. For all other states, this is not sufficient, as the system is n-dimensional. The only exception is the two-level system with $n = 2$ and $j = \frac{1}{2}$. In this case, the SCS of Eq. (2.43) can be brought to the well-known form

$$|\vartheta, \varphi\rangle = \cos\left(\frac{\vartheta}{2}\right) \left|\frac{1}{2}, -\frac{1}{2}\right\rangle + \sin\left(\frac{\vartheta}{2}\right) e^{i\varphi} \left|\frac{1}{2}, \frac{1}{2}\right\rangle, \tag{2.45}$$

which is the most general form of a pure state in a two-level system. Larger spin systems, $n > 2$, can be visualised more appropriately using the Husimi Q representation [54, 55],

$$Q_\Psi(\vartheta, \varphi) = \frac{2j+1}{4\pi} |\langle \vartheta, \varphi | \Psi \rangle|^2, \tag{2.46}$$

which is proportional to the overlap of a general state $|\Psi\rangle$ with the SCS $|\vartheta, \varphi\rangle$. The Q-function is normalised to 1 and allows for the reconstruction of the system's state. Some exemplary Q-functions are shown in Fig. 2.6.

Particularly relevant SCS are the so-called circular states [9]. Circular states are the Rydberg states in which the angular momentum takes its extremal value of $|m| = \ell = n - 1$. They are located at the outermost "tips" of the Stark manifold; one example being the north-pole of the Bloch sphere of the lowest diagonal ladder on the right-hand side ($m \geq 0$) of the Stark manifold. Circular states can decay via only one channel, namely from $|n, \ell\rangle$ to $|n-1, \ell-1\rangle$, giving rise to an increased lifetime proportional to n^5 corresponding to tens of milliseconds. Their name derives from the toroidal shape of their orbital, which is shown in Fig. 2.7 (b). The electron is confined to a narrow ring around the ionic core while being completely delocalised in the azimuthal direction. This results in almost Bohr-like orbits in which the electron describes a concise orbit around the ionic core. The ring has a radius $r_n = n^2$ and a relative dispersion of only $\Delta r_n / r_n \approx 1/\sqrt{2n}$ [9]. For $n = 51$, the orbit has a radius of 2601 Bohr radii which is 300 times larger than the radius of the ground state atom, while the torus itself has a width of only around 260 Bohr radii. Their high magnetic quantum number renders them highly sensitive to magnetic fields. Since the eccentricity quantum number μ vanishes, on the other hand, they are in first order insensitive to electric fields. Both properties make them most useful candidates for quantum sensing applications.

3

FAST NAVIGATION IN THE STARK MANIFOLD

Circular Rydberg atoms are an ideal tool for applications in quantum technology due to their particularly long lifetime. For example, they were a key component in microwave cavity quantum electrodynamics (CQED) experiments of Serge Haroche and co-workers [9, 56], which ultimately led to the award of the Nobel prize in 2012. In recent years, circular Rydberg atoms attracted attention as quantum sensors [23] for the Rydberg constant [57], magnetic [58] and electric fields [59]. For the measurement of classical fields with high accuracy, the key properties of Rydberg atoms are their large magnetic and eccentricity quantum numbers, m and μ, in the circular and low-angular-momentum states, respectively. To measure, for example, a magnetic field with quantum-enhanced sensitivity, the atom can be brought into a superposition of two opposite circular states with opposite magnetic quantum numbers, i.e. $m = n-1$ and $m = -n+1$. Figuratively speaking, a magnetic field would then "pull" the two parts of the superposition in opposite directions rendering the overall state highly sensitive to the magnetic field strength.

Electric fields, on the other hand, can be measured using a superposition of two states with different eccentricity quantum numbers μ to which the Stark shift is proportional (cf. Eq. (2.23)). Ref. [59] presents the preparation of a superposition of a circular state with a low-angular-momentum state. While the former is insensitive to the electric field, the latter shows the strongest Stark shift proportional to n^2. This state can be visualised as the superposition of two coherent states at the north and the south pole of the generalised Bloch sphere. Since coherent states have the highest resemblance to classical states, this superposition can be understood as a cat state, in analogy to the famous Schrödinger cat thought experiment.

The sensitivity of the measurement protocol is mostly limited by its repetition rate and the fidelity of the state preparation. A fast protocol is particularly important, as the coherence of the sensor state decays over time. The high sensitivity of Rydberg atoms to external fields is a curse and a blessing at once, as the sensor reacts not only to the field we aim to measure but also to interfering stray fields. This results in fast decoherence which significantly decreases the sensitivity of the quantum sensor.

In this chapter, we tackle both increased fidelity and speed-up of the electrometer protocol by using optimal control theory. We start by giving an overview of the numerical methods required for propagating and optimising the dynamics in the Stark manifold in Sec. 3.1. Afterwards, we present a protocol for fast and accurate circularisation in Sec. 3.2, and for the preparation of a cat-like state for quantum-enabled electrometry in Sec. 3.3. The results presented in this chapter are the continuation of the work presented in [1] and have already been published in [60] and [61]. The latter is a joint publication with experimentalists from Laboratoire Kastler Brossel (LKB) at Collège de France, Paris, showing the successful experimental realisation of the theoretical proposal.

3.1 Methods for quantum dynamics and control

In this section, we present the general methods used for simulating and optimising quantum dynamics and discuss the particular case of the dynamics in the Stark manifold. The code is implemented in Fortran 95. Moreover, we made extensive use of, and contributed to, the QDYN library [62], which provides methods for the simulation of quantum dynamics and optimal control. We start by summarising the implementation of the Hamiltonian of rubidium in Sec. 3.1.1, and continue by presenting the numerical methods for time-propagation and optimisation of quantum dynamics in Sec. 3.1.2 and Sec. 3.1.3, respectively.

3.1.1 Implementation of the rubidium Hamiltonian

In order to implement the matrix elements of the rubidium atom we utilise the spherical basis. The full Hamiltonian,

$$\hat{H}(t) = \underbrace{\hat{H}_0 + F_{\text{DC}}\,\hat{z}}_{\hat{H}_{\text{drift}}} + F_{\text{RF}}^{\pm}(t)\,(\hat{x} + i\hat{y}) + (F_{\text{RF}}^{\pm}(t))^*\,(\hat{x} - i\hat{y})\,, \tag{3.1}$$

consists of several parts. The field-free eigenenergies of $\hat{H}_0$, i.e. the diagonal elements of $\hat{H}$, are given by the modified, hydrogenic eigenenergies including the quantum defects as shown in Eq. (2.6). In our simulations, we consider quantum defects up to second order for $\ell \leq 3$ and up to first order for $4 < \ell \leq 7$; higher orders are not provided in literature and lead to insignificant energy shifts. The detailed values, corresponding to rubidium 85 for $n \geq 20$, are given in Appendix A.1. In principle, the quantum defects, $\delta_{n\ell j}$, depend on the total angular momentum j. Throughout this chapter, we neglect spin-orbit coupling and set $\delta_{n\ell} \approx \delta_{n\ell,j=\ell+\frac{1}{2}}$, resulting in a Hilbert space dimension of n^2 per n-manifold instead of $2n^2$ when including spin-orbit coupling.

The second term describes the interaction of the Rydberg atom with a DC field requiring us to evaluate the matrix elements of $\hat{z}$. The matrix elements can be split into an angular and a radial part as explained in Sec. 2.1.3. The angular part is given by the matrix elements in Eq. (B.5). The radial part of an alkali atom, however, can no longer be calculated analytically. The potential of

an alkali atom, $\hat{V}_{\text{alkali}}(\hat{\boldsymbol{r}})$ (cf. Eq. (2.10)), is spherically symmetric but not the Coulomb potential. It is deeper and pulls the nodes of the radial wavefunction closer to the origin. Far from the ionic core, however, the potential approximates the Coulomb potential. In this regime, the radial Schrödinger equation can be solved numerically by modelling the initial pull as a phase shift between the hydrogen-like and alkali radial wave functions. To this end, we use Numerov's method [44, 8], that can be applied to solve differential equations of the form

$$\frac{d^2X}{dx^2} = g(x)X(x). \tag{3.2}$$

If the coordinate x is discretised into a equidistant grid with step size Δx, the value of $X(x+\Delta x)$ can be calculated recursively from two previous points via

$$\Big(1 - T(x+\Delta x)\Big)X(x+\Delta x) = \Big(2 + 10T(x)\Big)X(x) - \Big(1 - T(x-\Delta x)\Big)X(x-\Delta x) \tag{3.3}$$

with $T(x) = \Delta x^2 g(x)/12$. The error of the method is of the order Δx^6. To bring the radial Schrödinger equation in Eq. (2.4) to the desired form, we make the substitutions [63]

$$x = \sqrt{r}, \quad X_{n\ell}(x) = r^{3/4} R_{n\ell}(r) \tag{3.4}$$

with $R_{n\ell}(r)$ being the radial wave function, leading to

$$g(x) = 8m_r\big(V_{\text{alkali}}(r) - E\big)x^2 + \frac{\left(2\ell+\frac{1}{2}\right)\left(2\ell+\frac{3}{2}\right)}{x^2}. \tag{3.5}$$

To avoid divergence and unphysical results at short range, the integration is performed inwards starting from the outer radius $r_o = 2n(n+15)$, which is much larger than the classical turning point, to an inner radius of $r_i = \alpha_c^{1/3}$, where α_c is the static dipole polarisability, with a step size $\Delta x = 0.01$ [64]. We find an absolute error of the order 10^{-8} when comparing the radial wavefunctions of hydrogen, known analytically, to the solutions obtained using our implementation of Numerov's method. Using the radial wavefunctions, $X_{n\ell}(x_i)$, we can evaluate the radial overlap of the matrix elements in Eq. (2.11) by numerical integration,

$$\int dr\, r^{k+2} R_{n\ell}(r)\, R_{n'\ell'}(r) = \int dx\, 2x^{2k+2} X_{n\ell}(x)\, X_{n'\ell'}(x) \to \sum_i 2\,(x_{i+1} - x_i)\, x_i^{2k+2}\, X_{n\ell}(x_i)\, X_{n'\ell'}(x_i),$$

with $k = 1$ for the z-operator, as it is a rank-1 tensor.

With this, we have all ingredients needed to obtain the matrix elements of the z-operator in the spherical basis and the DC field potential. The time-independent part of the Hamiltonian, also called the drift $\hat{H}_{\text{drift}}$, is then numerically diagonalised giving us the eigenvalues and eigenstates of the atom in a DC field. We refer to this as the DC-dressed basis. Note that the parabolic basis is an approximation to this numerically exact result for small values of the DC field and no quantum defects. All subsequent simulations are performed in the DC-dressed basis.

The last two terms of the full Hamiltonian in Eq. (3.1) are related to the RF field which drives dynamics in the Stark manifold as discussed in Sec. 2.3. As denoted in Eq. (3.1), the pulse couples to the $\hat{x} \pm i\hat{y}$ operators whose angular matrix elements are given in Eq. (B.5) while the radial part can be calculated using Numerov's method as explained above. In general, the amplitude $F^{\pm}_{\mathrm{RF}}(t)$ of the drive depends on time and can be divided into an oscillation with the central frequency ω_{RF} and a time-dependent, complex envelope $S_{\mathrm{RF}}(t)$ as

$$
\begin{aligned}
F^{\pm}_{\mathrm{RF}}(t) &= S_{\mathrm{RF}}(t) e^{\mp i(\omega_{\mathrm{RF}} t + \phi_{\mathrm{RF}})} && \text{(3.6a)}\\
&= \big(\mathrm{Re}\left\{S_{\mathrm{RF}}(t)\right\} + i\,\mathrm{Im}\left\{S_{\mathrm{RF}}(t)\right\}\big)\big(\cos(\omega_{\mathrm{RF}} t + \phi_{\mathrm{RF}}) \mp i\,\sin(\omega_{\mathrm{RF}} t + \phi_{\mathrm{RF}})\big) && \text{(3.6b)}\\
&= \underbrace{\mathrm{Re}\left\{S_{\mathrm{RF}}(t)\right\}\cos(\omega_{\mathrm{RF}} t + \phi_{\mathrm{RF}}) \pm \mathrm{Im}\left\{S_{\mathrm{RF}}(t)\right\}\sin(\omega_{\mathrm{RF}} t + \phi_{\mathrm{RF}})}_{\mathrm{Re}\left\{F^{\pm}_{\mathrm{RF}}(t)\right\}} \\
&\quad + i\,\underbrace{\big(\mathrm{Im}\left\{S_{\mathrm{RF}}(t)\right\}\cos(\omega_{\mathrm{RF}} t + \phi_{\mathrm{RF}}) \mp \mathrm{Re}\left\{S_{\mathrm{RF}}(t)\right\}\sin(\omega_{\mathrm{RF}} t + \phi_{\mathrm{RF}})\big)}_{\mathrm{Im}\left\{F^{\pm}_{\mathrm{RF}}(t)\right\}}. && \text{(3.6c)}
\end{aligned}
$$

Equation (3.6a) corresponds to the way the pulse was implemented in the code. The full expression of the RF field follows as[1]

$$
\begin{aligned}
\boldsymbol{F}^{\pm}_{\mathrm{RF}}(t) &= F^{\pm}_{\mathrm{RF}}(t)(\boldsymbol{e}_x + i\boldsymbol{e}_y) + (F^{\pm}_{\mathrm{RF}}(t))^{*}(\boldsymbol{e}_x - i\boldsymbol{e}_y) && \text{(3.7a)}\\
&= 2\,\mathrm{Re}\left\{F^{\pm}_{\mathrm{RF}}(t)\right\}\boldsymbol{e}_x + 2i\,\mathrm{Im}\left\{F^{\pm}_{\mathrm{RF}}(t)\right\}\boldsymbol{e}_y && \text{(3.7b)}\\
&= 2\,\mathrm{Re}\left\{S_{\mathrm{RF}}(t)\right\}\big(\cos(\omega_{\mathrm{RF}} t + \phi_{\mathrm{RF}})\boldsymbol{e}_x \pm \sin(\omega_{\mathrm{RF}} t + \phi_{\mathrm{RF}})\boldsymbol{e}_y\big) \\
&\quad + 2\,\mathrm{Im}\left\{S_{\mathrm{RF}}(t)\right\}\big(\cos(\omega_{\mathrm{RF}} t + \phi_{\mathrm{RF}} + \tfrac{\pi}{2})\boldsymbol{e}_x \pm \sin(\omega_{\mathrm{RF}} t + \phi_{\mathrm{RF}} + \tfrac{\pi}{2})\boldsymbol{e}_y\big). && \text{(3.7c)}
\end{aligned}
$$

Equation (3.7c) reveals the physical interpretation of the complex envelope $S_{\mathrm{RF}}(t)$. If $S_{\mathrm{RF}}(t) \in \mathrm{Re}$, the expression simplifies to one circularly polarised field which we call the first quadrature of the field. If we considered the field strength to be constant, $S_{\mathrm{RF}}(t) = F_{\mathrm{RF}}$, we would obtain the drive from Eq. (2.31). Using this quadrature and assuming for simplicity $\phi_{\mathrm{RF}} = 0$, we can rotate the Bloch vector around the X-axis of the generalised Bloch sphere (cf. Eq. (2.40)). If, on the other hand, $S_{\mathrm{RF}}(t) \in \mathrm{Im}$, the first quadrature vanishes and only the so-called second quadrature survives, which is phase shifted by $\pi/2$ with respect to the first one. For $\phi_{\mathrm{RF}} = 0$, the second quadratures induces rotations around the Y-axis of the generalised Bloch sphere. When combining both quadratures, i.e. by choosing a complex envelope $S_{\mathrm{RF}}(t) \in \mathbb{C}$, we can rotate the Bloch vector in arbitrary directions. ϕ_{RF} can be tuned to rotate the rotation axes of the two quadratures in the XY-plane. As discussed before, σ^{+} (σ^{-})-polarised light induces excitations in $\hat{\boldsymbol{J}}_1$ ($\hat{\boldsymbol{J}}_2$).

[1] Eq. (3.7c) can be compared to Eq. (10) in [60]. They differ by a factor of 2 because the RF field strength F_{RF} was defined differently. In Eq. (2.31), we defined $\boldsymbol{F}^{\pm}_{\mathrm{RF}}(t) = 2F_{\mathrm{RF}}\big(\cos(\omega_{\mathrm{RF}} t + \phi_{\mathrm{RF}})\boldsymbol{e}_x \pm \sin(\omega_{\mathrm{RF}} t + \phi_{\mathrm{RF}})\boldsymbol{e}_y\big)$ while in [60], we set $\boldsymbol{F}^{\pm}_{\mathrm{RF}}(t) = F_{\mathrm{RF}}\big(\cos(\omega_{\mathrm{RF}} t + \phi_{\mathrm{RF}})\boldsymbol{e}_x \pm \sin(\omega_{\mathrm{RF}} t + \phi_{\mathrm{RF}})\boldsymbol{e}_y\big)$. With the convention used in this thesis, the x-component of the drive is equal to $2\mathrm{Re}\left\{F^{\pm}_{\mathrm{RF}}(t)\right\}$ while in the publication, it is equal to $\mathrm{Re}\left\{F^{\pm}_{\mathrm{RF}}(t)\right\}$, and accordingly for y.

The full Hilbert space of a Rydberg atom is, strictly speaking, infinitely dimensional, as n can take arbitrary positive integer values. It is therefore necessary to truncate the Hilbert space in order to perform numerics. Since we are interested in the dynamics within one Stark manifold, and we only employ RF pulses, it would be sufficient to consider only the states of a single n-manifold. However, the DC field couples states of neighbouring Stark manifolds and the quantum defect might bring low-angular-momentum states of higher manifolds closer to the central n-manifold. To calculate the DC-dressed eigenvalues with high precision, we therefore have to include states in neighbouring manifolds when diagonalising the drift Hamiltonian.

In our simulations, we take all the states with $n \pm \Delta n$ with $\Delta n = 4$ into account. For $n \sim 50$, this leads to an accuracy of 10^{-6} in the energy levels and transition matrix elements of the central n-manifold [61]. In a second step, we remove states from the Hilbert space which are unlikely to be populated during a propagation due to a large detuning or vanishing matrix elements. Since RF pulses only couple states within diagonal ladders (cf. Sec. 2.3.1), we can luckily neglect a large part of the Stark manifold. As discussed in more detail in Sec. 3.2, we are interested in the dynamics on the lowest diagonal ladder of the Stark manifold with $m \geq 0$. To increase the precision, we take the lowest two diagonal ladders into account during propagations and optimisations. In summary, we have reduced the size of the Hilbert space from around 2500 ($= n^2$) states in the full Stark manifold to only 100 ($= 2n - 1$). All calculations were cross-checked by comparing them to calculations with a Hamiltonian defined on a larger Hilbert space that contains all states of the central n-manifold. From this, we find that the truncation allows to find the same final state population within a precision of $5 \cdot 10^{-5}$ [61]. The code for the description and manipulation of the Hamiltonian of the Rydberg atoms was implemented by myself based on previous work by Dr. Daniel Reich while using the data structures provided by the QDYN library [62].

3.1.2 Propagation

To determine the response of a quantum state to an external drive, we have to propagate the state in time. The temporal evolution of a quantum state is fully determined by time-dependent Schrödinger equation,

$$i\frac{\partial}{\partial t}\left|\Psi(t)\right\rangle = \hat{H}(t)\left|\Psi(t)\right\rangle . \tag{3.8}$$

For a time-independent Hamiltonian, $\hat{H}(t) = \hat{H}$, the solution of the Schrödinger equation can be found by integration, leading to

$$\left|\Psi(t)\right\rangle = \hat{U}(t)\left|\Psi(0)\right\rangle = e^{-i\hat{H}t}\left|\Psi(0)\right\rangle , \tag{3.9}$$

with the time-evolution operator $\hat{U}(t)$ and where we have set the initial time $t_0 = 0$ and $\hbar = 1$. If E_n and $|n\rangle$ are the eigenvalues and eigenstates of the Hamiltonian, respectively, the time-

propagated state can be calculated via

$$|\Psi(t)\rangle = \sum_n e^{-iE_n} \langle n|\Psi(0)\rangle |n\rangle . \tag{3.10}$$

If the eigenstates and -values of the Hamiltonian are not known, the Hamiltonian needs to be diagonalised. As the diagonalisation scales as N^3 with the dimension N of the Hilbert space, this exact propagation method quickly becomes numerically infeasible [65].

In general, it is sufficient to know the result of a propagation with a certain accuracy. For instance, it is sufficient to calculate the population of a target state with a fidelity that is consistent with the measurement accuracy in a real experiment. We can therefore expand the time-evolution operator in a polynomial series. However, the expansion of the exponential according to its definition,

$$\hat{U}(t) = e^{-i\hat{H}t} = \sum_{n=0}^{\infty} \frac{1}{n!} \left(-i\hat{H}t\right)^n , \tag{3.11}$$

converges rather slowly and is numerically unstable [66]. Instead, the exponential can be expanded in any polynomial series,

$$e^{-i\hat{H}t} \approx \sum_{n=0}^{N_c} a_n P_n \left(-i\hat{H}t\right) , \tag{3.12}$$

where $P_n(x)$ is a polynomial of degree n and a_n are the expansion coefficients up to a finite order N_c. If $N_c \to \infty$, the expansion becomes exact. It can be shown that the fastest converging polynomials are the Chebychev polynomials [66, 67, 68]. As Chebychev polynomials are only defined in the interval $[-i, i]$, the Hamiltonian is normalised using its spectral radius which can be obtained using the Arnoldi method [69]. An alternative approach to propagation is given by Newton's method [70, 71]. It has the advantage of also being able to solve the Liouville-von Neumann equation with a dissipative term, or the Schrödinger equation with non-Hermitian Hamiltonians. In this chapter, we used the implementation of the Chebychev propagator as provided by the QDYN library [62].

To solve the dynamics of a time-dependent problem, we use the piecewise-constant approximation, see Fig. 3.1. The amplitude of the driving field can be approximated on a time grid with the step size Δt by the pulse value in the centre of the time interval. If the time grid for the propagation of the state has n_t steps, the pulse is discretised in $n_t - 1$ steps. The state is propagated from the first time step to the second using the approximated pulse value inbetween. Then, the overall time-evolution operator is the product of the time-evolution operators at each time step. To control the error introduced by the piecewise-constant approximation of the Hamiltonian the step size must be chosen sufficiently small [65].

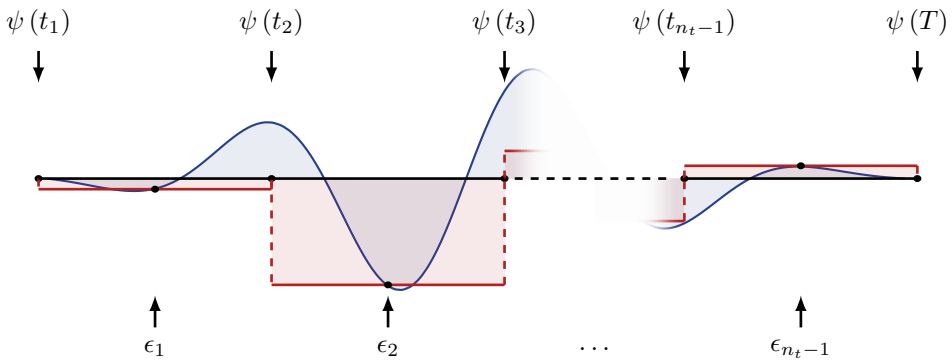

Figure 3.1: Sketch of the piecewise-constant approximation (red) of an exemplary drive (blue). The ψ's on top indicate the time grid of the states, while the ϵ's at the bottom indicate the time grid of the pulses.

3.1.3 Optimisation

Since the time evolution of a quantum system depends on the Hamiltonian, we can steer the dynamics by choosing the control fields carefully. We consider the Hamiltonian to be of bilinear form [72],

$$\hat{H}(t) = \hat{H}_{\text{drift}} - \sum_k \hat{H}_k \epsilon_k(t), \tag{3.13}$$

for which the resulting time-depending Schrödinger equation is linear with respect to the states and the control pulses ϵ_k. The drift $\hat{H}_{\text{drift}}$ contains the time independent part of the full Hamiltonian while the (time-independent) drive Hamiltonians $\hat{H}_k$ are coupled to control fields $\epsilon_k(t)$. If the aim is to perform a specific operation on a quantum system, two questions arise. The first one is: Can the task be performed at all? This question can be answered by controllability analysis, which determines whether a quantum system can be brought from any arbitrary initial to any desired target state [27]. If the answer is positive, the ensuing question is: How do we reach the optimisation goal? One tool to answer this is optimal control theory (OCT) [27] which aims to derive pulse shapes that accomplish the desired task in the best way possible, e.g. with the highest possible fidelity. An example of one such task is the so-called state-to-state optimisation where the goal is to find the field which drives the initial state $|\Psi(0)\rangle$ towards a desired target state $|\Psi_t\rangle$. The success of this process can be quantified by the cost functional [73],

$$J_T = 1 - |\langle \Psi(T) | \Psi_t \rangle|^2, \tag{3.14}$$

where $|\Psi(T)\rangle$ is the state at the final time T. The functional depends implicitly on the driving fields ϵ_k and it is zero if and only if the optimisation target has been reached. The cost functional in Eq. (3.14) is only one specific example for the state-to-state optimisation. In more general terms, cost functionals J can cover a set of N initial and target states, $\{|\psi_j(0)\rangle\}$ and $\{|\psi_{t,j}\rangle\}$, respectively,

and arbitrary final time functionals $J_T\big[\{|\psi_j(T)\rangle\}\big]$. Moreover, we can impose constraints $g_a\big[\{\epsilon_k\}\big]$ to the fields and $g_b\big[\{|\psi_j(t)\rangle\}\big]$ to the states at intermediate times leading to the general form [74]

$$J\big[\{|\psi_j\rangle\},\{\epsilon_k\}\big] = J_T\big[\{|\psi_j(T)\rangle\}\big] + \int_0^T dt\,\Big(g_a\big[\{\epsilon_k\}\big] + g_b\big[\{|\psi_j(t)\rangle\}\big]\Big)\,. \tag{3.15}$$

In numerical optimal control, a guess pulse is optimised in an iterative manner to successively decrease the value of the functional. In general, there are two basic categories of optimisation algorithms. The gradient-free methods employ only evaluations of the functional. They are often based on having a set of guess pulses whose performance is compared and the ones with the weakest performance are replaced. They are easy to implement but converge generally rather slowly. In matters of experimental application, gradient-free methods allow for closed-loop control where a real measurement determines the figure of merit and the adjustment of the control parameters can be performed in real time. Prominent examples are the downhill-simplex (or Nelder-Mead) method [75], CRAB [76] or genetic algorithms [77].

The Nelder-Mead method is one of the most prominent and popular optimisation algorithms due to its simple implementation and intuitive interpretation. The general idea is to construct a $N+1$ dimensional simplex for a N-dimensional parameter space. In two dimensions, this would be a triangle. The algorithm then replaces the point with the worst performance by a new one, for instance by reflecting it through the centre of the simplex. Depending on the performance of the new point, it is further expanded or contracted. By repeating this procedure, the simplex "walks downhill" towards the minimum of the optimisation landscape. This method is particularly effective if the number of optimisation parameters is small. Moreover, no additional knowledge about the model has to be known, as it only requires the evaluation of the functional making it very versatile. In particular, the final time T can be one optimisation parameter itself.

The other category are gradient-based algorithms providing in general a faster convergence. As indicated by their name, these algorithms require to calculate the gradient of the functional. However, the analytical expression of the gradient is not always available. Gradient-based methods can be further divided into concurrent and sequential schemes. The former update the control parameters individually, like e.g. the GRAPE algorithm [78]. The latter optimise the parameters subsequently. For instance, Krotov's method [79] and its adaption to quantum dynamics [80, 81, 73, 74] is a prominent example of a sequential, gradient-based algorithm which is the method of choice in the following. Gradient-based algorithms are usually used in an open-loop control scheme where the pulses are first optimised numerically and afterwards implemented in a real experiment. We follow the same approach in this work.

The most crucial advantage of Krotov's method is the assured monotonic convergence of the functional [74],

$$J\left[\left\{|\psi_j\rangle\right\},\left\{\epsilon_k^{(i+1)}\right\}\right] \leq J\left[\left\{|\psi_j\rangle\right\},\left\{\epsilon_k^{(i)}\right\}\right]. \tag{3.16}$$

For simplicity, we consider only one control field $\epsilon(t)$ in the following. Moreover, we consider no state-dependent constraints and write the constraints in Eq. (3.15) as [74]

$$g_a\big[\epsilon(t)\big] = \frac{\lambda_a}{S(t)}\left(\epsilon(t) - \epsilon_{\text{ref}}(t)\right)^2, \quad g_b\big[\{|\psi_j(t)\rangle\}\big] = 0 \tag{3.17}$$

with a shape-function $S(t) \in [0,1]$ and a weight λ_a of the of the pulse-dependent constraint. The function g_a penalises a change in the field intensity with respect to some reference pulse $\epsilon_{\text{ref}}(t)$ which is usually chosen to be the pulse from the previous iteration. This can be used to avoid strong changes in the pulse amplitude and to ensure a smooth switching on and off of the pulse by choosing a shape function that goes to zero at the beginning and end of the time interval.

The update formula for Krotov's method can be derived using variational calculus and is given by [74]

$$\Delta\epsilon(t) = \frac{S(t)}{\lambda_a}\,\text{Im}\left\{\sum_{j=1}^{N}\left\langle \chi_j^{(i)}(t)\right|\left.\frac{\partial\hat{\text{H}}[\epsilon(\text{t})]}{\partial\epsilon}\right|_{\epsilon^{(\text{i}+1)}(\text{t})}\left|\psi_j^{(i+1)}(t)\right\rangle\right\} \tag{3.18}$$

with $\Delta\epsilon(t) = \epsilon^{(i+1)}(t) - \epsilon^{(i)}(t)$ and the co-states $|\chi^{(i)}\rangle$ which are the result of a backwards propagation under the old pulse

$$\frac{\partial}{\partial t}\left|\chi_j^{(i)}(t)\right\rangle = -i\hat{H}^{\dagger(i)}\left|\chi_j^{(i)}(t)\right\rangle. \tag{3.19}$$

The states $|\psi_j^{(i+1)}\rangle$, on the other hand, are forward-propagated under the new pulse,

$$\frac{\partial}{\partial t}\left|\psi_j^{(i+1)}(t)\right\rangle = -i\hat{H}^{(i+1)}\left|\psi_j^{(i+1)}(t)\right\rangle. \tag{3.20}$$

They are connected via the boundary condition,

$$\left|\chi_j^{(i)}(T)\right\rangle = -\left.\frac{\partial J_T}{\partial\left\langle\psi_j\right|}\right|_{\psi_j^{(i)}(T)}. \tag{3.21}$$

On first sight, it seems contradictory that new pulse $\epsilon^{(i+1)}(t)$ is necessary to calculate the pulse update $\Delta\epsilon(t)$. Indeed, at this point the sequential nature of the algorithm comes into play.

The first step is to choose a guess pulse $\epsilon^{(0)}(t)$ and use it to propagate the initial state $|\psi_j(0)\rangle$ forward in time. Now the co-state can be calculated using Eq. (3.21) giving $|\chi_j^{(0)}(T)\rangle$. Afterwards, the actual algorithm starts as depicted in Fig. 3.2. The co-state $|\chi_j^{(0)}(T)\rangle$ is backwards-propagated with the old pulse (cf. Eq. (3.19)). Afterwards, the pulse update at the first point in time is calculated using the initial state $|\psi_j(0)\rangle$ (cf. Eq. (3.18)). Then, this state is forward-propagated by one time step using the updated pulse value (cf. Eq. (3.20)). This is repeated until the final state $|\psi_j^{(1)}(T)\rangle$ is reached and the first iteration is completed. The algorithm thus takes updates of

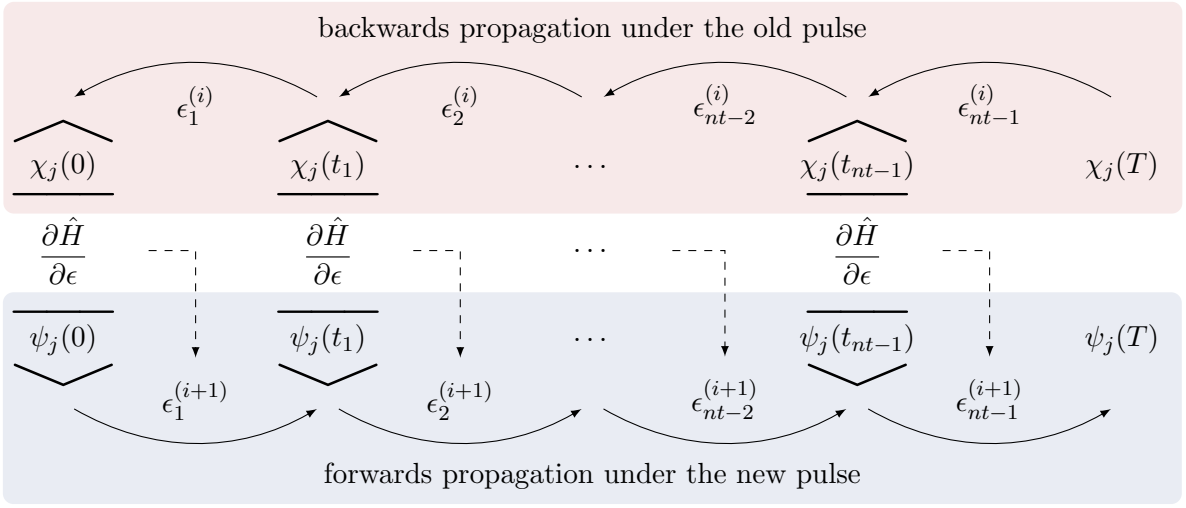

Figure 3.2: Visualisation of the sequential update scheme in Krotov's method on a time grid. The scheme starts on the upper right corner with the co-state $\chi_j(T)$.

earlier times into account when updating the pulse at subsequent time points, hence the name sequential algorithm. The whole sequence can be repeated until the desired fidelity or convergence is reached. Strictly speaking, monotonic convergence is only guaranteed in the continuous case. However, if the pulse update of one iteration is small enough, which can be ensured by the function g_a in Eq. (3.17), monotonic convergence is also preserved in the discretised version. In this work, we used the implementation of Krotov's method provided by the QDYN library [62].

3.2 Fast and accurate circularisation

The process of exciting a Rydberg atom from a low-angular-momentum to the circular state with $\ell = n - 1$ is called circularisation. The former, i.e. the 'initial' state of the circularisation, has to be prepared beforehand from a ground state atom, in our case rubidium in the state $5S_{1/2}$ [59, 82]. First, the rubidium atoms are optically excited using three laser fields in the presence of a weak DC field. The target state of the optical excitation, $|nf, m = 2\rangle$, can be accurately addressed due to its quantum defect (cf. Fig. 2.1, the f-state is separated from the rest of the n-manifold such that it can be addressed selectively via a resonant driving pulse). Second, the DC field is slowly increased to its final value. This enlarges the spacing of the states in the Stark manifold, and the state $|nf, 2\rangle$ becomes adiabatically the lowest lying state of the $m = 2$-ladder (cf. Fig. 2.4 (b)) from which we start the circularisation.

There are two very different approach to the circularisation. One is based on a rapid adiabatic passage [19, 83], which relies on the slow transformation of instantaneous eigenstates using chirped RF pulses or slow variations of the DC field. Here, fidelities close to 100% are achievable but, as is typical for adiabatic methods, the time required for the circularisation is very long,

namely several microseconds. This poses a problem for protocols where the population is split into two parts which move rather independently in the Hilbert space, like quantum sensing. The two parts of the superposition accumulate large dynamic phases which are error-prone due to imperfections in the control. The resulting dephasing renders the states useless for applications in quantum-enhanced sensing and metrology, such that adiabatic passage does not provide a viable route. Another method is the fast coherent transfer of population by coupling to a radio frequency (RF) field with a well-defined polarisation [82]. A (near-)resonant RF drive induces Rabi oscillation between a low-angular-momentum state and the circular one. As discussed in Sec. 2.3, the circularisation can be interpreted as the rotation of a SCS from the south to the north pole of the generalised Bloch sphere. Rabi oscillation allows the circularisation to proceed in about $200\,\mathrm{ns}$. However, the transfer rate was limited to about 80%.

While the two preparation methods provide either fast or accurate circularisation, the combination of the two remained an open challenge. In the following, we show how to improve the circularisation in terms of fidelity and speed by using OCT. We start by discussing the unoptimised dynamics using π-pulses in Sec. 3.2.1. Afterwards, we choose an improved guess pulse as a starting point for Krotov's method and present the optimised pulse shape in Sec. 3.2.2. We further discuss its robustness and quantum speed limit in Sec. 3.2.3 and Sec. 3.2.4, respectively. Finally, we present the main results of the experiment in Sec. 3.2.5. The theoretical results presented in the sections Sec. 3.2.1 to Sec. 3.2.4 mainly stem from [60] while the experimental results in Sec. 3.2.5 were published in [61].

3.2.1 Circularisation using π-pulses

As a first guess for the optimisation, we choose an RF π-pulse driving σ^+-transitions within the lowest diagonal ladder with $m \geq 0$ of the manifold (i.e. the right-hand side in Fig. 2.3). Note that the results can be generalised easily to $m \leq 0$ by changing the polarisation of the RF pulse. This pulse represents the state of the art in the experiment before we have started the project [82]. Due to the quantum defect, the pulse is near-resonant with transitions to the right side of the initial state, whereas it is detuned from the transition to the left side (cf. Fig. 2.5). We thus expect population to be driven to higher-angular-momentum states only. Because only states in the lowest diagonal ladder play a significant role during the circularisation, we denote these states by $|m\rangle$ for the sake of simplicity. The initial state becomes $|2\rangle$ and the target circular state $|n-1\rangle$.

Following Ref. [52], we choose the $n = 51$-manifold and $F_{\mathrm{DC}} = 2.346\,\frac{\mathrm{V}}{\mathrm{cm}}$. The quasi-resonant frequency of the ladder is $\omega_{\mathrm{stark}} = 229.6\,\mathrm{MHz}$, which has been calculated using the first-order Stark splitting of hydrogen (cf. Eq. (2.23)). The chosen guess pulse is a σ^+-polarised RF pulse with central frequency $\omega_{\mathrm{RF}} = 230\,\mathrm{MHz}$ and amplitude $F_{\mathrm{RF}} = 18\,\frac{\mathrm{mV}}{\mathrm{cm}}$. Using Eq. (2.39), the Rabi frequency of this pulse is $\Omega_{\mathrm{RF}}/2\pi = 3.52\,\mathrm{MHz}$. From this, the time to perform a π-pulse can be calculated to be $t_\pi = \pi/\Omega_{\mathrm{RF}} = 142\,\mathrm{ns}$. The pulse has a flat-top shape with sine-squared edges lasting $10\,\mathrm{ns}$ each. The total duration of the pulse, $t_{\mathrm{stop}} = 138\,\mathrm{ns}$, has been adjusted to

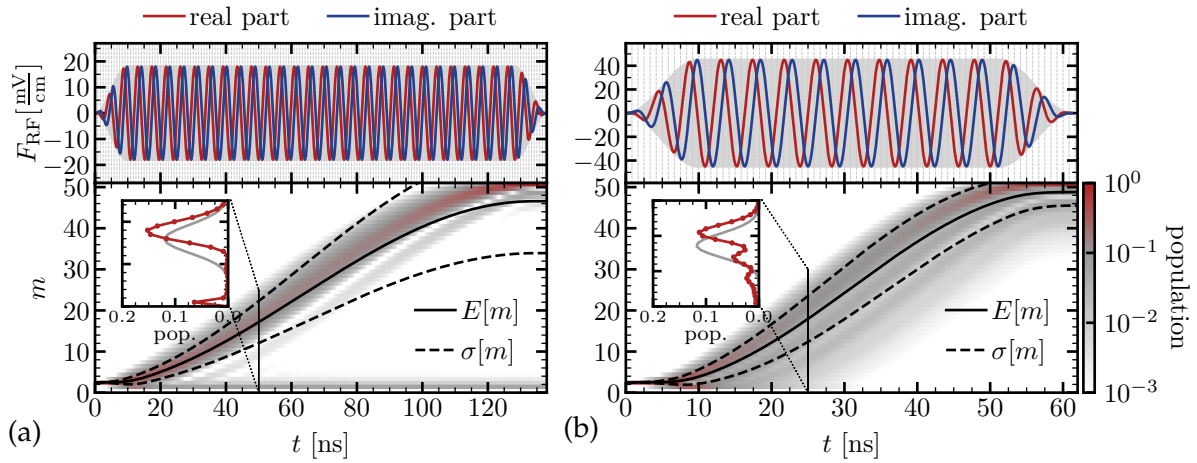

Figure 3.3: Top: RF π-pulse shapes (grey) and their real and imaginary parts (red and blue lines, respectively) for (a) $F_{\mathrm{RF}} = 18\,\frac{\mathrm{mV}}{\mathrm{cm}}, t_{\mathrm{stop}} = 138\,\mathrm{ns}$, (b) $F_{\mathrm{RF}} = 45\,\frac{\mathrm{mV}}{\mathrm{cm}}, t_{\mathrm{stop}} = 66.9\,\mathrm{ns}$. Bottom: Corresponding distribution of the population over the lowest diagonal ladder. Note the logarithmic scale in the colour bar. The expectation value $E[m]$ and the standard deviation $\sigma[m]$ are indicated by the solid and dashed lines, respectively. The inset displays a snapshot of the population distribution (red) and the distribution of the closest SCS (a) $\vartheta = 0.62\pi, \varphi = 0.49\pi$, (b) $\vartheta = 0.60\pi, \varphi = 0.50\pi$ (grey line).

match a π-pulse. The pulse and its real and imaginary part as defined in Eq. (3.6c) are shown in Fig. 3.3 (a) (top). The small deviation between t_{stop} and t_π stems from the shape of the pulse and the deviations of the Hilbert space of rubidium from the idealised, hydrogenic one which was used to calculate t_π and Ω_{RF}. Most importantly, the initial state, $|2\rangle$, does not coincide with the South pole of the Bloch sphere. Instead, it corresponds to a ring on the Bloch sphere around the Z-axis with $Z \approx -0.9$ (the radius of the sphere being normalised to 1).

The final population in the circular state is 81% with an expectation value of m equal to 46. This indicates that the population is spread over several ladder states, as can be seen in Fig. 3.3 (a) (bottom). A large fraction of the missing population (6% of the total population) can be found in the state $|1\rangle$. This effect can be attributed to an insufficient detuning of the RF pulse from the $|2\rangle \to |1\rangle$ transition. The detuning $\delta^{\mathrm{RF}}_{m,m+1} = (E_{m+1} - E_m) - \omega_{\mathrm{RF}}$ with respect to the frequency ω_{RF} of the driving field are (compare to Fig. 2.5 (b))

$$\delta^{\mathrm{RF}}_{0,1} = -159.64\,\mathrm{MHz}, \tag{3.22a}$$

$$\delta^{\mathrm{RF}}_{1,2} = -47.05\,\mathrm{MHz}, \tag{3.22b}$$

$$\delta^{\mathrm{RF}}_{2,3} = -2.54\,\mathrm{MHz}. \tag{3.22c}$$

The quantum defect barely affects the $m = 2$-ladder and $\delta^{\mathrm{RF}}_{2,3}$ is nearly resonant with the RF pulse, while the detuning from $\delta^{\mathrm{RF}}_{0,1}$ is large enough to prevent a significant population of state $|0\rangle$. However, the rather small detuning from $\delta^{\mathrm{RF}}_{1,2}$ allows for an off-resonant drive towards state

$|1\rangle$. While some of this population remains trapped in state $|1\rangle$, another part is reflected from the lower bound of the ladder and follows the main packet towards the circular state with a small delay. This can be seen from the light grey streak slightly below the main red path, the strong deviation of the expectation value of m from the centre of the population distribution and the large standard deviation.

Moreover, the inset in Fig. 3.3 (a) displays the population distribution at the intermediate time, $t = 50\,\mathrm{ns}$, together with the closest SCS $|\psi_{\mathrm{SCS}}^{(\vartheta=0.62\pi,\varphi=0.49\pi)}\rangle$. The coordinates of the latter where calculated from the expectation values of the three spatial components of the angular momentum vector for the system state $|\psi(t = 50\,\mathrm{ns})\rangle$. Apparently, the upper peak of $|\psi(t = 50\,\mathrm{ns})\rangle$ is more narrow than a SCS and the residual population in the low-m states affects the position of $|\psi_{\mathrm{SCS}}^{(\vartheta,\varphi)}\rangle$ on the m-axis significantly. Morover, the second order Stark effect introduces an anharmonicity to the ladder which leads to an azimuthal drift of the state on the Bloch sphere. Thus, the overlap of $|\psi_{\mathrm{SCS}}^{(\vartheta=0.62\pi,\varphi=0.49\pi)}\rangle$ and $|\psi(t = 50\,\mathrm{ns})\rangle$ is only 65%. As explained in Sec. 2.3, a SCS can be rotated into the target circular state in a very natural way. However, due to the deviation from a perfect SCS, part of the population at the final time is spread over several states neighbouring the target.

To summarise our observations from Fig. 3.3 (a), the fidelity obtained with a π-pulse is limited by (i) loss to $|1\rangle$, (ii) delay due to reflection from the lower end of the ladder, and (iii) an imperfectly-shaped SCS. These effects together result in an infidelity of about 19% at the final time. It would now be possible to use the π-pulse directly as a guess field to start the optimisation, which provides an optimised pulse leading to a fidelity of 99%. However, such a brute force approach comes at the expense of rather complex optimised fields with an undesirably large spectral bandwidth and a high field strength. Having the experimental feasibility of the optimised pulse in mind, it is much more advantageous to first exploit the available physical insight and construct an improved guess pulse before starting the optimisation.

3.2.2 Optimisation of an improved guess pulse

We now utilise our findings to construct an improved guess pulse which is subsequently optimised using OCT. We start by estimating the maximal speed up of the circularisation that can be expected. As with any dynamics on the Bloch sphere, the fastest rotation is obtained when the highest possible field amplitude is employed. Here, we choose $F_{\mathrm{RF}} = 45\,\frac{\mathrm{mV}}{\mathrm{cm}}$ leading to $\frac{\Omega_{\mathrm{RF}}}{2\pi} = 8.8\,\mathrm{MHz}$. As shown in Fig. 3.3 (b), we find that with this amplitude, a π-pulse can be performed in $61.2\,\mathrm{ns}$. This is again slightly faster than the analytical prediction for a π-pulse, which is $66.9\,\mathrm{ns}$. While this amplified π-pulse is more than twice as fast as the one in the previous section, its fidelity is decreased to 63%. Obviously, for larger field strengths, the non-resonant run-off of population becomes more significant. We can conclude, as suggested by our findings in the previous section, that the accurate preparation of the SCS itself needs some time in addition to the $61.2\,\mathrm{ns}$ for the mere rotation of a SCS. Our approach is thus to split the circularisation into the preparation of a SCS and a subsequent rotation of the SCS into the circular state.

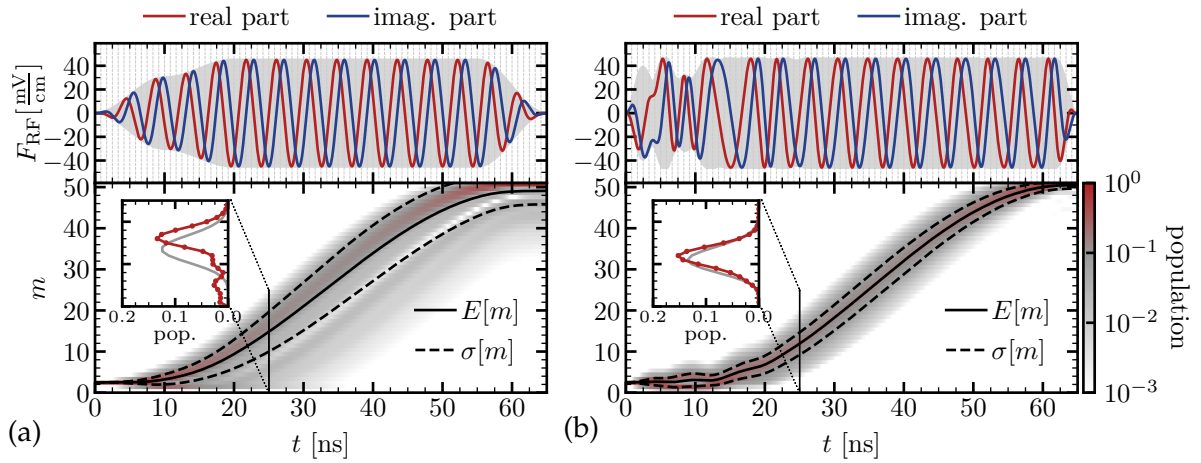

Figure 3.4: Same as Fig. 3.3 but for the two-step amplitude pulse (a) and the optimised pulse leading to a fidelity of 99% (b). The grey lines in the inset show the population distribution of the closest SCS (a) $\vartheta = 0.65\pi, \varphi = 0.50\pi$, (b) $\vartheta = 0.69\pi, \varphi = 0.54\pi$.

We therefore change the shape of the guess pulse in order to avoid population running off to the state $|1\rangle$ and allowing sufficient time for the preparation of the SCS. To this end, the initial amplitude of the pulse is decreased for some nanoseconds before the amplitude is ramped up to the maximum value, $45\,\frac{\mathrm{mV}}{\mathrm{cm}}$ (see an example in Fig. 3.4 (a)). The total length of the pulse, referred to as two-step amplitude pulse, is then adjusted to match a π-pulse. The lower the initial amplitude and the longer the initial plateau, the longer the pulse.

The approach to obtain high fidelity with the shortest possible duration is to increase the pulse duration gradually (by decreasing the amplitude of the initial plateau) until the desired fidelity can be reached under given constraints. Note that higher fidelities could easily be realised in the calculations. However, this is not meaningful in view of application in an experiment where detector efficiency, DC electric field inhomogeneities, electric field noise and other experimental imperfections [59] intrinsically limit the measurable fidelity. We seek to increase the fidelity of the two-step amplitude pulse by employing Krotov's method (cf. Sec. 3.1.3). The optimisation is performed until the functional crosses the threshold $J_T = 10^{-2}$, which corresponds to a fidelity of 99%. The considered shape function $S(t)$ in the pulse constraints g_a (cf. Eq. (3.17)) is the previously described sine-squared function. To ensure experimental feasibility, the absolute value of the amplitude is constrained to values smaller than $46\,\frac{\mathrm{mV}}{\mathrm{cm}}$. Spectral components driving either σ^--polarised transitions, or σ^+-polarised transitions above 460 MHz are suppressed in view of experimental feasibility. This is most simply achieved by cutting the amplitude and spectrum of the pulse to the allowed range after each iteration. While such a procedure typically results in loss of monotonic convergence of the optimisation [84, 85, 86], in our case J_T does converge monotonically due to the high quality of the guess pulse.

It turns out that the shortest possible pulse that allows for a successful optimisation has a duration of $65\,\mathrm{ns}$, see Fig. 3.4 (a). Its initial amplitude has been decreased to $30\,\frac{\mathrm{mV}}{\mathrm{cm}}$. After $10\,\mathrm{ns}$ the amplitude is increased to the maximum value, $45\,\frac{\mathrm{mV}}{\mathrm{cm}}$. This increase takes another $10\,\mathrm{ns}$ and uses a sine-squared shape. The edges of the pulse are unchanged. The new guess pulse leads to a fidelity of 74%, which is already a significant gain compared to the simple $61.2\,\mathrm{ns}$ π-pulse. Notably, the final population in state $|1\rangle$ under the new guess pulse is decreased to only 6×10^{-6}. The optimised pulse reaches the target with 99% fidelity. All in all, 1390 iterations were needed to cross the threshold. One iteration requires a computation time of $\sim 50\,\mathrm{s}$ on a standard workstation for the considered part of the manifold (i.e. the two lowest diagonal ladders with $m \geq 0$).

Comparison of the guess and optimised pulse, cf. top panel of Fig. 3.4, reveals that the pulse is mainly changed in the low-amplitude step while it is left nearly unaltered in the high-amplitude step except for a shortening of the edge time. The shorter edge times and the stronger time dependence in the beginning of the pulse lead to a broadening of the spectrum but no conspicuous resonances appear in the spectrum other than the near-resonant transitions at $230\,\mathrm{MHz}$ (data not shown).

Inspection of the population dynamics under the optimised pulse in Fig. 3.4, reveals that the population is focused onto a few states with a small standard deviation and without any significant population remaining in the low-m states. Moreover, it confirms the already predicted evolution: In the beginning, a SCS is generated, which is then driven towards the target state easily. As can be seen in the inset, the state at $t = 25\,\mathrm{ns}$ is very close to an SCS. Indeed, its overlap with the closest SCS $|\psi_{\mathrm{SCS}}^{(\vartheta=0.69\pi,\varphi=0.54\pi)}\rangle$ indicated by the grey line is 98.9%.

A deeper understanding of the dynamics is most easily gained when the process is considered in a frame rotating with ω_{RF}. This removes fast oscillations with ω_{RF} and reveals the complex shape function $S_{\mathrm{RF}}(t)$ (cf. Eq. (3.7c)) which allows for conclusions about the dynamics on the generalised Bloch sphere. As explained Sec. 3.1.1, its real and imaginary part correspond to the envelopes of the two quadratures of the field. For $\phi_{\mathrm{RF}} = 0$, which is what we assumed for the guess pulse, the first quadrature induces a rotation around the X-axis of the generalised Bloch sphere, while the second quadrature induces a rotation around the Y-axis. To obtain $S_{\mathrm{RF}}(t)$, we demodulate the optimised pulse with the carrier frequency ω_{RF}; the result is shown in Fig. 3.5 (a). It can be seen that the first quadrature is the dominating one, as the red curve coincides with the envelope of the pulse for most of the time.

The role of the two quadratures becomes evident when considering the evolution of the state on the Bloch sphere as shown in Fig. 3.5. It is constructive to consider the evolution driven by the guess pulse first (dashed lines in bottom panel in (a) and Bloch spheres in (b)). The guess pulse consists of the unoptimised first quadrature only, which induces a rotation around the X-axis. Since the initial state corresponds to a ring around the Z-axis on the Bloch sphere, population with positive Y-components is rotated to higher Z-values whereas population with negative Y-components is rotated towards $|1\rangle$. This off-resonant transition needs $1/(2\delta_{1,2}^{\mathrm{RF}}) = 10.6\,\mathrm{ns}$, which is additionally accompanied by a rotation around the Z-axis (cf. Z-component of $\vec{\Omega}$ in Eq. (2.40)).

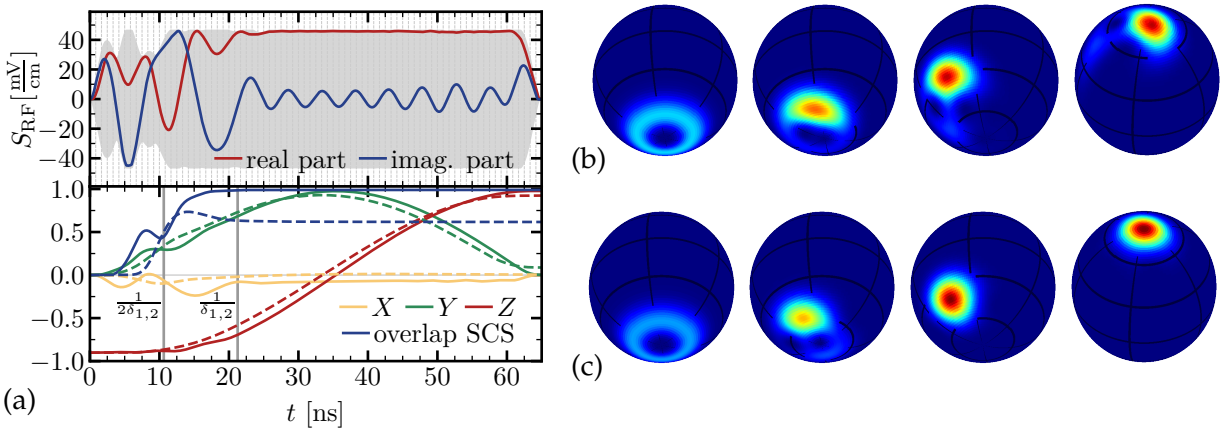

Figure 3.5: (a) Shown on top is the complex shape function $S_{\mathrm{RF}}(t)$ of the optimised pulse. The pulse is separated in its real and imaginary part while the envelope is represented by the grey shade in the background. The bottom shows the temporal evolution of the Bloch vector coordinates X, Y and Z in a frame rotating with ω_{RF} and of the overlap of the propagated state with the closest SCS. Shown are the dynamics driven by the guess pulse (dashed lines) and optimised pulse (solid lines). The vertical lines show the time scale of the detuned $|2\rangle \rightarrow |1\rangle$ transition. (b-c) Snapshots of the Q-function of the population on the generalised Bloch sphere in a frame rotating with ω_{RF} as driven by the guess pulse (b) and the optimised pulse (c) at $t = 0$, 10, 21, and 65 ns (from left to right). The first three panels show the south pole of the Bloch sphere, the right-most ones show the north pole.

Because the rotation only affects part of the state, the cylindrical symmetry of the initial state is broken. This can be seen from the dip in the X-component at 10.6 ns. The accumulated population in $|1\rangle$ then oscillates back towards $|2\rangle$ at $1/\delta_{1,2}^{\mathrm{RF}} = 21.2\,\mathrm{ns}$. Afterwards, the shape of the state does not change anymore (as can be seen from the constant overlap with a SCS) and the X-component is increasing only a little due to the second-order Stark shift. While, at the final time, the values of X, Y and Z are close to the target, the inaccurate shape of the state due to the dynamics in the first approximately 20 ns is the main cause of the insufficient final fidelity.

Thus, the main task of the optimised pulse is to improve the shape of the state. It is evident from Fig. 3.5 that the first 21 ns of the pulse are designated to generate the required high-fidelity SCS. When the initial state splits in the very beginning, as explained above, both quadratures contribute to a clear separation of the two parts. This can be seen in Fig. 3.4 (b) from the partitioning of the population into two distinct branches around 10 ns. In particular, the part with $m > 2$ is brought to a SCS-like shape much earlier, at 8 ns, than for the guess pulse (cf. peak in the overlap of the state with a SCS in Fig. 3.5). The X-value goes to zero here because the SCS-like state is located exactly opposite of the remaining population in $|1\rangle$. When the population that has been driven to $|1\rangle$ joins the SCS-like state, the overlap decreases a bit before reaching its maximal value of 99% after 21.2 ns, in agreement with the time scale of the off-resonant oscillation to $|1\rangle$. Note that the remaining inaccuracy is retained until the end and is the main cause of the final error of 1%.

The polar angle of the closest SCS $|\psi_{\text{SCS}}^{(\vartheta,\varphi)}\rangle$ amounts to $\vartheta = 0.75\pi$. The time that is required to rotate this state towards the North pole with the maximally allowed field strength is given by $T = \vartheta/\Omega_{\text{RF}} = 42\,\text{ns}$. This rotation is visible in Fig. 3.5 by the smoothly increasing Z-component and the flat shape of the first quadrature. At the same time, the second quadrature helps to adjust the X-component of the state to compensate for the drift due to the second-order Stark effect. The peak of the second quadrature at $62.5\,\text{ns}$ induces a final adjustment of the X-component and kicks the SCS to the circular state. Finally, by adding a small overhead due to the edges of the pulse, the calculated time scales are in full agreement with the duration of the numerically determined time-optimal pulse.

To corroborate our finding on "time-optimality", we have tested several values for initial and final pulse amplitude, duration and start of the amplitude ramp. It turns out that the crucial parameter for the success of the optimisation under the given constraints is the pulse duration. This confirms the discussion of the previous paragraph. In fact, several different guess pulses with the same duration lead to almost the same optimised pulse. Pulses which are longer than $65\,\text{ns}$ can also be optimised to the desired fidelity within a similar number of iterations (of the order of 2000). On the other hand, no shorter pulse (such as the $61.2\,\text{ns}$ pulse described above) can be optimised to the desired fidelity under the given constraints within at least 10^4 iterations.

3.2.3 Robustness analysis

In our simulations, we have assumed perfect conditions, such as a stable DC field and perfect modulation of the optimised pulses. To estimate the performance of our theoretical predictions under experimental conditions, we investigate the stability of the optimised pulse with respect to different sources of noise: coarse graining of the driving field and fluctuating DC and RF field strengths.

In an experiment, the optimised pulse is realised by an arbitrary waveform generator (AWG), which samples the pulse at discrete points in time. The AWG is limited to a frequency bandwidth of $480\,\text{MHz}$ for two channels. This constraint is fulfilled by the optimised pulse due to the bandwidth restriction during the optimisation. In addition, the maximum sampling rate of $1.2\,\text{GS/s}$ leads to a temporal step size of $0.83\,\text{ns}$. The step size is depicted as the vertical, dashed lines in the background of all the RF pulses shown above. This limitation might have a severe impact on the fidelity.

To examine the influence of the limited resolution, we perform a coarse graining of the optimised pulse; in between two time steps, the pulse shape is interpolated linearly, see Fig. 3.6 (a) (top). This is a reasonable approximation of the real behaviour of the pulse between two time steps. A piecewise-constant approach has also been tested and leads to almost the same results. In particular, at the maxima and minima of the pulse, there is a significant difference between the original and the coarse-grained pulse. As a result, the increase in the m expectation value is too slow, which results in a final fidelity of only 22% while the most populated state is $|49\rangle$. Note that

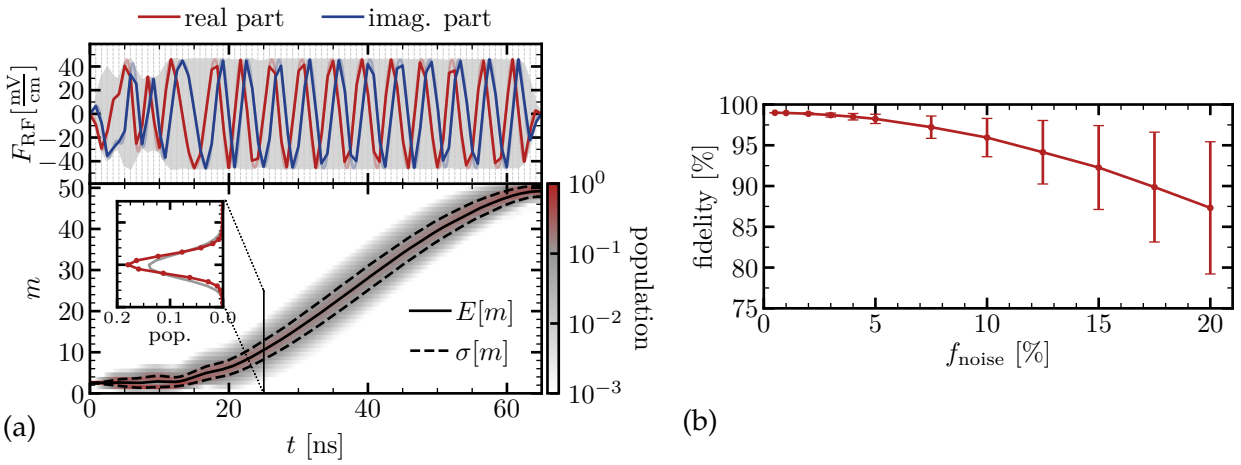

Figure 3.6: (a) Same as Fig. 3.3 but for the coarse grained optimised pulse. The light red/blue lines indicate the original, unmodified pulse. The grey lines in the inset show the population distribution of the closest SCS with $\vartheta = 0.71\pi$. (b) Fidelity of the optimised pulse as a function of noise strength, f_{noise}. Shown are the averaged values from 1000 repetitions with randomly generated noise. The error bars indicate the standard deviation σ. The line serves as a guide for the eye.

the evolution of the population in Fig. 3.6 (a) (bottom) looks very similar to the original one but it is not steep enough. The maximum at the right-most edge is not located at $|50\rangle$ but $|49\rangle$. It might thus be possible to attenuate the effect of coarse graining by increasing the amplitude carefully.

A more elegant way to solve this problem consists in shaping directly the two quadratures. This corresponds to an optimisation in the rotating frame and is shown in Fig. 3.5 (top). It essentially circumvents the issue of limited time resolution altogether since the time dependence of the complex shape function $S_{\mathrm{RF}}(t)$ is sufficiently slow to be almost insensitive to the coarse graining. Thus, the fidelity decreases by only 0.06% compared to the original pulse without coarse graining. This is a striking improvement compared to the brute force approach and highlights once more the importance of choosing the proper frame of reference.

The second most important source of noise are fluctuations in the DC and RF fields. In theory, the DC field is assumed to be perfectly static, which is not the case in a real experiment. DC field fluctuations lead to an uncertainty in the position of the energy levels in the Stark manifold. To check the stability of the pulse with respect to this noise, we have calculated the Hamiltonian for DC field amplitudes of $F_{\mathrm{DC}} \pm \Delta F_{\mathrm{DC}}/2$ with $\Delta F_{\mathrm{DC}} = 50\,\mu\mathrm{V/cm}$ and $150\,\mu\mathrm{V/cm}$, corresponding to the best and worst case scenarios in a real experiment, respectively. Then, we have propagated the initial state under the action of each of these Hamiltonians and of the optimised two-step amplitude pulse. It turns out that, in both cases, the loss of fidelity with respect to the original DC field amplitude is of the order of 10^{-4} only. The robustness of our optimised pulse can be understood as follows. An offset in the DC field leads to the accumulation of an erroneous phase. This phase is proportional to the DC field offset and the pulse duration. The high stability of the optimised pulse is thus a direct result of its short duration.

Next, we consider amplitude noise in the RF pulse. To investigate its influence, we simulate fluctuations by adding a white-noise stochastic contribution. The noisy amplitude $\widetilde{F_{\text{RF}}}(t)$ is realised as

$$\widetilde{F_{\text{RF}}}(t) = (1 + R \cdot f_{\text{noise}}) F_{\text{RF}}(t)\,, \tag{3.23}$$

where $R \in [-1, 1]$ is a random number and $f_{\text{noise}} \in [0, 1]$ is the noise strength. Note that the range of f_{noise} implies amplitude fluctuations of at most up to a factor of two with respect to the original pulse. To avoid discontinuities, the random number R is fixed for a half-period, i.e. between two zeros of the pulse. In other words, we assume the fluctuations to occur on a time scale slower than half a period of the RF pulse ($\sim 2\,\text{ns}$). Moreover, the x- and y-component are modified independently such that we also account for polarisation noise in the simulation.

The impact of the RF amplitude noise on the fidelity of the target state is evaluated by repeating the propagation 1000 times, each with a different realisation of Eq. (3.23), for noise strengths between 0.5% and 20%. As can be seen from Fig. 3.6 (b), the fidelity decreases for higher noise strengths and the spread becomes larger. For example, a fidelity of 95.9% is expected on average for a noise level of 10%. This roughly corresponds to the present estimate of amplitude fluctuations in the experiment [52, 82], a value that could be reduced with simple experimental improvements. Even at a level of 10% amplitude noise, the optimised pulse leads to significantly faster and more accurate circularisation than achieved with e.g. a π-pulse [52, 82].

3.2.4 Quantum speed limit

Quantum mechanics itself sets a natural lower bound on the minimal time that is needed to realise a certain dynamics [87]. In the following, we investigate the quantum speed limit for the circularisation beyond (present) experimental constraints using optimal control theory. The speed limit has been investigated for multi-partite systems such as entangling gates between atomic qubits [88] or transport in a spin chain [29]. In these cases, it is the interaction strength between the subsystems that sets the speed limit. Here, such a limit is absent. To the best of our knowledge, this is the first time that the speed limit for unary (i.e. single) system dynamics in a realistic model is considered.

To speed up the circularisation, we gradually increase the field strength of the guess pulse. We first discuss the QSL for our model and then examine the implications for the actual atom. No constraints on the optimised pulse are included except for Eq. (3.17). The optimisation is performed until the functional crosses the threshold $J_T = 10^{-2}$. For each value of t_{stop}, we have tested several guess pulses with different edge times and field strengths. In Fig. 3.7, we have plotted the number of iterations required to reach the desired fidelity for the best guess, i.e. the pulse that needs the least number of iterations. It is evident from the figure that the number of iterations increases as the pulse becomes shorter. The fluctuations in the data points can be credited to the high sensitivity of the optimisation to the guess pulse. In principle, Fig. 3.7

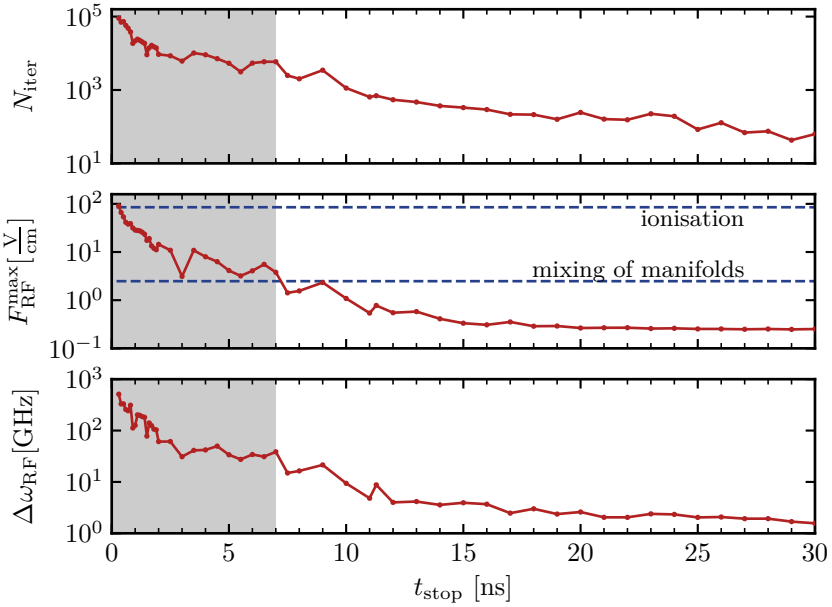

Figure 3.7: Number of required iterations N_{iter} to reach a fidelity of $J_T = 10^{-2}$ together with the required maximal field strength $F_{\text{RF}}^{\text{max}} = \max_t |F_{\text{RF}}(t)|$ and bandwidth $\Delta\omega_{\text{RF}}$ of the corresponding optimised pulse for different pulse lengths t_{stop}. The two field strengths where the adjacent manifolds start to mix with the central n-manifold and where the atom is ionised are marked by horizontal dashed lines. The grey background indicates the region where the model ceases to be predictive. The red lines serve as a guide for the eye.

suggests that it is possible to circularise the atom within less than 1 ns. However, when the field strength of the optimised pulse increases dramatically, our model ceases to be predictive for the actual atomic system since we account for a small part of the Hilbert space (i.e. the lowest two diagonal ladders) only.

The first approximation to break down is the neglect of higher diagonal ladders in the $n = 51$-manifold. For strong amplitudes of the driving field, off-resonant transitions and transitions to higher diagonal ladders (which are only allowed due to a mixing of parabolic states by higher order Stark effects and thus only play a role for strong fields) are no longer suppressed. However, since those transitions are more strongly detuned and have smaller dipole elements than the transitions on the lowest diagonal ladder, the latter dominate the dynamics and a re-optimisation is possible to reach the desired fidelity under strong drives in principle. The optimised fields certainly look different but the possibility of reaching the target state is not affected. Nevertheless, the numerical calculations become rather demanding. One iteration of a pulse with $t_{\text{stop}} = 7\,\text{ns}$ needs a computation time of about 6 s in our model (involving 101 states). In contrast, when all states of the central n-manifold are considered (~ 2500 states), one iteration of the optimisation requires approximately ten minutes. The total computation time is given by that estimate multiplied by the number of iterations, which is of the order of 10^4 for $t_{\text{stop}} = 7\,\text{ns}$. The number of iterations further increases when decreasing t_{stop}.

The next approximation that breaks down is omission of adjacent Stark manifolds. As the driving RF field becomes stronger, the states in the Stark manifold get increasingly dressed and the energy spacing increases. Once the dressing is strong enough to induce a crossing of adjacent manifolds, the instantaneous eigenenergies of our model significantly differ from the ones obtained when considering the full atomic system. As a result, our model does not describe the actual atom any more. In the following, we derive an approximation for the critical RF field strength where the Stark splitting of two adjacent Stark manifolds becomes larger than their separation, or in other words, the field strength where two neighbouring Stark manifolds touch.

For reasons of simplicity we neglect the quantum defect here and assume a resonant driving RF pulse. Because the position of the centre of a manifold scales as $1/(2n^2)$ (cf. Rydberg formula in Eq. (2.5)), the central n-manifold crosses the upper $(n+1)$-manifold before crossing the lower $(n-1)$-manifold. In presence of a DC field, both Stark manifolds, n and $n' = n+1$, experience a Stark shift and become broader in energy. The Stark shift is proportional to the eccentricity quantum number μ which takes its maximal possible absolute value, $|\mu| = n-1$, at the top and the bottom of the $m = 0$-ladder (cf. Eq. (2.23) and Fig. 2.3). In addition, the energy levels get dressed by the RF field. The eigenstates of a perfect spin-J system coupled to a field mode are separated in energy by the Rabi frequency $\Omega = |\vec{\Omega}|$ (cf. Eq. (2.40)) [52]. When each pair of states acquires an additional energy splitting of Ω, the top and bottom of the diagonal spin ladder are shifted by $\Omega(n-1)/2$ with respect to the middle of the ladder. Adding up all three terms, the position of states at the top $(+)$ or bottom $(-)$ of the $m = 0$-ladder is given by

$$E_n^{\pm} = -\frac{1}{2n^2} \pm \frac{3}{2}(n-1)n\, F_{\text{DC}} \pm 3n\, F_{\text{RF}}\, \frac{n-1}{2}. \tag{3.24}$$

Solving $E_{51}^{+} = E_{52}^{-}$ (as the top of the $n = 51$ manifold touches the bottom of the $n' = n+1 = 52$ manifold) for F_{RF} with $F_{\text{DC}} = 2.346\,\frac{\text{V}}{\text{cm}}$ results in a critical field strength of $2.5\,\frac{\text{V}}{\text{cm}}$ for the driving field. This value is in agreement with the numerical calculation of the instantaneous eigenenergies of the $n = 50$ to 52 manifolds for different RF field strengths when taking the quantum defect into account.

As a result, our model ceases to be predictive for RF field strengths above this value, which, according to Fig. 3.7, concerns all pulses that are shorter than approximately $7\,\text{ns}$. For these RF fields strengths, our model provides no longer an appropriate description of the Rydberg atom and it is not possible to draw any definite conclusion about the possibility to circularise the atom with sufficient confidence. While it may still be possible to reach the target circular state under these very strong and broad pulses, the numerical effort to check the hypothesis poses a serious obstacle. When considering the extended Hilbert space containing all states with $n = 51 \pm 1$ and $m \geq 0$ (~ 4000 states), the computation time of one iteration increases to one hour. Thus, the optimisation becomes numerically infeasible because more than 10^4 iterations are necessary to provide the desired fidelity.

Eventually, when the field strength of the RF field is increased even further, a hard physical bound is reached when the fields are strong enough to ionise the atom. For states on the lowest diagonal ladder, the order of magnitude of the necessary field strength is given by the static field ionisation threshold, $E = 1/(9n^4)$ [8], which is $83\,\frac{\mathrm{V}}{\mathrm{cm}}$ for $n = 51$.

In summary, we find the speed limit to be determined by the internal structure of the atom. In other words, the speed limit is defined in terms of the spectrum of the field-free Hamiltonian [87] but for real physical systems, this Hamiltonian is typically an idealisation. For very strong external control fields, this idealisation ceases to be valid. It is thus important to keep the assumptions on which the Hamiltonian is based in mind when determining the quantum speed limit.

3.2.5 Experimental implementation

The last and final step is the implementation of optimised RF pulse shapes for fast circularisation in the experiment at the Laboratoire Kastler Brossel (LKB) at Collège de France. The experiment is performed on a thermal beam of ^{85}Rb atoms effusing from on oven. The beam crosses the experimental structure constructed of two plane-parallel electrodes, which produce the static electric field, $\boldsymbol{F}_{\mathrm{DC}} = F_{\mathrm{DC}}\boldsymbol{e}_z$, and four ring electrodes for the RF field generation. At the centre of the structure, three laser beams cross in the horizontal plane to excite the ground state atoms to the Rydberg regime at time $t = 0\,\mathrm{ns}$. By carefully tuning the laser beams, the atoms are selectively excited to $|nf, m = 2\rangle$ within the Stark manifold. At this point, the actual experiment, e.g. the fast circularisation, can be performed. Afterwards, when the atoms have left the structure, they are detected via state selective field ionisation which allows for resolving energy levels of different n-manifolds and of different m-levels within in the same manifold. Further details on the experimental setup and the experimental aspects of the following protocol can be found in [61, 3].

In order to provide pulse shapes which are optimised for the experimental setup at the time, we repeat the optimisation while taking new experimental insights into account. We now assume the $n = 52$-manifold and a DC field of $F_{\mathrm{DC}} = 2.5\,\frac{\mathrm{V}}{\mathrm{cm}}$. The quasi-resonant frequency of the ladder is $\omega_{\mathrm{stark}} = 249.5\,\mathrm{MHz}$, which has been calculated using the first-order Stark effect. Accordingly, the central frequency of the σ^+-polarised RF pulse in the experiment, and hence the frequency of the theoretical guess pulse, was chosen to be $\omega_{\mathrm{RF}} = 250\,\mathrm{MHz}$. The critical low-$m$ states show a detuning of

$$\delta_{0,1}^{\mathrm{RF}} = -178.4\,\mathrm{MHz}, \tag{3.25a}$$

$$\delta_{1,2}^{\mathrm{RF}} = -59.2\,\mathrm{MHz}, \tag{3.25b}$$

$$\delta_{2,3}^{\mathrm{RF}} = -4.7\,\mathrm{MHz}. \tag{3.25c}$$

with respect to the RF pulse and are slightly larger than for $n = 51$ (cf. Eq. (3.22)). As in the previous section, we consider in the simulations the lowest two diagonal ladders of the Stark manifold with $m \geq 0$ leading to a total Hilbert space size of 103.

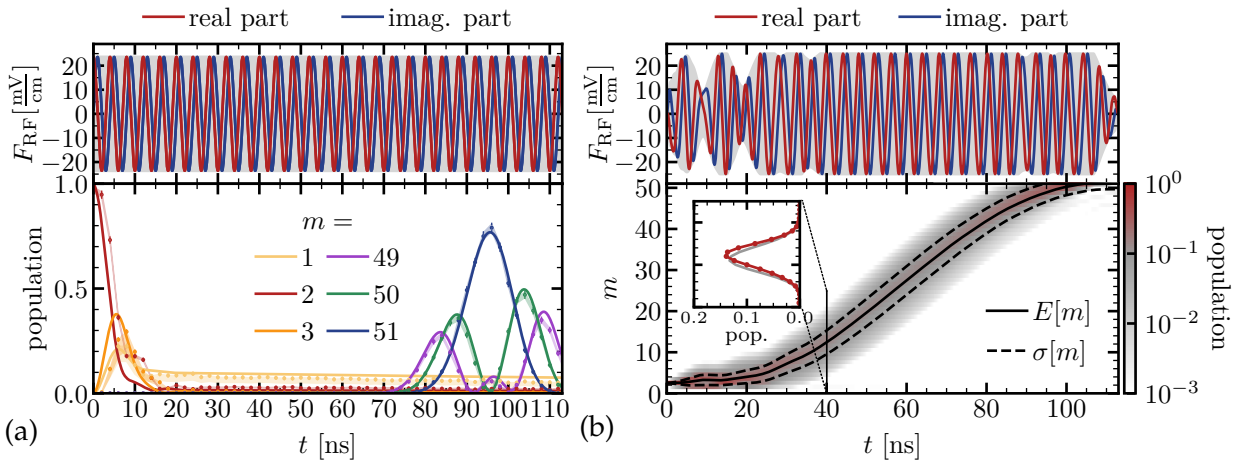

Figure 3.8: (a) Circularisation with a square pulse. Top: Shape of an RF π-pulse (grey) and its real and imaginary part for $F_{\mathrm{RF}} = 23.65\,\frac{\mathrm{mV}}{\mathrm{cm}}$ and $t_{\mathrm{stop}} = 114\,\mathrm{ns}$. Bottom: Evolution of the population of six different $|m\rangle$ levels as a function of the duration t of the RF pulse. The points are experimental with statistical error bars. The shaded areas shows the error range which are increased for levels $m = 1$ and 3 due to the calibration uncertainty [3]. The solid lines correspond to the numerical simulation of the experiment. (b) Circularisation with the 99%-optimised pulse under the current experimental constraints. Same as Fig. 3.3. The grey lines in the inset show the population distribution of the closest SCS with $\vartheta = 0.68\pi, \varphi = 0.49\pi$.

Without prior optimisation, the circularisation can be performed within $96\,\mathrm{ns}$ and has a fidelity of $79(1)\%$ in the experiment, see Fig. 3.8 (a). The solid lines show the numerical simulation using a plain RF pulse with a central frequency of $\omega_{\mathrm{RF}} = 250\,\mathrm{MHz}$, a flat-top shape with $6\,\mathrm{ns}$ edges and a fixed amplitude of $F_{\mathrm{RF}} = 22.8\,\frac{\mathrm{mV}}{\mathrm{cm}}$. The agreement between the experimental points and the simulations is excellent. Only for the low-m state do we see a small deviation between the two. This can be attributed to different methods the populations are recorded in the simulations and the experiment. In the experiment, an RF pulse which has been truncated to the duration τ is applied to the atom for each time step τ, i.e. by setting the amplitude to zero for $t > \tau$. Due to the response of the RF circuit and the presence of the cryostat, the pulse that is seen by the atoms is not identical to the one that has been programmed. Most importantly, the signal does not end at time τ sharp but decays over a short period of time. For high-m, the diagonal ladder is nearly harmonic and the ringdown simply rotates the state a bit further on the Bloch sphere. For low-m, on the other hand, the ladder is strongly anharmonic and the ringdown has a significant effect on the state, as can be seen in Fig. 3.8 (a).

We now optimise the circularisation to higher fidelities and constrain the pulse during the numerical optimisation in order to ensure experimental feasibility. As described before, we consider a flat-top shape function $S(t)$ with sine-squared edges lasting $10\,\mathrm{ns}$ each to account for the finite time it takes to switch the pulse on and off in the experiment. The field strength of the RF pulse is limited to $|F_{\mathrm{RF}}| = 25\,\frac{\mathrm{mV}}{\mathrm{cm}}$. Even though higher fields are in principle feasible, the response of the electrodes becomes highly non-linear beyond this point. We therefore suppress higher fields

to produce pulses which are more stable with respect to amplitude noise. Note that, while we optimise the field strengths of the x- and y-component of the RF pulse directly, the experimental control knobs are two time-dependent voltages, $V_r(t)$ and $V_i(t)$, generated by two outputs of an AWG. The voltages control RF mixers which modulate the amplitudes $F_r(t)$ and $F_i(t)$ of the two quadratures of the σ^+-polarized RF field as given in Eq. (3.7c) with $\phi_{\text{RF}} = 0$, i.e.

$$\boldsymbol{F}^+_{\text{RF}}(t) = F_r(t)\big(\cos(\omega_{\text{RF}}t)\boldsymbol{e}_x + \sin(\omega_{\text{RF}}t)\boldsymbol{e}_y\big) + F_i(t)\big(-\sin(\omega_{\text{RF}}t)\boldsymbol{e}_x + \cos(\omega_{\text{RF}}t)\boldsymbol{e}_y\big) \tag{3.26}$$

with $F_r(t) = 2\text{Re}\{S_{\text{RF}}(t)\}$ and $F_i(t) = 2\text{Im}\{S_{\text{RF}}(t)\}$. The dependency between the signal $V_{r,i}(t)$ delivered by AWG and the field amplitudes $F_{r,i}(t)$ which the atoms feel inside the cryostat is non-trivial and has been measured beforehand.

Similarly, also the frequency range that can be generated in the experiment is limited. The capabilities to generate very high frequencies are limited by the step size of the AWG ($1\,\text{ns}$). Moreover, the noise increases beyond a window of about 140 and $360\,\text{MHz}$ due to the response of the RF circuit and the influence of the cryostat. Even though lower and higher frequencies are in principle attainable to a certain degree in the experiment, limiting the pulse to this frequency window produces pulses with a higher stability in the experiment. The frequency was thus limited to this window by truncating the spectrum of the optimised pulse after each iteration using a flat-top shape function with sine-squared edges of $20\,\text{MHz}$. Incidentally, our choice of the n-manifold and the value of the DC field were motivated by matching the sweet spot of the frequency window around $250\,\text{MHz}$ with the first order Stark splitting of the Stark manifold.

The guess pulse is chosen to have a flat-top shape and a fixed amplitude F_{RF}. In order to find the pulse which circularises the atoms with a high fidelity in the shortest possible time, we perform the optimisation using Krotov's method several times using guess pulses with different lengths. We start by setting the field strength of the guess pulse to the maximal value of $25\,\frac{\text{mV}}{\text{cm}}$ and adjusted the duration of the pulse to match a π-pulse, i.e. $100\,\text{ns}$. Then, we tried to optimise the pulse to a fidelity of 99% while restricting the amplitude and the bandwidth as described before. While the population of the initial state $|m = 2\rangle$ is driven towards the circular state with 80% fidelity using this guess pulse, it can only be optimised towards a fidelity of 95% within the experimental constraints. Thus, we successively decreased the amplitude of the guess pulse and extended its length until the optimisation converged and the target fidelity was reached. The optimisation first succeeded for a guess pulse with $F_{\text{RF}} = 22\,\frac{\text{mV}}{\text{cm}}$ leading to a total duration of $t_{\text{stop}} = 113\,\text{ns}$ within 410 iterations of Krotov's method. Note that no two-step amplitude approach was employed here. As mentioned above, this is not strictly necessary and the important factor is the length of the pulse being long enough to perform the circularisation.

The optimised pulse shape and the resulting dynamics are shown in Fig. 3.8 (b). The optimised pulse is qualitatively very similar to the one discussed in the previous sections and can be separated into two parts: the formation of a SCS during the first $40\,\text{ns}$ (cf. inset in lower panel) and its subsequent rotation towards the north pole during the flat sequence of $73\,\text{ns}$ length.

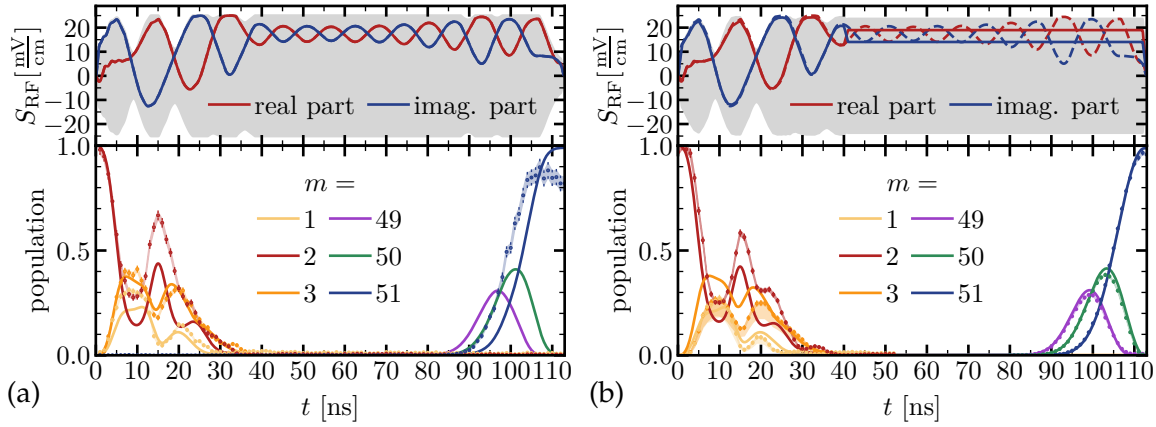

Figure 3.9: (a) First circularisation attempt using the quadratures of the 99%-optimised pulse under the current experimental constraints. Same as Fig. 3.8 (a) but with the complex shape function of the optimised pulse on top. (b) Circularisation using the modified quadratures (solid lines). The dashed lines in the upper plot show the unmodified quadratures as a reference.

As discussed in Sec. 3.2.3, implementing the RF signal in the AWG directly would lead to a significantly decreased fidelity, as the step size of the AWG is not sufficient to resolve the fast oscillation of the pulse. Instead, we demodulate the pulse with the central frequency of the RF, 250 MHz, and a phase of $\pi/4$. As shown in the upper panel in[1] Fig. 3.9 (a), the resulting quadratures are much flatter which simplifies their generation using the AWG. Beyond this, first tests in the experiments have shown that near-zero amplitudes and zero crossings might cause stronger amplitude noise. Demodulating the pulse with a phase of $\pi/4$ has the benefit of resulting in two quadratures of roughly the same amplitude.

In Fig. 3.9 (a) (lower panel), we present the evolution of the population of six different states on the diagonal ladder as measured in the experiment and simulated numerically. In the experiment, a circular state population of about 88% can be reached. While this is already an improvement compared to the unoptimised π-pulse, we notice deviations between theory and experiment. The RF pulse seems to be slightly stronger in the experiment as the population in the circular state rises several nanoseconds earlier than in the simulations. This hints to a calibration problem of the RF field strength in the experiment, or to a loss of RF amplitude due to the coarse graining in the AWG (as discussed in Sec. 3.2.3). Moreover, the population of $|m = 2\rangle$ spikes to unexpectedly high values of about 70% at 20 ns. The other two low angular momentum states $|m = 1\rangle$ and $|m = 3\rangle$, on the other hand, stay close to the simulated value. When presenting the unoptimised π-pulse, we have already discussed that the hard cut of the RF pulse in the experimental implementation, which is required to detect populations at intermediate times, can have a significant effect on the recorded signal. As the optimised pulses are more involved and strongly modulated, this effect is likely to be aggravated when considering optimised pulses.

[1]Note that the field strength F_{RF} differs by a factor of 2 between Fig. 3.9 and [61], e.g. Fig. 4, because of the aforementioned relations $F_r(t) = 2\mathrm{Re}\{S_{\mathrm{RF}}(t)\}$ and $F_i(t) = 2\mathrm{Im}\{S_{\mathrm{RF}}(t)\}$. While in this thesis, we show the real and imaginary parts of the complex shape function $S_{\mathrm{RF}}(t)$, the paper shows $F_{r,i}(t)$.

We can use our knowledge on the underlying dynamics to improve the fidelity in the experiment and the agreement with the theory. First, we can compensate for RF amplitude calibration uncertainty to first order by scaling the first $40\,\mathrm{ns}$ of both quadratures by a factor λ close to one. As we suspect the RF power being too high in the experiment, we expect $\lambda < 1$. Secondly, we know that for $t > 40\,\mathrm{ns}$, the state has the shape of a SCS and the optimised pulse merely has to rotate it towards the north pole of the Bloch sphere. The oscillations in the optimised pulse shapes after $40\,\mathrm{ns}$ therefore seem unnecessary. Upon closer examination, it turns out that they are caused by the frequency filtering. The frequency filter is approximately of rectangular shape and has a width of $\Delta\omega = 220\,\mathrm{MHz}$. The corresponding Fourier transformed signal is proportional to a sinc function, $\mathrm{sinc}(x) = \sin(x)/(x)$, with $x = \Delta\omega t/2$. The resulting oscillation in the time domain has a period of about $14\,\mathrm{ns}$ which matches the oscillation in Fig. 3.9. This observation corroborates our suspicion that the oscillations after $40\,\mathrm{ns}$ are indeed not essential for the success of the optimisation. Consequently, we flatten the amplitudes of the two quadratures, i.e. set them to constant values $F_{r,i}(t) = F^c_{r,i}$, for $t > 40\,\mathrm{ns}$ in order to simplify their sampling in the AWG. Moreover, this new pulse shape allows for performing a "closed loop" optimisation directly on the experimental signal: we optimise the amplitudes F^c_r and F^c_i independently in order to maximise the measured circular state population in the experiment. The ratio between the quadratures determines the direction of the rotation axis while the area under the quadratures determines the Rabi angle of the rotation. Only if the ratio between the two quadratures is well-adjusted do we hit the north pole of the Bloch sphere accurately.

We perform the adjustment of the optimised quadratures in two steps. We first set a scaling factor λ, and afterwards the two constant amplitudes $F^c_{r,i}$ of the quadratures for $t > 40\,\mathrm{ns}$ were adjusted to maximize the circular state population. It was found that a value of $\lambda = 0.95$ leads to the highest value of circular state population with the lowest population of the second highest states of the diagonal ladder. Around this value, the dependency of the transfer fidelity on λ is very flat, indicating that the optimised pulse is stable with respect to small amplitudes fluctuations.

In Fig. 3.9 (b), we present the flattened pulse shapes and the final dynamics in the experiment and the theoretical simulation. We reach the circular state with a fidelity of $96.2(3)\%$ in $113\,\mathrm{ns}$ in the experiment. While this is slightly lower than the theoretically predicted 99%, it has to be compared to the previous experimental fidelity using other circularisation methods. While the adiabatic circularisation allows for a high fidelity of 99.5%, it is very slow and takes a few microseconds. The time needed for circularisation using an unoptimised π-pulse, on the other hand, is comparable to our protocol but only allows for fidelities of $79(1)\%$. We provide both fast and accurate circularisation using optimised pulse shapes. The circular state is reached within merely about 25 oscillations of the RF field. The transition speed is ultimately limited by the RF power available to the experiment. With stronger RF sources, the time for the circularisation can be reduced even further (cf. the discussion on the quantum speed limit in Sec. 3.2.4). The agreement between the experimental points and the theory predictions are remarkable at the

upper end of the ladder (i.e. for $t > 80\,\mathrm{ns}$). However, there are significant deviations for the low-m states at the beginning of the sequence. These already occurred for the unoptimised π-pulse and were discussed above. The agreement could be improved by performing a thorough analysis of the experimental filter functions and modify the input signal accordingly. Distortions of the signal can mostly be attributed to the response of the electronics, such as the RF circuit, and the cryostat. However, such an analysis is tedious and complicated. Most importantly, the experiment does not possess a sensor inside the cryostat which could measure the signal directly at the level of the atoms. We have started analysing the response but did not achieve a real improvement given the limited data we had at hand. As the final fidelity of the circular state preparation is our main target and sufficient for our purpose, we did not investigate on it further.

It shall finally be mentioned that the preservation of coherence in the experiment under the optimised pulse has been tested by checking that the protocol does not spoil a coherent superposition with a reference level. They used an intricate Ramsey scheme involving forwards and backwards propagations under the optimised pulse, proving its high stability and versatility. They found a very high fringe visibility of $0.891(6)$ which is mainly limited by electric field noise. When the field noise was extrapolated to zero the value increases to 1, showing that the optimised pulse preserves coherence extremely well. This is mostly relevant if the optimised pulse shall be used to create or preserve superposition, as we do in the next section.

3.3 Electrometric cat states

Optimal control theory is more powerful than merely improving existing protocols such as the circularisation of Rydberg atoms. It also enables to prepare a highly non-classical superposition in the Stark manifold for which no intuitive preparation method is known. In Sec. 3.3.1, we motivate the choice of our target state by its utility in quantum metrology. Afterwards, in Sec. 3.3.2, we present the results of the optimisation and the experimental realisation, both of which have been published in [61].

3.3.1 Choosing the target state

The general idea of quantum metrology is to measure a physical quantity with enhanced sensitivity, beyond what is classically possible, by means of quantum strategies [23, 24, 25, 26]. The most simple form is the quantum estimation problem in which the value of a continuous parameter x, for instance a quantum phase, is to be measured. For simplicity, we only consider pure states and closed quantum systems in the following. Usually, the strategy to recover the value of x can be divided into the following steps:

1. Initialisation of the quantum sensor in a known state $|\psi_0\rangle$.
2. Transformation into the initial sensing state, $|\psi_s^0\rangle = \hat{U}_\mathrm{c}\,|\psi_0\rangle$.
3. Sensing period: Evolution of the sensing state under the influence of the quantity to be measured, $|\psi_s^x\rangle = \hat{U}(x)\,|\psi_s^0\rangle$.
4. Evolution of the final sensing state into observable states, often chosen to be $|\psi_x\rangle = \hat{U}_\mathrm{c}{}^\dagger\,|\psi_s^x\rangle$.
5. Read-out of the final state of the quantum sensor, $|\psi_x\rangle$.

If the initial state is equal to the sensing state, $|\psi_0\rangle = |\psi_s^0\rangle$, and if the final sensing state is read out directly, $|\psi_x\rangle = |\psi_s^x\rangle$, steps 2 and 4 could be omitted, respectively. The final read-out (step 5) can be expressed in terms of a set of Hilbert space operators $\{\,\hat{P}_i\,\}$ that form a positive operator valued measure (POVM). The probability $p_i(x)$ to measure the outcome i if the sensor is in the final sensing state $|\psi_x\rangle$ is given by [26]

$$p_i(x) = \mathrm{Tr}\left\{\hat{P}_i\,|\psi_x\rangle\langle\psi_x|\right\}. \tag{3.27}$$

The measurement outcome depends on the final sensing state and thus on the value of x. The sensitivity with which the value of x can be deduced from the measurement outcomes is given by the Cramér-Rao bound [25],

$$\Delta x \geq \frac{1}{\sqrt{F(x)}} \tag{3.28}$$

where $F(x)$ is the Fisher information. Roughly speaking, the Fisher information measures the amount of information on x that can be extracted from a probability distribution $p_i(x)$. Equation (3.28) is the best sensitivity given from this specific POVM. An accuracy bound which is independent of the POVM can be found by minimising Eq. (3.28) with respect to all possible POVM. This results in the quantum Cramér-Rao bound,

$$\Delta x \geq \frac{1}{\sqrt{J(x)}} \tag{3.29}$$

where $J(x)$ is the quantum Fisher information [25]. In the simple case where the final sensing state can be written as $|\psi_s^x\rangle = e^{-i\hat{H}x}\,|\psi_s^0\rangle$, the quantum Cramér-Rao bound takes the simple form of an uncertainty relation

$$\Delta x \geq \frac{1}{2(\Delta\hat{H})_{|\psi_s^0\rangle}}, \tag{3.30a}$$

$$\text{with}\quad (\Delta\hat{H})_{|\psi_s^0\rangle} = \sqrt{\langle\hat{H}^2\rangle_{|\psi_s^0\rangle} - \langle\hat{H}\rangle^2_{|\psi_s^0\rangle}} \tag{3.30b}$$

being the spread of the operator $\hat{H}$ on the initial sensing state $|\psi_s^0\rangle$.

The best precision for estimating the value of x that can be obtained from a single measurement is thus fully determined by the energy variance of the Hamiltonian on the initial state. We now consider the problem of estimating the rotation angle x about the Z-axis of the generalised Bloch sphere of a spin-j system. The rotation can be written as $\mathcal{R}_Z(x) = e^{-i\hat{J}_Z x}$ (cf. Eq. (2.41)). The simplest choice of an initial state is a SCS which is quasi-classical and has minimal uncertainty (cf. Sec. 2.3.2). The SCS with the largest spread $\Delta\hat{J}_Z$ can be found at the equator. SCS at the north or south pole, on the other hand, are invariant under rotations about the Z-axis. The single-shot sensitivity of estimating the rotation angle x with a SCS $|\vartheta = \pi/2, \varphi\rangle$ is equal to [26, 59],

$$\Delta x_{\text{SCS}} \sim \frac{1}{\sqrt{2j}}, \tag{3.31}$$

which is called the standard quantum limit (SQL). In order to increase the value of the quantum Fisher information and to gain a quantum enhancement, it is necessary to employ non-classical states. One option to achieve this goal is by using a superposition of SCS, so-called cat states. They can be written as $|\psi_{\text{cat}}\rangle = \frac{1}{\sqrt{2}}\left(|0,0\rangle + |\vartheta,0\rangle\right)$, where we have chosen the coordinate system of the Bloch sphere such that the first state of the superposition is located on the north pole and the second state in the XZ-plane, for simplicity. The resulting single-shot sensitivity is [26, 59]

$$\Delta x_{\text{cat}} \sim \frac{1}{j(1-\cos\vartheta)}. \tag{3.32}$$

For $\vartheta = \pi$, which corresponds to a superposition of two SCS at opposite pole of the Bloch sphere, the sensitivity reaches its maximal value

$$\Delta x_{\text{HL}} \sim \frac{1}{2j}, \tag{3.33}$$

which is called the Heisenberg limit (HL) [89]. It is the fundamental limit to the precision of a measurement and ultimately originating from Heisenberg-like uncertainty relations. Another method of achieving a precision beyond the SQL is by using spin squeezed states [90, 26, 91].

In the following, we consider the specific quantum estimation problem in which we use Rydberg atoms as sensors for measuring electric field strengths based on preceding work by our collaborators at the LKB at Collège de France presented in Ref. [59]. The large spin-j system can be identified with the lowest diagonal ladder of the Stark manifold with $j = (n-1)/2$ as defined in Eq. (2.27) where the circular state $|n\text{C}\rangle$ corresponds to the north pole $|\vartheta = 0, \varphi = 0\rangle$. The general idea of the Rydberg atom electrometer is as follows: In a frame rotating with the frequency ω_{RF} of the RF pulse, any detuning δ between the energy splitting of the ladder, ω_{stark}, and the RF, $\delta = \omega_{\text{stark}} - \omega_{\text{RF}}$, induces a rotation of the Bloch vector around the Z axis (cf. generalised Rabi frequency in Eq. (2.40)). This can be written as a rotation $\mathcal{R}_Z(x)$ with $x = \delta\tau$ where τ is the interrogation time. As ω_{stark} depends on the value of the DC field, the phase x contains information on the DC field amplitude.

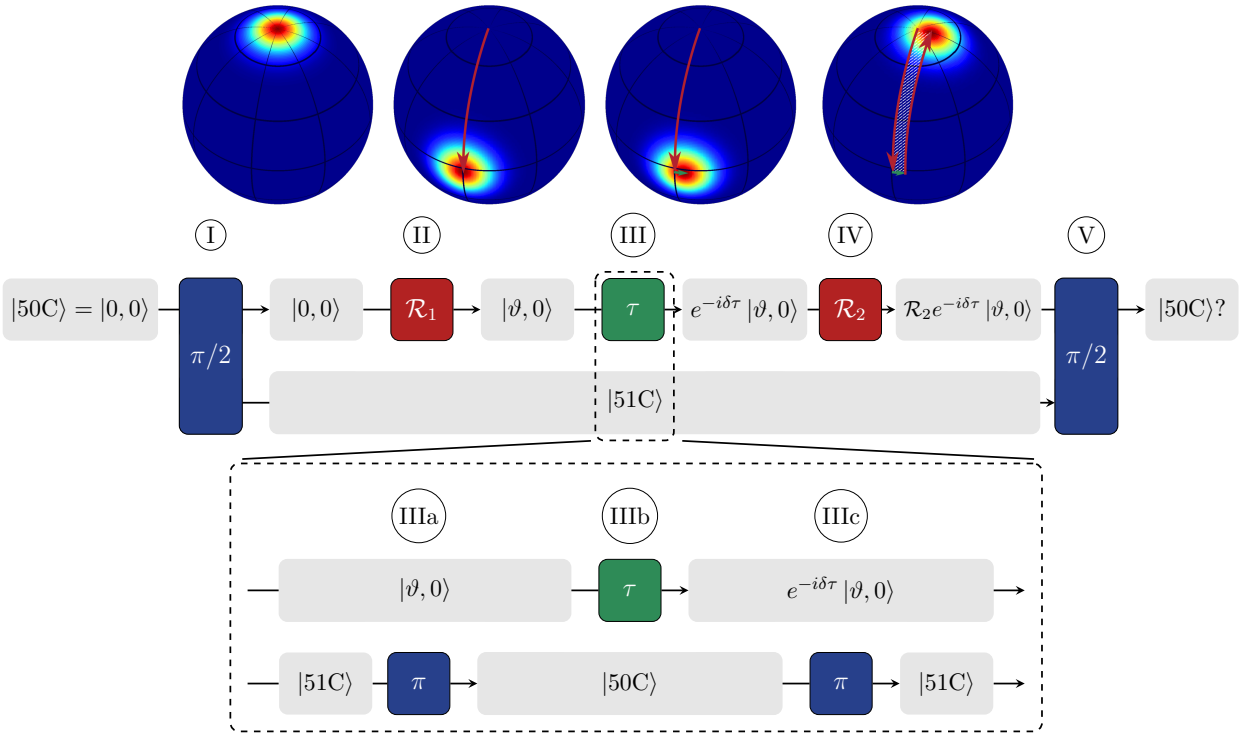

Figure 3.10: Ramsey sequence for measuring an electric field. A detailed explanation in given in the main text. Gray boxes indicate states, blue boxes MW pulses, red boxes RF pulses and the green box the interrogation time. The circled Roman numbers label the steps. The Bloch spheres on top visualise the Q-function on the generalised Bloch sphere of the lowest diagonal ladder of the $n = 51$-manifold after the first four steps, respectively. The arrows on the Bloch sphere visualise the effect of the RF pulses (red) and the interrogation time (green). The dashed box at the bottom indicates an alternative approach which brings the reference state back to the $n = 50$ manifold.

The cat state $|\psi_{\text{cat}}\rangle$ from above can be prepared experimentally by using a combination of MW and RF pulses as described in the following. The specific measurement protocol is an example of a Ramsey interferometry measurement and depicted in Fig. 3.10. First, the Rydberg atom is initialised in a circular state, $|\psi_0\rangle = |n\text{C}\rangle = |0, 0\rangle$, with $n = 50$ in this case (first Bloch sphere in Fig. 3.10). The initial sensing state $|\psi_s^0\rangle = |\psi_{\text{cat}}\rangle$ is prepared in three steps: First, a $\pi/2$-microwave (MW) pulse (step I in Fig. 3.10) shelves half of the population in a different Stark manifold such that the other half can be manipulated as required. Second, the state $|0, 0\rangle$, is rotated towards lower latitudes into the SCS $|\vartheta, 0\rangle$ by $\mathcal{R}_1 = \mathcal{R}(\vartheta, 0)$ (cf. Eq. (2.42)) using a resonant RF pulse (second Bloch sphere, step II). Since the Stark splitting differs between the $n = 50$ and $n = 51$-manifolds, the shelved population in $|51\text{C}\rangle$ is mostly unaffected by the RF. Finally, the shelved population can be brought back to the $n = 50$ manifold using a MW pulse (step IIIa). The initial sensing state is then the cat state $|\psi_s^0\rangle = \frac{1}{\sqrt{2}}(|0, 0\rangle + |\vartheta, 0\rangle)$. In the limit of $\vartheta = \pi$, this state can also be written as $|j, j\rangle + |j, -j\rangle$

The next step is the actual sensing period (step IIIb). Any detuning between the Stark splitting and the RF, δ, induces a rotation of the SCS round the Z-axis of the Bloch sphere. After the interrogation time τ, the SCS $|\vartheta, 0\rangle$ has accumulated a field dependent phase, $x = \delta\tau$, or in other words, rotated by an angle x around the Z axis (third Bloch sphere). Afterwards, the preparation of the cat state is inverted to prepare the read-out. For this, the population $|0, 0\rangle$ is shelved once more in the $n = 51$ manifold using a MW pulse (step IIIc). Then, the SCS which remains in $n = 50$ is brought back towards the north pole of the sphere by applying a second RF pulse $\mathcal{R}_2 = (\vartheta, \pi)$ (fourth Bloch sphere, step IV). Finally, the two parts of the superposition are recombined with a $\pi/2$-MW pulse on the $|50\text{C}\rangle \leftrightarrow |51\text{C}\rangle$-transition (step V). The final read-out is performed by measuring the population in the circular state $|50\text{C}\rangle$.

If the Stark frequency is equal to the RF frequency, $\delta = 0$, the initial state $|50\text{C}\rangle$ is recovered at the end of the sequence. If δ is small but non-zero, the final SCS after step IV is overlapping with $|50\text{C}\rangle = |0, 0\rangle$ and the probability of finding this half of the population in $|50\text{C}\rangle$ is only slightly smaller than one. However, the SCS has accumulated a quantum phase due to its trajectory on the Bloch sphere (indicated by the white dashed area in the fourth Bloch sphere Fig. 3.10). This "global phase" of the SCS can be measured by superposing it with a reference state, namely $|51\text{C}\rangle$. The final $\pi/2$-MW pulse (step V) is able to reveal that phase as the final population in $|50\text{C}\rangle$ depends on it and accordingly on δ. The sensitivity of measuring the value of the DC field is finally given by $\sigma_{\text{cat}} \sim 1/(\tau j(1 - \cos\vartheta))$, equivalently to Eq. (3.32). For $\vartheta = \pi$, which corresponds to a superposition of the north and south pole of the Bloch sphere, the HL $\sigma_{\text{HL}} \sim 1/(2j\tau)$ is reached. Lastly, it shall be noted that the two MW pulses IIIa and IIIc, which transfer the reference state from $n = 51$ to 50 and back, do not affect the sensitivity of the protocol at all. They were thus omitted in the experiment as they extend the time required to perform the protocol without any benefit. The steps IIIa to c in the dashed box in Fig. 3.10 can thus be replaced by step III (the sensing period).

Our aim is now to improve the presented measurement scheme further by employing OCT. There are two ways in achieving this. First, the actual sensitivity in the experiment depends on the value of ϑ and the fidelity of the SCS after the rotation. The lowest diagonal of the Stark manifold is not a perfectly harmonic spin-j system due to higher order Stark effects and the quantum defect. Consequently, the SCS dephases during the rotation $\mathcal{R}_1$ and the distortion is stronger, the closer the state is to the south pole of the sphere. As a result, the second RF pulse $\mathcal{R}_2$ is not able to bring the population back to the north pole of the sphere. However, we have shown in the previous section that OCT can be used to efficiently transfer population from one end of the ladder to the other. By replacing the plain RF pulse $\mathcal{R}_2$ by the optimised pulse for fast circularisation and $\mathcal{R}_1$ by the its time-inverse, we can rotate the circular state down to the $|m = 2\rangle$ state and thus achieve a large superposition close to the fundamental limit $\vartheta \approx \pi$. In fact, the fast circularisation pulse has already been used successfully for quantum metrology achieving precisions below the SQL in the experiment [3].

A second, more interesting approach is to omit the MW pulses altogether and prepare a cat state starting directly from the circular state $|50\text{C}\rangle$, i.e. combining the pulses I, II and IIIa into one optimised RF pulse. As MW pulses are one order of magnitude slower than RF pulses, an optimised protocol using RF pulses only would increase the repetition rate significantly. We have thus optimised a pulse that prepares a superposition of the north pole (i.e. the circular state $|n\text{C}\rangle$) and the $m = 1$-state close to the south pole,

$$|\psi_s^0\rangle = \frac{1}{\sqrt{2}} \left(|m = 1\rangle + |n\text{C}\rangle \right). \tag{3.34}$$

This superposition is a promising candidate for quantum metrology, as its two parts have very different properties. The circular state with $m = n - 1$ and eccentricity quantum number $\mu = 0$ is completely insensitive to electric fields and serves as a reference. The state $|m = 1\rangle$, on the other hand, is highly sensitive with $\mu \propto n^2$. The preparation of the cat state can be interpreted as a $\pi/2$-pulse on a large 50-photon transition which can be achieved using optimal control, as we show in the following section.

3.3.2 Cat state preparation

We start the preparation of the cat state in Eq. (3.34) from the lowest state of the $m = 2$ ladder in the $n = 52$ Stark manifold, $|m = 2\rangle$. To quantify the mismatch of the state-to-state optimisation, we have employed the same functional from Eq. (3.14). The target state has been set to

$$|\Psi_t^{\text{split}}\rangle = \frac{1}{\sqrt{2}} \left(e^{i\phi_t} |1\rangle + |51\rangle \right). \tag{3.35}$$

The relative phase ϕ_t is fixed but arbitrary. We have tested several phases which all lead qualitatively to the same result and thus decided for $\phi_t = \pi$ leading to a relative phase of -1 between the two parts of the superposition. Moreover, the balance between the two parts could be tuned if desired and numerical tests showed that the optimisation is also successful for unequal weights.

In the simulations, we have assumed the same part of the Hilbert space and the same constraints as for the fast circularisation described above. As a guess pulse, we have used a circularly polarised RF pulse with a flat-top shape with a length of $150\,\text{ns}$, an amplitude of $22\,\frac{\text{mV}}{\text{cm}}$ and a central frequency of $250\,\text{MHz}$. As it has the same amplitude as the guess pulse of the fast circularisation above, the circular state reaches its maximal population around $113\,\text{ns}$. At $150\,\text{ns}$, there is only a small fraction of 0.0002% of the population in the circular state while the $|m = 1\rangle$ is populated with about 5%. This results in a poor fidelity of 2.4% for the guess pulse. During the optimisation with Krotov's method, the bandwidth window has been slightly shifted to frequencies between 130 and $320\,\text{MHz}$ with edges of $50\,\text{MHz}$ width, such that the centre of the window, $225\,\text{MHz}$, is slightly smaller than before. This has been done with the knowledge, that we not only have to address the transitions to larger m-values, which are nearly harmonic with a transition frequency of $250\,\text{MHz}$, but also the $|m = 1\rangle \leftrightarrow |m = 2\rangle$ transition which is detuned by $59.2\,\text{MHz}$. All remaining constraints have been left unchanged.

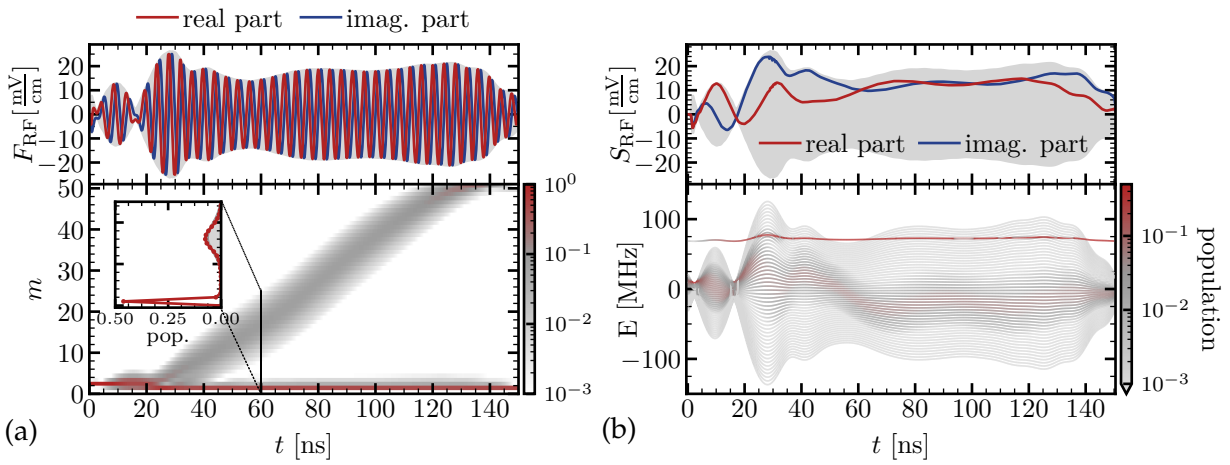

Figure 3.11: Optimised cat state preparation with the 99%-optimised pulse under the current experimental constraints. (a) Same as Fig. 3.3. The grey line and the grey shade in the inset indicate the population distribution of the closest SCS with $\vartheta = 0.61\pi$ when considering the states $|m > 2\rangle$ only. (b) Shown on top is the complex shape function of the optimised pulse when demodulating the pulse with a phase of $\pi/4$. The pulse is separated in its real and imaginary part while the envelope is represented by the grey shade in the background. The bottom shows the time evolution of the instantaneous eigenstates of the atom-RF field Hamiltonian in the rotating frame, also called the "dressed states". The vertical position of the lines in reflects the instantaneous energy of the corresponding state, and their colour show the population at time t.

The preparation of the cat state could be optimised to a fidelity of 99% after only 77 iterations of Krotov's method. The remarkably fast convergence (when compared to the required 410 iterations of the fast circularisation) is an indicator that the duration of the protocol has not been pushed to the speed limit. Indeed, we have determined the minimal time to perform the protocol only with a resolution of 10 ns, as we found this sufficient for our purposes. Pulses shorter than 140 ns did allow for optimising the process to the desired fidelity of 99% from which we can conclude that the speed limit has increased with respect to the fast circularisation.

In Fig. 3.11 (a), we present the optimised pulse and the resulting dynamics on the lowest diagonal ladder of the $n = 52$-Stark manifold. We can identify three parts of the optimised pulse with very distinct roles. In the first tens of nanosecond, we see that, even when starting with a simple RF guess pulse, the optimised pulse manages to split the population into two branches. The pulse shelves half of the population in a superposition of $|m = 1\rangle$ and $|m = 2\rangle$ (see high peak in inset in lower panel of (a)) which is an eigenstate of the time-dependent Hamiltonian and thus a dark state to the RF field. At the same time, the pulse forms a SCS centred at higher levels with $m \sim 10$. During the next ~ 90 ns, the RF pulse rotates the SCS towards the north pole of the generalised Bloch sphere, i.e. the circular state, while leaving the dark state unaltered. This interpretation can be corroborated by considering the time-evolution of the instantaneous eigenstates of the coupled atom and RF Hamiltonians in the lower panel of Fig. 3.11 (b). The RF pulse dresses the eigenstates of the atom and modifies the instantaneous eigenenergies which

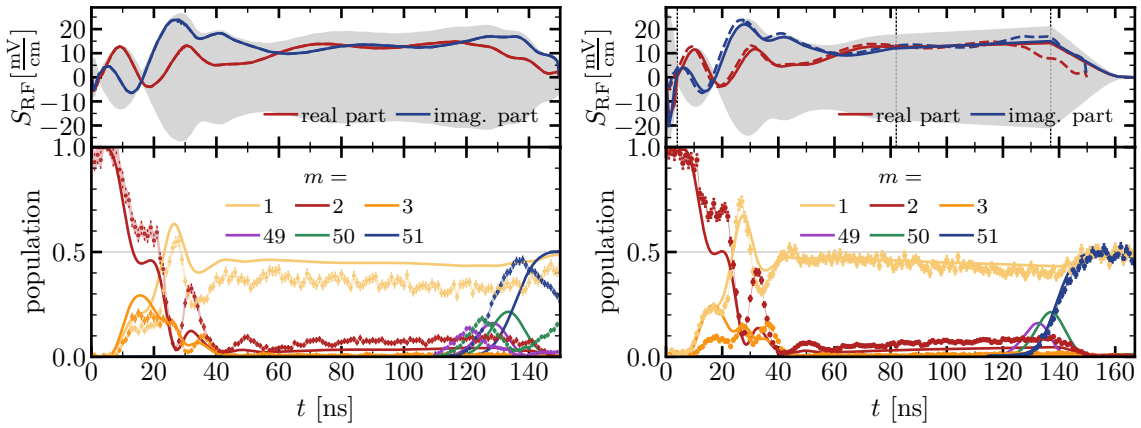

Figure 3.12: Optimised cat state preparation using the normal (a) and the modified (b) quadratures (solid lines) of the 99%-optimised pulse under the current experimental constraints. Same as Fig. 3.9 (b). The coloured dashed lines in the upper panel in (b) show the unmodified quadratures as a reference. The vertical dashed lines in (b) indicate the time points where the modifications took place (see main text). The solid lines in the lower panel in (b) correspond to the numerical simulation using the flattened pulse without the increased first lobe.

is apparent from the obvious similarity between the shape of the optimised quadratures in the upper panel of (b) and of the dressed states as a function of time. The circularisation of the SCS causes a complex interference pattern in the dressed-state picture. However, we discover a separated energy level around 70 MHz in the dressed-state basis which stays populated with about 50% during most of the pulses duration – the dark state. During the last $\sim$ 15 ns, the pulse is smoothly switched off which adiabatically transforms the dark state into $|1\rangle$ and the SCS ends up in the circular state. As it turned out, the undesirable trapping of the population in $|m = 1\rangle$, that we have observed during the unoptimised circularisation and identified as the main source of population loss, is now the enabler for the preparation of the cat state.

Before testing the pulse in the experiment, we perform one adjustment. We see that the optimised pulse does not go down to zero at the beginning and the end of the time interval. This is due to the cutting of the bandwidth after the last iteration of Krotov's method. To facilitate the experimental implementation we add 1 ns before the beginning of the pulse and switch in on smoothly using a sine-squared edge. Then, the pulse is shifted by 1 ns on the time grid such that the pulse starts at 0 ns. The same was done at the end of the pulse. In Fig. 3.12 (a), we present the experimental data when employing these optimised quadratures directly. As with the circularisation, we see a qualitative agreement between the experimental measurements and the theoretical predictions. However, we also see similar deviations as before. The circular state population rises earlier in the experiment hinting towards a too high RF field strength. The population of the dark state, on the other hand, is slightly lower than predicted. At its maximal point, the circular state reaches a population of 45% while $|m = 1\rangle$ reaches 43% at the end of the pulse, indicating that we are already close to the target state.

Similarly to the fast circularisation, we can use our physical insights to simplify and improve the optimised pulse for the experimental implementation. Firstly, we employ a global scaling factor during the first $80\,\mathrm{ns}$ of the pulse of 0.925 to compensate for amplitude calibration uncertainty and the observed too-high field strength. When employing this modification alone, the circular state population is much closer to the theoretical prediction and rises to about 50% at the end. The population in $|m = 1\rangle$, however, decreases even further. This is probably due to the overall changed amplitude of the pulse which also changes the population of the dark state. Before turning to this, we simplify the shape of the second part of the pulse. As shown in Fig. 3.12 (b), we replace the second half of the pulse, $t > 80\,\mathrm{ns}$, with linearly increasing, between 80 and $136\,\mathrm{ns}$, and decreasing, 136 and $167\,\mathrm{ns}$, amplitudes of the control voltages of each quadrature. In doing so, we have a single parameter to optimise for each quadrature, i.e. the amplitude at time $136\,\mathrm{ns}$. The linear ramps enables us to tune the rotation angle of the SCS by independently changing the pulse area for each quadrature, while ensuring that the phase and amplitude of the RF field vary slowly enough for the dark state to adiabatically remain shelved in the instantaneous dressed state. The second ramp is slightly longer in the experiment than in the simulation and hence lengthens the overall pulse duration to compensate for the non-linear dependency between the RF field strength and the applied voltages. However, these optimisations were not sufficient to increase the population in $|m = 1\rangle$. We found that the final balance depends strongly on the applied voltage during the first $4\,\mathrm{ns}$ of the pulse. Hence, we rescale the amplitudes of the quadratures for $t \leq 4\,\mathrm{ns}$ by a separate factor α. We found that the balance between the two parts of the superposition can be tuned by changing the value of α and we obtained an equal superposition for $\alpha = 2.8$. Lastly, the linear ramp was reoptimised for the new beginning of the pulse.

Figure 3.12 (b) shows the dynamics in the Stark manifold as driven by the modified pulse quadratures. The experimental data and the simulation reveal an excellent agreement. The final target state population in the experiment (averaged over the last six points) is $P_C = 48(1)\%$ in the circular state and $P_{m=1} = 48.4(8)\%$ in $|m = 1\rangle$. In the simulation, we achieved a fidelity of 99% ($P_C = 50.2\%$ and $P_{m=1} = 48.6\%$). While we achieve a perfect balance and a great agreement for $|m = 1\rangle$, the population in the circular state is slightly lower in the experiment. Lastly, the coherence of the cat state has been examined in the experiment in a similar fashion as for the fast circularisation. A high fringe visibility of $0.80(1)$ has been found which amounts to $0.97(2)$ when extrapolated to zero field noise. Using the determined degree of coherence in the experiment, the fidelity of the cat state preparation in the experiment could be calculated to be 93%.

3.4 Summary

We have shown in this chapter how to navigate the Stark manifold of Rydberg atoms using optimal control theory by means of two examples. First, we have significantly improved the circularisation of Rydberg atoms in terms of time and fidelity as compared to conventional methods. Beyond deriving the optimal pulse shape, we have demonstrated together with our collaborators from Laboratoire Kastler Brossel (LKB) at Collège de France their experimental feasibility as shown in Fig. 3.9 (b).

This result was largely enabled by the elaborate theoretical study of the optimised pulse. Most importantly, we were able to understand the dynamics induced by the optimised pulse and found that they can be decomposed into two steps: the preparation of a spin-coherent state (SCS) and its subsequent rotation towards the North pole of the generalised Bloch sphere spanned by a subspace of the Stark manifold. This insight allowed us to fine-tune the field quadratures in the experiment to compensate for experimental uncertainties, thus enabling the high fidelity of circular state preparation in the experiment. Moreover, we have tested the optimised pulse for robustness against various sources of noise. We found the pulse to be very stable which can mostly be attributed to the short duration and small bandwidth of the pulse. We found the largest source of noise to be the coarse-graining of the optimised pulse due to the implementation in a arbitrary waveform generator (AWG). We could solve this problem by demodulating the optimised pulse with the central radio frequency and shaping only the weakly time-dependent envelopes instead. RF calibration uncertainties, on the other hand, can be compensated for by scaling the amplitude of the optimised field in the experiment with great success. Lastly, we have investigated the fundamental speed limit for circularisation when easing the experimental constraints as shown in Fig. 3.7. We found that the time scale for preparing a SCS is given by the detuning of the RF pulse from undesired transitions, whereas the time to rotate the SCS to the North pole is determined solely by the Rabi frequency. A further speed up would thus be possible by using (a) a larger DC field strength, which increases the detuning, and (b) a larger RF field strength, which allows for faster rotation. For the given DC field strength, increasing the RF field strength could, in principle, bring the circularisation time down to about $10\,\mathrm{ns}$. However, the control fields become so strong that eventually the theoretical model ceases to be reliable. Moreover, this would come not only at the price of large RF amplitudes but also of a much broader spectral bandwidth. Therefore, given the present experimental technology, circularisation times much below $50\,\mathrm{ns}$ do not seem realistic.

In the second example, we have successfully employed optimal control to prepare a non-trivial superposition of a low- and high-angular-momentum state for which no intuitive preparation method was known beforehand. The preparation of the Schrödinger-cat-like state can be interpreted as a $\pi/2$-pulse on a large 50-photon transition. A similar state with much lower distance between the two parts of the superposition could previously only be prepared experimentally by using a sequence of several RF and MW pulses, thus within several microseconds.

Again, the optimised control field allowed us remarkable insights into the dynamics in the Stark manifold and the pulse can be split into three steps: (1) the generation of a superposition of a SCS on the one hand, and a low-m_ℓ state which is dark towards the RF on the other hand, (2) the rotation of the SCS towards the north pole which leaves the low-m_ℓ state unaffected, and (3) the undressing of the system by switching off the RF adiabatically, thus transforming the dark state into the desired $m_\ell = 1$ state at the south pole while bringing the SCS to the north pole. The deep insight into the dynamics allowed for fine-tuning the preparation and achieving a high fidelity in the experiment, as presented in Fig. 3.12 (b).

The two presented protocols for the preparation of circular states and cat states are very valuable in several fields of quantum technology. Circular states are useful in many areas of quantum technology, such as quantum metrology but also quantum computing [92, 93] and quantum simulation [94]. The fast circularisation scheme could significantly decrease the time required for initialisation of circular states as well as increase their fidelity. The circularisation, interpreted as the excitation of Rydberg states from low- to high-angular-momentum states, can also serve for the microwave-to-optical single-photon conversion [95, 96]: While low-angular-momentum Rydberg states couple to optical photons and thus have short lifetimes, circular states do not. Circular states do, however, couple strongly to microwave photons. In other words, it is circularisation from low- to high-angular-momentum states, together with its inverse process, that provides the link to interface optical and microwave photons. However, such an interface will work reliably only when the transfer proceeds both sufficiently fast and with high accuracy. Beyond the "standard" circularisation, optimal control could also assist the atom-specific preparation of circular or near-circular states required for the quantum simulation of transport phenomena [97].

The main benefit of the cat state is its applicability for quantum metrology [59], thus acting as a sensing state for measuring electric field strengths at the Heisenberg limit even under dissipation [98]. As opposed to the conventional approach presented in Fig. 3.10, no MW pulses are required when using the cat states. The protocol can thus be sped up by one order of magnitude from micro- to a few hundred nanoseconds. In the current experimental setup, however, the repetition rate is not limited by the MW pulses but by the time-of-flight of the atoms through the experimental setup, which is about $300\,\mu s$. The cat state would thus be most useful in a setup with trapped atoms where the repetition rate is mainly limited by the actual protocol time and could hence be greatly reduced by suppressing the MW pulses.

4

IMPROVED MODELLING OF ALKALINE-EARTH ATOMS

The field of Rydberg physics has focused for a long time on the study of alkali atoms with a single valence electron. The similarities to hydrogen render them easy to describe in theoretical terms, as only slight modifications via the quantum defect suffice to model the dynamics of the valence electron. There are, however, reasons to move forward and extend the study to atoms with more electrons. Due to the very long lifetime of Rydberg atoms, the optical transition back to the ground state occurs at a very low rate rendering the detection of alkali Rydberg atoms via fluorescence difficult [18]. Circular states do not possess an optical transition at all and are thus impervious to visible light. Additionally, trapping of alkali Rydberg atoms remains a challenging task even if optical trapping has been demonstrated experimentally [99, 100, 101]. Due to the exaggerated response of Rydberg atoms, they react very differently to external perturbations than ground state atoms, rendering it difficult to trap both kinds of alkali atoms in the same potential.

Atoms with two valence electrons, such as alkaline-earth atoms, offer a new degree of freedom for studying and controlling Rydberg atoms [31, 102]. The electron that remains in the core (the "inner" electron), after the other one has been excited to the Rydberg regime (the "outer" electron), leaves the ionic core optically active. This allows, for instance, for confining Rydberg atoms in an optical lattice via optical dressing of the inner core electron which can be used for quantum simulation of many-body physics [103, 104]. If the outer electron is in a low-angular-momentum state, doubly excited states of strontium auto-ionise due to the interaction between the two electrons [105]. Auto-ionisation, however, can be avoided by exciting the Rydberg electron to high-angular-momentum states. The absence of auto-ionisation allows for probing the state of the outer electron. This can be used to optically image the atoms via resonant light scattering off the ionic core [106] and even to distinguish low- from high-angular-momentum states [107]. Moreover, the auto-ionisation rate of doubly excited states decrease rapidly as the inner electron is excited which raises the possibility to create doubly excited planetary atoms [108, 109]. All in all, the additional electron offers great new possibilities for quantum technologies by trapping, cooling or observing the fluorescence of Rydberg atoms.

In this work, we focus on the study of rubidium's "big brother" strontium, which is located right next to it in the periodic table. The additional electron requires an adapted model with respect to alkali atoms which is why we lay out the theoretical methods for describing alkaline-earth atoms available in literature in Sec. 4.1. This includes a thorough discussion of the role of the spin in one- and two-electron systems and the single-active electron (SAE) model. Despite a qualitatively good agreement with experimental data for high-ℓ states, the model fails to reproduce the spectrum of strontium for lower angular momenta, as shown in Sec. 4.2. The main reason is the interaction of the electrons with each other or their respective orbitals playing a significant role. We therefore propose a physically motivated modification of the SAE model which reproduces the experimental data with high fidelity. We focus on the study of Stark maps of strontium measured experimentally by our collaborators at Laboratoire Kastler Brossel (LKB) at Collège de France. In the remainder of Sec. 4.2, we optimise our model parameters using the provided experimental data. As a proof-of-concept and first application, we utilise our model to study and optimise the circularisation of strontium in Sec. 4.3. Note that we have compiled an appendix listing the employed parameters in Appendix A.2 and the technical details within this chapter in Appendix C, which we refer to throughout this chapter.

4.1 Methods for modelling alkaline-earth atoms

The Hamiltonian of hydrogen-like atoms as given in Eq. (2.2) describes the electrostatic interaction between the positively charged core and the negatively charged electron. It can be generalised to two-electron atoms by writing [110]

$$\hat{H}_{\text{ae}} = \hat{T}_1 + \hat{V}_{\text{ae}}(\hat{r}_1) + \hat{T}_2 + \hat{V}_{\text{ae}}(\hat{r}_2) + \hat{V}_{12}(\hat{r}_1, \hat{r}_2) \tag{4.1}$$

with the kinetic energy of a single electron, $\hat{T}_i = \hat{p}_i^2/2m_r$ and the potential $\hat{V}_{\text{ae}}(\hat{r}_i)$ of the atom's ionic core. In the case of strontium, this is the potential of the Sr^{2+} ion while for helium-like ions, i.e. atoms with only two electrons in total, it would simply be the Coulomb potential $\hat{V}_{\text{C}}(\hat{r})$ with a suitable value of Z (cf. Eq. (2.2)). Lastly, the term $\hat{V}_{12}$ describes the interaction between the two valence electrons

$$\hat{V}_{12}(\hat{r}_1, \hat{r}_2) = \frac{1}{|\hat{r}_1 - \hat{r}_2|}. \tag{4.2}$$

When dealing with Rydberg states of strontium, where the inner electron is in the ground state and outer electron is excited to the Rydberg regime, the Hamiltonian of alkaline-earth atoms in Eq. (4.1) can be approximated by a single-active-electron model as shown in Sec. 4.1.1.

While the Coulomb force is the strongest interaction in the atom and thus dominates its behaviour, the Hamiltonian in Eq. (4.1) is but an approximation to the full problem, as it neglects relativistic effects. The rigorous way to obtain relativistic corrections is via solving the Dirac equation [111]. The Dirac equation results from combining quantum mechanics with special relativity

by ensuring that particles transform properly under Lorentz transformations. This leads to the appearance of Pauli spin matrices in the Hamiltonian which ultimately entails the introduction of the spin degree of freedom. In Sec. 4.1.2, we introduce spin orbitals and angular momentum coupling for one- and two-electron atoms. For one-electron atoms, this gives rise to the total angular momentum $\hat{\boldsymbol{j}}$. As the electrostatic potential of hydrogen-like atoms does not depend on the spin, the eigenstates hence obtain an additional two-fold degeneracy. The quantum defects, however, depend on j which partly lifts the degeneracy in alkali atoms. For alkaline-earth atoms, the angular momentum coupling is more intricate and the spin has a larger effect on the atomic spectrum. We show that the individual spins of the two electrons couple to the total spin $\hat{\boldsymbol{S}}$ which ultimately affects the symmetry of the orbitals and lifts the degeneracy between states with different values of S. Furthermore, additional relativistic corrections constitute the fine structure of atoms, the most prominent one being the spin-orbit coupling shown in Sec. 4.1.3. We end the section by elaborating on the numerical implementation and evaluation of the matrix elements of strontium in Sec. 4.1.4.

4.1.1 Single-active-electron (SAE) model

We now present an approximation to the two-electron Hamiltonian of alkaline-atoms in Eq. (4.1). We start by regrouping the terms as

$$\hat{H}_{\text{ae}} = \hat{H}_1 + \hat{H}_2, \tag{4.3a}$$

$$\text{with} \quad \hat{H}_1 = \hat{T}_1 + \hat{V}_{\text{ae}}(\hat{r}_1) + \hat{V}_{12}(\hat{r}_1, \hat{r}_2), \tag{4.3b}$$

$$\hat{H}_2 = \hat{T}_2 + \hat{V}_{\text{ae}}(\hat{r}_2), \tag{4.3c}$$

where we labelled the outer electron with 1 and the inner electron with 2. The term $\hat{H}_2$ describes the energy of the inner electron and $\hat{H}_1$ the energy of the outer electron plus the interaction. For strontium, $\hat{V}_{\text{ae}}$ corresponds to the potential of the Sr^{2+} ion. We now assume that the inner electron is and stays in its ground state, $|5s\rangle$, which is an eigenstate of $\hat{H}_2$. If the outer electron is furthermore in the Rydberg regime, i.e. $r_2 \ll r_1$ for the most important part of the wave function, the interaction $\hat{V}_{12}$ between the two electrons can in zeroth order be approximated by $1/r_1$ [43]. This can be interpreted as a perfect shielding of the Sr^{2+} ionic core charge by the inner electron. We can therefore focus on the dynamics of the outer electron and reduce the problem to an effective one-electron problem which gives rise to the name single-active-electron (SAE) model. With this approximation, we can write the eigenstates as $|5s, R\rangle$ where $|R\rangle$ is a Rydberg state of the outer electron. In order to improve the model and account for imperfect shielding at small distances, we can incorporate the effect of the inner electron into an effective potential $\hat{V}_{\text{SAE}}(\hat{r})$ (where we have dropped the index 1) [32],

$$\hat{V}_{\text{SAE}}(\hat{r}) = -\frac{Z_\ell(\hat{r})}{\hat{r}}, \tag{4.4}$$

where $Z_\ell(\hat{r})$ is the effective charge,

$$Z_\ell(\hat{r}) = 1 + (Z-1)e^{-\alpha_1^\ell \hat{r}} + \alpha_2^\ell \hat{r}\, e^{-\alpha_3^\ell \hat{r}}. \tag{4.5}$$

Moreover, we account for the core polarisability induced by the outer electron,

$$\hat{V}_{\text{pol}}(\hat{r}) = -\frac{\alpha_c}{2\hat{r}^4}\left(1 - e^{-(\hat{r}/r_c^\ell)^6}\right), \tag{4.6}$$

which is a modified expression of higher accuracy as compared to Eq. (2.9). The values of the model parameters are listed in Appendix A.2.2. The eigenstates $|R\rangle$ of the outer electron are thus eigenstates of $\hat{T}_1 + \hat{V}_{\text{SAE}}(\hat{r}_1) + \hat{V}_{\text{pol}}(\hat{r}_1)$. Similarly as has been done for alkali atoms, the effect of the modified core potential can be represented by quantum defects which can be interpreted as scattering phase shifts of the wave function outside the core region with respect to the hydrogenic one. The explicit form of the potential plays a role when calculating the matrix elements of the position operator as described in Sec. 4.1.4.

As a final note, we want to mention that there are more elaborate methods for modelling alkaline-earth atoms than the one described in this section. One of them is multichannel quantum defect theory (MQDT) [112] which describes the eigenstates of the atom as a linear combination of scattering channels. As such, it builds up on the single quantum defect theory which interprets quantum defects as phase shifts of the wave function with respect to the hydrogenic one. Another approach is a configuration interaction (CI) expansion of eigenstates using a two-active-electron (TAE) model based on the Hamiltonian in Eq. (4.1) [31, 110]. Since we, however, are mostly interested in singly excited Rydberg states of strontium, we expect the SAE model to be sufficient for our purpose. The validity of this assumption is tested thoroughly in Sec. 4.2, when comparing simulations of the SAE model to experimental data.

4.1.2 Angular momentum coupling

We now derive the formalism for coupling the spin and the angular momentum of a single particle [43, 113] which allows us to describe alkali atoms in a basis which is more adapted to represent the energy shift described by the quantum defect. When including the spin degree of freedom, the state of the electron can be written as so-called spin orbitals,

$$|\psi\rangle = |\phi\rangle \otimes |\xi\rangle = |n\ell m_\ell\rangle \otimes |s m_s\rangle = |n\ell m_\ell s m_s\rangle\,. \tag{4.7}$$

The spatial part, $|\phi\rangle$, represents the eigenfunctions of the Coulomb problem as introduced and discussed thoroughly in Sec. 2.1.1. Note that we have added a subscript to m_ℓ to emphasize that it is the projection associated with the angular momentum quantum number ℓ. The spin part, $|\xi\rangle$, can be characterised by the spin of the electron, $s = \frac{1}{2}$, and its projected value m_s onto the quantisation axis. Analogous to the orbital angular momentum operator $\hat{\boldsymbol{l}}$ (cf. Eq. (2.3)), the spin

operator $\hat{\boldsymbol{s}}$ satisfies the relations

$$\hat{\boldsymbol{s}}^2 \left|sm_s\right\rangle = s(s+1)\left|sm_s\right\rangle = \tfrac{3}{4}\left|sm_s\right\rangle, \tag{4.8a}$$

$$\hat{s}_z \left|sm_s\right\rangle = m_s \left|sm_s\right\rangle = \pm\tfrac{1}{2}\left|sm_s\right\rangle. \tag{4.8b}$$

Note that, in this chapter, we denote operators with lower-case letters to highlight that they act on single particles. As the Hamiltonian of hydrogen-like atoms given in Eq. (2.2) does not depend on the spin, the spin orbitals are still eigenfunctions of that Hamiltonian. The spin merely introduces an additional two-fold degeneracy, leading to a total degeneracy of $2n^2$ of each energy level.

The two angular momenta $\hat{\boldsymbol{l}}$ and $\hat{\boldsymbol{s}}$ can be coupled to the total angular momentum,

$$\hat{\boldsymbol{j}} = \hat{\boldsymbol{l}} + \hat{\boldsymbol{s}}, \tag{4.9}$$

which fulfils

$$\hat{\boldsymbol{j}}^2 \left|jm_j\right\rangle = j(j+1)\left|jm_j\right\rangle, \tag{4.10a}$$

$$\hat{j}_z \left|jm_j\right\rangle = m_j \left|jm_j\right\rangle, \tag{4.10b}$$

where m_j is the projection associated with j such that $m_j = -j, \ldots, j$. The quantum numbers are connected via $j = \ell \pm \frac{1}{2}$ for $\ell > 0$ and $j = \frac{1}{2}$ for $\ell = 0$, and the projections fulfil $m_j = m_\ell + m_s$. The spin orbitals can then be written in terms of the total angular momentum by performing a basis transformation,

$$\left|jm_j\ell s\right\rangle = \sum_{m_\ell m_s} \left|\ell m_\ell s m_s\right\rangle \left\langle \ell m_\ell s m_s | jm_j \ell s\right\rangle \equiv \sum_{m_\ell m_s} C^{jm_j}_{\ell m_\ell s m_s} \left|\ell m_\ell s m_s\right\rangle, \tag{4.11}$$

where we have omitted the principal quantum number n for simplicity. The constants $C^{jm_j}_{\ell m_\ell s m_s} = \langle \ell m_\ell s m_s | jm_j \ell s\rangle$ in Eq. (4.11) are the Clebsch-Gordan coefficients. They are connected to the Wigner 3j symbols via

$$\begin{pmatrix} j_1 & j_2 & j_3 \\ m_1 & m_2 & m_3 \end{pmatrix} = \frac{(-1)^{j_1 - j_2 - m_3}}{\sqrt{2j_3+1}} \left\langle j_1 m_1 j_2 m_2 | j_1 j_2 j_3 - m_3\right\rangle = \frac{(-1)^{j_1 - j_2 - m_3}}{\sqrt{2j_3+1}} C^{j_3 - m_3}_{j_1 m_1 j_2 m_2}. \tag{4.12}$$

Linear combinations such as Eq. (4.11) can therefore also be written as

$$\left|j_1 j_2 j_3 m_3\right\rangle = (-1)^{j_2 - j_1 - m_3}\sqrt{2j_3+1} \sum_{m_1 m_2} \begin{pmatrix} j_1 & j_2 & j_3 \\ m_1 & m_2 & -m_3 \end{pmatrix} \left|j_1 m_1 j_2 m_2\right\rangle. \tag{4.13}$$

In the case of Eq. (4.11), we can identify $j_1 = \ell$, $j_2 = s$ and $j_3 = j$. We refer to the basis $|\ell m_\ell s m_s\rangle$ as the uncoupled and to $|jm_j\ell s\rangle$ as the coupled basis. Both are eigenfunctions to the hydrogen-like Hamiltonian in Eq. (2.2). When considering fine-structure corrections, however, the uncoupled basis is not suitable any more as will be explained in more detail in Sec. 4.1.3.

When considering systems with two (valence) electrons, the coupling becomes more intricate as four angular momenta have to be coupled: the orbital angular momenta $\hat{l}_i$ and the spins $\hat{s}_i$ of the two particles with $i = 1, 2$. There are two different ways of coupling the two electrons. The first way is the so-called the jj-coupling. Here, we first couple the spin and angular momentum of each electron independently as in the single-electron case (cf. Eq. (4.9)). Afterwards, the two angular momenta $\hat{\boldsymbol{j}}_1$ and $\hat{\boldsymbol{j}}_2$ are coupled to the total angular momentum $\hat{\boldsymbol{J}}$, where the upper case letter indicates that it is a two-particle operator. The two steps can be summarised as

$$\hat{\boldsymbol{j}}_i = \hat{\boldsymbol{l}}_i + \hat{\boldsymbol{s}}_i, \quad i = 1, 2 \tag{4.14a}$$

$$\hat{\boldsymbol{J}} = \hat{\boldsymbol{j}}_1 + \hat{\boldsymbol{j}}_2. \tag{4.14b}$$

The single electron operators $\hat{\boldsymbol{j}}_i$ fulfil the relations of Eq. (4.10). The eigenvalues of $\hat{\boldsymbol{J}}^2$ are $J(J+1)$ with $J = |j_1 - j_2|, \ldots, j_1 + j_2$. Both coupling steps can be evaluated using Eq. (4.13). In summary, the jj-coupled states can be denoted as $|JM_J j_1 j_2\rangle$ where $M_J = -J, \ldots, J = m_{j_1} + m_{j_2}$ is the projection of $\hat{\boldsymbol{J}}$ and eigenvalue of $\hat{J}_z$ (equivalently to j and m_j).

The other way to couple the two electrons is the so-called Russell-Saunders, or, LS-coupling. Here, we first couple the angular momenta $\hat{\boldsymbol{l}}_i$ and the spin $\hat{\boldsymbol{s}}_i$ of the two particles with $i = 1, 2$ to the total angular momentum $\hat{\boldsymbol{L}}$ and the total spin $\hat{\boldsymbol{S}}$ as

$$\hat{\boldsymbol{L}} = \hat{\boldsymbol{l}}_1 + \hat{\boldsymbol{l}}_2, \tag{4.15a}$$

$$\hat{\boldsymbol{S}} = \hat{\boldsymbol{s}}_1 + \hat{\boldsymbol{s}}_2. \tag{4.15b}$$

The eigenvalues of $\hat{\boldsymbol{L}}^2$ and $\hat{\boldsymbol{L}}_z$ are $L(L+1)$ and M_L, respectively, with $L = |\ell_1 - \ell_2|, \ldots, \ell_1 + \ell_2$ and $M_L = m_{\ell_1} + m_{\ell_2} = -L, \ldots, L$. Equivalently, the eigenvalues of the spin operator $\hat{\boldsymbol{S}}^2$ are $S(S+1)$ with $S = 0, 1$. We call states with $S = 0$ singlets ($M_S = 0$) and $S = 1$ triplets ($M_S = 0, \pm 1$). In terms of the uncoupled basis and using Eq. (4.13), they can be written as

$$|S = 0, M_S = 0\rangle = \tfrac{1}{\sqrt{2}} \left(|\uparrow, \downarrow\rangle - |\downarrow, \uparrow\rangle\right), \tag{4.16a}$$

$$|S = 1, M_S = 1\rangle = |\uparrow, \uparrow\rangle, \tag{4.16b}$$

$$|S = 1, M_S = 0\rangle = \tfrac{1}{\sqrt{2}} \left(|\uparrow, \downarrow\rangle + |\downarrow, \uparrow\rangle\right), \tag{4.16c}$$

$$|S = 1, M_S = -1\rangle = |\downarrow, \downarrow\rangle, \tag{4.16d}$$

where we have used the abbreviations $|s_1 = \frac{1}{2}, m_{s_1}, s_2 = \frac{1}{2}, m_{s_2}\rangle \equiv |m_{s_1} m_{s_2}\rangle$ for the uncoupled basis on the right-hand side where $\uparrow$ ($\downarrow$) indicates $m_{s_i} = +\frac{1}{2}$ ($m_{s_i} = -\frac{1}{2}$). From Eq. (4.16), we see that singlets are antisymmetric and triplets symmetric with respect to interchange of the two electrons. Finally, the angular momentum $\hat{\boldsymbol{L}}$ and the spin $\hat{\boldsymbol{S}}$ are coupled to the total angular momentum $\hat{\boldsymbol{J}}$ equivalently to Eq. (4.9) with $M_J = -J, \ldots, J = M_L + M_S$ resulting in the basis $|JM_J LS\rangle$. For short, we denote states in the LS-basis using the spectroscopic notation ${}^{2S+1}L_J$ where the angular momentum L is given by a capital (e.g. $S, P, D, \ldots$ for $L = 0, 1, 2, \ldots$).

The symmetry of the spin eigenstates in Eq. (4.16) directly affects which orbital wave functions they can be combined with. Equivalently to the single electron case in Eq. (4.7), we can write the two-particle wave function as spin orbitals, $|\Psi\rangle = |\Phi\rangle \otimes |\Xi\rangle$. The spin part $|\Xi\rangle$ is given by the singlet and triplet states from Eq. (4.16). The orbital part $|\Phi\rangle$, on the other hand, can be written as a product of single particle wave functions $|\phi_1\rangle_i$ and $|\phi_2\rangle_i$, where the indices 1 and 2 label two arbitrary single particle orbitals and the index i labels the index of the particle. As electrons are indistinguishable particles, the orbitals have to be (anti-)symmetrised as

$$|\Phi^{\pm}\rangle = \frac{1}{\sqrt{2}} \left(|\phi_1 \phi_2\rangle \pm |\phi_2 \phi_1\rangle \right) \tag{4.17}$$

with the abbreviation $|\phi_i\rangle_1 \otimes |\phi_j\rangle_2 \equiv |\phi_i \phi_j\rangle$. For fermions, the total spin orbital $|\Psi\rangle$ has to be anti-symmetric with respect to particle exchange. We can therefore follow that singlet states (which are anti-symmetric) are only allowed in combination with symmetric spatial orbitals, $|\Phi^+\rangle$. Conversely, triplet states (which are symmetric) are only allowed in combination with the anti-symmetric spatial orbital $|\Phi^-\rangle$.

In our case, we are interested in a singly excited Rydberg state of strontium where the outer electron is excited to the Rydberg regime, $|\phi_1\rangle = |R\rangle$, while the other electron is in the ground state, $|\phi_2\rangle = |5s\rangle$ (cf. Sec. 4.1.1). The only allowed spin orbitals are thus

$$|\Psi^+\rangle = \frac{1}{\sqrt{2}} \big(|5s, R\rangle + |R, 5s\rangle \big) \otimes |S = 0, m_s\rangle \,, \tag{4.18a}$$

$$|\Psi^-\rangle = \frac{1}{\sqrt{2}} \big(|5s, R\rangle - |R, 5s\rangle \big) \otimes |S = 1, m_s\rangle \,. \tag{4.18b}$$

Even though the alkaline-earth Hamiltonian in Eq. (4.1) does not depend on the spin degree of freedom, the interaction between indistinguishable particles suffices to partially lift the degeneracy. In our case, where the interaction between the two distant electrons is small, the energy correction can be calculated using perturbation theory. When denoting the perturbation as $\hat{W} = \hat{V}_{12} - \frac{1}{r_1}$, where the second term corresponds to the zero-order approximation of interaction as discussed in Sec. 4.1.1, the energy correction is given to first order by [43]

$$\langle \Psi^{\pm} | \hat{W} | \Psi^{\pm} \rangle = \langle \Phi^{\pm} | \hat{W} | \Phi^{\pm} \rangle \langle \Xi | \Xi \rangle = J \pm K, \tag{4.19a}$$

$$J = \langle 5s, R | \hat{W} | 5s, R \rangle \,, \tag{4.19b}$$

$$K = \langle 5s, R | \hat{W} | R, 5s \rangle \,. \tag{4.19c}$$

In writing this formula, it has been assumed that $|5s\rangle$ and $|R\rangle$ are orthogonal to zero-order. Although $|5s\rangle$ and $|R\rangle$ are eigenstates of different Hamiltonians, they are eigenstates with different ℓ values such that the angular part leads to a vanishing overlap [43]. J from Eq. (4.19a) is called the Coulomb and K the exchange term. The Coulomb term reflects the Coulomb interaction between the two electronic orbitals. The exchange term originates from the indistinguishability of the elec-

trons and can be interpreted as the frequency with which the electrons exchange their state. The positive sign in Eq. (4.19a) corresponds to singlet states for which the energy is raised and the negative sign to triplet states for which the energy is lowered; the energy splitting between them is called the exchange energy. For low-angular-momentum states, the exchange energy is of the order of Gigahertz and is thus the major influence of the spin on the spectrum of alkaline-earth atoms. The effect of the exchange energy is usually included in the quantum defect, which, for alkaline-earth atoms, therefore also depends on S.

4.1.3 Fine-structure corrections

As mentioned in the beginning of this section, the Hamiltonians of Eqns. (2.2) and (4.1) are mere approximations where relativistic effects are neglected. For weakly relativistic systems, it is not necessary to solve the Dirac equation rigorously and the significant corrections can be obtained by employing perturbation theory [43, 113]. The resulting Dirac equation shows three correction terms which constitute the so-called fine structure of the atom.

The first term attributes for the relativistic correction of the kinetic energy, i.e. the relativistic variation of the electron's mass with its velocity. The operator is diagonal in the $|n\ell m\rangle$ basis and for hydrogen-like atoms, the correction can be written as

$$E_{\mathrm{r}} = -\frac{\alpha^2 Z^4}{2n^3}\left(\frac{1}{\ell+\frac{1}{2}} - \frac{3}{4n}\right) \tag{4.20}$$

with the fine-structure constant α. It can be seen that the correction vanishes for large n and ℓ values. The second correction is called the Darwin term which shifts the energy of s-orbitals only due to a modified effective potential of the nucleus resulting from rapid quantum oscillations of the electron. For hydrogen-like atoms, it takes the form

$$E_{\mathrm{D}} = \frac{\alpha^2 Z^4}{2n^3}. \tag{4.21}$$

As both corrections are diagonal in the spherical basis and decay with increasing ℓ and n, they can be included into the quantum defect.

The last and most important term is the spin-orbit coupling. It arises due to the coupling of the magnetic moment of the electron spin with the magnetic field seen by the electron due to its motion in the electrostatic field of the proton. The spin-orbit coupling can be written as

$$\hat{V}_{\mathrm{so}}(\hat{r}) = \frac{\alpha^2 Z}{2}\frac{\hat{\boldsymbol{l}}\cdot\hat{\boldsymbol{s}}}{\hat{r}^3}. \tag{4.22}$$

Using Eq. (4.9), the matrix elements of $\hat{\boldsymbol{l}}\cdot\hat{\boldsymbol{s}}$ can be calculated to

$$\langle jm_j\ell s|\hat{\boldsymbol{l}}\cdot\hat{\boldsymbol{s}}|jm_j\ell s\rangle = \frac{1}{2}\Big(j(j+1) - \ell(\ell+1) - s(s+1)\Big), \tag{4.23}$$

while non-diagonal elements vanish. Inserting this into Eq. (4.22) results in the known expression from Eq. (2.8). The spin-orbit coupling lifts the degeneracy between states with different values of j, ℓ and s, while s-orbitals do not show spin-orbit coupling. The effect of the spin-orbit coupling can also be included into the quantum defect introducing a j-dependence which renders the coupled basis $|jm_j\ell s\rangle$ more suitable than the uncoupled one. As a result, m_ℓ and m_s are strictly speaking no longer good quantum numbers. In Chapters 2 and 3, we have neglected spin-orbit coupling for alkali atoms by approximating $\delta_{n\ell} \approx \delta_{n\ell,j=\ell+\frac{1}{2}}$.

The spin-orbit coupling can be generalised to two-electron systems as [113]

$$\hat{V}_{\text{so}}(\hat{r}_1, \hat{r}_2) = \frac{\alpha^2 Z}{2}\left(\frac{\hat{\boldsymbol{l}}_1 \cdot \hat{\boldsymbol{s}}_1}{\hat{r}_1^3} + \frac{\hat{\boldsymbol{l}}_2 \cdot \hat{\boldsymbol{s}}_2}{\hat{r}_2^3}\right). \tag{4.24}$$

To evaluate this expression, we have to distinguish two limiting cases. If the Rydberg electron is in a high-angular-momentum state, the overlap between the two orbitals is negligible causing a vanishing exchange energy. The spin-orbit coupling is dominant, the jj-coupled basis $|JM_J j_1 j_2\rangle$ is preferred and the spin-orbit coupling in Eq. (4.24) can be evaluated straight-forwardly. If, on the other hand, the exchange energy is much larger than the spin-orbit coupling, which is the case if the Rydberg electron is in low-angular-momentum states, the LS-basis is preferred. The angular part of the spin-orbit coupling can be considered similarly as given in Eq. (4.23) (by replacing lower by upper case operators/quantum numbers) while the radial part requires a more thorough treatment [113]. Equation (4.23) shows that singlets ($S = 0$ and $J = L$) do not show spin-orbit coupling. Moreover, the $\hat{\boldsymbol{L}} \cdot \hat{\boldsymbol{S}}$ coupling commutes with both $\hat{\boldsymbol{L}}^2$ and $\hat{\boldsymbol{S}}^2$, and therefore lifts the degeneracy between singlets and triplets. In literature, this effect is usually taken into account via J, L and S-dependent quantum defects, thus implicitly assuming the limiting case of the LS-basis being the preferred one. We discuss and investigate the two competing regimes more thoroughly in Sec. 4.2 when discussing the energy levels and the Stark map of strontium.

Finally, it shall be mentioned that the Dirac equation could be expanded to the next higher order. This would entail relativistic effects due to the magnetic moment of the proton's spin which contribute to the hyperfine structure. However, they can be neglected for our purposes, as the corrections are about three orders of magnitude smaller than the fine structure [113].

4.1.4 Implementation of the strontium Hamiltonian

In order to perform simulations with strontium, some modifications have to be included in the program we have used in Chapter 3. As before, we consider the Rydberg atom in an external electric field and write the Hamiltonian of strontium as

$$\hat{H} = \hat{H}_{\text{ae}} + \hat{z}F_{\text{DC}}. \tag{4.25}$$

We therefore have to (1) implement the eigenstates and energies of $\hat{H}_{\text{ae}}$ in a suitable basis and (2) calculate the matrix elements of $\hat{z}$ for strontium.

For the field free Hamiltonian $\hat{H}_{\text{ae}}$, we use the results presented in the previous sections and choose the LS-basis $|JM_JLS\rangle$ as the computational basis[1]. This is the basis commonly used in literature, as the quantum defects depend on J, L and S (e.g. [114]). The quantum defects account for the SAE potential, the exchange energy and the fine structure and thus fully describe the spectrum of strontium at zero DC field. We employ the quantum defects for strontium as listed in Appendix A.2.1. In short, we have implemented quantum defects up to $L = 5$, exchange energy for $1 \leq L \leq 4$, and spin-orbit coupling for triplets with $L = 1$ and 2. Note that the resulting Hilbert space is four times larger than in the previous chapter because we now consider singlets and triplets while we have neglected spin-orbit coupling for rubidium.

When employing a DC (or equivalently an RF) field, we have to evaluate the matrix elements of the $\hat{z}$ ($\hat{x} \pm i\hat{y}$) operator. To this end, we have to transform the states to the $|LM_LSM_S\rangle$ basis, as the angular part of the matrix elements (as given in Eq. (2.11)) depend on M_L. The dipole matrix elements can then be calculated as follows,

$$\langle J'M'_JL'S|T^{(1)}_q|JM_JLS\rangle = \sum_{M_L}\sum_{M'_L} C^{J'M'_J}_{L'M'_LSM_S} C^{JM_J}_{LM_LSM_S} \langle L'M'_L|T^{(1)}_q|LM_L\rangle\,, \tag{4.26}$$

where the sums run over $M_L = M_J \pm \frac{1}{2}$ and $M'_L = M'_J \pm \frac{1}{2}$. The matrix element of $T^{(1)}_q$ in the $|LM_L\rangle$ basis can be calculated using Eq. (B.5), as they are independent of the spin degree of freedom. Note that it is not necessary to return to the uncoupled basis $|\ell m_\ell s m_s\rangle_1 \otimes |\ell m_\ell s m_s\rangle_2$, where the indices denote the two electrons, by undoing the coupling of the $\hat{\boldsymbol{l}}_i$ to $\hat{\boldsymbol{L}}$ and $\hat{\boldsymbol{s}}_i$ to $\hat{\boldsymbol{S}}$ (cf. Eq. (4.15)) to calculate the influence of the DC field on the outer, active electron only. Since we assume that the inner electron, which we have denoted by the index 2, is in the ground state, it has the quantum numbers $\ell_2 = m_{\ell_2} = 0$. We hence know that $L = \ell_1$ and $M = m_{\ell_1}$ and Eq. (4.26) already gives the required information about the Stark effect of the outer electron.

To evaluate the radial part of the matrix elements, a basis transformation is not necessary. We solve the radial Schrödinger equation to obtain the radial wave functions using Numerov's method as explained in Sec. 3.1.1. To this end, we replace the Coulomb potential by the adapted potential

$$\hat{V}_{\text{sr}}(\hat{r}) = \hat{V}_{\text{SAE}}(\hat{r}) + \hat{V}_{\text{pol}}(\hat{r}) + \hat{V}_{\text{so}}(\hat{r}) \tag{4.27}$$

with the SAE potential $\hat{V}_{\text{SAE}}$ from Eq. (4.4), the core polarisability $\hat{V}_{\text{pol}}$ from Eq. (4.6), and the spin-orbit coupling $\hat{V}_{\text{so}}$ from Eq. (4.22). The model parameters are summarised in Appendix A.2. It turns out that the modifications given by the potential in Eq. (4.27) do not change the matrix elements significantly with respect to a plain Coulomb potential which corroborates our assumption that most of the properties of strontium are captured by a simple model of one electron interacting with a single charge in the centre.

[1] We neglect cross-terms due to the (anti-)symmetrisation of the orbitals in the simulations since they are much smaller than the direct terms.

4.2 Optimising the Stark map of strontium

When one valence electron of strontium is excited to the Rydberg regime while the other one stays in the ground state, the single-active electron approximation could be expected to describe the atom very well. However, it turns out that the experimentally measured Stark map can not be reproduced accurately using the SAE model as shown in Sec. 4.2.1. We therefore propose physically motivated modifications which allow for reproducing the measured Stark map. Afterwards, in Sec. 4.2.2, we perform a parameter optimisation to determine the model parameters directly from the experimental data. Lastly, in Sec. 4.2.3, we present the results of the optimisation in several Stark maps.

4.2.1 Benchmark and modification of the SAE model

Stark maps show the position of the energy levels of (in this case) Rydberg atoms as a function of the DC field (cf. Fig. 2.4). They nicely illustrate the Stark splitting and thus contain information about the eigenenergies at zero DC field, the matrix elements of the $\hat{z}$ operator and, accordingly, the wave functions of the atom. A good agreement between a theoretical model and experimental data in the Stark map is therefore a good indicator for an adequate model. In the experiment, however, it is challenging to measure the bare energies of the atom directly, such as depicted in Fig. 2.4, and often, the transition frequencies between different eigenstates are recorded instead. Figure 4.1 (a) shows as an example the Stark map of strontium for transitions from the reference state $50^1F_3, m_j = 2$. The selected energy window shows transitions to the singlet and triplet states of[1] $49g$. The lines show the simulations using the model described in Sec. 4.1 and the points depict the measurements in the experiment performed by our collaborators at LKB. Due to the selection rule of $\Delta m_j = 1$, only the states with $m_j = 1, 2, 3$ are of relevance which is why only those m_j ladders are shown in the figure. We see that the agreement between simulations and experiment is very poor despite a qualitatively similar behaviour. Already at zero DC field, the states do not possess the correct energy. At higher fields, the experiment reveals four "bundles" of states while in the simulations, we find two which correspond to the singlets and triplets, respectively. This comes at no surprise, as the implemented quantum defects of the g-states account only for the exchange energy but not for spin-orbit coupling (values listed in Appendix A.2.1). Both problems could be fixed by introducing well-adjusted, J-dependent quantum defects. Beyond this, the figure reveals that two different states are being populated at zero field in the experiment. We would not expect this from our model, as only singlets can be populated when the reference state is a singlet due to selection rules. Moreover, the experiment detects an avoided crossing of two lines between 30 and $45\ \frac{\mathrm{V}}{\mathrm{m}}$ (lowest two branches of points close to the green line) while no such feature is visible in the simulations.

[1] Since we employ the SAE model, we effectively only describe single valence electron while implicitly, we always deal with two electrons. If possible, we employ lower or upper case letters to denote the quantum numbers depending on which property we want to highlight or which ones are dominating, the single- or two-electron ones.

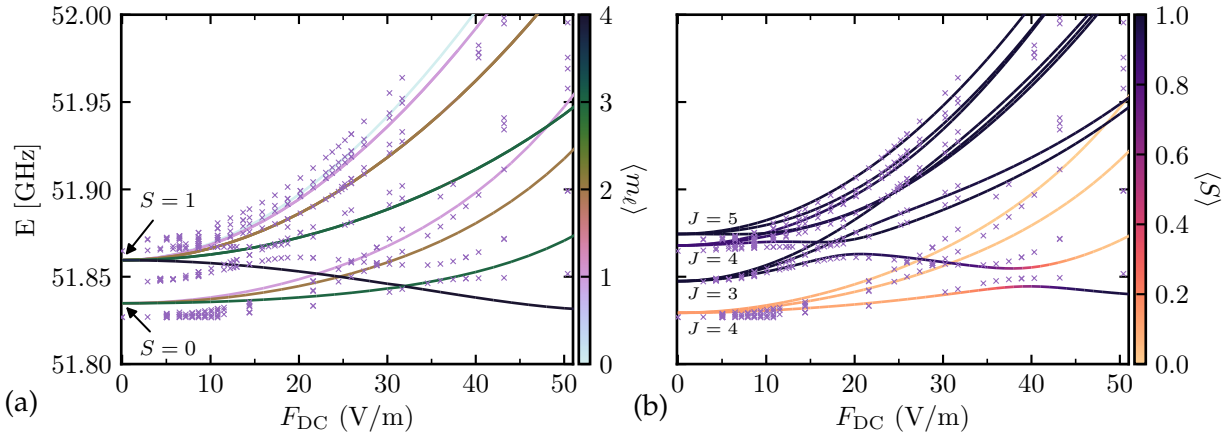

Figure 4.1: Stark map from $50^1F_3, m_j = 2$ to $49g$ for $m_j = 1, \ldots, 3$. The used quantum defects are listed in Appendix A.2.1. The line colour indicates the expectation value of m_ℓ (a) and S (b), the crosses indicate the experimental measurements. Shown are the data without additional $\hat{l}_1 \cdot \hat{s}_1$ coupling (a) and with a coupling of $\omega_{49g}/2\pi = 3\,\mathrm{MHz}$ (b). The expectation values of S at zero field in (b) are (from bottom to top) 0.14, 1, 0.86 and 1.

From the observations made in Fig. 4.1, we can conclude which properties are missing in our model and how to improve it. Most importantly, our model cannot explain the population of two states at zero field when starting in a singlet. As only transitions to singlet states are allowed, we can conclude that the singlet and triplet states have to mix. This can be explained as follows: If the outer valence electron is in a high-angular-momentum state, its overlap with the inner electron is small. The electrons are thus almost independent, the exchange energy vanishes and the states can not necessarily be identified as "singlets" or "triplets" any longer. Each particle couples its own spin $\hat{s}_i$ to its own angular momentum $\hat{l}_i$, and the jj-basis is thus the preferred one. The spin-orbit coupling is thus very different for the two electrons and must be considered independently as given in Eq. (4.24). This expression can be simplified since the inner electron is in a s-state, $\ell_2 = 0$, and therefore $\hat{\boldsymbol{l}}_2 \cdot \hat{\boldsymbol{s}}_2 = 0$. The only remaining term is

$$\hat{V}_{\mathrm{so}}^{j_1} = \frac{Z\alpha^2}{2} \frac{\hat{\boldsymbol{l}}_1 \cdot \hat{\boldsymbol{s}}_1}{\hat{r}_1^3}. \tag{4.28}$$

This potential introduces an energy shift and couples states with the same J, M_J and L but different S as can be seen from its matrix elements,

$$\langle JM_JLS'|\hat{V}_{\mathrm{so}}^{j_1}|JM_JLS\rangle = \omega_{n\ell} \sum_{j_1} C(j_1)\Big(j_1(j_1+1) - \ell_1(\ell_1+1) - s_1(s_1+1)\Big), \tag{4.29}$$

where $\ell_1 = L$ and $s_1 = \frac{1}{2}$. Moreover, $C(j_1)$ is a combination of Clebsch-Gordan coefficients and we have defined the j_1-coupling strength[1] $\omega_{n\ell}$. We provide a thorough derivation of the constant

[1]Note that the j_1-coupling strength $\omega_{n\ell}$ uses the lower case omega, as it refers to the single-electron operators.

$C(j_1)$ and a motivation of the coupling strength $\omega_{n\ell}$ in Appendix C.1. In short, $C(j_1)$ describes the transition from the $|JM_JLS\rangle$ to the $|JM_Jj_1j_2\rangle$ basis which is required to calculate the matrix elements of $\hat{\boldsymbol{l}}_1 \cdot \hat{\boldsymbol{s}}_1$.

The influence of j_1-coupling is visualised in Fig. 4.2 (a) which shows the splitting of the energy levels at zero field as a function of $\omega_{n\ell}$. The green and blue line correspond to the triplets $J = L \pm 1$ which are not mixed but merely shifted in energy. For $L = 4$, the green line corresponds to $J = L - 1 = 3$ for which $\langle j_1 \rangle = \frac{7}{2}$ such that the energy is shifted by $-5\omega_{n\ell}$ (by evaluating the parentheses in Eq. (4.29)). Equivalently, the blue line shows the triplet with $J = 5$ which corresponds to $\langle j_1 \rangle = \frac{9}{2}$ and an energy shift of $+4\omega_{n\ell}$. The singlet and triplet with $J = L = 4$, on the other hand, are being mixed as can be seen from the curvature of the red lines. Evaluation of the Clebsch-Gordan coefficients reveal that their j_1 expectation value is around 4 which induces a shift of about $\frac{3}{4}\omega_{n\ell}$ up (for the singlet) or down (for the triplet).

We perform a first test of our conjecture that j_1-coupling improves the agreement between the simulated and experimentally measured Stark map in Fig. 4.1 (a). For $L = 4$ (G), we expect j_1-coupling and exchange energy to compete which results in an energy splitting as depicted in Fig. 4.3 (b). We assume a j_1-coupling of $\omega_{49g}/2\pi = 3\,\mathrm{MHz}$ and re-compute the Stark map. The result is shown in Fig. 4.1 (b). It is clearly visible that the two bundles of states in panel (a) have split up into four according to their J values. As visualised by the line colour, the singlet and triplet with $J = 4$ mix, resulting in S-expectation values of 0.14 and 0.86, respectively. Since the former triplet ${}^3G_4$ has now singlet character, it can be populated at zero field in agreement with the observation in the experiment. For higher fields, the states mix further such that previously unattainable states can get populated. Moreover, we now observe two anti-crossings around $17\,\frac{\mathrm{V}}{\mathrm{m}}$ and $40\,\frac{\mathrm{V}}{\mathrm{m}}$ in the simulations which were not present in (a) but predicted by the experiment. We conclude that the j_1 coupling improves the agreement of theory and experiment significantly.

The mixing of eigenstates is a direct consequence of $\hat{\boldsymbol{l}}_1 \cdot \hat{\boldsymbol{s}}_1$ not commuting with $\hat{\boldsymbol{S}}^2$ such that S is not a good quantum number any more. The exchange energy, on the other hand, splits the singlets and triplets. In fact, they are competing effects. The exchange energy is stronger when the overlap between the two electrons is large, i.e. for small ℓ_1, while the j_1-coupling dominates for large ℓ_1. The composition of the eigenstates thus depends on the ratio between exchange energy and j_1-coupling strength. For instance, if the exchange energy was set to zero in Fig. 4.2 (a), the red lines would not have any curvature but lie on top of the green and blue ones. In the next subsection, we characterise the strength of the two effects for different values of $L = \ell_1$.

In order to facilitate the fitting procedure in the following, we perform one more adjustment before. Note that for low-angular-momentum states, the spin-orbit coupling is proportional to $\hat{\boldsymbol{L}} \cdot \hat{\boldsymbol{S}}$ as described in Sec. 4.1.3. This also lifts the degeneracy between different J states but does not mix singlets and triplets. As a result, the quantum defect given in the literature depends on J, L and S. However, Eq. (4.23) reveals that the shift between states with different values of J is, in fact, not independent. Equivalently to the single-electron case and the j_1-coupling, we can

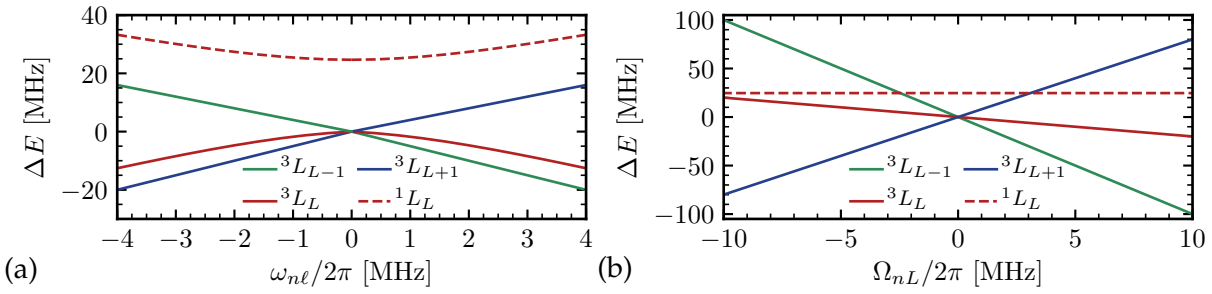

Figure 4.2: Energy shift due to j_1-coupling as given in Eq. (4.29) (a) and LS-coupling as given in Eq. (4.30) (b) for a g-state. Note that, since the singlets and triplets with $J = L$ mix in (a), the notation ${}^{2S+1}L_J$ is not strictly correct any more for $\omega_{\ell_1 s_1} \neq 0$ and $J = L$. In both panels, the zero of energy was set to the triplet state for $\omega = 0$. The exchange energy was set to $24.665\,\mathrm{MHz}$.

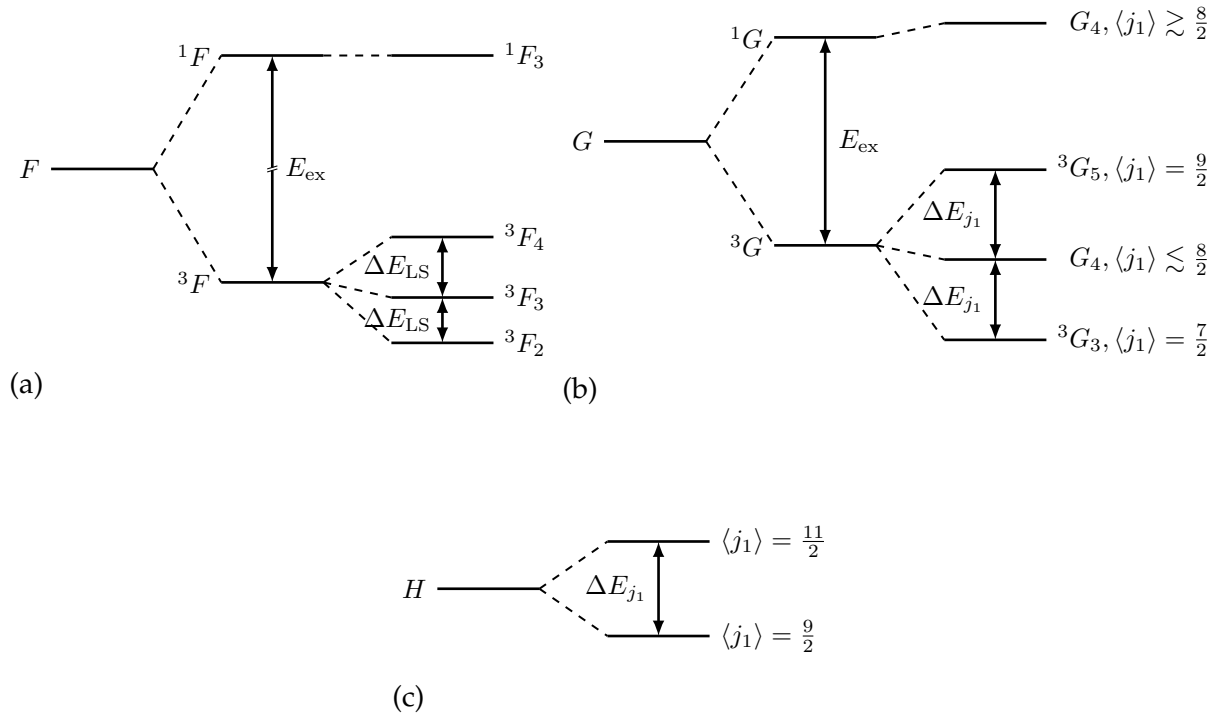

Figure 4.3: (a) Exchange energy E_{ex} (not to scale) and spin-orbit coupling $\Delta E_{\mathrm{LS}} \propto (J(J+1) - L(L+1) - S(S+1))$ of the $L = 3$ (F) state using the notation ${}^{2S+1}L_J$. (b) Exchange energy E_{ex} and spin-orbit coupling $\Delta E_{j_1} \propto (j_1(j_1+1) - \ell_1(\ell_1+1) - s_1(s_1+1))$ of the $L = 4$ (G). A small shift ΔE_{LS} is not visible on this scale. (c) Spin-orbit coupling $\Delta E_{j_1} \propto (j_1(j_1+1) - \ell_1(\ell_1+1) - s_1(s_1+1))$ of the $L = 5$ (H) with no significant exchange energy.

write for the two-electron case

$$\langle JM_J LS|\hat{V}_{\text{so}}^{LS}|JM_J LS\rangle = \Omega_{nL}\Big(J(J+1) - L(L+1) - S(S+1)\Big), \tag{4.30}$$

where we have defined the LS-coupling strength[1] Ω_{nL} which depends on the radial part and hence on n and L. We therefore move to a physically motivated parametrisation instead of merely employing different quantum defects δ_{JLS}. A non-zero Ω_{nL} lifts the degeneracy between states with different values of J, L and S. Opposed to a quantum defect, however, it guarantees that the splitting is proportional to the expectation value of $\hat{\boldsymbol{L}} \cdot \hat{\boldsymbol{S}}$. Figure 4.2 (b) shows the splitting of the energy levels at zero field as a function of the LS-coupling strength Ω_{nL}. It is clearly visible that the singlet is not affected by LS-coupling which was expected as $J = L$ for singlets such that the expression in parentheses in Eq. (4.30) vanishes. As a consequence, singlets and triplets do not mix under LS-coupling. Fundamentally, this is because $\hat{\boldsymbol{L}} \cdot \hat{\boldsymbol{S}}$ commutes with $\hat{\boldsymbol{S}}^2$ which leaves the S quantum number invariant. The triplets, on the other hand, split linearly according to their J-value. More specifically, for $L = 4$ and by evaluating Eq. (4.30), the three triplets $J = 3, 4, 5$ are shifted by $-10\Omega_{nL}$, $-2\Omega_{nL}$ and $8\Omega_{nL}$, respectively.

In summary, we are adding two terms to the Hamiltonian which implement two different kinds of spin-orbit coupling,

$$\tfrac{1}{2}\hat{V}_{\text{so}}^{tot} = \Omega_{nL}\hat{\boldsymbol{L}} \cdot \hat{\boldsymbol{S}} + \omega_{n\ell}\hat{\boldsymbol{l}}_1 \cdot \hat{\boldsymbol{s}}_1, \tag{4.31}$$

where the factor half stems from Eq. (4.23). This choice of parametrisation, however, is arbitrary because it can be rewritten as

$$\Omega_{nL}\hat{\boldsymbol{L}} \cdot \hat{\boldsymbol{S}} + \omega_{n\ell}\hat{\boldsymbol{l}}_1 \cdot \hat{\boldsymbol{s}}_1 = \Omega_{nL}\hat{\boldsymbol{l}}_1 \cdot (\hat{\boldsymbol{s}}_1 + \hat{\boldsymbol{s}}_2) + \omega_{n\ell}\hat{\boldsymbol{l}}_1 \cdot \hat{\boldsymbol{s}}_1 = \widetilde{\Omega}_{nL}\hat{\boldsymbol{L}} \cdot \hat{\boldsymbol{S}} + \widetilde{\omega}_{n\ell}\hat{\boldsymbol{l}}_1 \cdot \hat{\boldsymbol{s}}_2, \tag{4.32}$$

since $\hat{\boldsymbol{L}} = \hat{\boldsymbol{l}}_1$ and with $\widetilde{\Omega}_{nL} = \Omega_{nL} + \omega_{n\ell}$ and $\widetilde{\omega}_{n\ell} = -\omega_{n\ell}$. The left-most expression suggests that the spin-orbit coupling of the outer electron ($\hat{\boldsymbol{l}}_1 \cdot \hat{\boldsymbol{s}}_1$) is dominant. The right-most expression, on the other hand, suggests that the inner electron's spin couples to the orbital angular momentum of the outer electron ($\hat{\boldsymbol{l}}_1 \cdot \hat{\boldsymbol{s}}_2$), i.e. the coupling of the inner electron to the magnetic field of the outer one. Using our parametrisation, it is not possible to distinguish both interpretations.

Figure 4.3 summarises the effect of exchange energy, j_1 and the LS-coupling for three different angular momentum states L. The relatively low-angular-momentum state F (a) shows strong exchange energy. The levels have strong singlet/triplet character, the spin-orbit coupling is proportional to $\hat{\boldsymbol{L}} \cdot \hat{\boldsymbol{S}}$ and lifts the degeneracy between the three triplet states. The high-angular-momentum state H (c), on the other hand, is dominated by j_1-coupling. Singlets and triplets mix, and the levels are two-fold degenerate. As observed in the Stark map from Fig. 4.1, the G-state (b) shows an intermediate behaviour where exchange energy and j_1-coupling are of the same order of magnitude. This qualitative behaviour is discussed in more detail in the following sections.

[1] Note that the LS-coupling strength Ω_{nL} uses the upper case omega, as it refers to the two-electron operators.

4.2.2 Optimisation of the model parameters

We now turn to the question how to determine the values of the model parameters: the quantum defects $\delta^{^{2S+1}\mathrm{L}}$, which effectively establish an energy splitting between singlets and triplets resulting from the exchange energy, and the spin-orbit coupling strengths Ω_{nL} and $\omega_{n\ell}$. In theory, the coupling constants can be determined from the radial matrix elements. However, the calculation of the radial part requires the radial wave functions which are not necessarily reliable when using the SAE model. The SAE potential in Eq. (4.4) cannot attribute for electronic correlations such as the mixing of singlet and triplets states which we observe for the G state. Instead, our approach is to fit the model parameters directly to the experimental data.

However, we do not try to fit the Stark manifold directly, but we use the absolute energies that have been measured in the experiment at zero DC field, as listed in Appendix A.2.3, to fit the quantum defects and spin-orbit couplings. More specifically, we fit the four parameters to each set of states with a fixed n and ℓ independently. We calculate the error of the simulation by using a least-squares approach,

$$\epsilon = \sum_i \left(E_i^{\text{theo}} - E_i^{\text{exp}} \right)^2 , \tag{4.33}$$

where E_i^{theo} and E_i^{exp} are the theoretical and experimental energy levels, respectively, and i runs over all the considered experimental data points. Accordingly, ϵ has the unit MHz^2 and its square-root can be interpreted as the average mismatch of the theoretical and experimental points. We assign experimental and theory lines beforehand, such that every theory point is fitted to the correct experimental point. Note that ϵ does not have an upper bound but approaches zero as the theoretical simulation reproduces the experimental data points. We set a target error of $\epsilon \leq 0.01\,\mathrm{MHz}^2$. This corresponds to the precision of the experimental spectroscopy due to the Doppler effect[1]. As a starting point for the optimisation, we assume quantum defects as given in Appendix A.2.1 with $\omega_{n\ell} = \Omega_{nL} = 0$.

We have given a general introduction to optimisation methods in Sec. 3.1.3. In Chapter 3, we have used the gradient-based Krotov algorithm to optimise the RF pulse shaped for the fast navigation in the Stark manifolds of Rydberg atoms. Now, we change the strategy and perform a gradient-free parameter optimisation, since the number of optimisation parameters is very small. More specifically, we use the Subplex algorithm [116] provided by the Python *NLopt* package [117] which is a more robust and efficient variant of the Nelder-Mead method [75]. We connect the Fortran program and the Python optimisation using the F2PY Fortran to Python interface generator by NumPy [118].

[1] Depending on the direction of the microwave, the Doppler effect can shift its frequency up to $\pm 70\,\mathrm{kHz}$ [115]. Since the direction of the MW is unknown, this sets the uncertainty of the frequency measurements in the experiment.

Optimisation of f states

We optimise the parameters for each set of states with a fixed value of n and ℓ quantum numbers separately. We start with the f states, $\ell = 3$, which is the lowest angular momentum we are considering. In this case, experimental data is provided for the $n = 48$ to 54 manifolds (cf. Appendix A.2.3). However, only for $n = 48$ are the energies of all four energy levels known. For $n = 50$ and 52, the singlet and two of three triplets are known. We therefore focus on the optimisation of these three n-values. After first, preliminary optimisations, we found that the j_1-coupling is vanishingly small for all three manifolds and therefore set $\omega_{nf} = 0$. The initial error of the theoretical points is around $1200\,\mathrm{MHz}^2$. After the parameter optimisation, we find the following optimised parameters:

n	ϵ [MHz^2]	$\Omega_{nF}/2\pi$ [MHz]	$\delta^{1\mathrm{F}}$	$\delta^{3\mathrm{F}}$
orig.	$\approx$ 12000	0	$\delta_0^{1\mathrm{F}}$ = 0.08707, $\delta_2^{1\mathrm{F}}$ = -2	$\delta_0^{3\mathrm{F}}$ = 0.111867, $\delta_2^{3\mathrm{F}}$ = -2.2
48	0.7488	6.126743	0.0866934	0.1121021
50	0.0094	5.311711	0.0867488	0.1121091
52	0.0074	4.723026	0.0867919	0.1119283

Table 4.1: Original (first row) and optimised LS-couplings Ω_{nL} and quantum defects $\delta_i^{2S+1\mathrm{L}}$ of the f states for singlets and triplets, where i is the order of the quantum defects in the modified Rydberg-Ritz expression in Eq. (2.7). If i is not specified, $i = 0$ is assumed with vanishing higher order.

It is important to note that $48f$, which is the only set for which the energies of all four states are provided by the experiment, is the only one for which the error did not fall below the threshold of $0.01\,\mathrm{MHz}^2$. We have tested different guess parameters and tried to include j_1-coupling but nothing allowed for diminishing the error. We found that this is due to the limited freedom in choosing the positions of the triplets with respect to each other. As shown in Fig. 4.4 (a), any tuning of Ω_{nL} would increase the fidelity of one point at the expense of at least one other. The j_1-coupling cannot compensate for this, as the triplet with $J = L$ is bent downwards independently of the sign of $\omega_{n\ell}$, cf. Fig. 4.2 (b). Qualitatively, Fig. 4.4 (a) suggests that the red line would require a push upwards, which cannot be induced by j_1-coupling. At this point, it is not possible to say if the problem lies in an insufficient model or inaccurate experimental data. To clear this point, more experimental data would be required.

To obtain quantum defects and LS-coupling constants which are valid for all n values, we fit the optimised parameters from Tab. 4.1 to suitable functions. First, the LS-coupling is fitted to a power law of the form

$$\Omega_{nL} = 10^a n^b. \tag{4.34}$$

We expect the coupling constant to be proportional to $\langle \hat{\boldsymbol{r}}^{-3} \rangle$ which for hydrogen scales as $(n\ell)^{-3}$ [8].

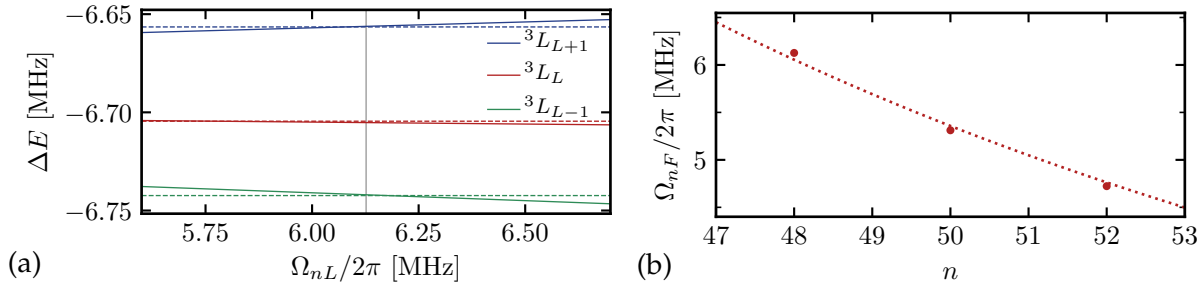

Figure 4.4: (a) Energy shift of the triplet states 48^3F due to LS-coupling Ω_{nL}. The zero of energy was set to the centre of the $n = 48$ manifold. The horizontal dashed lines indicate the experimental measurements. The vertical grey line indicates the optimal value that has been found. (b) LS-coupling Ω_{nL} as a function of the principal quantum number n. The points show the optimised values from Tab. 4.1, the dashed line is the fit from Eq. (4.35).

We thus assume $b = -3$ and fit the value of a using the *optimize* package provided by *SciPy*. We obtain the function

$$\Omega_{nF}/2\pi = 10^{5.826}\,\mathrm{MHz}\,n^{-3} = 1.931\,\mathrm{MHz}\left(\frac{50}{n}\right)^3 \tag{4.35}$$

with a standard error of 0.003 in a. The optimised values and the fit are shown in Fig. 4.4 (b).

Next, we fit the optimised quantum defects to the modified Rydberg-Ritz expression given in Eq. (2.7). However, for the singlets, it is not actually necessary to optimise the quantum defects as given above, but they result directly from inverting the Rydberg formula (cf. Eq. (2.6)),

$$\delta^{^{2S+1}\mathrm{L}} = n - \sqrt{\frac{-R}{E_n}}, \tag{4.36}$$

where R is the Rydberg constant of strontium [102]. Inserting the energies of the singlets from Appendix A.2.3 gives us the quantum defects from $n = 48$ to 54 as shown in Fig. 4.5 (a, points). We now fit these points to the modified Rydberg-Ritz expression,

$$\delta^{^{2S+1}\mathrm{L}} = \delta_0^{^{2S+1}\mathrm{L}} + \frac{\delta_2^{^{2S+1}\mathrm{L}}}{(n - \delta_0^{^{2S+1}\mathrm{L}})^2}, \tag{4.37}$$

which results in the parameters,

$$\delta_0^{^1\mathrm{F}} = 0.087369 \pm 0.000003, \quad \delta_2^{^1\mathrm{F}} = -1.549 \pm 0.007, \tag{4.38}$$

as shown in Fig. 4.5 (a, line) and where the errors reflect the standard error of the fit.

Next, we turn to fitting the optimised data of the triplets from Tab. 4.1 to Eq. (4.37). In this case, only three data points are available, one of which has a large error ($48f$) and the other two were optimised using incomplete data. We fit them in the same fashion as the singlets to the

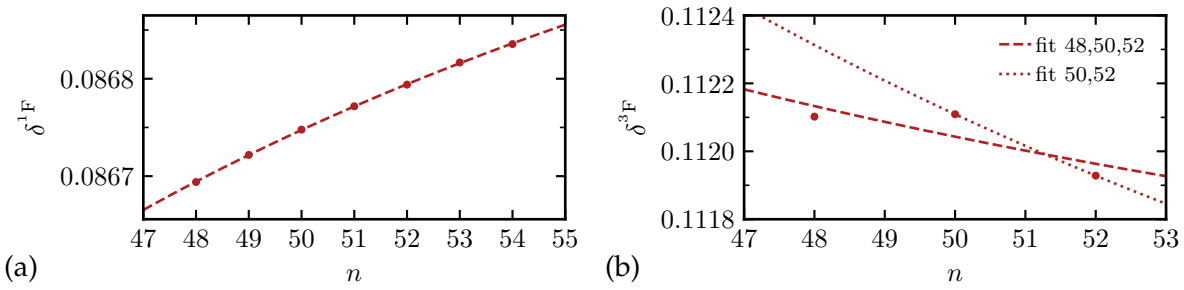

Figure 4.5: Quantum defect of the singlet (a) and triplet (b) F states as a function of the principal quantum number n. The points show calculated values using Eq. (4.36) for the singlets and the optimised values from Tab. 4.1 for the triplets. The dashed lines show the fit of Eq. (2.7) using all data points. The dotted line in (b) shows the fit when only considering the points $n = 50$ and 52.

expression in Eq. (4.37) and the resulting parameters are

$$\delta_0^{^3\mathrm{F}} = 0.1110 \pm 0.0007, \quad \delta_2^{^3\mathrm{F}} = 2.63 \pm 1.77, \tag{4.39}$$

see dashed line in Fig. 4.5 (b). The fit is obviously worse than for the singlets which is not surprising given the low quality of the data and the parameter optimisation. As an alternative, we have fitted the quantum defects considering $n = 50$ and 52 only resulting in

$$\delta_0^{^3\mathrm{F}} = 0.1097, \quad \delta_2^{^3\mathrm{F}} = 5.95, \tag{4.40}$$

(dotted line) which do not have a fitting error, since we are fitting two points with two degrees of freedom. Due to the lacking triplet points, this fit does not necessarily deliver reliable results but it might be more suitable when describing the $n = 50$ and 52 manifolds. As mentioned above, more experimental data is necessary to improve the quality of this fit.

Finally, we summarise the optimisation of the F states as follows:

	$\Omega_{nF}/2\pi$ [MHz]	$\delta_0^{^1\mathrm{F}}$	$\delta_2^{^1\mathrm{F}}$	$\delta_0^{^3\mathrm{F}}$	$\delta_2^{^3\mathrm{F}}$
orig.	0	0.08707	-2	0.111867	-2.2
opt.	$10^{5.826}n^{-3}$	0.087369	-1.549	$\left\{\begin{matrix}0.1110\\0.1097\end{matrix}\right\}$	$\left\{\begin{matrix}2.63\\5.95\end{matrix}\right\}$

Table 4.2: Original and optimised LS-couplings Ω_{nL} and quantum defects $\delta_i^{^{2S+1}\mathrm{L}}$ of the f states for singlets and triplets, where i is the order of the quantum defects in the modified Rydberg-Ritz expression in Eq. (2.7). The set of values for the quantum defect of the triplets correspond to the fit of $n = 48, 50, 52$ (upper number) and $n = 50, 52$ (lower number), respectively.

Optimisation of g states

We continue by fitting the $49g$ state, as it is the only g state for which all four energy levels were measured in the experiment. Since ultimately, we are interested in the Stark map around $49g$ (as shown in Fig. 4.1), this is sufficient for our purposes. If the model parameters shall be determined for other n-manifolds with high precision, more experimental data is required. The initial quantum defects (cf. Appendix A.2.1) lead to an error of about $2700\,\mathrm{MHz}^2$. The parameter optimisation reduces the error below the desired threshold and we stopped the optimisation at $\epsilon = 0.009\,\mathrm{MHz}^2$ which results in the following optimised parameters:

	$\omega_{49g}/2\pi$ [MHz]	$\Omega_{49G}/2\pi$ [MHz]	$\delta^{^1\mathrm{G}}$	$\delta^{^3\mathrm{G}}$
orig.	0	0	0.038	0.03844
opt.	2.720488	-0.0195798	0.0383956	0.0388679

Table 4.3: Original and optimised j_1-couplings $\omega_{n\ell}$, LS-couplings Ω_{nL} and quantum defects $\delta^{^{2S+1}\mathrm{L}}$ of the $49g$ states.

The quantum defects were only slightly adjusted by the optimisation. The dominating coupling is the j_1-coupling and the splitting between the triplets is fine-tuned by a small LS-coupling. The observations are in agreement with our expectation of G being an intermediate state (cf. Fig. 4.3 (b)). The states show strong j_1-coupling, thus reflecting the beginning independence of the two electrons, which is consistent with a decreased exchange energy (as compared with the F states). The LS-coupling is non-vanishing but much smaller than the j_1-coupling. In fact, the energy shift induced by Ω_{49G} is of the order of $100\,\mathrm{kHz}$ and could be the result of detection noise. More experimental data would be required to gain more insight.

During the parameter optimisation we noted that the outcome is particularly sensitive to the guess parameters. If the guess parameter of $\omega_{n\ell}$ is chosen badly, e.g. $\omega_{49g} = 0$, the optimisation runs into the wrong minimum with $\omega_{49g}/2\pi = -3.3\,\mathrm{MHz}$ and $\Omega_{49G}/2\pi = 0.31\,\mathrm{MHz}$. While this combination leads to a similarly high fidelity at zero field, it does not reproduce the avoided crossing observed in the experimental Stark map of Fig. 4.1 around $40\,\frac{\mathrm{V}}{\mathrm{m}}$. The opposite sign of ω_{49g} (as compared to the value listed in Tab. 4.3) inverses the order of the J states (cf. Fig. 4.2 (a)) which leads to wrong coupling at higher fields. We thus chose a positive guess value which then resulted in the optimised values from Tab. 4.3 which reproduce the avoided crossing, as shown in Sec. 4.2.3.

Optimisation of h states

Lastly, we consider the $\ell = 5$ (h) states. In the experiment, it was possible to determine three doublets of h states, namely for $n = 48, 52$ and 54. For h states, we do not expect to see any exchange energy or LS-coupling Ω_{nL} but only j_1-coupling $\omega_{n\ell}$ which splits the states according to their j_1 value (cf. Fig. 4.3 (c)). As there is no exchange energy, the states split linearly as shown

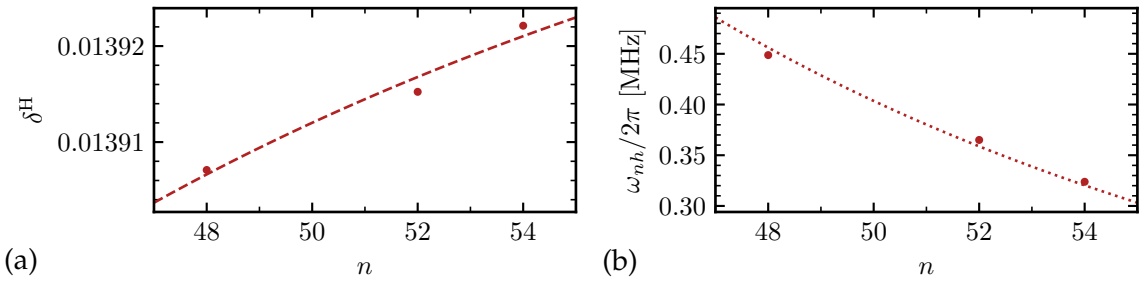

Figure 4.6: Quantum defect δ^{L} (a) and j_1-coupling $\omega_{n\ell}$ (b) of the h states as a function of the principal quantum number n. The points show the optimised values from Tab. 4.4. The dashed lines show the result of the fit with the parameters given in Eq. (4.41) and (4.42), respectively.

by the green and blue line in Fig. 4.2 while the singlet and triplet with $J = L = 5$ mix and split in the same way. We therefore set $\delta^{\mathrm{H}} \equiv \delta^{^1\mathrm{H}} = \delta^{^3\mathrm{H}}$ (no exchange energy) and $\Omega_{nH} = 0$. The optimisation succeeds in reducing the error below the desired threshold for all three manifolds, and the optimised parameters are:

n	$\omega_{nh}/2\pi$ [MHz]	δ^{H}
orig.	0	0.0134759
48	0.448723	0.01390709
52	0.365062	0.01391523
54	0.323817	0.01392212

Table 4.4: Original (first row) and optimised j_1-couplings $\omega_{n\ell}$ and quantum defects $\delta^{^{2S+1}\mathrm{L}} = \delta^{\mathrm{L}}$ of the h states.

The optimised parameters can be fitted as described for the f state. The quantum defects are fitted to Eq. (2.7) resulting in

$$\delta_0^{\mathrm{H}} = 0.013975 \pm 0.000011, \quad \delta_2^{\mathrm{H}} = -0.158 \pm 0.029. \tag{4.41}$$

The data points and the fit are shown in Fig. 4.6 (a). Regarding the j_1-coupling, we see that the determined values of $\omega_{n\ell}$ are weaker than for the G states. This was to be expected, since $\langle \hat{\boldsymbol{r}}^{-3} \rangle$ scales (for hydrogen) as $(n\ell)^{-3}$ [8] and thus decreases with ℓ. We fit ω_{nh} using the same ansatz as for the Ω_{nL}-coupling given in Eq. (4.34) with $n = -3$ and we obtain the values

$$\omega_{nh}/2\pi = 10^{4.703}\,\mathrm{MHz}\, n^{-3} = 0.404\,\mathrm{MHz} \left(\frac{50}{n}\right)^3 \tag{4.42}$$

with a standard error of 0.005 in the exponent. The data points and the fit are shown in Fig. 4.6 (b).

Before finishing this section and proceeding with discussing the optimised Stark map, we present a short summary of our findings. We have optimised the f, $49g$ and h states and deter-

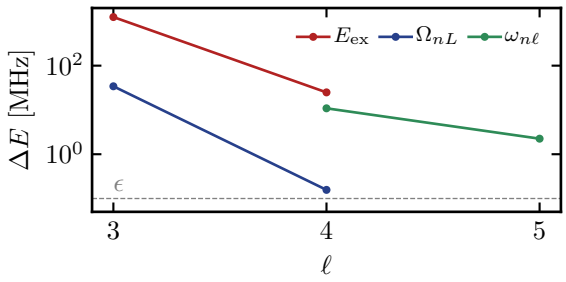

Figure 4.7: Energy shift induced by the exchange energy E_{ex}, LS-coupling Ω_{nL} and j_1-coupling $\omega_{n\ell}$ of f, g and h states. Missing data points indicate zero energy shifts. The horizontal dashed line indicates the precision of the fit and in the experiment.

mined the quantum defects for singlets and triplets, effectively determining the exchange energy, and the spin-orbit couplings, Ω_{nL} and $\omega_{n\ell}$, which minimise the mismatch between the theoretical calculation of the energy levels at zero field and the experimentally measured ones. A summary is shown in Fig. 4.7. The optimised values of the f state are shown in Tab. 4.2. The f state shows strong exchange energy and LS-coupling Ω_{nL}, since the overlap and thus the interaction between the two electrons is strong. Regarding the g-state, we could only investigate the $49g$-state, as no further experimental data were available. The exchange energy is weaker than for the f state as the overlaps between the electrons decrease. As a result, the states show strong j_1- and weak LS-coupling, as listed in Tab. 4.3. For the h states, we did not observe LS-coupling or exchange energy, resulting in the same quantum defects for singlets and triplets as given in Eq. (4.41). Instead, it showed j_1-coupling as given in Eq. (4.42), indicating the independence of the two electrons. All optimised parameters are summarised in Appendix A.2.4. Our findings are in agreement with our expectations (cf. Fig. 4.3) and our model, which is based on physical principles, proved to be able to reproduce the measured energy levels with high accuracy.

We close this part with a final remark. For $\ell = 4$ and 5, the fit gives a spin-orbit coupling that is mainly proportional to $\hat{\boldsymbol{l}}_1 \cdot \hat{\boldsymbol{s}}_1$. Note that the experimental data do not allow us to determine whether breaking the spin symmetry of singlets and triplets is due to the coupling of the angular momentum of the Rydberg electron to its spin, $\hat{\boldsymbol{l}}_1 \cdot \hat{\boldsymbol{s}}_1$, or to the spin of the inner electron, $\hat{\boldsymbol{l}}_1 \cdot \hat{\boldsymbol{s}}_2$. The parameters

$$\omega_{n\ell}\hat{\boldsymbol{L}} \cdot \hat{\boldsymbol{S}} - \omega_{n\ell}\hat{\boldsymbol{l}}_1 \cdot \hat{\boldsymbol{s}}_1 = +\omega_{n\ell}\hat{\boldsymbol{l}}_1 \cdot \hat{\boldsymbol{s}}_2 \tag{4.43}$$

would fit the data as well (compare to Eq. (4.32) for $\Omega_{nL} = 0$). The energy of the levels would be exactly the same, and the interpretation would be similar; the only difference being that the quantum number j_1 would be replaced by k corresponding to $\hat{\boldsymbol{k}} = \hat{\boldsymbol{l}}_1 + \hat{\boldsymbol{s}}_2$ in the analysis.

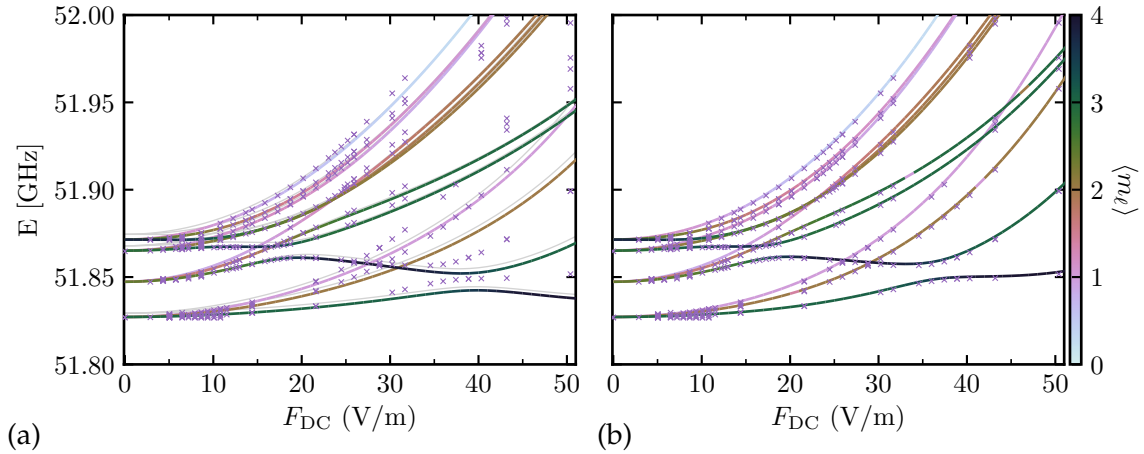

Figure 4.8: Stark map from $50^1F_3, m_j = 2$ to $49g$ for $m_j = 1, \ldots, 3$ after the parameter optimisation. The line colour indicates the expectation value of m_ℓ, the crosses indicate the experimental measurements. (a) considers the optimised quantum defects and spin-orbit coupling constants. (b) also considers quantum defects for i and j. The light grey lines in the background of (a) indicate the Stark map from Fig. 4.1 (a).

4.2.3 Optimised Stark maps

We now turn to the evaluation and discussion of the updated Stark map under the optimised parameters of the previous section. The reference is the Stark map of Fig. 4.1 (a) showing the transitions from the reference state $50^1F_3, m_j = 2$ towards $49g$ for $m_j = 1, \ldots, 3$. The updated version is presented in Fig. 4.8 (a). It can be seen that the mismatch at zero field (on the left-hand side) decreased significantly. However, the curves still deviate noticeably at higher DC field amplitudes. We therefore include higher order quantum defects, $\ell > 5$, to improve the accuracy. The quantum defects for $\ell = 6$ (i) and 7 (j) can be derived from spectroscopy data [115] using Eq. (4.36). For example, the quantum defect of the j states were calculated from the energy splitting between $50h, j_1 = \frac{9}{2}$ and $49j$ measured in the experiment. The results are

$$\delta_0^{\mathrm{I}} = 0.006, \quad \delta_0^{\mathrm{J}} = 0.003. \tag{4.44}$$

The updated Stark map is shown in Fig. 4.8 (b). The agreement between theory and experiment is remarkable. It might seem surprising that the i and j states affect the structure of the f and g states, as they are far away. However, it turns out that their presence and mixture with neighbouring states induced by the DC field heavily influences the Stark map of the g state. Interestingly, we found that the fidelity of the Stark map in the discussed energy window was even slightly higher when we only considered the quantum defect of the i state and did not include δ_0^{J} yet. However, when considering higher DC fields, the overall fidelity increases when including δ_0^{J}. It might therefore be fruitful to measure the quantum defects of the i and j states, and possibly even higher quantum defects, with a higher precision in the experiment.

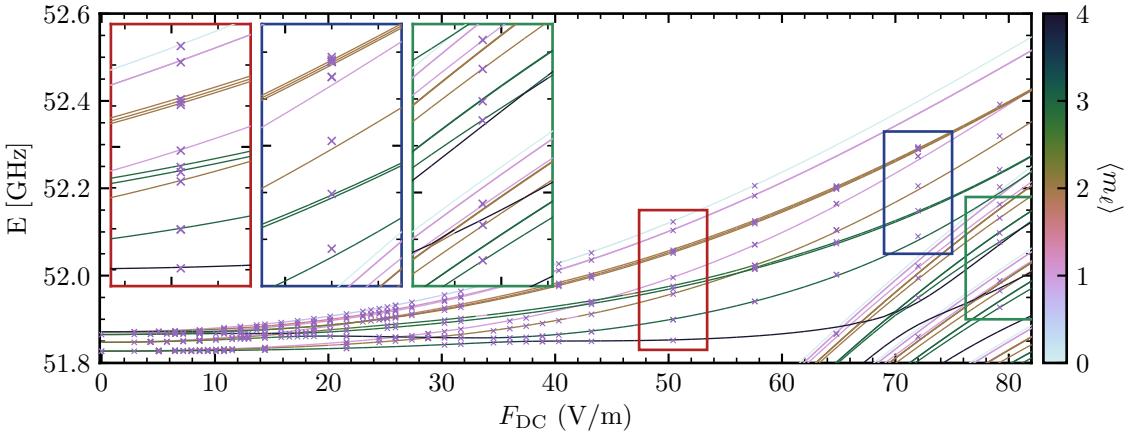

Figure 4.9: Same as Fig. 4.8 (b) but on a larger scale. The insets show a zoom as indicated by the coloured rectangles. The red and green inset show the good agreement between simulation and experiment for medium fields and within the Stark manifold, respectively. The blue inset shows the mismatch arising at higher DC fields.

To summarise, we have significantly improved the agreement between the simulated and experimentally measured Stark map by optimising the parameters of our physically motivated model using only experimental data points at zero DC field, cf. Fig. 4.8. The simulations reproduce the experimental points until DC fields around $65\,\frac{\mathrm{V}}{\mathrm{m}}$ and within the Stark manifold with high accuracy as shown in Fig. 4.9 (red and green inset). It is only for larger fields (blue inset) that a stronger deviation emerges. We have tried to improve the accuracy at higher fields by optimising the radial part of the wave function directly. In doing so, we attempted to compensate for errors in the potential due to the SAE approximation by accounting for mixing of energy levels. However, any improvement in fidelity at the considered DC field increased the error at higher fields or within the Stark manifold (around the green inset). The overall increase of fidelity was furthermore not satisfying. More details on the attempted optimisation of the radial part can be found in Appendix C.2.

In the next section, we investigate the dynamics within the Stark manifold $n = 51$ and we therefore conclude this section by briefly considering the corresponding Stark map when starting from the reference state $52^1F, m_j = 2$, see Fig. 4.10 (a). In this case, experimental data is available for high fields until $140\,\frac{\mathrm{V}}{\mathrm{m}}$ which are reproduced very well by the simulations (see also inset). The experimental points which do not seem to match any theoretical line stem from transitions to the higher manifold, i.e. from $52^1F, m_j = 2$ towards $n = 53$. The corresponding theoretical lines are not shown in the plot. The high fidelity of the presented Stark map inclines us to the conjecture that we mainly fail to simulate the curvature of the g-state when it joins the Stark manifold in Fig. 4.9 with high accuracy. The mismatch between theory and experiment might therefore decrease again at higher fields when the g-state merged with the Stark manifold. In the same way as we noticed that the hydrogenic behaviour of rubidium dominates for states within the Stark

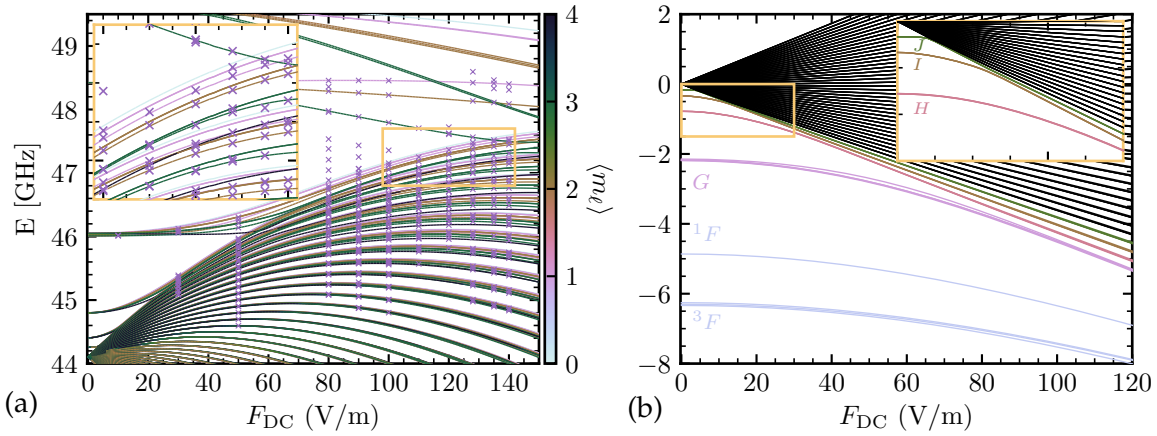

Figure 4.10: (a) Stark map from $52^1F_3, m_j = 2$ towards $n = 51$ for $m_j = 1, 2, 3$ using the optimised parameters when having fitted the f-states for $n = 48, 50, 52$ (upper number in Tab. 4.2). The line colour indicates the expectation value of m_ℓ, the crosses indicate the experimental measurements. The inset shows a zoom as indicated by the coloured rectangle. (b) Stark map around $n = 51$ showing the bare energy levels. The line colour indicates the ℓ value at zero field. The zero of energy was set to the $n = 51$ level of hydrogen.

manifold, the same might be true for strontium and the SAE model. Additional data would be necessary to prove this conjecture. We conclude that the improved model derived in this section delivers promising results and seems to be suitable for investigating the dynamics within the Stark manifold. On a final note, we would like to mention that we checked the accuracy of the model for other Stark maps. One further example is shown in Appendix C.3.

4.3 Circularisation of strontium

Ultimately, the goal is to use strontium atoms for quantum technology applications such as quantum metrology which requires the accurate control of the dynamics within the Stark manifold. In the previous section, we presented the first step which is the optimisation of the employed model. In this section, we explore the possibilities of controlling the dynamics within the Stark manifold. A mandatory requirement for this is an accurate model of the system. As a proof-of-principle, we examine the well-known circularisation of the Rydberg atom. If it is possible to circularise the strontium atoms with a high fidelity, it is a promising indicator that we will be able to control strontium similarly to rubidium in the future.

The Stark map of strontium for $n = 51$ is shown in Fig. 4.10 (b). In the experiment, the circularisation is performed at a DC field of $110\,\frac{\mathrm{V}}{\mathrm{m}}$. The figure shows that at this field the g state has already joined the Stark manifold but the f state has not yet – the situation is thus slightly different than for rubidium. The initial state of the circularisation is the lowest state of the $m_j = 2$ ladder at the considered field. To reduce the computational cost, we neglect states with $\langle \hat{\boldsymbol{S}} \rangle > 0.999$ (i.e. states with at least 99.9% triplet character). Of the remaining states, we only

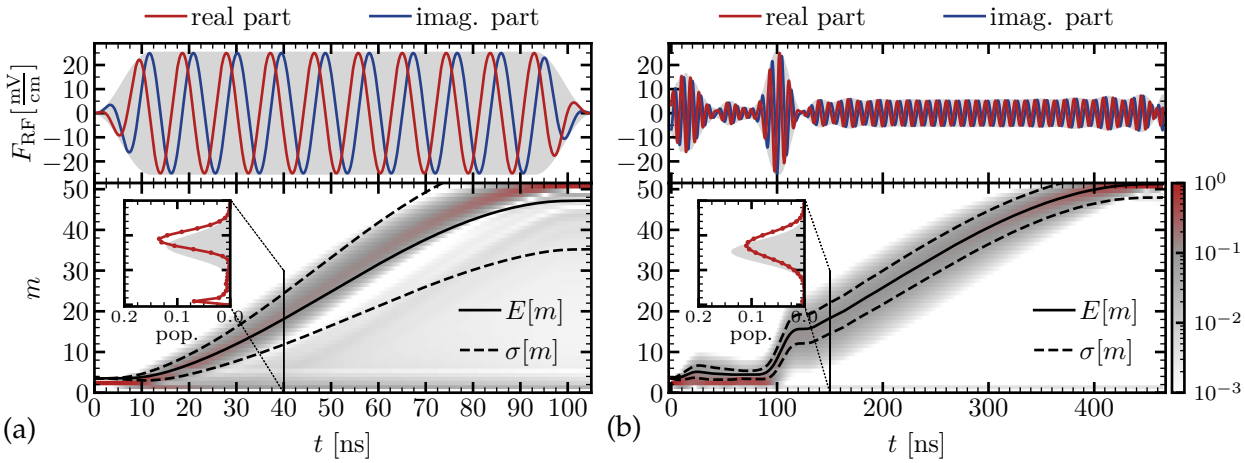

Figure 4.11: Circularisation of strontium at $F_{\mathrm{DC}} = 110\,\frac{\mathrm{V}}{\mathrm{m}}$ in the $n = 51$ manifold using a π-pulse (a) and the (b) 99%-optimised pulse under experimental constraints. Top: RF π-pulse shapes (grey) and their real and imaginary parts (red and blue lines, respectively). Bottom: Corresponding distribution of the population over the lowest diagonal ladder of singlet states. Note the logarithmic scale in the colour bar. The expectation value $E[m]$ and the standard deviation $\sigma[m]$ are indicated by the solid and dashed lines, respectively. The inset displays a snapshot of the population distribution (red) and the distribution of the closest SCS with (a) $\vartheta = 0.60\pi$, (b) $\vartheta = 0.62\pi$ (grey shade).

consider the lowest two diagonal ladders of the Stark manifold and states which are very close to it. These additional states are mixtures of singlets and triplets arising from the j_1-coupling of g and h states. We end up with a Hilbert space of dimension 105.

We now study the circularisation of strontium atoms using a π-pulse. We choose an initial RF amplitude of $F_{\mathrm{RF}} = 25\,\frac{\mathrm{mV}}{\mathrm{cm}}$, which is the maximum used for rubidium, and assume a circularly polarised RF-pulse with sine-squared edges of 12 ns length. To determine the frequency ω_{RF} enabling the most efficient population transfer, we perform a parameter optimisation. We find that we can circularise strontium with 81% fidelity using a frequency of $\omega_{\mathrm{RF}} = 107.63\,\mathrm{MHz}$ within 105 ns. The pulse and the dynamics on the lowest diagonal (singlet) ladder are shown in[1] Fig. 4.11 (a). Despite being very similar to the circularisation of rubidium (compare to Fig. 3.3), subtle differences arise. Most strikingly, the population is spread out more strongly over the ladder as can be seen from the grey streaks in the lower right part of the plot. Moreover, the $m = 1$ state is not the only one to get significantly populated in the beginning. Instead of a sharp peak at $m = 1$, population can be found in a small range from $m = 1$ to approximately 4 (see inset). The dark state of strontium is thus much broader than for rubidium. We have also tested the influence of the radial part optimisation on the circularisation as described in the end of Appendix C.2. We found that the dynamics within the Stark manifold are not significantly affected by further optimisation of the Hamiltonian and conclude that the result of the propagation is reliable.

[1]Note that for singlets $m \equiv m_j = m_\ell$.

As a last proof-of-concept, we optimise the circularisation of strontium using Krotov's method. The procedure is similar to the one described in Sec. 3.2.5 for rubidium. However, as the central frequency of the RF, $\omega_{\text{RF}} = 107.63\,\text{MHz}$, is not within the previous window (140 to $360\,\text{MHz}$), the filter had to be adjusted. Since the experimental setup has changed, it is unknown which frequency window would be most suitable. We therefore choose a window between 60 and $160\,\text{MHz}$ which is centred around the central frequency, while the flat-top shape function with sine-squared edges of $20\,\text{MHz}$ is retained. Regarding the optimisation, we have tested several guess pulses with varying amplitude F_{RF} between 3 and $25\,\frac{\text{mV}}{\text{cm}}$ and adjusted the length to fit a π-pulse. The resulting pulses vary in length between 770 and $105\,\text{ns}$. Then, we have tried to optimise each guess pulse to a fidelity of 99% using Krotov's method. The shortest pulse which succeeded in optimising the dynamics had a length of $465\,\text{ns}$ and an initial amplitude of $5\,\frac{\text{mV}}{\text{cm}}$. The optimised pulse and the dynamics on the lowest diagonal ladder of the Stark manifold are shown in Fig. 4.11 (b). It is striking that the pulse is about four times longer than for rubidium. The optimised pulse shows two strong peaks around 10 and $100\,\text{ns}$ while staying close to the guess amplitude for the remainder of the time. The population is thus excited to a SCS-like state in two steps. However, the overlap with a SCS is lower than has been observed for rubidium as can be seen from the grey shade in the inset. Instead, the population distribution is slightly broader and asymmetric with more population towards lower states. This is most likely due to the higher spread of population in the guess pulse. As a result, the standard deviation of m is comparatively high at the end of the pulse. The final population of the circular state is 98.7%.

The generally low amplitude of the pulse, apart from the two peaks, suggests that shorter pulses are possible if more sophisticated guess pulses are employed. Indeed, we found that pulses down to $111\,\text{ns}$ (corresponding to a guess pulse with $F_{\text{RF}} = 23\,\frac{\text{mV}}{\text{cm}}$) were able to optimise the dynamics to an error of $2.5\cdot10^{-2}$ in the target state population. Further increase of fidelity was then prevented by the experimental constraints. Since the exact constraints are yet unknown, a further decrease of pulse length seems very likely. As a comparison, we have optimised the original π-pulse with $t_{\text{stop}} = 105\,\text{ns}$ without experimental constraints. The optimisation succeeded and the optimised pulse had a peak amplitude of $75\,\frac{\text{mV}}{\text{cm}}$ and a bandwidth of around $550\,\text{MHz}$ including components of the opposite polarisation. It therefore seems that the bandwidth is the major limiting factor when trying to achieve high fidelities under experimental constraints.

We conclude that it is possible to circularise strontium with high accuracy under experimental constraints. However, a more thorough optimisation including more sophisticated guess pulses is necessary to circularise strontium on a similar timescale as rubidium. As the exact experimental constraints are not yet known, it is beneficial to wait until this information is available, as especially the bandwidth is a crucial factor for the feasibility of the optimisation. Moreover, we could not compare the numerical propagation to experimental data yet which would allow us to test the quality of our model. If necessary, the model parameters could be fine-tuned to improve the agreement between theory and experiment, hence enabling high-fidelity control of strontium Rydberg atoms.

4.4 Summary

In this chapter, we have studied Stark maps of strontium around the state $49g$ and found that the single-active electron (SAE) model proposed in literature does not predict the outcome of experiments accurately. We have therefore developed an improved, physically motivated model which could reproduce the experimental data with high fidelity as shown in Fig. 4.9. We found an excellent agreement until DC fields $65\,\frac{\mathrm{V}}{\mathrm{m}}$ and also at higher fields within the Stark manifold. Deviations only emerge for fields around $70-80\,\frac{\mathrm{V}}{\mathrm{m}}$ where the g-state joins the Stark manifold. The study of the Stark manifold around $n = 51$ revealed excellent agreement for fields up to $140\,\frac{\mathrm{V}}{\mathrm{m}}$, shown in Fig. 4.10 (a), for which no data was available around $70\,\frac{\mathrm{V}}{\mathrm{m}}$. If necessary, the accuracy of the model parameters could be improved if more experimental data was provided.

The pivotal adjustment was the introduction of an additional spin-orbit coupling term which we referred to as j_1-coupling. This term accounts for independent spin-orbit coupling of the two electrons and mixes singlet and triplet states which was not covered by the single electron picture. This stands in contrast to a simple spin-orbit coupling proportional to $\hat{\boldsymbol{L}} \cdot \hat{\boldsymbol{S}}$ of the coupled system, referred to as LS-coupling, which commutes with the total spin $\hat{\boldsymbol{S}}^2$. We obtained the optimal parameters for both kinds of spin-orbit coupling and the quantum defects, which effectively implement the exchange energy between singlets and triplets, by performing a parameter optimisation. More specifically, we have employed a gradient-free method in order to minimise the mismatch between the model and experimentally recorded data points at zero DC field.

We found that for f-states ($\ell = 3$), the exchange energy is the dominant contribution and the spin-orbit coupling can be described by simple LS-coupling. The high-angular-momentum h-states ($\ell = 5$), on the other hand, show strong j_1-coupling without exchange energy. In both cases, we fitted the obtained values to suitable functions of the principal quantum number n, thus allowing for extrapolation to other n-manifolds. The g-state ($\ell = 4$) lies in the intermediate range where exchange energy and spin-orbit coupling are of the same order of magnitude. We further included high quantum defects of $\ell = 6$ and 7 into the simulations. A summary of the optimised model parameters can be found in Appendix A.2.4.

As the overall goal of our study was to pave to way to optimal control of strontium atoms, we have performed a first test by investigating the circularisation of strontium as shown in Fig. 4.11. We found that a π-pulse with a duration of $105\,\mathrm{ns}$ populates the circular state with 81% fidelity. We then have optimised the pulse using Krotov's method under preliminary experimental constraints. We found optimised pulse shapes reaching 99% fidelity within $465\,\mathrm{ns}$. The pulse shape suggests, however, that shorter times are feasible if the guess pulse was designed more intricately. We found, for instance, that shorter pulses with $111\,\mathrm{ns}$ duration could circularise strontium with fidelities up to 97.5%. The optimisation thus needs further investigation once the final experimental conditions are known and experimental tests have yet to be conducted. However, our preliminary tests suggest that fast and accurate circularisation under experimental constraints is possible.

5

QUANTUM SIMULATION OF OPEN QUANTUM SYSTEMS

In an ideal world, it would be possible to completely isolate quantum systems from their surroundings. In reality, however, every system unavoidably interacts with its environment, may it be via stray fields or particles, thermal fluctuations or other sources of noise. Generally, this interaction results in a loss of energy or phase information – also called decoherence – which can never be entirely controlled, neglected nor avoided. In particular in the delicate field of quantum technology, already small disturbances can render entire protocols useless due to decoherence or the decay of quantum states. At the same time, control strategies unavoidably introduce a source of noise into the quantum system, for instance via fluctuating field strengths. It is thus necessary to balance a sufficient isolation of the quantum system with the required level of control [30]. Moreover, the readout of information itself, which is a crucial step of quantum information processing, effectively introduces decoherence into the system. It is thus not sufficient to try to suppress decoherence altogether, but it is necessary to study and understand open quantum system, in order to rise to the challenge of controlling open quantum systems for quantum technologies.

The theory of open quantum systems [33] aims to describe or approximate the dynamics in quantum systems that interact with their environment, also called the bath. How the quantum system is influenced by its surrounding depends on the nature of the environment and their coupling with each other. In many cases, the dynamics of the open quantum systems can be described in the so-called Markov approximation which can be interpreted as an information flow from the system to the bath only. In the most general case, however, the system can retrieve information from the bath at later times, in which case the bath is said to have a "memory". These processes are called non-Markovian [119, 35]. Non-Markovian dynamics are ubiquitous in condensed phase [120] but inherently difficult to describe and study [121]. They are thus subject of current research, as many important questions are still open. One of them is the role of non-Markovianity in the engineering and control of open quantum systems, or in other words, if non-Markovianity can in certain cases be an asset for control [122, 123, 124].

Studying open quantum systems is difficult because the environment is usually not controllable, very large and partly unknown. An ideal framework for solving this problem can be found

in the field of quantum simulation [34]. The central idea of quantum simulation is to use a controllable quantum system in order to study another more complex, less controllable one. This method is predominantly used to study many-body dynamics in condensed matter physics [34] but application to open quantum systems is also most natural [125, 126]. What is missing to date is an open system quantum simulator that allows us to fully tune the strength of memory effects. This is essential to study the role of non-Markovianity in the engineering and control of open quantum systems.

In this thesis, we capitalise on the idea of quantum simulation and model a quantum simulator for open quantum systems using Rydberg atoms. To this end, we exploit the formal analogy between the theory of open quantum systems and the measurement process to induce a tunable source of dissipation in a quantum system. More specifically, we consider a cavity quantum electrodynamics (cavity QED) setup and induce dissipation in a photonic mode of a microwave cavity by performing controlled measurements using circular Rydberg atoms. In particular, we model a quantum simulator which is fully tunable between the Markovian and non-Markovian regime independently from the strength of dissipation.

To this end, we start by giving an introduction into the required methods for describing open quantum systems and quantum measurements in Sec. 5.1. Afterwards, we present the model for our open quantum system simulator in Sec. 5.2 where we explore the parameter landscape of the simulator when controlling it with a single pulse. In Sec. 5.3, we extend the scheme to two control pulses and show how to tune memory effects and dissipation independently from each other. Note that the results of these chapter have already been published in [127].

5.1 Methods for open quantum systems

The state of a closed quantum system can be fully described by a state vector $|\psi\rangle$ in Hilbert space. Its time evolution is determined by the Schrödinger equation whose solutions can be represented in terms of unitary time-evolution operators $\hat{U}(t, t_0)$,

$$|\psi(t)\rangle = \hat{U}(t, t_0)\,|\psi(t_0)\rangle\,, \tag{5.1}$$

propagating the state from the initial time t_0 to the final time t. If we consider a statistical mixture of quantum systems, on the other hand, the systems' state can generally not be described by a state vector in Hilbert space. Instead, we define the density operator [33],

$$\hat{\rho} = \sum_{\alpha} w_\alpha\,|\psi_\alpha\rangle\langle\psi_\alpha|\,, \tag{5.2}$$

where the w_α are positive weights and the $|\psi_\alpha\rangle$ are normalised state vectors. If only one $w_{\alpha_0} = 1$ while all the others are 0, the state is called pure. In all other cases, the system is said to be in a mixed state. When a specific basis $\{|n\rangle\}$ is chosen, the matrix elements of the density operator

can be written as a matrix $\boldsymbol{\rho} = (\rho_{nm})_{nm}$ with the matrix elements

$$\rho_{nm} = \langle n|\hat{\rho}|m\rangle = \sum_{\alpha} w_\alpha \langle n|\psi_\alpha\rangle \langle \psi_\alpha|m\rangle . \tag{5.3}$$

The density matrix $\boldsymbol{\rho}$ is normalised, $\mathrm{Tr}\{\boldsymbol{\rho}\} = \sum_n \rho_{nn} = 1$, hermitian, $\rho_{nm} = \rho^*_{mn}$, and positive semi-definite, $\boldsymbol{\rho} \geq 1$. The diagonal elements, ρ_{nn}, are real, non-negative numbers and can be interpreted as the population of the state $|n\rangle$. The off-diagonal elements, ρ_{nm}, are in general complex and describe the coherence between the states $|n\rangle$ and $|m\rangle$. The density matrix allows for a clear distinction between pure and mixed states by defining the so-called purity

$$\gamma = \mathrm{Tr}\left\{\boldsymbol{\rho}^2\right\}, \tag{5.4}$$

which fulfils $\frac{1}{N} \leq \gamma \leq 1$ with N being the dimension of the Hilbert space. The purity takes its maximal value, $\gamma = 1$, if and only if the state is pure.

For density matrices, the Schrödinger equation takes the form

$$\frac{d}{dt}\hat{\rho}(t) = -i\left[\hat{H}(t),\, \hat{\rho}(t)\right] \tag{5.5}$$

which is also called the Liouville-von Neumann equation. An alternative way of writing this equation is in Liouville space, i.e. the space in which the density operator becomes a column vector, as

$$\frac{d}{dt}\hat{\rho}(t) = \hat{\hat{\mathcal{L}}}(t)\hat{\rho}(t) \tag{5.6}$$

where $\hat{\hat{\mathcal{L}}}$ is a super operator, i.e. an operator acting on operators. It is called the Liouville operator and is equivalent to the Hamilton operator in Hilbert space.

When dealing with open quantum systems, the state of the system can no longer be described by a single state vector $|\psi\rangle$ in Hilbert space. Instead, the density matrix formalism proves to be more suitable. In the following, we first discuss how to describe the dynamics of open quantum systems using dynamical maps. In Sec. 5.1.2, we discuss the formal analogy between the theory of open quantum systems and indirect quantum measurements. In Sec. 5.1.3, we present the Lindblad master equation – the generalisation of the Liouville-von Neumann equation for Markovian open quantum systems – and discuss the approximations made during its derivation. Finally, we go beyond the Markov approximation and discuss non-Markovian dynamics as well as suitable measures of non-Markovianity in Sec. 5.1.4. Note that the content of this section is mostly based on [33] unless noted otherwise.

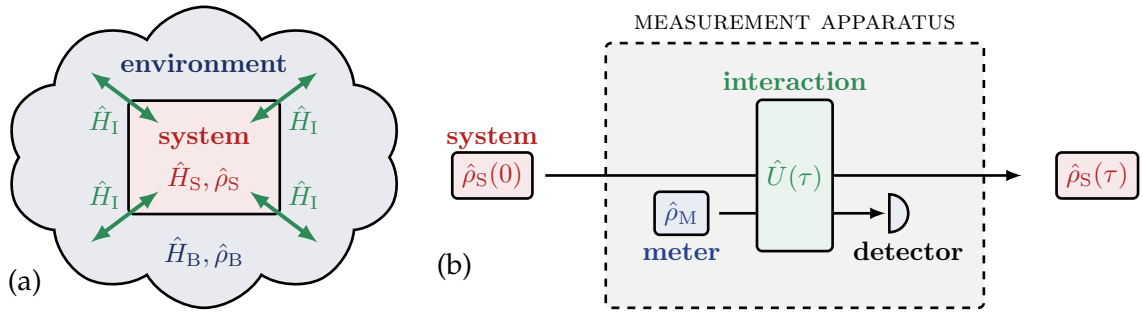

Figure 5.1: Sketch of an open quantum system (a) and an indirect measurement (b) with the system in red, the environment/meter in blue and the interaction in green.

5.1.1 Dynamics of open quantum systems

An open quantum system can be described as a quantum system S coupled to another, typically larger quantum system B which is called the environment, reservoir or bath, see Fig. 5.1 (a). The three terms are often used synonymously (as we do in this thesis) while they are sometimes used to highlight certain properties of B. The combined system $S + B$ is commonly assumed to be closed, i.e. decoupled from an even bigger environment. Strictly speaking, this is only true if the environment covers the whole universe. However, it is usually sufficient to include only those degrees of freedom into the bath B which have a considerable effect on the subsystem S. The dynamics of the resulting system $S + B$ can then be described as unitary. Note that the division into system and bath is not always clear-cut. Usually, the system S includes those degrees of freedom that we are interested in, have access to or control over. The environment, on the other hand, is often very large and we cannot control it.

The total Hamiltonian of the combined system can be written as

$$\hat{H}(t) = \hat{H}_S \otimes \hat{\mathbb{1}}_B + \hat{\mathbb{1}}_S \otimes \hat{H}_B + \hat{H}_I(t) \tag{5.7}$$

where $\hat{H}_{S,B}$ are the Hamilton operators of the system or bath, respectively, $\hat{\mathbb{1}}$ is the identity operator and $\hat{H}_I(t)$ describes the interaction between system and bath. The dynamics of the density operator of the combined system, $\hat{\rho}(t)$, is determined by the Hamiltonian $\hat{H}(t)$. All observables refer (by definition of S) to the system S only, $\hat{A} = \hat{A} \otimes \hat{\mathbb{1}}_B$. The expectation value of $\hat{A}$ can thus be written as

$$\langle \hat{A} \rangle = \mathrm{Tr}\left\{\hat{A}\hat{\rho}\right\} = \mathrm{Tr}_S\left\{\hat{A}\hat{\rho}_S\right\} \tag{5.8}$$

where

$$\hat{\rho}_S = \mathrm{Tr}_B\left\{\hat{\rho}\right\} \tag{5.9}$$

is called the reduced density operator of the system with Tr_B being the partial trace over the

Hilbert space of the bath. The calculation of the partial trace can be understood as an averaging over the degrees of freedom which are not of interest or not accessible, and thus reflects our ignorance towards the state of the bath. As system and bath are generally entangled after some interaction time, tracing out the bath decreases the coherence of the system which can be interpreted as a loss of information. This process is also called decoherence.

When evaluating the partial trace of the Liouville-von Neumann equation from Eq. (5.6), we obtain a differential equation describing the time evolution of the open quantum system,

$$\frac{d}{dt}\hat{\rho}_{\mathrm{S}}(t) = -i\mathrm{Tr}_{\mathrm{B}}\left\{\left[\hat{H}(t),\,\hat{\rho}(t)\right]\right\}, \tag{5.10}$$

whose solution can be expressed equivalently to Eq. (5.1) as

$$\hat{\rho}_{\mathrm{S}}(t) = \mathrm{Tr}_{\mathrm{B}}\left\{\hat{U}(t,t_0)\hat{\rho}(t_0)\hat{U}^{\dagger}(t,t_0)\right\}, \tag{5.11}$$

where $\hat{U}(t,t_0)$ is the time-evolution operator of the full system $S+B$. The time-evolution of the system can be expressed in terms of the dynamical map $\hat{V}(t,t_0)$ as

$$\hat{\rho}_{\mathrm{S}}(t) = \hat{V}(t,t_0)\hat{\rho}_{\mathrm{S}}(t_0) \tag{5.12}$$

where $\hat{V}(t,t_0)$ lives in the Hilbert space of the system. In order to obtain a more explicit expression for the dynamical map, we first assume that S and B are initially separable and can be written as $\hat{\rho}(t_0) = \hat{\rho}_{\mathrm{S}}(t_0)\otimes\hat{\rho}_{\mathrm{B}}$. We further express the density matrix of the environment in its spectral decomposition

$$\hat{\rho}_{\mathrm{B}} = \sum_{\alpha}\lambda_{\alpha}\left|\phi_{\alpha}\right\rangle\!\left\langle\phi_{\alpha}\right|, \tag{5.13}$$

with $\{\ |\,\phi_{\alpha}\rangle\ \}$ being an orthonormal basis in the environment's Hilbert space. Inserting both into Eq. (5.11), we obtain

$$\begin{aligned}\hat{\rho}_{\mathrm{S}}(t) = \hat{V}(t,t_0)\hat{\rho}_{\mathrm{S}}(t_0) &= \sum_{\beta}\left\langle\phi_{\beta}\right|\hat{U}(t,t_0)\left(\hat{\rho}_{\mathrm{S}}(t_0)\otimes\hat{\rho}_{\mathrm{B}}\right)\hat{U}^{\dagger}(t,t_0)\left|\phi_{\beta}\right\rangle \\ &= \sum_{\alpha\beta}\lambda_{\alpha}\left\langle\phi_{\beta}\right|\hat{U}(t,t_0)\left|\phi_{\alpha}\right\rangle\hat{\rho}_{\mathrm{S}}(t_0)\left\langle\phi_{\alpha}\right|\hat{U}^{\dagger}(t,t_0)\left|\phi_{\beta}\right\rangle \\ &= \sum_{\alpha\beta}\hat{W}_{\alpha\beta}(t)\hat{\rho}_{\mathrm{S}}(t_0)\hat{W}_{\alpha\beta}{}^{\dagger}(t)\end{aligned} \tag{5.14}$$

with the Kraus operators

$$\hat{W}_{\alpha\beta}(t) = \sqrt{\lambda_{\alpha}}\left\langle\phi_{\beta}\right|\hat{U}(t,t_0)\left|\phi_{\alpha}\right\rangle, \tag{5.15}$$

which satisfy the condition $\sum_{\alpha\beta}\hat{W}_{\alpha\beta}{}^{\dagger}(t)\hat{W}_{\alpha\beta}(t) = \hat{\mathbb{1}}_{\mathrm{S}}$. Note that the sum representation in Eq. (5.14) is not unique, since the Kraus operators depend on the choice of basis. In the spe-

cial case with only one Kraus operator, we recover unitary dynamics. As the dynamical map can be expressed in terms of Kraus operators, it represents a convex-linear, completely positive and trace-preserving (CPT) quantum operation [14]. If t is not fixed, the dynamical map forms a one-parameter family $\{ \hat{V}(t, t_0) \mid t \geq t_0 \}$ (with $\hat{V}(t_0, t_0)$ being the identity) which describes the whole future of the system.

5.1.2 Quantum measurements

In the following, we show that the interaction of an open quantum system with its environment can equivalently be interpreted as the continuous observation of the system by the environment and vice versa. For this, we consider the indirect measurement of a quantum object via its interaction with another quantum system called the meter. In general, the advantage of such an indirect measurement is that it reduces the back-action of the measurement onto the quantum object – the most extreme case of back-action being the detection of the quantum object via a destructive measurement such as absorption or ionisation. An indirect measurement scheme can be divided into the following three steps (see also Fig. 5.1 (b)):

1. The meter is prepared in a known initial state $\hat{\rho}_{\mathrm{M}} \in \mathcal{H}_{\mathrm{M}}$ with $\mathcal{H}_{\mathrm{M}}$ being the Hilbert space of the meter. The quantum system is in an unknown state $\hat{\rho}_{\mathrm{S}}(0) \in \mathcal{H}_{\mathrm{S}}$ with $\mathcal{H}_{\mathrm{S}}$ being the Hilbert space of the system. The initial state of the combined system can then be written as $\hat{\rho}(0) = \hat{\rho}_{\mathrm{S}}(0) \otimes \hat{\rho}_{\mathrm{M}}$.

2. The system and the meter interact during a time τ under the action of the time-evolution operator $\hat{U}(\tau)$ corresponding to the dynamics induced by the interaction Hamiltonian $\hat{H}_{\mathrm{I}} \in \mathcal{H}_{\mathrm{S}} \otimes \mathcal{H}_{\mathrm{M}}$ (cf. Eq. (5.7) with changed subscript $B \to M$). The state of the full system after the interaction is

$$\hat{\rho}(\tau) = \hat{U}(\tau) \left(\hat{\rho}_{\mathrm{S}}(0) \otimes \hat{\rho}_{\mathrm{M}}\right) \hat{U}^{\dagger}(\tau). \tag{5.16}$$

3. The state of the meter is measured destructively via a classical detector.

In more detail, destructive measurement of meter proceeds as follows. We assume that the detector measures the meter observable

$$\hat{\mathcal{R}} = \sum_{\beta} r_{\beta} \hat{\Pi}_{\beta} \tag{5.17}$$

with $\hat{\mathcal{R}} \in \mathcal{H}_{\mathrm{M}}$ and where r_β are the eigenvalues and $\hat{\Pi}_\beta = |\varphi_\beta\rangle\langle\varphi_\beta|$ the projectors onto the eigenstates $|\varphi_\beta\rangle$. The probability to measure the outcome r_β can be calculated using Eq. (5.8) to

$$P(\beta) = \mathrm{Tr}\left\{\hat{\Pi}_\beta \hat{\rho}(\tau)\right\}. \tag{5.18}$$

The probabilities are normalised to one, $\sum_\beta P(\beta) = 1$. The state of the system after the measurement of the meter is

$$\hat{\rho}'_{\mathrm{S},\beta}(\tau) = P(\beta)^{-1} \langle\varphi_\beta|\hat{\rho}(\tau)|\varphi_\beta\rangle \,, \tag{5.19}$$

with $\hat{\rho}'_{\mathrm{S},\beta}(\tau) \in \mathcal{H}_\mathrm{S}$. If the measurement outcome is not recorded and the sub-ensembles are remixed afterwards, the measurement is called non-selective and the post-measurement state can be written as

$$\hat{\rho}'_\mathrm{S}(\tau) = \sum_\beta P(\beta)\hat{\rho}'_{\mathrm{S},\beta}(\tau) = \sum_\beta \langle\varphi_\beta|\hat{\rho}(\tau)|\varphi_\beta\rangle \,. \tag{5.20}$$

If we now insert the time-evolved state from Eq. (5.16) and express the state of the meter in its spectral decomposition (compare Eq. (5.13)), we arrive at

$$\begin{aligned}
\hat{\rho}'_\mathrm{S}(\tau) &= \sum_\beta \langle\varphi_\beta|\hat{U}(\tau)\,(\hat{\rho}_\mathrm{S}(0)\otimes\hat{\rho}_\mathrm{M})\,\hat{U}^\dagger(\tau)|\varphi_\beta\rangle \\
&= \sum_{\alpha\beta} \lambda_\alpha \langle\varphi_\beta|\hat{U}(\tau)|\phi_\alpha\rangle\,\hat{\rho}_\mathrm{S}(0)\,\langle\phi_\alpha|\hat{U}^\dagger(\tau)|\varphi_\beta\rangle \\
&= \sum_{\alpha\beta} \Omega_{\alpha\beta}\hat{\rho}_\mathrm{S}(0)\Omega_{\alpha\beta}{}^\dagger
\end{aligned} \tag{5.21}$$

with the measurement operators

$$\Omega_{\alpha\beta} = \sqrt{\lambda_\alpha}\,\langle\varphi_\beta|\hat{U}(\tau)|\phi_\alpha\rangle \,. \tag{5.22}$$

The measurement operators live in the Hilbert space of the system, $\Omega_{\alpha\beta} \in \mathcal{H}_\mathrm{S}$, and describe the change of the system's state induced by measuring the meter in state $|\varphi_\beta\rangle$. If the meter is in a pure state, $\hat{\rho}_\mathrm{B} = |\phi\rangle\langle\phi|$, the index α vanishes and the measurement operators simplify to $\Omega_\beta = \langle\varphi_\beta|\hat{U}(\tau)|\phi\rangle$. Note the striking equivalence between indirect measurements and the theory of open quantum systems when comparing the measurement operators from Eq. (5.22) to the Kraus operators in Eq. (5.15). We can conclude that the meter can equally be interpreted as an environment observing the system as depicted in panels (a) and (b) of Fig. 5.1.

Before continuing the description of open quantum systems, we discuss two special cases of measurements. The first is the so-called quantum non-demolition (QND) measurement [128]. As mentioned above, quantum measurement usually cause a significant back-action on the measured system which, in the worst case, demolishes the system. The basic idea of a QND measurement is to avoid demolition but there are several ways of defining it in theoretical terms. The easiest picture is that a QND measurement yields one of the outcomes r_{β_0} with probability $P(\beta_0)$ (cf. Eq. (5.18)), and after the measurement the system is in the state $|\psi_{\beta_0}\rangle$. The meter thus does not add any perturbation and several repetitions of the same measurement yield the same outcome. A sufficient condition for a QND measurement is that the observable $\hat{\mathcal{R}}$ commutes with the time-evolution $\hat{U}$.

For the second scenario, we consider a series of direct, ideal and instantaneous measurements. Two measurements are separated by the time interval τ and if τ goes to zero, it is called a continuous measurement. We moreover assume the system to be initially in an eigenstate of the measurement operator, i.e. $|\psi(0)\rangle = |\psi_0\rangle$. In-between of the measurements, the dynamics of the system is given by the time-evolution operator $\hat{U}(\tau)$. For small τ, it can be expanded as

$$\hat{U}(\tau) = \hat{\mathbb{1}} - i\hat{H}\tau - \frac{1}{2}\hat{H}^2\tau - O(\tau^3). \tag{5.23}$$

After the first measurement, the probability to measure the system in its initial state is

$$p_0(\tau) = |\langle\psi_0|\hat{U}(\tau)\psi_0\rangle|^2 \approx 1 - (\Delta E_0)^2\tau^2 \tag{5.24}$$

with the energy uncertainty $(\Delta E_0)^2 = \langle\psi_0|\hat{H}^2|\psi_0\rangle - \langle\psi_0|\hat{H}|\psi_0\rangle^2$. After $N = T/\tau$ measurements, the probability to find the state in the initial state is

$$p_0(T) = \left(1 - (\Delta E_0)^2\frac{\tau T}{N}\right)^N \approx \exp\left(-(\Delta E_0)^2\tau T\right). \tag{5.25}$$

In the limiting case of continuous measurements ($\tau \to 0$), the probability to keep the system in the initial state is one, $p_0(T) \to 1$. This effect is called the quantum Zeno effect (QZE) in reference to the arrow paradox ("A watched arrow does not move.") by the antique philosopher Zeno of Elea. The fundamental reason for this is that, for small times τ, the state collapse due to the measurements occurs on a faster time scale than transitions to other states. This effect can be generalised to measurements of states other than the initial state. In this case, transitions to the measured states are forbidden, which effectively builds up a barrier in the Hilbert space. The dynamics are therefore confined to a subspace of the full Hilbert space, called the Zeno subspace. This effect is referred to as quantum Zeno dynamics (QZD) [129, 130, 131] and it can be used to control the dynamics of a quantum system as discussed in more detail in Sec. 5.2.

5.1.3 The Lindblad master equation

The Kraus representation from Eq. (5.14) is not always the most suitable form to describe the dynamics of an open quantum systems. In fact, it is not always possible to evaluate the Kraus operators in Eq. (5.15) explicitly. Instead, it often proves to be more convenient to describe the dynamics by a Hamiltonian which determines the time evolution of the system via the Schrödinger or Liouville-von Neumann equation in Eq. (5.5). In the following, we outline the derivation of a differential equation which describes the dynamics of an open quantum system equivalently to the Liouville-von Neumann equation for closed systems under certain approximations.

We sketch the derivation from a microscopic model as described in more detail e.g. in [33]. The starting point is the Hamiltonian of system and bath, $S + B$, as given in Eq. (5.7). First, this Hamiltonian is inserted into the Liouville-von Neumann equation of Eq. (5.5) and the bath

degrees of freedom are traced out. The first approximation, called the Born approximation, is to assume that the coupling between the system and bath is weak. As a result, the effect of the interaction onto the state of the bath $\hat{\rho}_{\mathrm{B}}$ is negligible and the full density matrix may be written as $\hat{\rho}(t) = \hat{\rho}_{\mathrm{S}}(t) \otimes \hat{\rho}_{\mathrm{B}}$ at all times t. In the second approximation, the Markov approximation, we assume that the time evolution of the system only depends on the present state $\hat{\rho}_{\mathrm{S}}(t)$ at all times. Another way of phrasing this is that memory effects of the bath are neglected. The result of this approximation is a time-local equation. It is important to note that these approximations, together named the Born-Markov-approximation, do not imply that the state of the bath was constant. It rather means that the time scale τ_B over which the bath correlation decays is much faster the timescale τ_R on which the system changes appreciably, i.e. $\tau_B \ll \tau_R$. We describe the dynamics on a coarse-grained time scale τ_R which does not allow to resolve the dynamics on a timescale τ_B. These approximations alone, however, do not guarantee that the resulting equation defines the generator of a dynamical semigroup. The final rotating wave approximation is used to average over rapidly oscillating terms. If these oscillations, which describe the high frequency components of the intrinsic evolution of the system, occur on a timescale τ_S which is much faster than τ_R, i.e. if $\tau_S \ll \tau_R$, they can can be neglected. Finally, we arrive at the so-called Gorini-Kossakowski-Sudarshan-Lindblad equation,

$$\frac{d}{dt}\hat{\rho}_{\mathrm{S}}(t) = -i\left[\hat{H},\, \hat{\rho}_{\mathrm{S}}(t)\right] + \sum_{k=1}^{N^2-1} \gamma_k \left(\hat{A}_{\mathrm{k}} \hat{\rho}_{\mathrm{S}}(t) \hat{A}_{\mathrm{k}}^{\dagger} - \frac{1}{2}\left\{ \hat{A}_{\mathrm{k}}^{\dagger}\hat{A}_{\mathrm{k}},\, \hat{\rho}_{\mathrm{S}}(t) \right\} \right), \tag{5.26}$$

which is the most general form of describing the dynamics of a Markovian open quantum system. The commutator represents the unitary part of the evolution equivalent to the Liouville-von Neumann equation Eq. (5.5). The right-hand side is called the dissipator, since it describes the effect of the environment on the system through the so-called Lindblad operators $\hat{A}_{\mathrm{k}}$. The non-negative quantities γ_k are the corresponding decay rates indicating the strength of the dissipation. The explicit form of the decay rates and Lindblad operators gives information on the kind of dissipation that occurs.

The explicit form of the Lindblad operators give further insight into the decay channels induced by the interaction of the system with the environment. If we consider for simplicity a two-level system with the states $|0\rangle$ and $|1\rangle$, a typical source of noise is the population relaxation from the excited to the ground state, $|1\rangle \to |0\rangle$. This can be interpreted as energy draining from the system to the bath and the corresponding Lindblad operator can be written as $\hat{A}_1 = |1\rangle\langle 0|$. A second example is the pure dephasing of the system. In this case, the coherence of the state decays over time and the Lindblad operator could be written as $\hat{A}_2 = |1\rangle\langle 1|$. The energy of the system is conserved during pure dephasing, since system and bath do not exchange energy.

In many cases, one consequence of dephasing is that a quantum system loses purity (as defined in Eq. (5.4)). If the system is initially in a superposition state, dephasing destroys coherence and mixes the state. However, this is not necessarily the case. If the two-level system is initially

in the ground state, $|0\rangle$, dephasing under the Lindblad operator $\hat{A}_2$ does not have any effect on the state. On the other hand, the superposition state $|\psi^+\rangle = \frac{1}{\sqrt{2}}(|0\rangle + |1\rangle)$ is transformed into an incoherent mixture of $|0\rangle$ and $|1\rangle$. In order to gauge the influence of the environment on the system, it is therefore useful to define a measure for the degree of mixing of a quantum state. To this end, we define the von Neumann entropy as the quantum analogue of the classical Shannon entropy,

$$S(\hat{\rho}) = -\mathrm{Tr}\left\{\hat{\rho}\ln\hat{\rho}\right\} \tag{5.27}$$

with $\ln = \log_2$. If furthermore λ_α denote the eigenvalues of $\hat{\rho}$, the von Neumann entropy can simply be calculated via

$$S(\hat{\rho}) = -\sum_\alpha \lambda_\alpha \ln \lambda_\alpha. \tag{5.28}$$

S is invariant under unitary operations and therefore changes under dissipative dynamics or measurements. If and only if $\hat{\rho}$ represents a pure state, $S = 0$. If $\hat{\rho}$ is a completely mixed state, on the other hand, S takes its maximal value of $\ln N$ with N being the dimension of the system. Given the example of a two-level system above, the superposition $|\psi^+\rangle$ has a vanishing entropy, while the entropy of the mixed state after dephasing increased to the maximal value $S = \ln 2$.

In practice, the calculation of the von Neumann entropy requires the diagonalisation of the density matrix. A measure which is easier to calculate is the so-called linear entropy. If we expand the von Neumann entropy to first order around a pure state, we arrive at

$$S_L = 1 - \gamma \tag{5.29}$$

where γ is the purity of the state. It is a lower approximation to the von Neumann entropy. It can easily be seen that the linear entropy can take values between $0 \leq S_L \leq 1 - \frac{1}{N}$. If and only if the state is pure, $\gamma = 1$, the linear entropy is minimal, $S_L = 0$. A completely mixed state with $\gamma = \frac{1}{N}$ has maximal linear entropy $1 - \frac{1}{N}$ which, as expected, is smaller than $S_{\max} = \ln N$ for all $N > 1$.

5.1.4 Non-Markovian dynamics

In realistic physical systems, the assumptions made during the derivation of the Lindblad master equation are often violated. Most importantly, the Markovian approximation, which assumes a memory-less environment, does not hold true in many cases. Only if the bath is very large or the coupling is weak can memory effects be neglected. If not, the state of the bath is changed considerably due to the interaction with the system and the Markov approximation breaks down. The main consequence of non-Markovian dynamics is that the evolution of the reduced system does not only depend on the current state $\hat{\rho}_\mathrm{S}(t)$ but also on earlier times. In the following, we discuss dynamics beyond the Markov approximation in more detail and discuss possible measures of non-Markovianity.

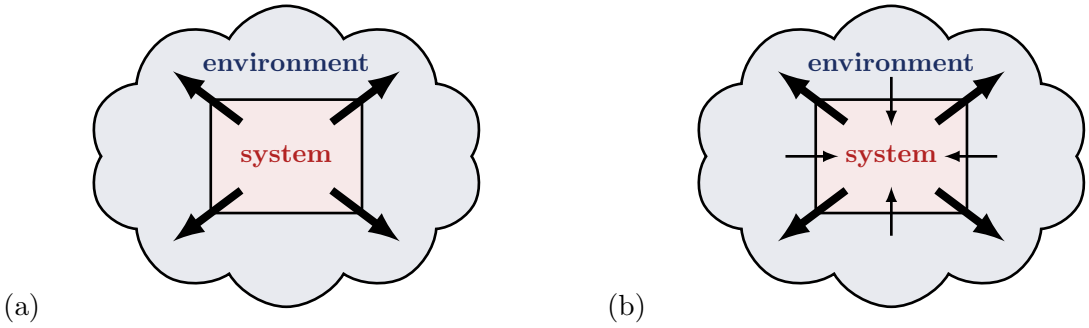

Figure 5.2: Sketch of the information flow (black arrows) in a Markovian (a) and non-Markovian (b) open quantum system.

One major difficulty when dealing with non-Markovian dynamics is the lack of a unique definition of non-Markovianity in quantum systems in literature [119, 35]. The terms Markovianity and non-Markovianity originate from well-defined classical stochastic processes. In classical terms, a stochastic process is called Markovian if the probability of a random variable X to take the value x_n at time t_n provided it took the value x_{n-1} at time t_{n-1} is uniquely determined and not affected by values of X at earlier times t_i with $i < n-1$. This definition can be interpreted as the already mentioned memoryless evolution. The problem with extending this definition to the quantum regime is that n-point probabilities always depend on the particular choice of the measurement scheme [35]. In the worst case, the measurement completely destroys system-environment correlations and therefore strongly influences the subsequent dynamics. The characterisation and quantification of memory effects should instead be independent of the measurement scheme and be based on the properties of the open systems density matrix instead.

In the following, we present one such approach to quantify non-Markovianity based on the notion of memory effects and the information flow between the system and environment [35], see Fig. 5.2. While in a Markovian process, the information always flows from the system to the bath (a), in a non-Markovian process, the information flows in both directions (b). Alternatively, this observation can be phrased in terms of the distinguishability between two quantum states: While a Markovian process tends to continuously decrease the distinguishability between any two states, a non-Markovian process could increase it. To construct a measure for non-Markovianity based on this property, it is first necessary to define a measure for the distance between two quantum states. One such measure is the trace distance,

$$\mathcal{D}\left(\hat{\rho}_1, \hat{\rho}_2\right) = \frac{1}{2}\,\mathrm{Tr}|\hat{\rho}_1 - \hat{\rho}_2|, \tag{5.30}$$

with $|\hat{A}| = \sqrt{\hat{A}^\dagger \hat{A}}$. The trace distance is a metric on the space of density matrices and can be used as a quantifier for the distinguishability of quantum states. Furthermore, it has the important

feature that all CPT maps $\hat{V}$ are contractions for this metric such that

$$\mathcal{D}\left(\hat{V}\hat{\rho}_1, \hat{V}\hat{\rho}_2\right) \leq \mathcal{D}\left(\hat{\rho}_1, \hat{\rho}_2\right). \tag{5.31}$$

A CPT map (such as the Lindblad master equation from Eq. (5.26)) can therefore never increase the distinguishability between two states. With

$$\sigma(t, \hat{\rho}_{1,2}(0)) = \frac{d}{dt}\mathcal{D}\left(\hat{\rho}_1(t), \hat{\rho}_2(t)\right) \tag{5.32}$$

being the rate of change of the trace distance, we can write this observation as $\sigma \leq 0$ for all times and initial state pairs. By definition of Ref. [35], processes are called non-Markovian if there exists an initial state pair for which $\sigma > 0$ at a certain time.

Based on this definition, it is possible to define a measure for non-Markovianity as the integrated backflow of information,

$$\mathcal{N}_{\mathrm{BLP}} = \max_{\hat{\rho}_{1,2}(0)} \int_{\sigma>0} dt\, \sigma(t, \hat{\rho}_{1,2}(0)) \tag{5.33}$$

which is commonly referred to as the BLP measure in reference to the last names of the authors of Ref. [35]. Note that the integration is carried out over all time intervals where σ is positive, and the maximum is taken over all pairs of initial states. The state pair which optimises the time integral is called the optimal state pair. By construction, $\mathcal{N}_{\mathrm{BLP}}$ is vanishing for Markovian processes. However, there is no upper bound to the measure, since the revivals of the trace distance can in principle persist forever. The main obstacle in using the BLP measure is finding the optimal state pair, since it requires an optimisation over the full Hilbert space of the system. In simple cases, the optimal state pair can be determined analytically [132]. However, once the optimal state pair is known, evaluation of this measure requires comparatively little numerical effort, as only the optimal state pair has to be propagated once.

Apart from the BLP measure, there are several other approaches to define and quantify the degree of non-Markovianity in a system. For instance, the measure proposed in Ref. [133] is linked to the change in volume of physical states that are dynamically accessible to a system and provides a geometrical interpretation of non-Markovianity in terms of an increase of this volume. Another approach is based on maximally entangling the system with an ancillary system and measuring a possible increase in entanglement caused by non-Markovian dynamics [134]. A final example proposes the use of negative decoherence rates for characterising non-Markovian dynamics [135], since, in fact, it is possible to write any time-local master equation in Lindblad-like form. For non-Markovian processes, the decay rates can become negative which can be interpreted as a "recoherence" of the system due to the information backflow from the environment. However, note that not every non-Markovian process can be written in a Lindblad-like form. More general approaches of non-Markovian master equations involve, for instance a memory kernel which requires an integration over past times of the evolution [136, 137, 135].

5.2 Exploring the parameter landscape of the quantum simulator

We now suggest a quantum simulator that allows for the study of the role of memory effects in the dynamics of open quantum systems. A particular feature of our simulator is the ability to engineer both Markovian and non-Markovian dynamics by means of quantum measurements and the quantum Zeno dynamics induced by them. We first present the model of our quantum simulator which is based on a bipartite quantum system in Sec. 5.2.1. Our setup is heavily inspired by a cavity QED experiment at Laboratoire Kastler Brossel (LKB) at Collège de France, Paris, which considers the interaction between photons in a microwave (MW) cavity and circular Rydberg atoms [138, 139]. In cavity QED [9], the interaction between light and matter is studied by confining light in a reflective cavity. In the famous experiments of Serge Haroche and his group, the cavity is constructed of two superconducting mirrors between which microwave modes are formed. The light then interacts with Rydberg atoms which fly through the cavity. The quantum simulator thus highlights another application of Rydberg atoms for quantum technologies. However, our setup is more general and can be applied to varies bipartite and even unary systems, as addressed throughout the text. The subsequent section are dedicated to explore the tunability of the quantum simulator and investigate how the parameters of the quantum measurement affect the character of the engineered open quantum system. To this end, we derive a suitable measure for non-Markovianity in Sec. 5.2.2 and discuss how the dissipation and the non-Markovianity can be controlled in the simulator in Sec. 5.2.3. Afterwards, we discuss the Markovian limit and derive a master equation in Lindblad form in Sec. 5.2.4.

5.2.1 The model

We take the system to be a harmonic oscillator,

$$\hat{H}_{\mathrm{S}} = \sum_n \omega n \left|n\right\rangle \left\langle n\right| , \tag{5.34}$$

where we have set the vacuum energy to zero, see Fig. 5.3 (a). The eigenstates $|n\rangle$ of the harmonic oscillator are called the Fock states. In a cavity QED setup, the harmonic oscillator corresponds to a photonic mode in a MW cavity [9]. The system is further coupled to a meter which we model by a three-level system with states $|h\rangle$, $|g\rangle$, and $|e\rangle$,

$$\hat{H}_{\mathrm{M}} = \omega' \left|g\right\rangle \left\langle g\right| + \left(\omega + \omega'\right) \left|e\right\rangle \left\langle e\right| . \tag{5.35}$$

They can be identified with three neighbouring circular states of a Rydberg atom as $|49\mathrm{C}\rangle \equiv |h\rangle$, $|50\mathrm{C}\rangle \equiv |g\rangle$, and $|51\mathrm{C}\rangle \equiv |e\rangle$ which all lie in the MW regime. The energy of $|h\rangle$ is set to zero and we assume the $|g\rangle \leftrightarrow |e\rangle$ transition to be resonant with the system frequency ω, which can easily be achieved by tuning the resonance of the cavity mode. The $|h\rangle \leftrightarrow |g\rangle$ transition is then far off-resonant with $\omega \ll \omega'$ as given by the Rydberg formula in Eq. (2.5). Transitions to higher or lower circular states are sufficiently far detuned from all other transitions and can thus be neglected.

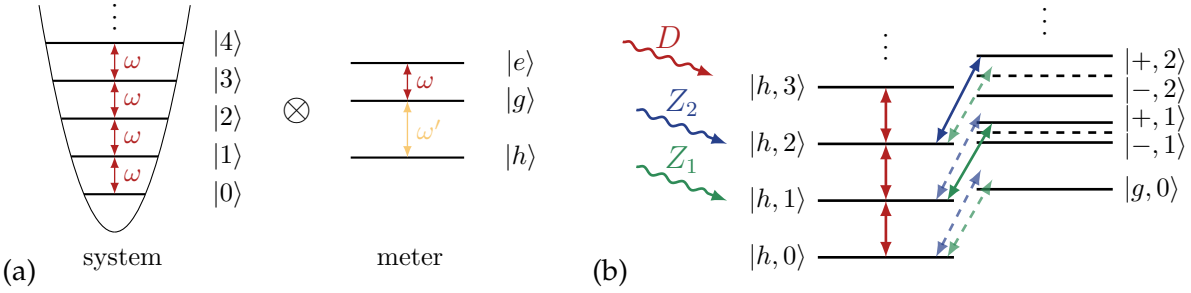

Figure 5.3: Energy level diagram of a bipartite system consisting of a harmonic oscillator and a few-level system in the bare (a) and dressed (b) basis. The arrows in (b) depict the three external fields: a drive D of the harmonic oscillator (red), and two Zeno pulses Z_1 (green) and Z_2 (blue) addressing the levels $|z = 1\rangle$ and $|z = 2\rangle$, respectively. Arrows with solid (light dashed) lines indicate (off-)resonant transitions.

The resulting interaction can be described by the Jaynes-Cummings model [9]. In the interaction picture with respect to the drift Hamiltonian, $\hat{H}_0 = \hat{H}_\mathrm{S} + \hat{H}_\mathrm{M}$, and after employing the rotating wave approximation, the interaction can be written as

$$\hat{H}_\mathrm{SM} = \frac{\Omega}{2}\left(\hat{\sigma}_{\text{-}}\hat{a}^\dagger + \hat{\sigma}_{+}\hat{a}\right) \tag{5.36}$$

with the Rabi frequency Ω, $\hat{\sigma}_{\text{-}} = |g\rangle\langle e| = \hat{\sigma}_{+}^\dagger$, and creation and annihilation operators $\hat{a}^{(\dagger)}$ for the harmonic oscillator. Note that the state $|h\rangle$ of the meter is decoupled from the harmonic oscillator. The eigenstates of $\hat{H}_\mathrm{SM}$ are the dressed states,

$$|g, 0\rangle\,, \quad |\pm, n\rangle = \frac{1}{\sqrt{2}}\left(|e, n-1\rangle \pm |g, n\rangle\right) \quad \text{for} \quad n \geq 1 \tag{5.37}$$

with eigenenergies (cf. Fig. 5.3 (b)),

$$E_n^\pm = \omega n \pm \frac{\Omega}{2}\sqrt{n}. \tag{5.38}$$

In addition to its coupling to the meter, the system is driven by a resonant classical source D with field strength α,

$$\hat{H}_\mathrm{D} = \alpha\hat{a}^\dagger + \alpha^*\hat{a}\,, \tag{5.39}$$

see red arrows in Fig. 5.3 (b). We assume the drive to be weak compared to the coupling with the meter, $\alpha \ll \Omega$, such that the system is only driven if the meter is in $|h\rangle$. In this limit, $\hat{H}_\mathrm{D}$ induces a displacement $\beta = -i\alpha\tau$ of the system's state,

$$\hat{U}_\mathrm{D}(\tau) = e^{-i\hat{H}_\mathrm{D}\tau} = e^{\beta\hat{a}^\dagger - \beta^*\hat{a}}. \tag{5.40}$$

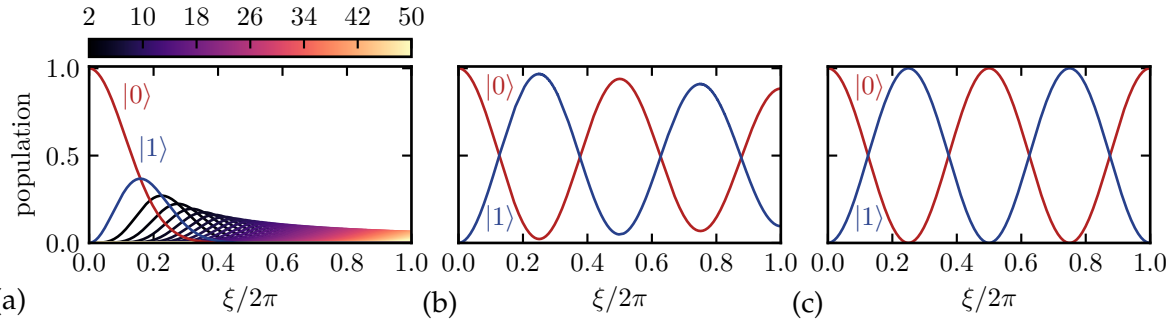

Figure 5.4: Dynamics in the harmonic oscillator with $\xi = -i\alpha t$, the initial state $|0\rangle$ and the Zeno level $z = 2$. (a) shows the free evolution without Zeno coupling or measurements. The colour bar indicates the number of the eigenstates $|n > 1\rangle$. (b+c) show the dynamics with measurements after a displacement of $\beta = 0.0126$ and a Rabi angle of $\phi_2 = \pi/2$ (b) and $\phi_2 = 2\pi$ (c). In both cases, the population is confined to the Zeno subspace $\{|0\rangle, |1\rangle\}$ and populations of higher states $|n > 1\rangle$ are not visible on this scale. The measurement induces a significant amount of dissipation in (b) while the subsystem is almost perfectly closed in (c).

Similarly, the total time evolution can be described using the rescaled coordinate $\xi = -i\alpha t$. Figure 5.4 (a) shows the dynamics of the harmonic oscillator when driven by the source D if the meter is in $|h\rangle$ (i.e. system and meter are decoupled).

A tunable source of dissipation is introduced by a series of indirect measurements of the system's state using identical meters (equivalently to Fig. 5.1 (b)). These measurements determine whether the system is in a specific Fock state $|z\rangle$, the 'Zeno level'. To this end, system and meter are coupled by a so-called Zeno pulse Z_z with coupling strength g_z which is resonant to the $|h, z\rangle \leftrightarrow |+, z\rangle$ transition,

$$\hat{H}_z = \frac{g_z}{2}\Big(|h, z\rangle \langle +, z| + |+, z\rangle \langle h, z| \Big), \tag{5.41}$$

where the subscript z indicates the Zeno level $|z\rangle$. The coupling is depicted in Fig. 5.3 (b) for the example of $z = 1$ (green) and $z = 2$ (blue). Z_z induces Rabi oscillations only if the system is in the Zeno level,

$$\hat{U}_{\mathrm{Z}}(\tau) = e^{-i\hat{H}_z\tau} = e^{\left(|h,z\rangle\langle +,z| + |+,z\rangle\langle h,z|\right)\frac{\phi_z}{2}}, \tag{5.42}$$

accumulating a Rabi angle $\phi_z = g_z\tau$ during the interaction time τ. As a result, there will only be population in the state $|+, z\rangle$ if there was population in $|z\rangle$ initially. A subsequent destructive measurement of the meter at time τ, corresponding to a partial trace over the meter, thus provides information on the population of $|z\rangle$. The system's state at the end of one time interval τ can be obtained in terms of the piecewise dynamics (cf. Eq. (5.11)),

$$\hat{\rho}_{\mathrm{S}}(t + \tau) = \mathrm{Tr}_{\mathrm{M}}\left\{ \hat{U}(\tau)\hat{\rho}(t)\hat{U}^{\dagger}(\tau) \right\} \tag{5.43}$$

with $\hat{U}(\tau) = e^{-i\left(\hat{H}_{\mathrm{D}}+\hat{H}_{\mathrm{SM}}+\hat{H}_{\mathrm{z}}\right)\tau}$. $\hat{\rho}$ and $\hat{\rho}_{\mathrm{S}}$ describe the state of the bipartite and reduced system, respectively. The sequence of coupling the system to a meter during time τ and performing a destructive measurement of the meter afterwards is repeated several times, with the new meter initially always in $|h\rangle$.

For small displacements of the system between two measurements, $|\beta| \ll 1$, the protocol gives rise to quantum Zeno dynamics (QZD, compare to Sec. 5.1.2). Hence, when choosing an initial state of the system below the Zeno level, $|n_0 < z\rangle$, the dynamics is confined to the Zeno subspace $\mathcal{H}_{\mathrm{z}} = \{|0\rangle, \ldots, |z-1\rangle\}$. The displacement β (due to the drive D) and the Rabi angle ϕ_z (due to the Zeno pulse Z_z) act as "knobs" to control the dynamics of the quantum simulator as shown for three exemplary cases in Fig. 5.4. Panel (a) shows the free evolution of the system when no Zeno pulses are employed, i.e. the system and meter stay uncoupled and the measurements of the meter has no effect on the system. In panels (b+c), the system and meter are coupled by a Zeno pulse with $\phi_2 = \pi/2$ and 2π, respectively. Measurements are performed after displacements of $\beta = 0.0126$. The quasi-continuous measurements induce QZD in both cases as can be seen clearly from the fact that no states higher than $|z = 1\rangle$ are being populated. The dynamics in (b) show strong signatures of dissipation due to the measurement as can be seen from the damped amplitude of the oscillation. The dynamics in (c), on the other hand, resemble those of a closed two-level system. These observations are discussed and explained more thoroughly in the following sections.

Before, we give some details on the numerical implementation of this model and the cavity QED experiment. All numerical calculations in this chapter were conducted with a truncated basis for the harmonic oscillator with $n_{\max}$ being large enough to avoid reflections on the upper end of the Hilbert space. Newton's method was used to perform time propagations (cf. Sec. 3.1.2). The values for the system parameters, such as the Rabi and transition frequencies, were chosen in agreement with cavity QED experiment proposed in Ref. [138]. In this experiment, the Rydberg atoms interact with the microwave cavity in an atomic fountain arrangement: the atoms are injected into the cavity vertically from underneath while they are accelerated downwards by their own gravity. The turning point of the atom's trajectory is adjusted to be in the centre of the cavity such that the interaction time between cavity and atom is sufficiently long to perform the experiment. Due to the cryostatic environment of the experiment and the long lifetime of circular states in Rydberg atoms, 'true' dissipation due to field energy damping or atomic relaxation is negligible on the relevant timescale. The atom is excited to the Rydberg regime when it is already located inside the cavity which marks the beginning of one sequence of the protocol. In order to specifically address a $|h, z\rangle \leftrightarrow |+, z\rangle$ transition using a Zeno pulse Z_z and distinguish it from the nearby $|h, z\rangle \leftrightarrow |-, z\rangle$ and $|h, z\rangle \leftrightarrow |-, z-1\rangle$ transitions, the duration Δt_Z of the pulse Z_z has to be long enough, namely $\Delta t_Z \gg 1/\left(\Omega|\sqrt{z+1} - \sqrt{z}|\right)$. The end of the experiment with total time T is triggered by ionising the atom within the cavity by field ionisation.

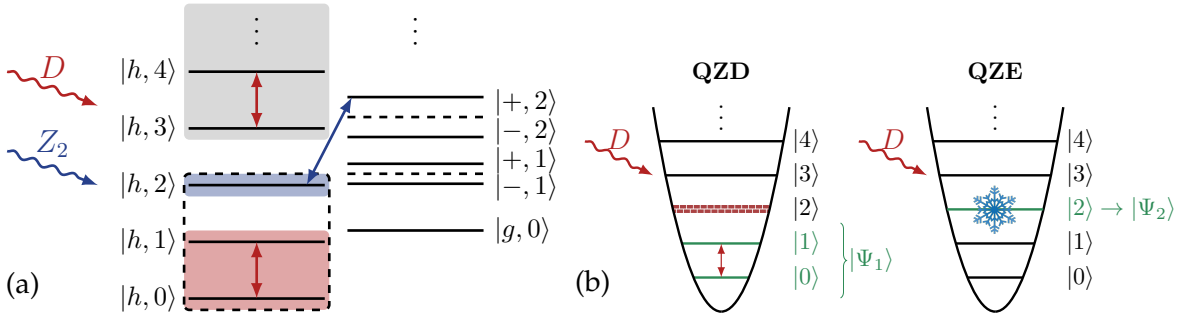

Figure 5.5: (a) Energy level diagram of the bipartite system indicating different subspaces: The Zeno subspace $\mathcal{H}_Z$ (red shaded), the Zeno level $|z=2\rangle$ (blue shaded), the extended Zeno subspace $\mathcal{H}_Z^+$ (black dashed box) and the subspace with purely unitary dynamics (grey shaded). (b) Illustration of the optimal state pair. In the Zeno limit, a state $|\Psi_1(0)\rangle = |\vartheta,\varphi\rangle$ within the Zeno subspace is confined by quantum Zeno dynamics (QZD). If the initial state is the one being measured, $|\Psi_2(0)\rangle = |z=2\rangle$, the state is frozen by the quantum Zeno effect (QZE).

5.2.2 Calculation of the non-Markovianity measure

In order to quantify the degree of non-Markovianity in the quantum simulator, we use the BLP measure, $\mathcal{N}_{\mathrm{BLP}}$, as introduced in Eq. (5.33). Evaluation of this measure requires comparatively little numerical effort, namely the propagation of only two well chosen initial states, which is crucial when considering the theoretically infinite dimensionality of the harmonic oscillator. Other measures mentioned in Sec. 5.1.4 either lead to qualitatively similar results (e.g. the geometrical measure from Ref. [133] when employing a truncated basis for the harmonic oscillator) or are not practical, since they increase the dimension of the Hilbert space even further (e.g. the entanglement-based measure from Ref. [134] using ancillary systems). An obstacle for using the BLP measure is that it requires optimisation over the system Hilbert space in order to identify the optimal state pair $(\hat{\rho}_1(t), \hat{\rho}_2(t))$. On first glance, this seems difficult for the infinitely large Hilbert space of a harmonic oscillator. Nonetheless, the BLP measure turns out to be suitable in our case since we can reduce the size of the subspace in which we have to perform the optimisation significantly by using our knowledge about the tailored interaction of the harmonic oscillator and the meter.

The reduction of the system size goes as follows, cf. Fig. 5.5 (a). We know that the Zeno pulse only affects the Zeno level and the level below since the dressed state we couple to is $|+,z\rangle = \frac{1}{\sqrt{2}}(|e,z-1\rangle + |g,z\rangle)$. If the initial state is located within the Zeno subspace $\mathcal{H}_Z$, signatures of non-Markovianity can only arise from population in states within the extended Zeno subspace $\mathcal{H}_Z^+ = \{|0\rangle, \ldots, |z\rangle\}$, whereas the dynamics in the remaining Hilbert space are purely unitary. Numerical tests confirm this conjecture. It is thus sufficient to consider only the extended Zeno subspace for the optimisation.

The optimisation can be further simplified by considering properties of optimal state pairs for the BLP measure in general. The BLP measure is defined as the integral over all times where the

trace distance is increasing (cf. Eq. (5.33)), maximised over all initial state pairs. Vice versa, we can conclude that the optimal state pair shows revivals of the trace distance for the longest time with a maximal peak amplitude as compared to all other state pairs. Ideally, the states oscillate between being fully distinguishable, with $\mathcal{D} = 1$, and fully indistinguishable, with $\mathcal{D} = 0$. Thus, the dynamics of the two states which form the optimal pair should be as different from each other as possible. In a qubit this can be realised by choosing the initial state pair to be orthogonal and on the boundary of the space of physical states [132]. In our model, the Zeno level and a state within the Zeno subspace, as shown in Fig. 5.5 (b), form such a pair. The former is subject to the quantum Zeno effect (QZE) which means that the population in the Zeno level is frozen. For the latter, quantum Zeno dynamics (QZD) are induced and the population never leaves the Zeno subspace. Thus, in an ideal Zeno situation ($\tau \to 0$), the trace distance of this pair of initial states is constant with $\mathcal{D} = 1$, i.e. it stays distinguishable forever. However, in a realistic system, the measurements leading to Zeno dynamics are not continuous but separated by short time intervals $\tau > 0$. During that time, the Zeno pulse introduces Rabi oscillations on the $|h, z\rangle \leftrightarrow |+, z\rangle$ transition (cf. Eq. (5.42)). The overlap between the two states varies with time, leading to oscillations of the trace distance which indicate information flow and non-Markovianity. In the following, we seek to calculate the time-dependent trace distance of such a state pair explicitly.

We start by describing the dynamics of the first state of the pair: a state in the Zeno subspace (left-hand panel in Fig. 5.5 (b)). In the Zeno limit, every state in the Zeno subspace is confined to it forever and is only driven coherently by the drive D (cf. Eq. (5.39)). In the special case of $z = 2$, an arbitrary state in the Zeno subspace can be parametrized by its Bloch angles,

$$|\vartheta, \varphi\rangle = \cos\left(\tfrac{\vartheta}{2}\right)|0\rangle + \sin\left(\tfrac{\vartheta}{2}\right) e^{i\varphi}|1\rangle \ , \tag{5.44}$$

and the unitary evolution induced by D takes the form

$$U_{z=2}(t) = e^{-i\left(\alpha|1\rangle\langle 0| + \alpha^*|0\rangle\langle 1|\right)t} = \cos(|\alpha|t)\begin{pmatrix} 1 & 0 \\ 0 & 1 \end{pmatrix} - i\sin(|\alpha|t)\begin{pmatrix} 0 & e^{-i\varphi_\alpha} \\ e^{i\varphi_\alpha} & 0 \end{pmatrix} \tag{5.45}$$

with $\alpha = |\alpha| e^{i\varphi_\alpha}$ being the amplitude of the field D. The eigenstates of this map are

$$|\vartheta = \tfrac{\pi}{2}, \varphi = \pm\varphi_\alpha\rangle = \frac{1}{\sqrt{2}}\left(|0\rangle + e^{\pm i\varphi_\alpha}|1\rangle\right) . \tag{5.46}$$

In the following, we choose α such that $-i\alpha T = 2\pi$ where T is the total duration of the protocol. We then obtain $\varphi_\alpha = \pi/2$ leading to $e^{\pm i\varphi_\alpha} = \pm i$.

The second state of the pair is the Zeno level, $|h, z\rangle$, and in the Zeno limit the Zeno pulse freezes the population in this state due to the QZE (right-hand panel in Fig. 5.5 (b)). On the timescale of the Zeno pulse, however, the pulse induces oscillations between the initial state and

the dressed state $|+, z\rangle$,

$$|\Psi_{|h,z\rangle}(t)\rangle = \cos\left(\frac{g_z t}{2}\right)|h, z\rangle + \sin\left(\frac{g_z t}{2}\right)|+, z\rangle \ , \tag{5.47}$$

while all other states $|h, n \neq z\rangle$ are unaffected by $\hat{H}_z$. The action of the drive D is negligible on the timescale τ since $\alpha \ll g_z$. For $g_z t = \pi$, the final state is the dressed state. At this point, the reduced density matrix of the system reads

$$\hat{\rho}_2\left(t = \frac{\pi}{g_z}\right) \equiv \hat{\rho}_2^{(\pi)} = \frac{1}{2}\Big(|z-1\rangle\langle z-1| + |z\rangle\langle z|\Big). \tag{5.48}$$

For $g_z t = 2\pi$, the population has oscillated back to the initial state.

We now consider the initial state pair $\{|\Psi_1(t=0)\rangle = |\vartheta, \varphi\rangle\,, |\Psi_2(t=0)\rangle = |2\rangle\}$ for the special case of a Rabi angle $\phi_2 = 2\pi$. In the beginning and end of each time interval τ, the state $|\Psi_2(t = n\tau)\rangle$ with n being an integer is in the Zeno level, the overlap between the two states is zero and the trace distance is one. No information is destroyed during the measurement at these points because the system and the meter are separable. In the middle of the interval, $|\Psi_2(n\tau + \tau/2)\rangle$ is in the state $\hat{\rho}_2^{(\pi)}$ which has the largest overlap with the level $|z-1\rangle$ that is possible when starting in the Zeno level. The trace distance thus oscillates quickly between 1 (at $t = n\tau$) and the lower envelope given by the trace distance of $|\Psi_1(t)\rangle = U_{z=2}(t)\,|\vartheta, \varphi\rangle$ evolving in the Zeno subspace and $|\Psi_2(t)\rangle$ being $\hat{\rho}_2^{(\pi)}$. If the Rabi angle is different from $\phi_2 = 2n\pi$, the system and meter are entangled at the time of the measurement. A measurement thus destroys coherence and decreases the trace distance. As a result, the integrated trace distance and hence the BLP measure are maximal for $\phi_2 = 2n\pi$ which is why we focus on this case.

To calculate the lower envelope trace distance (cf. Eq. (5.30)) we have to express both states in terms of density matrices. The density matrix of the state within the Zeno subspace is simply given by $\hat{\rho}_1(t) = |\Psi_1(t)\rangle\langle\Psi_1(t)|$ while we assume the second state to be in mixed state $\hat{\rho}_2^{(\pi)}$ (cf. Eq. (5.48)) all the time. Afterwards, we have to calculate the eigenvalues λ_i of the matrix $\hat{\rho}_{1-2}(t) = \hat{\rho}_1(t) - \hat{\rho}_2^{(\pi)}$. Using computer algebra and setting $\varphi_\alpha = \pi/2$, we obtain

$$\begin{aligned}
\lambda_1 &= -\frac{1}{2} \\
\lambda_{2,3} &= \frac{1}{4} \pm \frac{1}{4} i e^{-i\varphi} \Big\{ e^{2i\varphi}\big(4\sin(\theta)\cos(\varphi)\sin(2|\alpha|t) - 4\cos(\theta)\cos(2|\alpha|t) - 5\big) \Big\}^{1/2}
\end{aligned}$$

The envelope of the trace distance is then given by $\mathcal{D}\left(\hat{\rho}_1(t), \hat{\rho}_2(t)\right) = \frac{1}{2}\sum_{i=1}^{3}|\lambda_i(t)|$. The result is shown for the two extremal cases in Fig. 5.6 (a). If we choose $|\Psi_1\rangle$ to be one of the eigenstates of $U_{z=2}(t)$ (cf. Eq. (5.46)), the envelope of the trace distance is constant (dark blue line). If we choose $|\Psi_1\rangle = |\vartheta, \varphi = \{0, \pi\}\rangle$ such that it lies on the meridian of the Bloch sphere (dark red) the envelope of the trace distance undergoes slow oscillations due to the drive D (cf. Eq. (5.45)). The red curve in Fig. 5.6 (a) shows the case $|\Psi_1\rangle = |0\rangle$ where $\vartheta = 0$. A variation of ϑ simply shifts the curve on

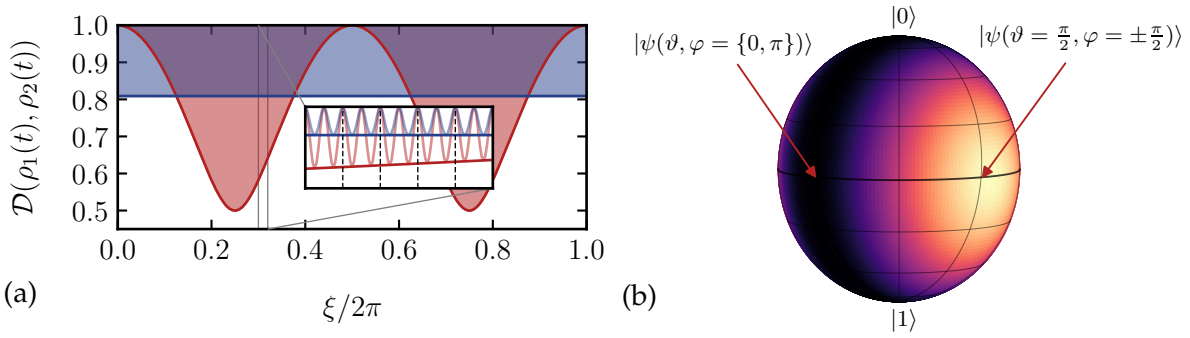

Figure 5.6: (a) Evolution of the trace distance for two different initial state pairs with Rabi angle $\phi_2 = 4\pi$ and a displacement $\beta = 0.025$ as a function of $\xi = -i\alpha t$. The state pairs are $|\Psi_1\rangle = |\vartheta = 0, \varphi = 0\rangle = |0\rangle$ (red) and $|\Psi_1\rangle = |\vartheta = \frac{\pi}{2}, \varphi = \frac{\pi}{2}\rangle = \frac{1}{\sqrt{2}}(|0\rangle + i\,|1\rangle)$ which is an eigenstate of $U_{z=2}(t)$ (blue), paired with the Zeno level $|\Psi_2\rangle = |2\rangle$. The dark lines show the result of the analytical calculation of the lower envelope, the light, fast oscillating lines show the numerical calculations. The inset shows the fast oscillation of the trace distance due to the Zeno pulse Z_2 acting on $|\Psi_2\rangle$. The vertical black dashed lines show the positions of the meter's measurement. (b) BLP measure $\mathcal{N}_{\text{BLP}}$ for different initial states $|\Psi_1\rangle = |\vartheta, \varphi\rangle$ on the Bloch sphere spanned by the Zeno subspace $\{|0\rangle, |1\rangle\}$. The second state of the state pair is the Zeno level $|\Psi_2\rangle = |2\rangle$ outside of this subspace. Yellow indicates the smallest, black the highest value. The parameters are $\beta = 0.025$ and $\phi_2 = 4\pi$. The data was obtained numerically but the analytical expression in Eq. (5.50) gives the same results.

the time axis. This is because the drive D induces a rotation around the y-axis for our choice of $\varphi_\alpha = \pi/2$ and every state that lies initially on that meridian stays on it. In more general terms, the rotation axis $\vec{n}_\alpha$ depends on the phase of the complex amplitude α as

$$\vec{n}_\alpha = (\cos\varphi_\alpha,\, \sin\varphi_\alpha,\, 0) = (\operatorname{Re}\alpha,\, \operatorname{Im}\alpha,\, 0)\,/|\alpha|. \tag{5.49}$$

The eigenstates are given by Eq. (5.46) and the states with $\varphi = \pm\varphi_\alpha + \pi/2$ evolves on a meridian through the Bloch sphere's poles.

The value of the BLP measure is now connected to the area enclosed by the lower envelope (dark line) and the $\mathcal{D} = 1$ line in Fig. 5.6 (a). The trace distance oscillates between the lower envelope and 1 every time a 2π pulse is completed on the $|h, 2\rangle \leftrightarrow |+, 2\rangle$ transition (see light lines indicating the numerical calculations). Since the BLP measure sums up all the areas where the trace distance is increasing, we have to sum n peaks per time τ for $\phi_2 = 2n\pi$ (see inset of Fig. 5.6 (a), there are $n = \phi_2/2\pi = 2$ peaks between two measurements). This leads to the final expression

$$\mathcal{N}_{\text{BLP}} = \sum_{j=1}^{nN} \left(1 - \mathcal{D}\left(\frac{j\tau}{n}\right)\right) \tag{5.50}$$

where $T = N\tau$. Note the remarkable agreement of the analytical envelope and the numerical

calculations in Fig. 5.6 (a) albeit the assumption of a perfect Zeno confinement. Finally, Fig. 5.6 (b) shows the BLP measure for different initial states $|\Psi_1\rangle$. The BLP measure takes a minimum for the eigenstates of $U_{z=2}(t)$ and a maximum for the states on the meridian with $\varphi = \{0, \pi\}$. This is because the blue area in Fig. 5.6 (a) which describes the evolution of the trace distance for the eigenstates is smaller than the red which describes the states on the meridian.

Summing up, the optimal state pair which leads to the maximal value of the BLP measure was found to be composed of the state $|\Psi_1\rangle = |\vartheta, \varphi = \pm\varphi_\alpha + \pi/2\rangle$ which lives in the Zeno subspace spanned by $\{|0\rangle, |1\rangle\}$ and depends on the phase φ_α of the complex amplitude α of the drive D, and the Zeno level $|z = 2\rangle$. For our choice of α, the optimal state pair is given by

$$|\Psi_1(\vartheta)\rangle = \cos\left(\tfrac{\vartheta}{2}\right)|0\rangle + \sin\left(\tfrac{\vartheta}{2}\right)|1\rangle\,, \quad |\Psi_2\rangle = |2\rangle \tag{5.51}$$

for all $\vartheta \in [0, 2\pi)$, and we take $\vartheta = 0$ in the following. Note that the calculations can be generalised to larger values of $z > 2$. The larger dimension of $U_z(t)$ (cf. Eq. (5.45)) turns the equations more complicated but the central results remain unchanged.

5.2.3 Tuning dissipation or non-Markovianity

We now discuss the quantum simulator subject to the drive D (which controls the displacement β) and one Zeno pulse $Z_{z=2}$ addressing the Zeno level $|z = 2\rangle$ (which controls the Rabi angle $\phi_{z=2}$). We choose the overall protocol duration T such that $-i\alpha T = 2\pi$ and we take the initial state of the harmonic oscillator to be the vacuum, $|n_0 = 0\rangle$. To quantify the amount of dissipation, we use the linear entropy S_L as defined in Eq. (5.29). For the following discussion and explanation of the system's dynamics it also proved to be useful to define a measure for the infidelity of the QZD. To this end, we introduce the population $P_{\bar{Z}}$ that has escaped from the Zeno subspace,

$$P_{\bar{Z}} = \sum_{n=z}^{\infty} \langle n|\hat{\rho}_{\mathrm{S}}(T)|n\rangle\,. \tag{5.52}$$

Figure 5.7 shows these two quantities together with the non-Markovianity measure for different values of the displacement and the Rabi angle. The figure shows that an arbitrary degree of dissipation S_L can be engineered by tuning β and ϕ_2 (panel b). Moreover, we observe a clear correlation between the dissipation and the infidelity of the QZD, $P_{\bar{Z}}$ (panel a). In particular, strong dissipation can be realised by a small ϕ_2 where the population leaves the Zeno subspace. Only in this case, the Zeno level $|2\rangle$, which is the only state being subject to dissipation due to the Zeno coupling, is being populated. Hence, it is constructive to understand the mechanisms leading to Zeno confinement in more detail, as there is more than one.

(i) QZD describes the effect of confining the dynamics of a system to a tailored subspace by frequent measurements. The dynamics shown in Fig. 5.7 agrees with this intuitive picture since the Zeno infidelity $P_{\bar{Z}}$ vanishes as the displacement β (which is proportional to the time between two measurements) goes to zero.

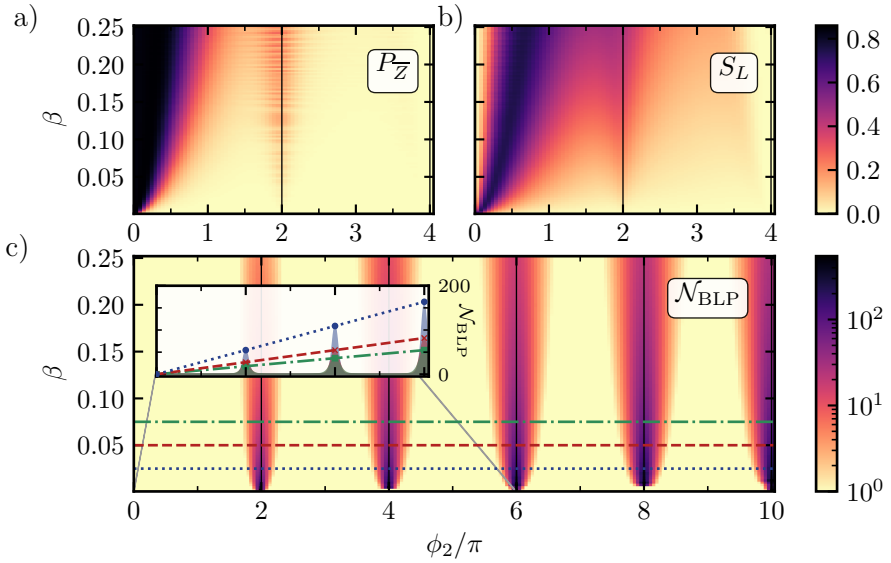

Figure 5.7: Infidelity $P_{\bar{Z}}$ of the quantum Zeno dynamics (a), dissipation S_L (b), and non-Markovianity measure $\mathcal{N}_{\mathrm{BLP}}$ (c) as a function of the displacement β due to the drive D and the Rabi angle ϕ_2 accumulated due to the Zeno pulse Z_2. Inset: $\mathcal{N}_{\mathrm{BLP}}$ as a function of ϕ_2 for $\beta = 0.025$ (blue dotted, circles, highest peaks), 0.050 (red dashed, crosses) and 0.075 (green dash-dotted, squares, smallest peaks) with linearly increasing peak heights. The data points which generate the linear functions were calculated analytically.

(ii) QZD can not only be induced by frequent measurements but also by strongly coupling the system to a meter. The latter can be interpreted as a "persuading gaze" [140] of the meter. In fact, the two cases are formally equivalent in the limit of a fast repetition rate and strong coupling [140]. In our case, the coupling strength between the harmonic oscillator and the three-level system is given by the field strength of the Zeno pulse, $g_z = \phi_z/\tau$, which is proportional to ϕ_z. Thus, the quality of the Zeno confinement is very good for large values of the Rabi angle ϕ_z even if β is large. For Rabi angles $\phi_z > 4\pi$, $P_{\bar{Z}}$ and S_L are vanishingly small which is why this parameter range is omitted in Fig. 5.7 (a) and (b).

(iii) The coupling between the Zeno level and the dressed state $|+, z\rangle$ induces a decay of the Zeno level's population to the level below, that is, back into the Zeno subspace. More explicitly, the Hamiltonian $\hat{H}_z$ (cf. Eq. (5.41)) induces Rabi oscillations as shown in Eq. (5.47). When performing a Zeno pulse with Rabi angle $\phi_z = g_z\tau \neq 2n\pi$, a fraction of $\sin^2\left(\frac{\phi_z}{2}\right)$ of the population that has been in the state $|h, z\rangle$ ends up in the state $|+, z\rangle$. According to the definition of the dressed states, half of the system is in the state $|z-1\rangle$ here, i.e. back in the Zeno subspace, which enhances the Zeno confinement. As a consequence, if the initial state was lying above the Zeno level, $n_0 > z$, the Zeno pulse has to be changed to be resonant to the $|h, z\rangle \leftrightarrow |+, z+1\rangle$ transition to induce the same effect. In this case, the population is "confined" to the Zeno subspace $\mathcal{H}_z = \{|z+1\rangle, \dots\}$, meaning it is excluded from the subspace with $n \leq z$.

(iv) For $\pi < \phi_z < 2\pi$, the phase of the $|h, z\rangle$ contribution in Eq. (5.47) is negative due to the cosine. This leads to an inversion of the dynamics back into the Zeno subspace which improves the QZD additionally.

Note that there is one exception to the correlation between dissipation S_L and the Zeno infidelity $P_{\bar{Z}}$. For $\phi_2 \to 0$, there is no dissipation even though the population leaves the Zeno subspace. In this case, the coupling between system and meter vanishes and the system evolves freely without dissipation.

The signatures of non-Markovianity are strongest for Rabi angles $\phi_2 = 2n\pi$ with n being an integer, cf. Fig. 5.7 (c). This is because for small β and every choice of $|z\rangle$, a pulse Z_z with $\phi_z = 2n\pi$ corresponds to the map $|h, z\rangle \mapsto (-1)^n |h, z\rangle$, i.e. the pulse changes only the phase of the Zeno level and no entanglement between system and meter is generated. In other words, this choice of ϕ_z results in a quantum non-demolition (QND) measurement (cf. Sec. 5.1.2) preserving the information of the system's state. In this case, the value of the non-Markovianity measure can be calculated analytically as shown in the previous section. The agreement between the analytical and the numerical calculation is remarkable, as can be seen by the data points in the inset of Fig. 5.7. They reveal a linear increase of the non-Markovianity measure with Rabi angle ϕ_2 for a given displacement β. For constant ϕ_2, in turn, the non-Markovianity measure decreases as β grows larger because the number of measurements $N = T/\tau \propto T/\beta$, and hence the number of $2n\pi$-pulses for fixed T decreases. If N is fixed instead of T, the value of the non-Markovian measure is roughly constant for a fixed value of ϕ_2.

In summary, we are able to induce both dissipation and non-Markovian dynamics in the proposed quantum simulator. In particular, a Zeno pulse with small Rabi angles $\phi_z \lesssim \pi$ induces strong dissipation due to the entanglement between the system and the meter at the time of the measurement. On the other hand, large memory effects are obtained with a Rabi angle $\phi_z = 2n\pi$ because system and meter remain separable at the time of the measurement and the distinguishability oscillates between 0 and 1 due to the strong coupling between the two subsystems. We next turn to the analysis of the Markovian regime and derive a suitable master equation of Lindblad form in the next section. Afterwards, we unite dissipation and non-Markovianity and enable independent tunability of both by combining two Zeno pulses as discussed in Sec. 5.3.

5.2.4 Realising the Markovian limit

For arbitrary values of z (i.e. lifting the assumption of $z = 2$) and Rabi angles $\phi_z \neq 2n\pi$, the system and meter are entangled at the end of each time interval τ. Measurement of the meter then erases information, resulting in less distinguishable states, such that the system dynamics becomes Markovian on the coarse-grained timescale τ. As explained in Sec. 5.1.3, the most general way to describe the dynamics of a Markovian open quantum system is by means of a Lindblad equation (cf. Eq. (5.26)). The explicit form of the decay rates and Lindblad operators gives information on the kind of dissipation occurring in an open quantum system and it provides us with

a recipe on how to control the open quantum system simulator. In the following, we derive the master equation in Lindblad form for the quantum simulator.

We start from the piecewise dynamics of Eq. (5.43) which describes the reduced state of the system after interacting with a meter during time τ. We assume to employ a single Zeno pulse Z_z which acts on an arbitrary Zeno level $|z\rangle$. The first step is to evaluate the partial trace and to derive the Kraus representation of the dynamical map (cf. Eq. (5.15) and Eq. (5.22)). To this end, we expand the time evolution operator $\hat{U}(dt)$ using the Baker-Campbell-Hausdorff formula up to first order,

$$\hat{U}(dt) = e^{-i\left(\hat{H}_{\mathrm{D}}+\hat{H}_{\mathrm{SM}}+\hat{H}_{\mathrm{z}}\right)dt} \approx e^{-i\hat{H}_{\mathrm{D}}dt}e^{-i\hat{H}_{\mathrm{SM}}dt}e^{-i\hat{H}_{\mathrm{z}}dt} = \hat{U}_{\mathrm{D}}(dt)\hat{U}_{\mathrm{SM}}(dt)\hat{U}_{\mathrm{z}}(dt).$$

The expression for the unitary evolution of the bipartite state, $\hat{U}(\tau)\hat{\rho}(t)\hat{U}^{\dagger}(\tau)$, can be simplified using two properties. First, we start each sequence of coupling the system to a meter with the separable initial state $\hat{\rho}(t) = \hat{\rho}_{\mathrm{S}}(t) \otimes |h\rangle\langle h|$, where $\hat{\rho}_{\mathrm{S}}(t)$ is the reduced state of the system and $|h\rangle$ is the initial state of the meter. Second, it is easy to see that $\left[\hat{H}_{\mathrm{SM}},\, \hat{\rho}_{\mathrm{S}}(t) \otimes |h\rangle\langle h|\right] = 0$ since $\hat{H}_{\mathrm{SM}}$ (cf. Eq. (5.36)) couples the system to the $|g\rangle \leftrightarrow |e\rangle$ transition of the meter. By combining both, we can evaluate the partial trace explicitly and arrive at

$$\hat{\rho}_{\mathrm{S}}(t+dt) = \sum_{j=h,g,e} w_{jh}\, \hat{U}_{\mathrm{D}}(dt)\, \hat{\rho}_{\mathrm{S}}(t)\, \hat{U}_{\mathrm{D}}^{\dagger}(dt)\, w_{jh}^{\dagger} \tag{5.53}$$

with $w_{jh} = \langle j|\, \hat{U}_{\mathrm{z}}(dt)\, |h\rangle$. To describe the dynamics in its most general form we write the Zeno Hamiltonian as

$$\hat{H}_z = \frac{g_z}{2}\Big(|h,z\rangle\langle +,n| + |+,n\rangle\langle h,z| \Big) \tag{5.54}$$

with n and z being arbitrary. Next, the unitary $\hat{U}_{\mathrm{z}}(dt)$ can be rewritten as

$$\hat{U}_{\mathrm{z}}(dt) = \hat{\mathbb{1}} - \left(1-\cos\tfrac{\phi_z}{2}\right)\big(|h,z\rangle\langle h,z| + |+,n\rangle\langle +,n| \big) - i\sin\tfrac{\phi_z}{2}\big(|h,z\rangle\langle +,n| + |+,n\rangle\langle h,z| \big)$$

with the Rabi angle $\phi_z = g_z dt$. Using this, the operators w_{jh} can be explicitly evaluated to

$$w_{hh} = \hat{\mathbb{1}}_{\mathrm{S}} - \left(1-\cos\tfrac{\phi_z}{2}\right)\hat{\Pi}_z\,, \tag{5.55a}$$

$$w_{gh} = -\tfrac{i}{\sqrt{2}}\sin\tfrac{\phi_z}{2}\,\hat{L}_{(z,n)}\,, \tag{5.55b}$$

$$w_{eh} = -\tfrac{i}{\sqrt{2}}\sin\tfrac{\phi_z}{2}\,\hat{L}_{(z,n-1)}\,, \tag{5.55c}$$

where

$$\hat{\Pi}_z = |z\rangle\langle z|\,, \quad \hat{L}_{(z,m)} = |m\rangle\langle z| \tag{5.56}$$

are system operators. As discussed in Sec. 5.1.2, the operators in Eq. (5.55) can be interpreted

both as the measurement operators of an indirect measurement and as the Kraus operators of an open quantum system's evolution. They depend only on the Zeno Hamiltonian and the meter's initial state.

We now derive a time-continuous master equation in Lindblad form from the Kraus operators. To this end, we assume the measurement to be performed continuously with constant rate $\kappa = \frac{1}{\tau}$ such that the number of measurements in a time interval dt is κdt. This can be interpreted as the "smearing" of one measurement over the whole time interval τ. As a result, evolution described by the master equation deviates from the one described by the piecewise dynamics on the timescale τ or for large values of τ. With this and when going to the interaction picture with respect to the coherent evolution $\hat{H}_\mathrm{D}$, we can rewrite Eq. (5.53) to [141]

$$\hat{\rho}_\mathrm{S}(t+dt) = \kappa\, dt \sum_{j=h,g,e} w_{jh}\, \hat{\rho}_\mathrm{S}(t)\, w_{jh}^\dagger + (1-\kappa\, dt)\ \hat{\rho}_\mathrm{S}(t)\,. \tag{5.57}$$

Finally, we calculate the derivative of the reduced state as

$$\frac{d\hat{\rho}_\mathrm{S}(t)}{dt} = \lim_{dt\to 0} \frac{\hat{\rho}_\mathrm{S}(t+dt) - \hat{\rho}_\mathrm{S}(t)}{dt} \tag{5.58}$$

and go back to the non-interacting picture [141],

$$\frac{d\hat{\rho}_\mathrm{S}(t)}{dt} = -i\left[\hat{H}_\mathrm{D},\, \hat{\rho}_\mathrm{S}\right] + \kappa \left(\sum_{j=h,g,e} w_{jh}\, \hat{\rho}_\mathrm{S}(t)\, w_{jh}^\dagger - \hat{\rho}_\mathrm{S}(t) \right). \tag{5.59}$$

Finally, the Kraus operators of Eq. (5.55) can be inserted and the terms rearranged the properties $\hat{\Pi}_z = \hat{\Pi}_z^2 = \hat{\Pi}_z{}^\dagger$ and $\hat{\Pi}_z = \hat{L}_{(z,m)}^\dagger \hat{L}_{(z,m)}$. We arrive at a Lindblad master equation of the form Eq. (5.26) with the coherent evolution driven by $\hat{H}_\mathrm{D}$ (in the commutator) and three Lindblad operators and decay rates,

$$\hat{L}_{(z,n)} = |n\rangle\langle z|\,, \qquad \gamma_{(z,n)} = \frac{1}{2}\sin^2\left(\frac{\phi_z}{2}\right), \tag{5.60a}$$

$$\hat{L}_{(z,n-1)} = |n-1\rangle\langle z|\,, \qquad \gamma_{(z,n-1)} = \frac{1}{2}\sin^2\left(\frac{\phi_z}{2}\right), \tag{5.60b}$$

$$\hat{\Pi}_z = |z\rangle\langle z|\,, \qquad \gamma_z = 4\sin^4\left(\frac{\phi_z}{4}\right). \tag{5.60c}$$

We now discuss some special cases of this equation to give some basic intuition. First, the case $n = z$ results in the original Zeno Hamiltonian from Eq. (5.41) where $|h,z\rangle$ is coupled to $|+,z\rangle$ as depicted by the red straight arrow in Fig. 5.8 (a). Note that this is the case discussed in Sec. 5.2.3. With the abbreviations $\hat{A} \equiv \hat{L}_{(z,z-1)} = |z-1\rangle\langle z|$, $\hat{\Pi} \equiv \hat{\Pi}_z = \hat{L}_{(z,z)} = |z\rangle\langle z|$, $\gamma_A \equiv \gamma_{(z,z-1)} = \frac{1}{2}\sin^2\frac{\phi_z}{2}$ and $\gamma_\Pi \equiv \gamma_z + \gamma_{(z,z)} = 4\sin^4\frac{\phi_z}{4} + \gamma_A$, we arrive at the simple mas-

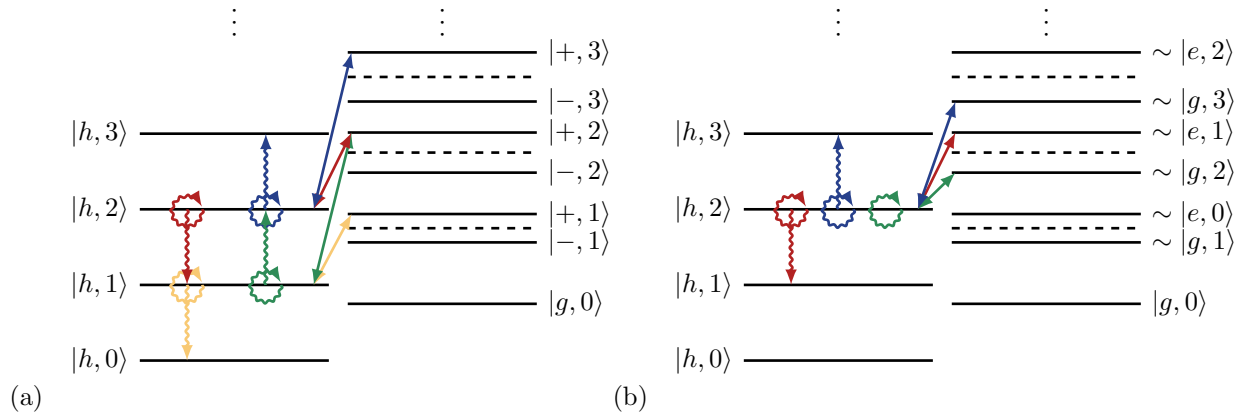

Figure 5.8: Decay channels in the resonant (a) and off-resonant (b) case for the Zeno level $|z = 2\rangle$ (and $|z = 1\rangle$ for the green and yellow arrows in (a)). The straight arrows in the middle of each panel indicate the driven transitions, the snaked arrows indicate the effective decay channels in the master equation. A circular, snaked array depicts dephasing.

ter equation

$$\frac{d\hat{\rho}_{\mathrm{S}}(t)}{dt} = -i\left[\hat{H}_{\mathrm{D}},\, \hat{\rho}_{\mathrm{S}}(t)\right] + \kappa\gamma_A\left(\hat{A}\hat{\rho}_{\mathrm{S}}(t)\hat{A}^\dagger - \frac{1}{2}\left\{\hat{A}^\dagger\hat{A},\, \hat{\rho}_{\mathrm{S}}(t)\right\}\right) + \kappa\gamma_\Pi\left(\hat{\Pi}\hat{\rho}_{\mathrm{S}}(t)\hat{\Pi} - \frac{1}{2}\left\{\hat{\Pi},\, \hat{\rho}_{\mathrm{S}}(t)\right\}\right) \tag{5.61}$$

The dependency of the decay rates on the Rabi angle in shown in Fig. 5.9 (a, solid lines). Given the definitions of $\hat{A}$ and $\hat{\Pi}$, $\kappa\gamma_A$ corresponds to the rate of population transfer from the Zeno level to the level below, and $\kappa\gamma_\Pi$ to the dephasing rate of the Zeno level (see red, snaked arrows in Fig. 5.8 (a)). The effect of the operator $\hat{A}$ can be identified with the projection the population back into the Zeno subspace as explained in Sec. 5.2.3, (iii). This becomes apparent by comparing the decay rate γ_A with the weight of the $|+,z\rangle$ contribution in Eq. (5.47).

The master equation provides yet another perspective, in addition to Fig. 5.7, to illustrate the functionality of the quantum simulator: The decay rates can be varied by tuning the experimentally accessible parameters ϕ_z and κ. To assess the agreement of the master equation (5.61) with the piecewise dynamics of Eq. (5.43) used to generate Fig. 5.7, we propagate the initial state $|0\rangle$ with $z = 2$ using both methods. Figure 5.9 (b) shows the difference in infidelity of the QZD, $P_{\bar{Z}}$, and in the linear entropy S_L between the two pictures. It can be seen that they show good agreement for small Rabi angles ϕ_2 or displacements β. However, the two pictures deviate if our assumptions during the derivation of the master equation are violated. Firstly, the agreement deteriorates for large β, since this contradicts the assumption of continuous measurements, $dt \to 0$. Secondly, we have used the Baker-Campbell-Hausdorff formula up to first order to derive the Kraus representation. We thus make an error which is of the order of the commutator of $\hat{H}_{\mathrm{D}}$ and $\hat{H}_{\mathrm{z}}$ which scales as $\phi_z\beta$. Therefore, the deviation also rises as ϕ_2 increases.

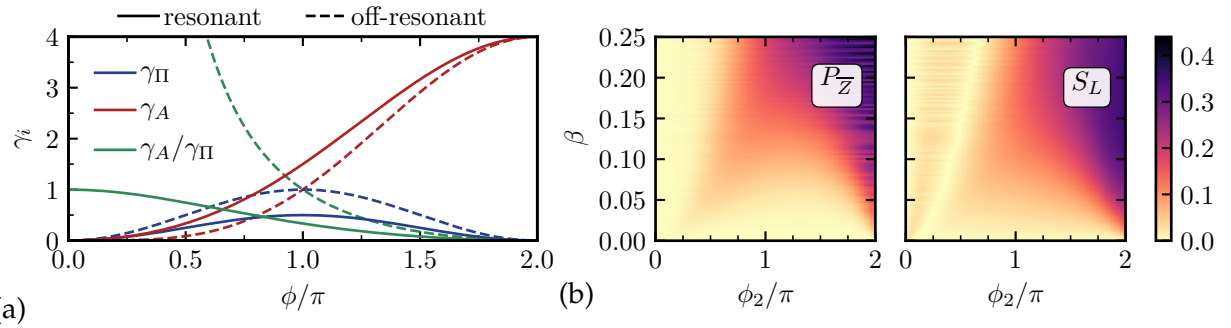

Figure 5.9: (a) Decay rates, γ_A and γ_Π, and their ratio for the resonant case coupling $|h,z\rangle \leftrightarrow |+,n=z\rangle$ (solid lines) and the off-resonant case coupling $|h,z\rangle \leftrightarrow |e,n=z-1\rangle$ (dashed lines). (b) Difference obtained when solving the master equation and using the piecewise dynamics for the Zeno infidelity $P_{\bar{Z}}$ and the dissipation S_L as a function of the displacement β and the Rabi angle ϕ_2.

Next, we briefly discuss the master equation for some other cases to illustrate its generality. For $n = z+1$, the Zeno Hamiltonian couples $|h,z\rangle$ to $|+,z+1\rangle$ (blue arrows in Fig. 5.8 (a)). Equation (5.60) leads to the Lindblad operators

$$\hat{B} \equiv \hat{L}_{(z,z+1)} = |z+1\rangle\langle z|\,, \quad \hat{\Pi} = \hat{\Pi}_z = \hat{L}_{(z,z)} = |z\rangle\langle z|$$

with the decay rates γ_Π and $\gamma_B = \gamma_A$ being identical to the previous case. The two cases $n = z+1$ and $n = z$ are hence similar but the Lindblad operator $\hat{B}$ now describes population excitation instead of relaxation.

Going to the off-resonant case allows for even broader generalization. We now assume the detuning $\Delta = \omega_{eg} - \omega_S$ between the transition frequencies of the harmonic oscillator, ω_S, and the $|g\rangle \leftrightarrow |e\rangle$ transition of the meter, ω_{eg}, to be non-vanishing. For large detuning $|\Delta| \gg \Omega$, the dressed states tend towards the uncoupled ones, $|+,n\rangle \sim |e,n-1\rangle$ and $|-,n\rangle \sim |g,n\rangle$ [9]. The remaining interaction leads to a slight shift of the bipartite energy levels which still allows for state selective excitation. If we now couple the $|h,z\rangle \leftrightarrow |e,n\rangle$ transition with a Zeno pulse, we are able to create the Lindblad operators $\hat{L}_{(z,n)} = |n\rangle\langle z|$ and $\hat{\Pi}_z = |z\rangle\langle z|$ where the corresponding decay rate can be calculated to be $\gamma^\Delta_{(z,n)} = 2\gamma_{(z,n)} = \sin^2\left(\frac{\phi_z}{2}\right)$ and $\gamma^\Delta_z \equiv \gamma_z = 4\sin^4\left(\frac{\phi_z}{4}\right)$. Incidentally, the ratio between the two decay rates is given by

$$\frac{\gamma^\Delta_{(z,n)}}{\gamma^\Delta_z} = \cot^2\left(\frac{\phi_z}{4}\right). \tag{5.62}$$

Figure 5.9 (a) shows the decay rates in the resonant case with $n = z$ (solid lines) and the off-resonant case with $n = z-1$ (dashed line) which both induce the same Lindblad operators $\hat{\Pi} = |z\rangle\langle z|$ and $\hat{A} = |z-1\rangle\langle z|$ (see also red arrow in (a) and (b) of Fig. 5.8). In the resonant case, the ratio never exceeds the value 1 rendering it impossible to engineer decay rates with $\gamma_A > \gamma_\pi$.

In the off-resonant case, on the other hand, the ratio varies between ∞ for $\phi_z = 0$ and 0 for $\phi_z = 2\pi$. By additionally adjusting the measurement rate κ, by which all the decay rates have to be multiplied, it is possible to tune the ratio and the amplitude of the decay rates arbitrarily.

Lastly, by choosing $n = z$ in the off-resonant case, the pulse induces pure dephasing $\hat{L}_{(z,z)} = \hat{\Pi}_z = |z\rangle\langle z|$ with the decay rate $\gamma_z^{\Delta} = \gamma_z + 2\gamma_{(z,z)} = 4\sin^4\left(\frac{\phi_z}{4}\right) + \sin^2\left(\frac{\phi_z}{2}\right)$ (see green arrow in Fig. 5.8 (b)). In the same spirit, we can couple $|h, z\rangle$ to $|g, n\rangle$ in the off-resonant case. This case is completely analogous to coupling to $|e, n\rangle$ but gives yet another degree of freedom to tailor the open systems dynamics.

While it may seem like the generation of arbitrary sets of Lindblad operators is hampered by connections between them due to the Rabi angles, the number of linked decay rates is actually very small. For instance, a coupling of the Zeno level $|h, z\rangle$ to the dressed state $|+, n\rangle$ induces the three Lindblad operators $\hat{\Pi}_z = |z\rangle\langle z|$, $\hat{L}_{(z,n)} = |n\rangle\langle z|$ and $\hat{L}_{(z,n-1)} = |n-1\rangle\langle z|$ whose decay rates γ_z, $\gamma_{(z,n)}$ and $\gamma_{(z,n-1)}$ (cf. Eq. (5.60)) all depend on the same Rabi angle ϕ_z. This can be reduced to two Lindblad operators, $\hat{\Pi}_z = |z\rangle\langle z|$ and $\hat{L}_{(z,n)} = |n\rangle\langle z|$, or even a single one describing pure dephasing $\hat{\Pi}_z$ (for $n = z$) simply by going to the off-resonant case, as explained above. In other words, only between one to three decay rates depend on the same Rabi angle.

The key to engineering decay rates which are independent from each other is to combine several Zeno pulses Z_i which address different transitions $|h, z_i\rangle \leftrightarrow |+, n_i\rangle$ with Hamiltonian $\hat{H}_{\mathrm{Z}} = \sum_{i=1}^{N_Z} \hat{H}_{z_i}$ where N_Z is the number of Zeno pulses employed.. The Rabi angles ϕ_{z_i} can then be tuned for each pulse independently leading to independent decay rates. Figure 5.8 (a) shows the combination of four exemplary Zeno pulses in the resonant case. The only exception to the compatibility of the pulses is that the same dressed state $|+, n'\rangle$ cannot be addressed with several pulses without introducing correlations, possibly undesired ones, of the decay channels. For instance, we cannot address the $|h, 2\rangle \rightarrow |+, 2\rangle$ transition (red arrow), inducing dephasing on $|2\rangle$ and deexcitation $|2\rangle \rightarrow |1\rangle$, and the $|h, 1\rangle \rightarrow |+, 2\rangle$ transition (green arrow), inducing dephasing on $|1\rangle$ and excitation $|1\rangle \rightarrow |2\rangle$, at the same time because both address $|+, 2\rangle$. This does not, however, reduce the generality of the scheme since simultaneous deexcitation, $|2\rangle \rightarrow |1\rangle$, and excitation, $|1\rangle \rightarrow |2\rangle$, can be replaced by an effective (de)excitation rate.

To summarise, the general Lindblad operators in Eq. (5.60) can induce various different dynamics: Taking the Zeno pulse to couple $|h, z\rangle$ to $|+, n\rangle$ with arbitrary z and n, it is possible to generate Lindblad operators $|z\rangle\langle z|$, $|n\rangle\langle z|$ and $|n-1\rangle\langle z|$ with tunable decay rates. For example, by choosing $n = z$, the Lindblad operators inducing population relaxation, $|z-1\rangle\langle z|$, while for $n = z+1$ they induce excitation, $|z+1\rangle\langle z|$, both in combination with dephasing $|z\rangle\langle z|$. Choosing the system to be off-resonant with respect to the $|g\rangle \leftrightarrow |e\rangle$ transition of the meter provides more freedom to adjust the decay rates. Taking the Zeno pulse to couple to the $|h, z\rangle \leftrightarrow |e, n\rangle$ transition allows to arbitrarily tune the ratio between dephasing $|z\rangle\langle z|$ and population transfer $|n\rangle\langle z|$. In particular, it allows for inducing pure dephasing in the special case of $n = z$. Finally, employing several pulses at the same time engineers arbitrary decay channels for every system state.

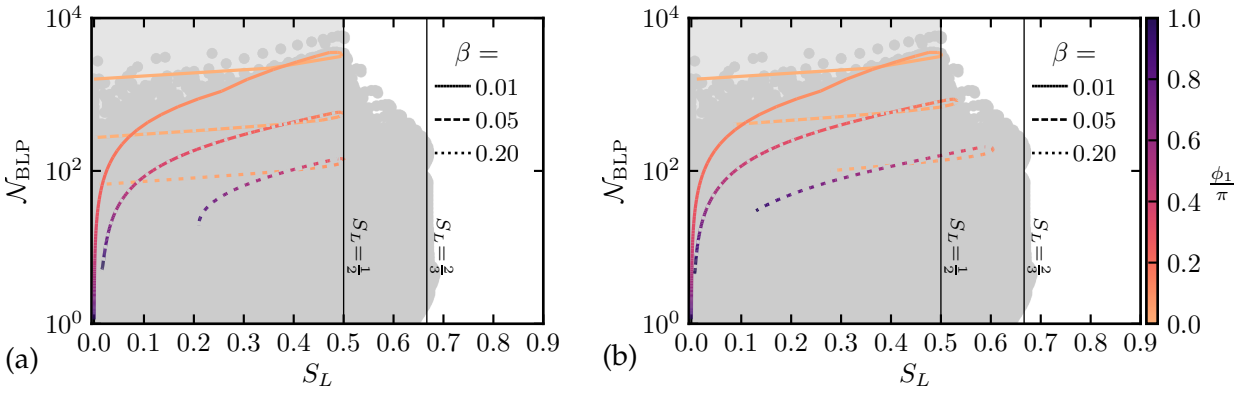

Figure 5.10: Attainable combinations of dissipation S_L and non-Markovianity $\mathcal{N}_{\mathrm{BLP}}$ using two Zeno pulses Z_2 and Z_1 with $-i\alpha T = 10\pi$ (dark grey dots). The light grey shading highlights the area which is attainable by an extended sampling range. Only the coloured lines are different between the two panels: they highlight the combinations of S_L and $\mathcal{N}_{\mathrm{BLP}}$ for a Rabi angle $\phi_2 = 4\pi$ (a) and 6π (b) with different values of displacement β and Rabi angle $\phi_1 \leq \pi$ as given by the line style and colour, respectively.

5.3 Independent tunability of non-Markovianity and dissipation

With a single Zeno pulse, dissipation and memory effects cannot be tuned independently. This shortcoming is remedied by employing two state-selective excitations simultaneously, for example Z_1 and Z_2 addressing states $|1\rangle$ and $|2\rangle$, cf. Fig. 5.3 (b) (in principle, any two non-degenerate states can be chosen). Even with two Zeno fields, only a single measurement needs to be carried out at the end of time interval τ. While Z_2 controls memory effects, Z_1 induces dissipation: Large memory effects are obtained with a Rabi angle $\phi_2 = 2n\pi$, and small ϕ_1 results in strong dissipation (for our values of the displacement β induced by the coherent drive D "small" is $\phi_1 < \pi$). The interplay of two pulses in the non-Markovian regime requires a numerical analysis.

First of all, when considering two Zeno pulses, Z_1 and Z_2, the optimal state pair is possibly different since all three states in the extended Zeno subspace $\mathcal{H}_Z^+$ take part in the non-unitary dynamics induced by the Zeno coupling and the measurement. A numerical re-optimisation was performed for the specific case of $\{\beta = 0.025, \phi_2 = 4\pi, \phi_1 = 0.25\pi\}$ providing both dissipation ($S_L = 0.48$) and a large amount of non-Markovianity (about twice as large as without having the second Zeno pulse Z_1). After optimising $|\Psi_1\rangle$ numerically (as described in detail for one Zeno pulse in Sec. 5.2.2), the optimal state pair for this set of parameters was found to be $\{|\Psi_1\rangle = |\psi(\vartheta = 0.56\pi, \varphi = 1.92\pi)\rangle\,, |\Psi_2\rangle = |2\rangle\}$. To be exact, this optimisation would have to be performed for all considered parameters $\{\beta, \phi_2, \phi_1\}$ and with considering choices other than $|\Psi_1\rangle = |\psi(\vartheta, \varphi)\rangle$ and $|\Psi_2\rangle = |2\rangle$ for the optimal state pair. However, the minimal and maximal value of the BLP measure differ by about 1% only and since the absolute value of the BLP measure is not important, we choose $\left\{|\Psi_1\rangle = \frac{1}{\sqrt{2}}\left(|0\rangle + |1\rangle\right),\, |\Psi_2\rangle = |2\rangle\right\}$ until the end of this chapter for simplicity.

Figure 5.10 shows the attainable combinations of dissipation strength S_L and memory effects $\mathcal{N}_{\text{BLP}}$ when varying the displacement β and the two Rabi angles ϕ_2 and ϕ_1. The grey dots in the background show all combinations of S_L and $\mathcal{N}_{\text{BLP}}$ obtained by sampling β from 0.01 to 0.5 in 80 steps, ϕ_2 from 2π to 12π in steps of 2π and ϕ_1 from 0 to 2π in steps of 0.01π. For simplicity, we discuss the example of $\phi_2 = 4\pi$ and $\phi_1 \leq \pi$ in more detail (indicated by the coloured lines in Fig. 5.10 (a)). For small values of ϕ_1 (yellow end of the lines), the dissipation S_L increases with ϕ_1 while keeping the non-Markovianity almost constant, as can be seen from the initially flat curves. For larger ϕ_1, the curves reach a clear boundary at a linear entropy of $S_L = \frac{1}{2}$, i.e. at the purity of the completely mixed two-level system state. This is because Z_2 creates a perfect Zeno barrier at $|2\rangle$ while Z_1 induces dissipation in the resulting two-dimensional Zeno subspace whose linear entropy is limited by $\frac{1}{2}$. When increasing ϕ_1 even further, the dissipation and non-Markovianity drop drastically because the pulse Z_1 induces a Zeno barrier at $|1\rangle$ and the dynamics become confined to the one-dimensional Zeno subspace $\{|0\rangle\}$. For a Rabi angle of $\phi_2 = 6\pi$, the situation looks similar as shown in panel (b). The main differences are that the maximal value of the BLP measure is higher and the linear entropy is not limited by $\frac{1}{2}$. The dependency of both the non-Markovianity and the dissipation on of ϕ_2 are discussed in detail in the following.

In the case of two combined Zeno pulses, Z_1 and Z_2, the dynamics depends on three control parameters (β, ϕ_1, ϕ_2). Since the values of all three parameters affect both the dissipation strength, quantified by the linear entropy S_L, and the non-Markovianity, measured by the BLP measure $\mathcal{N}_{\text{BLP}}$, the discussion of the tunability of the quantum simulator needs some special care and attention. We start by discussing the dependency of the dissipation and the non-Markovianity on the Rabi angle ϕ_2 which is induced by Z_2 addressing the state $|2\rangle$. We set $\phi_2 = 2n\pi$ with n being an integer in order to induce strong non-Markovianity and Zeno confinement as discussed in Sec. 5.2.3. In between, i.e. $\phi_2 \neq 2n\pi$, the signatures of non-Markovianity vanish quickly (compare to inset in Fig. 5.7 (c)) which also allows access to the Markovian regime. In the following, we show that ϕ_2 tunes the non-Markovianity also in the presence of the second Zeno pulse Z_1.

Figure 5.11 (a+b) shows the dissipation and the non-Markovianity as a function of the Rabi angle ϕ_2 for $\phi_1 = 0.05\pi$ and five different values of the displacement β. Panel (b) shows clearly that the non-Markovianity depends linearly on ϕ_2. For this reason, the light grey area in Fig. 5.10 is also accessible by extending the sampling range of ϕ_2 which increases the strength of non-Markovianity. The dependency of the dissipation on ϕ_2, on the other hand, is comparatively flat as can be seen in panel (a). The curves are flatter the smaller β. This points to ϕ_2 being a suitable knob to control the non-Markovianity in the quantum simulator. Most notably does a Rabi angle with uneven multiples of 2π, $\phi_2 = 2(2n+1)\pi$, and in particularly 2π, lead to more dissipation than even multiples, $\phi_2 = 4n\pi$. The reason for this lies in the non-commutativity of the Hamiltonians $\hat{H}_{\text{D}}$ (Eq. (5.39)) and $\hat{H}_z$ (Eq. (5.41)). For large interaction times τ (and accordingly large values of β), the pulse Z_z is not able to perform a perfect ϕ_z-pulse on the $|h, z\rangle \leftrightarrow |+, z\rangle$ transition because the dynamics is also affected by the drive D. As a consequence, the dressed state stays populated

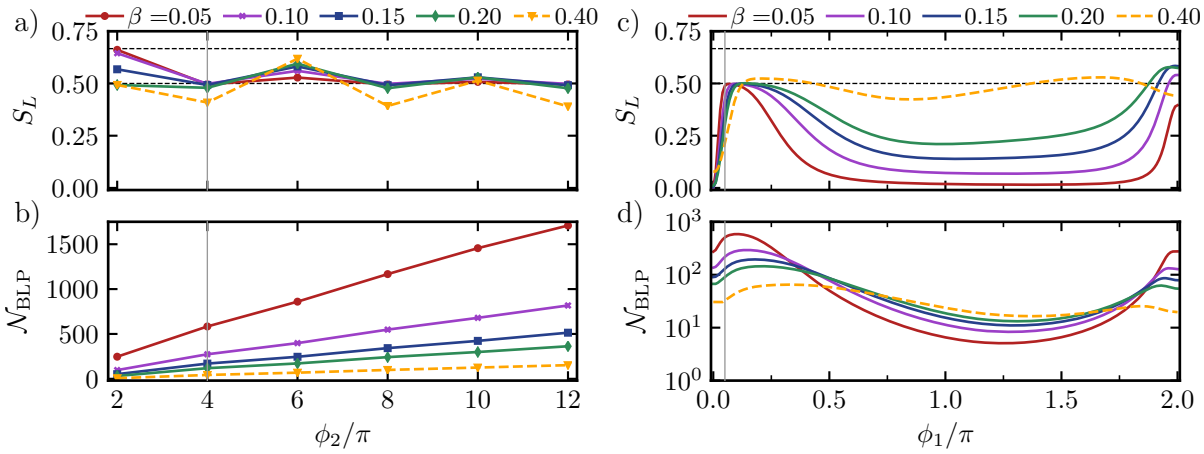

Figure 5.11: Dependency of the dissipation S_L (upper panels, a+c) and the non-Markovianity $\mathcal{N}_{\mathrm{BLP}}$ (lower panels, b+d) on the Rabi angle ϕ_2 (left panels, a+b) and on the Rabi angle ϕ_1 (right panels, c+d). In the left-hand panels, ϕ_1 was set to 0.05π (indicated by the vertical grey line in the right-hand panels) and in the right-hand panels, ϕ_2 was set to 2π (indicated by the vertical grey line in the left-hand panels). β is fixed as given by the key. The total duration T of each propagation was set to fulfil $-i\alpha T = 10\pi$. The horizontal black dashed lines in (a+c) indicate a linear entropy of $\frac{1}{2}$ and $\frac{2}{3}$, respectively.

at the time of the measurement and dissipation occurs. A pulse with $\phi_z = 4n\pi$, however, is less affected by the non-commutativity of the operators because the first and second half of the Zeno pulse differ in sign as shown in Eq. (5.47). In the same fashion as a spin-echo [142], the second half reverts the unwanted effects of the first one. As a result, a pulse with $\phi_2 = 4n\pi$ confines the dynamics of the system to the two-dimensional Zeno subspace created by it and the linear entropy cannot surpass the value of $\frac{1}{2}$ while a $\phi_2 = 2(2n+1)\pi$-pulse can. Only the exceptionally large value of $\beta = 0.4$ breaks this pattern, since the displacement in-between two measurements is too large to guarantee a proper Zeno confinement.

We now turn to discussing the dependency of the dissipation and the non-Markovianity on the Rabi angle ϕ_1, see panels (c+d). We added the pulse Z_1 with the intention of inducing dissipation in the two-dimensional Zeno subspace of the system and, in the following, we show that the dissipation S_L depends particularly strongly on ϕ_1 if ϕ_1 is very small.

As ϕ_1 is switched on ($\phi_1 \lesssim 0.1\pi$), the linear entropy rises rapidly from 0 to its maximal value $\frac{1}{2}$ while $\mathcal{N}_{\mathrm{BLP}}$ is only mildly modified. This points to ϕ_1 being a suitable knob to control the dissipation in the quantum simulator. Note that the maximal value of the non-Markovianity depends on β since $\mathcal{N}_{\mathrm{BLP}}$ is proportional to the number N of measurements performed during the total time T. As mentioned before, the linear entropy takes values larger than $\frac{1}{2}$ for exceptionally large values of β such as 0.4 because the Zeno coupling induced by the pulse Z_2 is not sufficient to generate Zeno confinement confinement. In order to provide full tunability of the dissipation in the Zeno subspace of the system, it is sufficient to consider this range of $\phi_1 \lesssim 0.1\pi$, where the dissipation takes all the possible values between 0 and $\frac{1}{2}$.

Nonetheless, we also discuss the parameter range after the peak of S_L in order to provide deep insight into the dynamics of the system. After the peak in dissipation and non-Markovianity, care must be taken since both quantities drop as ϕ_1 is increased further. In this parameter regime, Z_1 induces Zeno confinement at $|1\rangle$ which prevents dissipation from occurring. The confinement is stronger the smaller β and it also prevents a population of $|2\rangle$, which is the origin of memory effects, turning the dynamics Markovian. As $\phi_1 \to 2\pi$, the combination of two Zeno pulses Z_1 and Z_2 induce induce a strong disturbance of the initial state $|0\rangle$ while keeping it in the subspace $\{|0\rangle, |1\rangle, |2\rangle\}$. Hence, both the dissipation and the non-Markovianity rise significantly and the initial state drifts towards the completely mixed state with $S_L = \frac{2}{3}$ (compare to boundary in Fig. 5.10).

We want to stress that the Zeno pulses can not only be used to induce dissipation and non-Markovianity, but they can also confine the dynamics of the system to a subspace of adjustable size. In general, to confine the dynamics to a d-dimensional subspace, we simply need to choose the Zeno level $|z = d\rangle$ by adjusting the frequency of the Zeno pulse Z_z accordingly. The dimension of the system should therefore at least be three in order to enable non-trivial dynamics, but can be arbitrarily large and even infinite as in our setup. It is also possible to generate dissipation and memory effects on multiple system states $|z_i\rangle$ with $i \in \{1, 2, \ldots, N_Z\}$ by varying the frequency of a single Zeno pulse Z_z as a function of time or by employing multiple Zeno pulses Z_{z_i}. The number N_Z of maximally controlled states is then only limited by the number of control pulses available.

To conclude, we showed that we are able to tune the dissipation and the strength of memory effects independently from each other by employing two control pulses. In our example, we created the two-dimensional Zeno subspace $\{|0\rangle, |1\rangle\}$ by employing one Zeno pulse Z_2 addressing the Zeno level $|2\rangle$ with Rabi angles $\phi_2 = 2n\pi$. The value of the non-Markovianity measure depends linearly on the value of ϕ_2 and thus allows for tuning the strength of memory effects. In addition to that, we employed a second pulse Z_1 addressing the state $|1\rangle$ which lies within the Zeno subspace with a small Rabi angle. We showed that already very small Rabi angles $\phi_1 \lesssim 0.1\pi$ suffice to tune the dynamics in the subspace from closed to showing strong dissipation. Our finding can be generalised to subspaces with other size or a larger number of control pulses to induce more complex dynamics.

Before closing this chapter, we discuss possible experimental realisations of the proposed quantum simulator beyond cavity QED to emphasize the generality of our scheme. The bipartite system of a harmonic oscillator and a three-level system is very natural and can be found in many experimental setups. For instance, due to the formal similarities to cavity QED, a superconducting qubit coupled to a cavity in circuit QED [143] or a common vibrational mode of trapped ions together with ion qubit states [144] are equally suitable. Beyond this, our approach is not restricted to modelling the system as a harmonic oscillator. In fact, not even a bipartite setup is required—it is sufficient to identify two different subspaces in the quantum system, the 'system'

and 'meter' parts, and carry out state-selective measurements of the 'system' using the 'meter'. An example for a realisation in a single system would be a Bose-Einstein condensate (BEC) with hyperfine ground state levels encoding the system [145]. In general, realisation of our proposal requires three conditions to be met: (i) existence of a 'system' part whose dynamics are decoupled from the 'meter' part when driven by a classical source D, (ii) selective excitation of system states by driving transitions in the meter using one or several Zeno pulses Z_{z_i}, (iii) subjecting meter states to dissipation. Dissipation can be introduced by projective measurement of the meter, as in the cavity QED example, or it can be natural such as a fast decay. In the BEC experiment, the Zeno pulse drives transitions to an excited state hyperfine manifold such that the meter is subject to spontaneous decay. Note that in this case, the number N_Z of maximally controlled states is limited by the dimension of the 'meter' subspace, i.e. the excited hyperfine manifold.

5.4 Summary

In this chapter, we have proposed a quantum simulator for open quantum systems which is fully tunable between the Markovian and non-Markovian regime independently from the strength of dissipation. It is based on a series of indirect, state-selective measurements of a system by a meter. Controlling the specifications of the measurement then allows for tuning the properties of the resulting open quantum system as shown in Fig. 5.7. The control parameters are the displacement of the harmonic oscillator in-between two measurements, which quantifies the strength of the coherent evolution, and the Rabi angle induced by the control pulses, which can be interpreted as the coupling strength between system and meter. For a large range of control parameters, the measurement gives rise to Quantum Zeno dynamics which allows for confining the dynamics to a subspace of arbitrary size and which is why we refer to the control pulses as Zeno pulses. The dissipation inside the open system can be tuned by choosing the amount of entanglement between system and meter at the end of their interaction. Roughly speaking, the stronger their entanglement, the higher the dissipation. The frequencies of the Zeno pulses, in turn, determine which system levels are subject to dissipation.

We further employed the BLP measure, and derived the optimal state pair for the special case of a two-dimensional Zeno subspace analytically, in order to quantify the degree of non-Markovianity in the system. We found that the system can be tuned from memory-less to maximal display of memory effects where strongest signatures of non-Markovianity occur if system and meter remain separable at the time of the measurement. For the Markovian limit, we derived a Lindblad master equation (cf. Eq. (5.61)) which describes the dynamics and dissipation of the open quantum systems in terms of Lindblad operators. We demonstrated that it is possible to engineer essentially arbitrary decay channels and rates by combining several Zeno pulses, rendering the quantum simulator universal in the Markovian limit. Finally, the strength of dissipation and non-Markovianity can be engineered independently from each other by combining two Zeno pulses and carefully tuning their amplitudes as shown in Fig. 5.10. One pulse is then

used to truncate the Hilbert space and to induce memory effects, while the other pulse introduces dissipation in the Zeno subspace.

The proposed scheme can be customised in multiple ways. We have mainly discussed the implementation using one or two Zeno pulses at the same time to control the dynamics in a two-dimensional subspace of the harmonic oscillator. Generalisation to more pulses allows for the implementation of additional decay channels. It would, however, be interesting to investigate more complex control sequences, for instance by alternating different Zeno pulses or changing their strength as a function of time. Moreover, the timings of the measurements could be chosen to be non-equidistant or according to a waiting time distribution in order to emulate a random renewal process [103]. The population of the harmonic oscillator could further be controlled by sending "wiper" or "emitter atoms" through the cavity which selectively absorb or emit excitations. If allowed by the experimental setup, it would also be interesting to consider the effect of letting the same meter interact with the system several times in order to store information and bring it back at a much later time.

The proposed quantum simulator is very general and can be employed in various different experimental platforms. We have based the model on a harmonic oscillator being subject to repeated measurements by an anharmonic three-level systems. This choice was inspired by cavity quantum electrodynamics (QED), where the harmonic oscillator can be identified with a photonic mode of a microwave cavity, and the three-level system with three adjacent circular states of a Rydberg atom – highlighting yet another application of Rydberg atoms for quantum technologies. However, our model is in fact much more general as has been discussed in the end of Sec. 5.3.

6

SCATTERING OF RYDBERG ATOMS AND POLAR MOLECULES

Until this point in the thesis, we have only considered the interaction between Rydberg atoms and light. The large coupling between Rydberg atoms and microwave fields allows for studying the light-matter interaction at the level of single quanta [9]. It can be exploited for engineering various quantum technologies, such as quantum sensors and simulators [18], as has also been discussed in previous chapters of this thesis. However, there are reasons to go beyond the study of single atoms and their interaction with light. For instance, the study of the strong interaction between two Rydberg atoms is currently of high interest [20]. Depending on the initial states of the atoms, they either couple via dipole-dipole or van-der-Waals interaction. The two cases differ in their scaling with the principal quantum number n and the particles' distance. This tunable long-range interaction is an important tool for mimicking a Hamiltonian of choice – a major prerequisite for quantum simulation – rendering Rydberg atoms one of the most popular platforms for quantum simulation and quantum computing [17].

The interaction of Rydberg atoms with other systems, such as polar molecules, opens different possibilities. The large dipole moments of both systems allow for interactions over macroscopic distances which can, for instance, be used for manipulation of the molecule. Examples cover the cooling of external and internal molecular degrees of freedom [146, 147], the implementation of effective spin-spin interactions [148], and the readout and detection of molecular states [149, 40]. Also for quantum technologies a hybrid molecule-Rydberg-atom system would prove useful, for instance for the implementation of quantum gates in molecules [150]. However, most studies to date have approximated both the molecule and the Rydberg atom as dipoles, thus restricting themselves to dipole-dipole interactions. This approximation is questionable due to the large size of Rydberg orbitals, and accurate simulations of the scattering process including higher order interaction terms are still missing.

Here, we study the interaction between Rydberg atoms and polar molecules beyond the dipole-dipole approximation. We build a bridge from theoretically modelling the scattering process *ab initio* to predicting the scattering cross-section for a representative experiment. To this end, we start by outlining the theoretical framework for modelling polar molecules in Sec. 6.1.

Inspired by the experiment in Ref. [151], we consider ammonia molecules which can be modelled as symmetric top rotors with an additional inversion mode. Collisions between rubidium Rydberg atoms and the inversion mode of ammonia have already been studied successfully in several experiments [151, 152, 153]. Afterwards, in Sec. 6.2, we present our model for describing the scattering process between Rydberg atoms and polar molecules. Finally, we provide a prediction for the outcome of a realistic experiment when controlling the cross-section using the Stark effect of the Rydberg atom in Sec. 6.3. In the subsequent Chapter 7, we provide a thorough analysis of the multipolar character of the scattering process and discuss its application for the non-destructive detection of polar molecules.

6.1 Theory of polar molecules

We start by outlining the theoretical framework for describing polar molecules as presented for instance in Refs. [37, 38, 154]. A similarly concise summary can also be found in Ref. [155]. We start from the complete Hamiltonian of the molecule and present the reduction to the relevant degrees of freedom, namely the rotation of a rigid rotor, in Sec. 6.1.1. We then continue by presenting the eigenstates and matrix elements of symmetric top molecules in Sec. 6.1.2. Lastly, we discuss the inversion vibration mode of ammonia in Sec. 6.1.3 which plays the major role when considering their interaction with Rydberg atoms later.

6.1.1 The molecular Hamiltonian

Molecules are composed of several atoms and as such, their Hamiltonian is more complex than the atomic one. In general terms, it can be written as

$$\hat{H}_{\mathrm{mol}} = \hat{T}_{\mathrm{e}} + \hat{T}_{\mathrm{n}} + \hat{V}_{\mathrm{ee}} + \hat{V}_{\mathrm{nn}} + \hat{V}_{\mathrm{en}}, \tag{6.1}$$

where $\hat{T}$ and $\hat{V}$ are the kinetic and potential energy, respectively, and the subscripts declare the nuclear or electronic part. The three potentials describe the Coulomb interactions between electrons, nuclei, and between electrons and nuclei. Spin-dependent interactions as given by the (hyper)-fine structure are neglected. Depending on the kind of molecule, this Hamiltonian can include many particles and becomes unfeasible to handle quickly. In the following, we invoke several approximations to reduce the problem to the degrees of freedom that play a role in the interaction with Rydberg atoms.

First, the Born-Oppenheimer approximation [156] consists of the assumption that the electrons' movement is fast enough to respond almost instantaneously to a displacement of the nuclei. As a result, the electronic and nuclear motion can be separated and a product ansatz for the eigenfunctions of the Hamiltonian can be employed as

$$\Psi(\boldsymbol{r}_{\mathrm{e}}, \boldsymbol{r}_{\mathrm{n}}) = \psi_{\mathrm{e}}(\boldsymbol{r}_{\mathrm{e}}, \boldsymbol{r}_{\mathrm{n}})\psi_{\mathrm{n}}(\boldsymbol{r}_{\mathrm{n}}), \tag{6.2}$$

where $\boldsymbol{r}_\mathrm{e}$ and $\boldsymbol{r}_\mathrm{n}$ are the generalised coordinates of the electrons and nuclei in the space-fixed frame, and $\psi_\mathrm{e,n}$ their wave functions. The electronic wave functions $\psi_\mathrm{e}(\boldsymbol{r}_\mathrm{e}, \boldsymbol{r}_\mathrm{n})$ take the positions of the nuclei as a parameter, not a variable, as the electrons follow the nuclei adiabatically. Using Eq. (6.2), the Schrödinger equation of the full problem in Eq. (6.1) can be separated into an electronic part,

$$\hat{H}_\mathrm{e} \left|\psi_\mathrm{e}\right\rangle = \left(\hat{T}_\mathrm{e} + \hat{V}_\mathrm{ee} + \hat{V}_\mathrm{nn} + \hat{V}_\mathrm{en}\right) \left|\psi_\mathrm{e}\right\rangle = E_\mathrm{e}(\boldsymbol{r}_\mathrm{n}) \left|\psi_\mathrm{e}\right\rangle , \tag{6.3}$$

where $E_\mathrm{e}(\boldsymbol{r}_\mathrm{n})$ is the energy of the electronic state which depends parametrically on the position of the nuclei $\boldsymbol{r}_\mathrm{n}$, and a nuclear part,

$$\hat{H}_\mathrm{n} \left|\psi_\mathrm{n}\right\rangle = \left(\hat{T}_\mathrm{n} + E_\mathrm{e}(\hat{\boldsymbol{r}}_\mathrm{n})\right) \left|\psi_\mathrm{n}\right\rangle = E_\mathrm{n} \left|\psi_\mathrm{n}\right\rangle . \tag{6.4}$$

The energy of the electronic state therefore acts as an effective potential for the nuclear motion. The kinetic energy, in turn, can be written as

$$\hat{T}_\mathrm{n} = \frac{1}{2} \sum_\alpha m_\alpha \left(\dot{\hat{\boldsymbol{r}}}_\mathrm{n}\right)_\alpha^2 , \tag{6.5}$$

where α runs over all the nuclei and the dot denotes the time derivative. In general, the nuclei can be displaced from their equilibrium position, e.g., due to vibrational motion. In more general terms, the position of each nucleus can be expressed as

$$\left(\hat{\boldsymbol{r}}_\mathrm{n}\right)_\alpha = \hat{\boldsymbol{r}}_\mathrm{c} + \hat{\boldsymbol{S}}^{-1} \left(\hat{\boldsymbol{q}}_\alpha^0 + \Delta\hat{\boldsymbol{q}}_\alpha\right) , \tag{6.6}$$

where $\hat{\boldsymbol{r}}_\mathrm{c}$ is the centre-of-mass position, $\hat{\boldsymbol{q}}_\alpha^0$ is the equilibrium position of the α-th nucleus in the molecule-fixed frame, and $\Delta\hat{\boldsymbol{q}}_\alpha$ its displacement from that position. The origin of the molecule-fixed frame is set to the centre of mass $\hat{\boldsymbol{r}}_\mathrm{c}$ such that $\sum_\alpha m_\alpha \hat{\boldsymbol{q}}_\alpha^0 = 0$. The rotation matrix $\hat{\boldsymbol{S}}$ has dimension 3×3 and connects the molecule-fixed axes a, b, c (coordinates $\hat{\boldsymbol{q}}$) with the space-fixed axes X, Y, Z (coordinates $\hat{\boldsymbol{r}}$); an overview over the notation differences between the molecule- and spaced-fixed frame is given in Tab. 6.1. Using Eulerian angles $(\vartheta, \varphi, \chi)$, it can be written as [37]

$$S(\chi, \theta, \phi) = R_c(\chi) R_{Y'}(\theta) R_Z(\phi), \tag{6.7}$$

where R_i are rotation matrices. The X' axis is given by the intersection of the XY and cZ axis. Equation (6.7) is composed of three rotations: (1) the rotation of X and Y by an angle ϕ about Z into X' and Y', (2) the rotation of X' and Z by an angle θ about Y' into X'' and c, (3) the rotation of X'' and Y' by an angle χ about c into a and b. If $\boldsymbol{r}$ is a vector in the space-fixed frame and $\boldsymbol{q}$ is a vector in the molecule-fixed frame, they are connected via $\boldsymbol{q} = S\boldsymbol{r}$.

frame	axes	indices	proj. op.	proj. q.	ladder op.	dipole
molecule-fixed	abc	$\alpha\beta\gamma$	$\hat{J}_\mathrm{c}$	K	$\hat{J}^\pm$	$\hat{\boldsymbol{\mu}}$
space-fixed	XYZ	ijk	$\hat{J}_\mathrm{Z}$	M	$\hat{J}_\pm$	$\hat{\boldsymbol{d}}$

Table 6.1: Overview about the notation used to declare the space- and molecule-fixed axes. "proj. q." and "proj. op." stand for the projection quantum number and the corresponding operator, respectively. "ladder op." are the operators which change the corresponding projection by one. "dipole" is the dipole moment operator.

There are two constraints resulting from Eq. (6.6). The left-hand side has $3N$ degrees of freedom. On the right-hand side, there are three constraints contained in the centre-of-mass position $\hat{\boldsymbol{r}}_\mathrm{c}$ and three implicitly in the rotation matrix $\hat{\boldsymbol{S}}$. This reduces the number of degrees of freedom for the displacement $\Delta\hat{\boldsymbol{q}}_\alpha$ to $3N-6$ ($3N-5$ for linear molecules). The necessary constraints are imposed by the Eckart conditions [157]. The first condition, $\sum_\alpha m_\alpha \Delta\hat{\boldsymbol{q}}_\alpha = 0$, requires that the centre of mass does not change during the displacement. The second, $\sum_\alpha m_\alpha \hat{\boldsymbol{q}}^0_\alpha \times \Delta\hat{\boldsymbol{q}}_\alpha = 0$, excludes a change in angular momentum. When inserting Eq. (6.6) into Eq. (6.5) and employing these conditions, the kinetic energy can be written as

$$\hat{T}_\mathrm{n} = \frac{1}{2}\hat{\boldsymbol{\omega}}^T\hat{\boldsymbol{I}}\hat{\boldsymbol{\omega}} + \frac{1}{2}\sum_\alpha m_\alpha(\dot{\hat{\boldsymbol{q}}}_\alpha)^2 + \sum_\alpha m_\alpha\hat{\boldsymbol{\omega}}\cdot\left(\Delta\hat{\boldsymbol{q}}_\alpha\times\Delta\dot{\hat{\boldsymbol{q}}}_\alpha\right), \tag{6.8}$$

where $\hat{\boldsymbol{\omega}}$ is the angular velocity given by $(\hat{\boldsymbol{S}}\dot{\hat{\boldsymbol{S}}}^{-1})_{jk} = -\epsilon_{ijk}\hat{\omega}_i$, and $\hat{\boldsymbol{I}}$ the moment of inertia tensor with $\hat{I}_{ij} = \sum_\alpha m_\alpha(\delta_{ij}(\hat{\boldsymbol{q}}^0_{\alpha,k})^2 - \hat{\boldsymbol{q}}^0_{\alpha,i}\hat{\boldsymbol{q}}^0_{\alpha,j})$ where i,j,k indicate the spatial coordinates x,y,z in the molecule-fixed frame. The first term of Eq. (6.8) describes the rotational energy of the rigid molecule, the second the kinetic energy of its vibrations, and the third the vibration-rotation interaction. Typical rotational frequencies are of the order of 10^8 to 10^{12} Hz, vibrational frequencies 10^{12} to 10^{13} Hz [154]. As we are interested in coupling the molecules to transitions between different Rydberg states which lie in the microwave range (tens of Gigahertz), vibrational transition and vibration-rotation interactions can be neglected to a good approximation [37]. The remaining term is the rotational kinetic energy which can be written as

$$\hat{T}_\mathrm{rot} = \frac{1}{2}\hat{\boldsymbol{J}}^T\hat{\boldsymbol{I}}^{-1}\hat{\boldsymbol{J}}, \tag{6.9}$$

with the molecule-fixed, rotational angular momentum $\hat{J}_i = \partial\hat{T}_k/\partial\hat{\omega}_i = \hat{I}_{ij}\hat{\omega}_j$. If the symmetric matrix $\hat{I}_{ij}$ is diagonalised, the rotation of a rigid molecule can be described by

$$\hat{T}_\mathrm{rot} = \frac{1}{2}\left(I_a\hat{\omega}_a^2 + I_b\hat{\omega}_b^2 + I_c\hat{\omega}_c^2\right) = A\hat{J}_\mathrm{a}^2 + B\hat{J}_\mathrm{b}^2 + C\hat{J}_\mathrm{c}^2, \tag{6.10}$$

where a,b and c denote the principal axes of the inertia tensor, and the principal rotational constants are $A = 1/(2I_a)$ and accordingly for B and C. We assume that they are ordered as

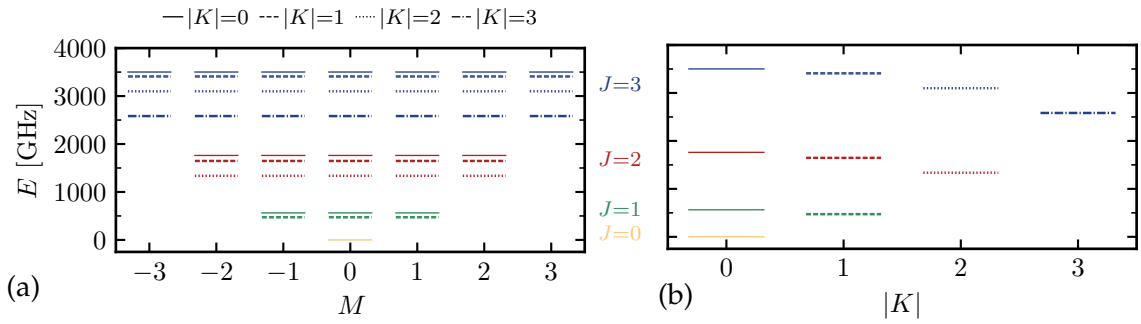

Figure 6.1: Rotational energy levels of the oblate symmetric top rotor exemplary for the ammonia molecule as a function of M (a) and K (b) for $J \leq 3$. The line colour indicates the value of J and the line style the $|K|$ value. All but $K = 0$ levels show a weak inversion splitting (barely visible on this scale).

$A \geq B \geq C$. The essence of the rigid-rotor approximation is that A, B and C are constants which results from neglecting variations due to vibrational motion [37].

In the following, we describe the energy levels and eigenstates of the rotational Hamiltonian. We assume the molecule to be in its electronic and vibrational ground state. As mentioned before, the energy needed to induce transitions in electronic and vibrational degrees of freedom is much larger than the ones we consider in the following ($\sim 10^{14} - 10^{15}$ Hz and $10^{12} - 10^{13}$ Hz, respectively) [154] and can hence be neglected.

6.1.2 Symmetric top molecules

Depending on the relative size of the rotational constants, molecules can be classified into one of four main categories:

1. Linear molecules: $I_a = I_b = 0$
2. Spherical top: $I_a = I_b = I_c$
3. Symmetric top: (a) prolate: $I_a < I_b = I_c$ (cigar shaped)
   (b) oblate: $I_a = I_b < I_c$ (saucer shaped)
4. Asymmetric top: $I_a < I_b < I_c$

Since we chose to consider the interaction between Rydberg atoms and ammonia molecules, which are oblate symmetric tops (3b), we focus on this kind in the following. All results can be generalised to prolate symmetric and asymmetric tops without difficulties. In case of oblate symmetric tops, the rotational Hamiltonian from Eq. (6.10) can be written as

$$\hat{H}_{\text{obl}} = B\left(\hat{J}_{\text{a}}^2 + \hat{J}_{\text{b}}^2\right) + C\hat{J}_{\text{c}}^2 = B\hat{\boldsymbol{J}}^2 + (C - B)\,\hat{J}_{\text{c}}^2, \tag{6.11}$$

where $\hat{J}_\mathrm{c}$ is the projection of the angular momentum $\hat{\boldsymbol{J}}$ onto the molecular symmetry axis. For ammonia, the rotational constants are $B = 293.681\,\mathrm{GHz}$ and $C = 190.403\,\mathrm{GHz}$ [158]. The eigenvalues of the Hamiltonian in Eq. (6.11) can be derived to be [37]

$$E_{JK}^\mathrm{rot} = BJ(J+1) + (C-B)K^2, \tag{6.12}$$

corresponding to the energy of the eigenstates $|JK\rangle$. Here, J is the quantum number associated with $\hat{\boldsymbol{J}}$ and K is the projection quantum number on the molecular symmetry axis associated with $\hat{J}_\mathrm{c}$. The energies are shown in Fig. 6.1 for the case of ammonia. Note that symmetric top eigenstates with $\pm K$ are degenerate resulting from the square in Eq. (6.12).

So far, we have considered the angular momentum and its projection in the molecule-fixed frame which leads to the quantum numbers J and K, respectively. However, it is also possible to treat the problem in the space-fixed coordinate system. Equivalently to the transformation of coordinates in Eq. (6.6), the rotation matrix $\hat{\boldsymbol{S}}$ transforms operators from the molecule-fixed to the space-fixed frame, e.g. $\hat{J}_\alpha = \hat{\boldsymbol{S}}\hat{J}_\mathrm{i}$. Note that we employ Greek letters α, β, γ to indicate the molecule-fixed frame while Latin indices i, j, k indicate the space-fixed frame (cf. Tab. 6.1). It can be shown [37] that the two angular momenta commute with each other, $\left[\hat{J}_\mathrm{i},\, \hat{J}_\alpha\right] = 0$, and with $\hat{\boldsymbol{J}}^2$. Therefore, the eigenstates of the oblate symmetric top[1] Hamiltonian can be characterised by the complete set of commuting observables $\hat{\boldsymbol{J}}^2$, $\hat{J}_\mathrm{c}$ and $\hat{J}_\mathrm{Z}$. They can be written as $|JKM\rangle$ and fulfil

$$\hat{\boldsymbol{J}}^2\,|JKM\rangle = J(J+1)\,|JKM\rangle\,, \tag{6.13a}$$
$$\hat{J}_\mathrm{c}\,|JKM\rangle = K\,|JKM\rangle\,, \tag{6.13b}$$
$$\hat{J}_\mathrm{Z}\,|JKM\rangle = M\,|JKM\rangle\,, \tag{6.13c}$$
$$\hat{J}^\pm\,|JKM\rangle = \sqrt{(J\mp K)(J\pm K+1)}\,|JK\pm 1M\rangle\,, \tag{6.13d}$$
$$\hat{J}_\pm\,|JKM\rangle = \sqrt{(J\mp M)(J\pm M+1)}\,|JKM\pm 1\rangle\,, \tag{6.13e}$$

where $\hat{J}^\pm = \hat{J}_\mathrm{a} \pm i\hat{J}_\mathrm{b}$ changes the molecule-fixed projection quantum number K by one, and $\hat{J}_\pm = \hat{J}_\mathrm{X} \pm i\hat{J}_\mathrm{Y}$ changes the space-fixed projection quantum number M by one. Finally, the molecules have to obey parity conservation in free space, as the Hamiltonian is invariant under this symmetry operation (as can be seen more easily in spatial representation given in e.g. [38]). While the states $|JKM\rangle$ are no parity eigenstates, the superpositions of degenerate eigenstates

$$|\psi^\pm_{J|K|M}\rangle = \frac{1}{\sqrt{2}}\big(\,|J|K|M\rangle \pm |J\text{-}|K|M\rangle\,\big) \tag{6.14}$$

are eigenstates of opposite parity. When considering the dipole matrix elements, it follows that transitions are only allowed between states of opposite parity, $|\psi^\pm_{J|K|M}\rangle \leftrightarrow |\psi^\mp_{J|K|M}\rangle$ [38].

[1] For prolate symmetric tops, $\hat{J}_\mathrm{c}$ is replaced by $\hat{J}_\mathrm{a}$.

	$J' = J+1$	$J' = J$	$J' = J+1$
$\langle J\|\|\hat{\boldsymbol{S}}\|\|J'\rangle$	$\frac{1}{(J+1)\sqrt{(2J+1)(2J+3)}}$	$\frac{1}{J(J+1)}$	$\frac{1}{J\sqrt{(2J+1)(2J-1)}}$
$\langle JK\|s_c\|J'K\rangle$	$\sqrt{(J+K+1)(J-K+1)}$	K	$\sqrt{(J+K)(J-K)}$
$\langle JK\|s^{\pm}\|J'K\pm1\rangle$	$\mp\sqrt{(J\pm K+1)(J\pm K+2)}$	$\sqrt{(J\mp K)(J\pm K+1)}$	$\pm\sqrt{(J\mp K)(J\mp K-1)}$
$\langle JM\|s_Z\|J'M\rangle$	$\sqrt{(J+M+1)(J-M+1)}$	M	$\sqrt{(J+M)(J-M)}$
$\langle JM\|s_{\mp}\|J'M\pm1\rangle$	$\mp\sqrt{(J\pm M+1)(J\pm M+2)}$	$\sqrt{(J\mp M)(J\pm M+1)}$	$\pm\sqrt{(J\mp M)(J\mp M-1)}$

Table 6.2: Matrix elements of the symmetric top states for the evaluation of Eq. (6.18) [37]. The first row shows the reduced matrix element independent of K and M, the next two rows show the matrix elements regarding the molecule-fixed frame with $s^{\pm} = s_a \pm i s_b$, and the last two rows show the matrix elements regarding the space-fixed frame with $s_{\mp} = s_X \mp i s_Y$.

Due to the pyramidal shape of ammonia, it possesses a permanent electric dipole moment $\hat{\boldsymbol{\mu}}$ (in the molecule-fixed frame) oriented along its symmetry axis, i.e. the c-axis. In order to calculate the interaction of ammonia (or any other polar molecule) with Rydberg atoms, we require the dipole matrix elements in the space-fixed frame, $\langle\psi|\hat{\boldsymbol{d}}|\psi\rangle$. To this end, the total molecular wave function is written as a product of the electronic part, $|\psi_e\rangle$, and the nuclear part, which can again be written as a rotational and a vibrational part, $|\psi_n\rangle = |\psi_{\text{vib}}\rangle\,|\psi_{\text{rot}}\rangle$. The expectation value of the dipole moment can then be expressed as

$$\langle\psi|\hat{\boldsymbol{d}}|\psi\rangle = \langle\psi_{\text{rot}}|\hat{\boldsymbol{d}}_{\text{ev}}|\psi_{\text{rot}}\rangle \tag{6.15}$$

with $\hat{\boldsymbol{d}}_{\text{ev}} = \langle\psi_e\psi_{\text{vib}}|\hat{\boldsymbol{d}}|\psi_e\psi_{\text{vib}}\rangle$. The dipole moment operator in the molecule-fixed frame, $\hat{\boldsymbol{\mu}}$, is connected to the one in the space-fixed frame via

$$\hat{\boldsymbol{d}}_{\text{ev}} = \hat{\boldsymbol{S}}\hat{\boldsymbol{\mu}}. \tag{6.16}$$

In the basis $|JKM\rangle$, the matrix elements of the i-th component of $\hat{\boldsymbol{d}}$ can be evaluated as

$$\langle JKM|\hat{d}_{\text{ev,i}}|J'K'M'\rangle = \sum_{\alpha}\mu_{\alpha}\,\langle JKM|\hat{S}_{\alpha i}|J'K'M'\rangle\,. \tag{6.17}$$

The matrix elements of the rotation matrix are given by the Wigner-Eckart theorem,

$$\langle JKM|\hat{S}_{\alpha i}|J'K'M'\rangle = \langle J||\hat{\boldsymbol{S}}||J'\rangle\,\langle JK|s_{\alpha}|J'K'\rangle\,\langle JM|s_i|J'M'\rangle\,. \tag{6.18}$$

The matrix elements on the right-hand side can be calculated analytically [37] and are listed in Tab. 6.2. The resulting selection rules are $\Delta J = 0, \pm1$, $\Delta K = 0, \pm1$ and $\Delta M = 0, \pm1$. For oblate

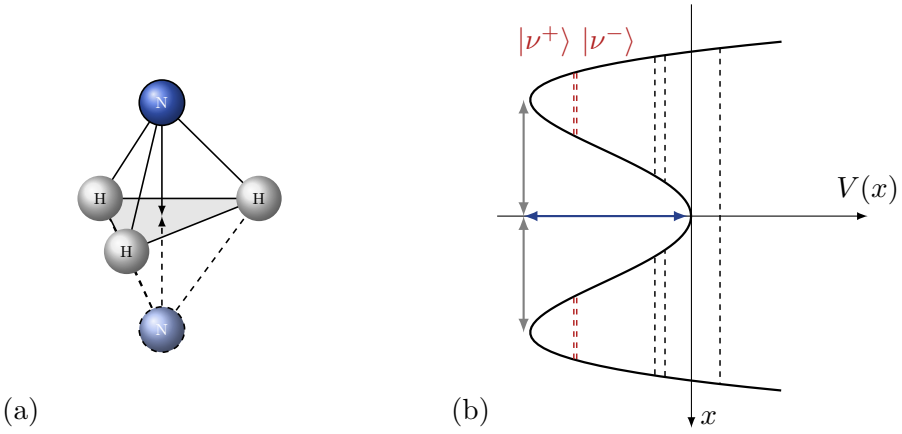

Figure 6.2: Inversion of ammonia. (a) Pyramidal shape of the ammonia molecule in its two orientations. (b) Double-well potential of the inversion vibration mode. The red levels indicate the first inversion mode.

symmetric tops, the dipole moment is oriented along the c axis, i.e. $\mu_a = \mu_b = 0$. As a result, the elements with $\alpha = a$ and b vanish. From $\langle JK|\hat{s}_c|J'K'\rangle$, which is vanishing unless $K = K'$, we obtain the selection rule $\Delta K = 0$ for symmetric top molecules.

Incidentally, if a DC field along the Z axis is applied, $\boldsymbol{F}_{\mathrm{DC}} = F_{\mathrm{DC}}\boldsymbol{e}_Z$, the molecules show a Stark splitting. The quantisation axis of the space-fixed frame is then defined by the DC field and only matrix elements with $i = Z$ survive. Oblate symmetric top molecules show a linear Stark shift which is proportional to the matrix element $\langle JKM|\hat{S}_{cZ}|JKM\rangle$. Higher orders can be calculated using perturbation theory. The existence of a linear Stark shift is correlated to the non-vanishing permanent electric dipole moment of symmetric top molecules. For $F_{\mathrm{DC}} = 1\,\frac{\mathrm{V}}{\mathrm{cm}}$ and $J = K = 1$, the Stark shift of ammonia is of the order of $100\,\mathrm{kHz}$ [37]. It is thus three orders of magnitude smaller than for Rydberg atoms and can be neglected.

6.1.3 Inversion of ammonia

Ammonia is an oblate symmetric top molecule constituted of three hydrogen atoms and one nitrogen atom arranged in a pyramidal shape as shown in Fig. 6.2 (a). Due to this arrangement, the molecule has a threefold axis of symmetry, meaning that rotations by $2\pi/3$ around the symmetry axis leave the Hamiltonian unchanged. The same is true for space inversion (transforming (x, y, z) into $(-x, -y, -z)$) and interchange of two hydrogenic nuclei. The eigenstates of the molecule should therefore be unaltered under these symmetry operations (up to a global phase). The basis states of symmetric top molecules, $|JKM\rangle$, however, do not fulfil this condition. It turns out that the superposition of $\big|\, J|K|M\big\rangle$ and $\big|\, J\text{-}|K|M\big\rangle$ (i.e. $|\psi^{\pm}_{J|K|M}\rangle$ in Eq. (6.14)) does not lead to eigenstates of the symmetry operations either. Rather, it is necessary to consider

the nuclear spin states. As a result, the eigenstates can be written as [159]

$$|\psi^{\epsilon}_{J|K|M}\rangle = \frac{1}{\sqrt{2}}\Big(|\, J|K|M\rangle \otimes \left|\psi^{|K|}_{H_3}\right\rangle + \epsilon|\, J\text{-}|K|M\rangle \otimes \left|\psi^{\text{-}|K|}_{H_3}\right\rangle\Big) \tag{6.19}$$

with $\epsilon = \pm 1$ ($\epsilon = +1$ for $K = 0$). The state $\left|\psi^{\pm|K|}_{H_3}\right\rangle$ is a superposition of the spin states of the three hydrogen atoms involving all possible permutations. $|K|$ appears as a phase factor which guarantees that $|\psi^{\epsilon}_{J|K|M}\rangle$ is an eigenstate of the symmetry operations. The specific form of $\left|\psi^{\pm|K|}_{H_3}\right\rangle$ is not relevant here (but can be found e.g. in [159]), as we are only interested in calculating the dipole matrix elements which do not depend on the nuclear spin.

In addition to the threefold axis of symmetry modifying the rotational states, ammonia shows another relevant property. The nitrogen atom can be located on either side of the base of the pyramid, which is constituted of the hydrogen atoms (cf. Fig. 6.2 (a)). This results in the nitrogen atom seeing a double-well potential as shown in Fig. 6.2 (b) where each well corresponds to the nitrogen atom being on either side of hydrogenic plane. This movement is a vibrational mode and is called the inversion, or "umbrella inversion", of nitrogen, as the molecule is flipped "inside out". If the potential barrier was infinitely high, the two states would be degenerate. When the potential barrier is finite, however, the nitrogen atoms can tunnel through the plane, resulting in an inversion of the molecular structure as shown in Fig. 6.2 (a). The two non-stationary states of nitrogen being left or right of the hydrogenic plane couple and lead to a splitting of the energy level for a sufficiently low barrier. The two lowest lying vibrational states are given by the symmetric and antisymmetric superposition of the nitrogen atom being left or right of the barrier (red levels in Fig. 6.2 (b)). The antisymmetric state, which we label $|\nu^-\rangle$, lies above the symmetric state, $|\nu^+\rangle$. The mean frequency of the inversion mode, $\omega^0_{\text{inv}} = 23.786\,\text{GHz}$ [38], and its transition dipole moment, $d_{\text{inv}} = 1.468\,\text{D}$ [160], were measured experimentally. One consequence of the inversion is that the molecule no longer has a permanent dipole moment. This can be understood intuitively as the nitrogen atom being located on both sides of the hydrogenic plane "at the same time". Instead, the transition dipole moment between the two inversion states plays a crucial role, which becomes apparent in the next section. Different from symmetric top molecules without inversion splitting, ammonia thus does not possess a linear Stark shift [161]. If a strong DC field is employed, the inversion states mix such that the nitrogen atom is located primarily left or right of the hydrogenic plane [38].

Experiments reveal that the inversion spectrum is very rich showing many spectral lines in the microwave regime (see Ref. [162] and references therein). It turns out that the inversion mode shows a fine structure which depends on the rotational quantum numbers J and K [163]. This can be understood qualitatively using classical arguments. The rotation of the molecule induces a centrifugal force proportional to the square of the angular momentum about this axis, i.e. K^2, which flattens the potential and increases the inversion splitting. Rotations around the axis perpendicular to the symmetry axis, however, elongate the molecule, increasing the potential

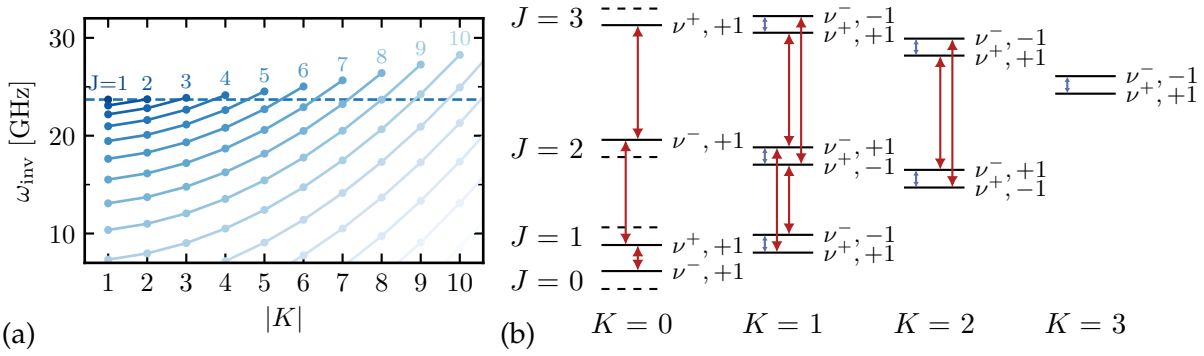

Figure 6.3: (a) Inversion splitting as a function of J and K as given in Eq. (6.20). (b) Rotation-inversion energy levels of ammonia and allowed dipole transitions for $J \leq 3$. Blue arrows indicate transitions within one inversion doublet, red arrows between inversion states with different J values. The label next to the states indicate the inversion level, $\nu^{\pm}$, and the ϵ value (± 1) used in Eq. (6.19). Dashed lines indicate missing states. The inversion splitting is not to scale.

barrier and decreasing the inversion splitting proportional to $J(J+1) - K^2$. When combining both effects, the inversion splitting can be written as [38]

$$\omega_{\text{inv}} = \omega_{\text{inv}}^0 - a\left(J(J+1) - K^2 + bK^2\right), \tag{6.20}$$

where higher orders $\mathcal{O}(J^4, J^2K^2, K^4)$ have been neglected [163]. The values of $a = 151.5\,\text{MHz}$ and $b = 59.9\,\text{MHz}$ were determined experimentally [38]. The dependence of ω_{inv} on J and K is shown in Fig. 6.3 (a).

If we now combine the inversion mode $|\nu^{\pm}\rangle$ and rotations $|\psi^{\epsilon}_{J|K|M}\rangle$, the eigenstates of ammonia can be written as a tensor product, $|\nu^{\pm}\rangle \otimes |\psi^{\epsilon}_{J|K|M}\rangle$. It can be shown that for fermionic nuclei (such as hydrogen for ammonia), the eigenstates have to fulfil [159]

$$\nu^{\pm}\,\epsilon\,(-1)^J = -1 \tag{6.21}$$

with $\nu^{\pm} = \pm 1$ characterising the inversion, i.e. $+1$ for the symmetric state $|\nu^+\rangle$ and -1 for the antisymmetric state $|\nu^-\rangle$. It follows that if J is odd (even), the symmetric inversion state $|\nu^+\rangle$ goes with $\epsilon = +1$ ($\epsilon = -1$) and the antisymmetric inversion state $|\nu^-\rangle$ with $\epsilon = -1$ ($\epsilon = +1$), see Fig. 6.3 (b).

Finally, the matrix elements of the eigenstates of ammonia shall be calculated, similar to the general symmetric top molecules shown in Eq. (6.18). The two factors $\langle J||\hat{\boldsymbol{S}}||J'\rangle$ and $\langle JM|s_i|J'M'\rangle$ are not affected by the properties of ammonia discussed above. As ammonia is an oblate symmetric top, the dipole moment is oriented along the c axis and we obtain the selection rules $\Delta J = 0, \pm 1$ and $\Delta K = 0$ (cf. end of Sec. 6.1.2). From Tab. 6.2, it can quickly be seen that the

matrix elements fulfil

$$\langle JK|\hat{s}_{\mathrm{c}}|JK\rangle = K = -\langle J\text{ -}K|\hat{s}_{\mathrm{c}}|J\text{ -}K\rangle\,, \tag{6.22a}$$

$$\langle JK|\hat{s}_{\mathrm{c}}|J+1\,K\rangle = \sqrt{(J+K+1)(J-K+1)} = \langle J\text{ -}K|\hat{s}_{\mathrm{c}}|J+1\text{ -}K\rangle\,. \tag{6.22b}$$

When now evaluating $\langle \nu^{\pm}\,\psi^{\epsilon}_{J|K|M}|\hat{s}_{\mathrm{c}}|\nu^{\pm'}\,\psi^{\epsilon'}_{J'|K|'M'}\rangle$, we find the selection rules

$$\Delta J = 0, \pm 1, \quad \Delta K = 0, \quad M = 0 \not\leftrightarrow M' = 0, \quad \nu^{\pm} \leftrightarrow \nu^{\mp}, \tag{6.23}$$

where $\leftrightarrow$ indicates allowed and $\not\leftrightarrow$ forbidden transitions. The dipole allowed transition for ammonia are shown in Fig. 6.3 (b). For simplicity, we denote the states by $|\nu^{\pm}JKM\rangle \equiv |\nu^{\pm}\rangle \otimes |\psi^{\epsilon}_{J|K|M}\rangle$ with $K = |K| > 0$ from now on. The value of ϵ is implicitly given by Eq. (6.21).

6.2 Modelling the scattering between polar molecules and Rydberg atoms

We develop in this section a suitable model to describe the scattering of polar molecules by Rydberg atoms. The general idea is to consider the particles approaching each other: the polar molecule interacts with the charge distribution of the Rydberg atom, and the strength of this interaction increases as the particles approach. If the particles are (close to) resonance and in suitable states, they interchange energy without emitting radiation. After the collision, the Rydberg atom contains information on the molecule and vice versa. As we discuss later, the energy transfer can serve as a witness for detecting the presence and measuring the state of the molecule. In this section, we develop a model for simulating the scattering process and computing the cross-section; we apply the model to a concrete example in the subsequent Sec. 6.3.

We assume the scattering process between rubidium Rydberg atoms and ammonia molecules[1] and consider a single scattering event only, i.e. one Rydberg atom interacting with one molecule, which is justified if the medium is sufficiently dilute. However, we account for ensemble effects by performing a statistical average over several initial scattering parameters later on. Further, a DC field is applied to induce the Stark effect in the Rydberg atom[2]. The full Hamiltonian can then be written as

$$\hat{H}(t) = \hat{H}^{(0)}_{\mathrm{ryd}} + \hat{V}^{\mathrm{DC}}_{\mathrm{ryd}} + \hat{H}^{(0)}_{\mathrm{mol}} + \hat{V}_{\mathrm{int}}(t), \tag{6.24}$$

where $\hat{H}^{(0)}_{\mathrm{ryd}}$ is the Hamiltonian of the Rydberg atom, $\hat{V}^{\mathrm{DC}}_{\mathrm{ryd}}$ is the interaction of the Rydberg atom with the DC field, $\hat{H}^{(0)}_{\mathrm{mol}}$ is the Hamiltonian of the molecule, and $\hat{V}_{\mathrm{int}}(t)$ is the interaction between the two particles. The latter describes the interaction of the molecule's electric dipole moment with the charge distribution of the Rydberg electron.

[1] Generalisation to other species is straight-forward.

[2] The Stark effect of the molecule is neglected as discussed in Sec. 6.1.2.

$\hat{H}^{(0)}_{\text{ryd}}$ is diagonal in the spherical basis $|\psi_{\text{ryd}}\rangle = |n\ell, m_\ell\rangle$ (using the spectroscopic notation) introduced in Sec. 2.2.2 with eigenenergies as given by Eq. (2.6) (including quantum defects but neglecting spin-orbit coupling). $\hat{V}^{\text{DC}}_{\text{ryd}}$ is given by Eq. (2.19) and gives rise to the Stark effect which can be treated as described in Sec. 2.2 and 3.1.1. In presence of a DC field, the spherical basis is not the eigenbasis of the Rydberg atom. However, low-angular-momentum states, which possess a large quantum defect, can still be labelled by $|n\ell, m_\ell\rangle$ for small DC field values, $F_{\text{DC}} < 5\,\frac{\text{V}}{\text{cm}}$. $\hat{H}^{(0)}_{\text{mol}}$ is diagonal in the basis $|\psi_{\text{mol}}\rangle = |\nu^{\pm} JKM\rangle$ with eigenenergies $E^{\text{rot}}_{JK} \pm E_{\text{inv}}/2$ (as given by Eqns. (6.12) and (6.20)). The combined system of Rydberg atom and molecule can be described in the product basis,

$$|\Psi\rangle = |\psi_{\text{ryd}}\rangle \otimes |\psi_{\text{mol}}\rangle\,, \tag{6.25}$$

where the subscripts label the state of the Rydberg atom and molecule, respectively.

The remainder of this section is organised as follows. We start by discussing the interaction potential $\hat{V}_{\text{int}}(t)$ between the Rydberg atom and the polar molecule in more detail and derive its multipole expansion in Sec. 6.2.1. Afterwards, in Sec. 6.2.2, we elaborate on how to simulate the scattering process between the two particles. Finally, in Sec. 6.2.3, we chose suitable subspaces of the Rydberg atom and molecule in order to study their interaction, and show how to calculate the scattering cross-section numerically.

6.2.1 Multipole expansion of the interaction potential

We model the interaction potential $\hat{V}_{\text{int}}(t)$ as a dipole $\hat{\boldsymbol{d}}$ (the polar molecule) interacting with the field induced by a charge distribution (the orbital of the Rydberg atom's valence electron),

$$\hat{V}_{\text{int}}(t) = \frac{\hat{\boldsymbol{d}} \cdot \left(\hat{\boldsymbol{r}}_{\text{ryd}} - \boldsymbol{r}_{\text{mol}}(t)\right)}{\left|\hat{\boldsymbol{r}}_{\text{ryd}} - \boldsymbol{r}_{\text{mol}}(t)\right|^3}. \tag{6.26}$$

We take $\hat{\boldsymbol{d}}$ to be the transition dipole moment of the inversion mode of ammonia in the space-fixed frame but it could equally be the permanent dipole moment of a polar molecule. $\hat{\boldsymbol{r}}_{\text{ryd}}$ is the position operator of the Rydberg electron. $\boldsymbol{r}_{\text{mol}}(t)$ is the distance from the molecule to the ionic core of the Rydberg atom. We treat this distance classically as discussed in more detail in Sec. 6.2.2.

Evaluating the matrix elements of the full interaction potential is challenging, which is why we perform a multipole expansion. This comes with the additional advantage that contributions of different order can be identified and analysed systematically. The first order term of the multipole expansion corresponds to the well-known dipole-dipole interaction as can be found in textbooks [164]. Nevertheless, we repeat its derivation for completeness and expand the potential beyond what can be found in standard textbooks to third order in the following.

For simplicity, we omit the operator hats in the derivation[1] and write the potential as

$$V(\boldsymbol{r}) = \frac{\boldsymbol{d}\cdot\boldsymbol{r}}{r^3}, \tag{6.27}$$

with $\boldsymbol{r} \equiv \boldsymbol{r}_{\text{ryd}} - \boldsymbol{r}_{\text{mol}}$ and $r = |\boldsymbol{r}|$. We carry out the multipole expansion in Cartesian coordinates and thus calculate the Taylor expansion of $V(\boldsymbol{r})$ for $\boldsymbol{r}_{\text{ryd}} \ll \boldsymbol{r}_{\text{mol}}$, i.e. we assume the distance between the Rydberg atom and the molecule $\boldsymbol{r}_{\text{mol}}$ to be much larger than the size of the Rydberg atom, $\boldsymbol{r}_{\text{ryd}}$. With $\mathcal{T}f(\boldsymbol{r};\boldsymbol{a})$ being the Taylor expansion of a function $f(\boldsymbol{r})$ about a point $\boldsymbol{a}$, we can write the multipole expansion of the interaction potential as

$$\begin{aligned}\mathcal{T}V(\boldsymbol{r};-\boldsymbol{r}_{\text{mol}}) = V(-\boldsymbol{r}_{\text{mol}}) &+ \sum_{\alpha=x,y,z} V_\alpha(-\boldsymbol{r}_{\text{mol}})\, r_{\text{ryd},\alpha} \\ &+ \frac{1}{2}\sum_{\alpha,\beta=x,y,z} V_{\alpha\beta}(-\boldsymbol{r}_{\text{mol}})\, r_{\text{ryd},\alpha}\, r_{\text{ryd},\beta} \\ &+ \frac{1}{6}\sum_{\alpha,\beta,\gamma=x,y,z} V_{\alpha\beta\gamma}(-\boldsymbol{r}_{\text{mol}})\, r_{\text{ryd},\alpha}\, r_{\text{ryd},\beta}\, r_{\text{ryd},\gamma} + \dots \qquad (6.28a)\\ \equiv V_0(-\boldsymbol{r}_{\text{mol}}) + V_1(-\boldsymbol{r}_{\text{mol}}) &+ V_2(-\boldsymbol{r}_{\text{mol}}) + V_3(-\boldsymbol{r}_{\text{mol}}) + \dots, \qquad (6.28b)\end{aligned}$$

where we have used $\boldsymbol{a} = -\boldsymbol{r}_{\text{mol}}$ (since $\boldsymbol{r} = -\boldsymbol{r}_{\text{mol}}$ for $\boldsymbol{r}_{\text{ryd}} = 0$) and $\boldsymbol{r} - \boldsymbol{a} = \boldsymbol{r}_{\text{ryd}}$. In Eq. (6.28a), we have defined the components of vectors as $\boldsymbol{r} = (r_x, r_y, r_z)^T$ and the partial derivatives as

$$V_\alpha(-\boldsymbol{r}_{\text{mol}}) = \left.\frac{\partial V(\boldsymbol{r})}{\partial r_\alpha}\right|_{-\boldsymbol{r}_{\text{mol}}},\ V_{\alpha\beta}(-\boldsymbol{r}_{\text{mol}}) = \left.\frac{\partial^2 V(\boldsymbol{r})}{\partial r_\alpha \partial r_\beta}\right|_{-\boldsymbol{r}_{\text{mol}}},\ V_{\alpha\beta\gamma}(-\boldsymbol{r}_{\text{mol}}) = \left.\frac{\partial^3 V(\boldsymbol{r})}{\partial r_\alpha \partial r_\beta \partial r_\gamma}\right|_{-\boldsymbol{r}_{\text{mol}}}. \tag{6.29}$$

In Eq. (6.28b), we have further defined $V_n(-\boldsymbol{r}_{\text{mol}})$ as the n-th order contribution of the multipole expansion. The matrix elements of each order can most easily be evaluated in the product basis of Eq. (6.25), as the partial derivatives in Eq. (6.29) depend only on molecular degrees of freedom, while the components of $\boldsymbol{r}_{\text{ryd}}$ refer to the Rydberg atom. For example, the first order contribution can be written as

$$\langle\Psi'|V_1(-\boldsymbol{r}_{\text{mol}})|\Psi\rangle = \sum_{\alpha=x,y,z} \langle\psi'_{\text{ryd}}|r_{\text{ryd},\alpha}|\psi_{\text{ryd}}\rangle\, \langle\psi'_{\text{mol}}|V_\alpha(-\boldsymbol{r}_{\text{mol}})|\psi_{\text{mol}}\rangle\,, \tag{6.30}$$

and equivalently for higher orders. The matrix elements of the position operator of the Rydberg atom can be calculated using spherical tensors as explained in Sec. 2.1.3 and Appendix B. The molecular part ultimately only requires the calculation of matrix elements of the dipole operator $\hat{\boldsymbol{d}}$ as we show in the following by evaluating the explicit form of the multipole contributions up to third order.

[1] As a reminder: the dipole moment $\hat{\boldsymbol{d}}$ of the molecule and the position $\hat{\boldsymbol{r}}_{\text{ryd}}$ of the Rydberg electron are operators, the position $\boldsymbol{r}_{\text{mol}}$ of the molecule is a classical vector.

The zeroth-order term corresponds to the monopole contribution and is equal to

$$V_0(-\boldsymbol{r}_{\text{mol}}) = V(-\boldsymbol{r}_{\text{mol}}) = -\frac{\boldsymbol{d}\cdot\boldsymbol{r}_{\text{mol}}}{r_{\text{mol}}^3}. \tag{6.31}$$

This term describes the interaction of the molecular dipole with the Rydberg electron located at the origin. As the total charge of the Rydberg atom is zero, however, we would expect the monopole contribution to vanish. It turns out that a non-vanishing monopole contribution is a relict of having neglected the interaction of the molecular dipole with the ionic core of the Rydberg atom. The two terms cancel out exactly, as the ionic core and the electron have opposite charge. We hence neglect the monopole term without invoking any approximation.

The first order term describes the dipole contribution. When using

$$\frac{\partial}{\partial r_\alpha}\frac{1}{r^3} = -\frac{3r_\alpha}{r^5},$$

the partial derivative of the potential from Eq. (6.29) equals

$$V_\alpha(-\boldsymbol{r}_{\text{mol}}) = \frac{d_\alpha}{r_{\text{mol}}^3} - \frac{3\,\boldsymbol{d}\cdot\boldsymbol{r}_{\text{mol}}\,r_{\text{mol},\alpha}}{r_{\text{mol}}^5}, \tag{6.32}$$

which depends on the molecule only. The matrix elements of the α component of the dipole operator, $\hat{d}_\alpha$, can be calculated as described in Sec. 6.1, resulting in the selection rules of Eq. (6.23). The Rydberg part, $\hat{r}_{\text{ryd},\alpha}$, requires the evaluation of a rank-one tensor $T_q^{(1)}$ (cf. Eq. (2.13)), i.e. matrix elements of $\hat{x}$, $\hat{y}$, and $\hat{z}$. This leads to the well-known dipole selection rules for the Rydberg atom

$$\Delta\ell = \pm 1, \quad \Delta m_\ell = 0, \pm 1 \tag{6.33}$$

as explained in Appendix B.1. When combing both, i.e. evaluating the sum over α in Eq. (6.28a), we arrive at the well-known formula for the dipole-dipole-interaction

$$\hat{V}_1(-\boldsymbol{r}_{\text{mol}}) = \frac{\hat{\boldsymbol{d}}\cdot\hat{\boldsymbol{r}}_{\text{ryd}}}{r_{\text{mol}}^3} - \frac{3\Big(\hat{\boldsymbol{d}}\cdot\boldsymbol{r}_{\text{mol}}\Big)\Big(\hat{\boldsymbol{r}}_{\text{ryd}}\cdot\boldsymbol{r}_{\text{mol}}\Big)}{r_{\text{mol}}^5}, \tag{6.34}$$

where we have added the operator hats for clarity and which scales as r_{mol}^{-3} as expected.

The second order term contains the quadrupole contribution of the Rydberg atom's charge distribution. The molecular part can be calculated to be

$$V_{\alpha\beta}(-\boldsymbol{r}_{\text{mol}}) = \frac{3}{2}\left(\frac{\boldsymbol{d}\cdot\boldsymbol{r}_{\text{mol}}\,\delta_{\alpha\beta} + 2d_{\text{mol},\alpha}r_{\text{mol},\beta}}{r_{\text{mol}}^5} - \frac{5\,\boldsymbol{d}\cdot\boldsymbol{r}_{\text{mol}}\,r_{\text{mol},\alpha}r_{\text{mol},\beta}}{r_{\text{mol}}^7}\right), \tag{6.35}$$

which again only requires the calculation of the dipole moments matrix elements similarly as for

the dipole case. For the Rydberg part, we need to evaluate matrix elements of rank-two tensors $T_q^{(2)}$, i.e. matrix elements of the products $\hat{x}\hat{x}$, $\hat{x}\hat{y}$, and so forth. The resulting quadrupole selection rules for the Rydberg atom are

$$\Delta\ell = 0, \pm 2, \quad \Delta m = 0, \pm 1, \pm 2, \tag{6.36}$$

as discussed in Appendix B.2. Inserting Eq. (6.35) into Eq. (6.28a) gives the formula for the dipole-quadrupole interaction,

$$\hat{V}_2(-\boldsymbol{r}_{\text{mol}}) = -\frac{3}{2}\left(\frac{2\left(\hat{\boldsymbol{d}}\cdot\hat{\boldsymbol{r}}_{\text{ryd}}\right)\left(\hat{\boldsymbol{r}}_{\text{ryd}}\cdot\boldsymbol{r}_{\text{mol}}\right)+\left(\hat{\boldsymbol{d}}\cdot\boldsymbol{r}_{\text{mol}}\right)\hat{\boldsymbol{r}}_{\text{ryd}}^2}{r_{\text{mol}}^5} - \frac{5\left(\hat{\boldsymbol{d}}\cdot\boldsymbol{r}_{\text{mol}}\right)\left(\hat{\boldsymbol{r}}_{\text{ryd}}\cdot\boldsymbol{r}_{\text{mol}}\right)^2}{r_{\text{mol}}^7}\right), \tag{6.37}$$

which scales as r_{mol}^{-4}.

Lastly, we consider the next higher order, namely the octupole contribution. The molecular part can be calculated to be [5]

$$\begin{aligned} V_{\alpha\beta\gamma}(-\boldsymbol{r}_{\text{mol}}) =& \frac{1}{2}\left(-\frac{3\,d_\alpha\,\delta_{\beta\gamma}}{r_{\text{mol}}^5} + \frac{15\left(\boldsymbol{d}\cdot\boldsymbol{r}_{\text{mol}}\,r_{\text{mol},\alpha}\,\delta_{\beta\gamma} + d_\alpha\,r_{\text{mol},\beta}\,r_{\text{mol},\gamma}\right)}{r_{\text{mol}}^7}\right. \\ &\left. - \frac{35\boldsymbol{d}\cdot\boldsymbol{r}_{\text{mol}}\,r_{\text{mol},\alpha}\,r_{\text{mol},\beta}\,r_{\text{mol},\gamma} + 105\,d_\alpha\left(r_{\text{mol},\alpha}^3\,r_{\text{mol},\gamma}\,\delta_{\alpha\beta} - r_{\text{mol},\alpha}^4\,\delta_{\alpha\beta\gamma}\right)}{r_{\text{mol}}^9}\right), \end{aligned} \tag{6.38}$$

which scales as r_{mol}^{-5}. For the Rydberg part, we need to evaluate matrix elements of rank-three tensors $T_q^{(3)}$, i.e. the products $\hat{x}\hat{x}\hat{x}$, $\hat{x}\hat{x}\hat{y}$, and so forth, as discussed in Appendix B.3. The octupole selection rules for the Rydberg atom result in

$$\Delta l = \pm 1, \pm 3, \quad \Delta m = 0, \ldots, \pm 3. \tag{6.39}$$

The formula for the dipole-octupole interaction, $\hat{V}_3(-\boldsymbol{r}_{\text{mol}})$, is not required for computing the matrix elements of the potential, since Eq. (6.38) in combination with Eq. (6.28a) is sufficient. As $\hat{V}_3(-\boldsymbol{r}_{\text{mol}})$ is moreover very complex and does not provide any further insight, we do not calculate it explicitly.

Using these equations, we are able to evaluate the matrix elements of the interaction potential up to third order in the multipole expansion. This allows for simulating and studying the dipole-dipole, dipole-quadrupole and dipole-octupole interaction between Rydberg atoms and polar molecules.

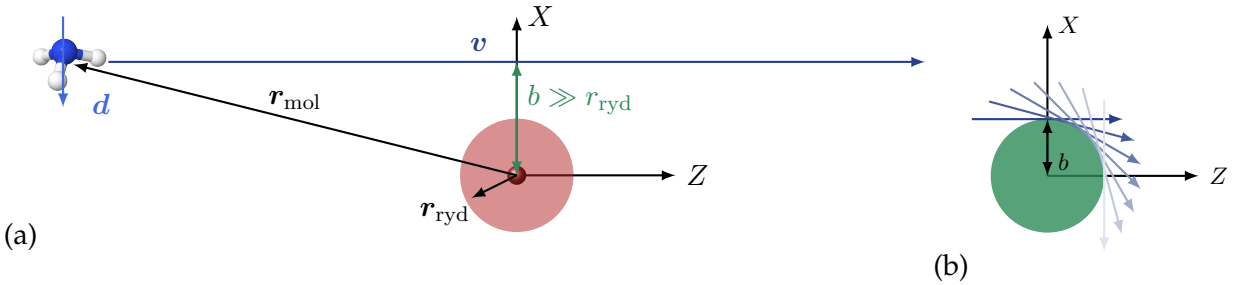

Figure 6.4: (a) Classical scattering trajectory between the molecule (blue) and the Rydberg atom (red) if the molecule flies in Z-direction as given in Eq. (6.41). The parameters are explained in the main text. (b) Direction of the trajectory $\boldsymbol{r}_{\text{mol}}^{\vartheta}(t)$ of Eq. (6.40) for different angles ϑ between the trajectory and the Z-axis; from $\vartheta = 0$ (dark blue, corresponding to the trajectory shown in (a)) to $\pi/2$ (light blue). The green circle indicates the impact parameter b which gives the minimal distance between the two dipoles.

6.2.2 Scattering process

We now turn to the description of the scattering process itself and consider a single scattering event only, as pointed out above. To this end, we assume the two particles to be initially infinitely far apart; they approach each other and finally move away from each other again. The process can be separated into two parts: the external degrees of freedom, i.e. the movement of the particles in space which we describe classically, and the internal degrees of freedom which we describe quantum mechanically.

We start with the classical scattering trajectory, see Fig. 6.4 (a). We set the origin of the coordinate system to the position of the ionic core of the Rydberg atom. Furthermore, we assume the molecule to perform a uniform motion with constant velocity v. This corresponds to neglecting any change in direction or magnitude of the molecule's translational motion caused by its interaction with the Rydberg atom. However, the electrostatic interaction between the two particles should deflect the molecule from its straight trajectory, especially if the impact parameter b is small. The influence of our approximation can be estimated as follows. As the potential $\hat{V}_{\text{int}}(t)$ is time-dependent, the energy of the internal degrees of freedom is not necessarily conserved during the scattering process. The energy expectation value changes if the particles exchange energy despite having different transitions frequencies. In a quantum description of the scattering process, the total energy is conserved and any internal change in energy causes a change in kinetic energy and vice versa. For most scattering parameters, we find the expected change in kinetic energy to be below 1%, meaning that the deflection is small. As we ultimately average the outcome of the simulation over many initial scattering parameters in order to account for ensemble effects, we expect the fluctuations in kinetic energy to average out. Moreover, as explained in the next section, we exclude very small impact parameters from the calculation of the cross-section, which lead to the largest change in kinetic energy.

The equation of motion for uniform motion is simply given by $\boldsymbol{v}(t) = \boldsymbol{v}_0$ with $|\boldsymbol{v}_0| = v$. Its solution can be written as $\boldsymbol{r}_{\text{mol}}(t) = \boldsymbol{v}_0 t + \boldsymbol{r}_0$. We define the impact parameter b to be the minimal distance between the two particles and we set the zero of time such that $r_{\text{mol}}(t = 0) = r_0 = b$. What is left to be determined is the orientation of the trajectory with respect to the quantisation axis defined by the direction of the DC field. In the most general case, the trajectory can be defined by three angles and the impact parameter b. If we imagine a sphere of radius b around the ionic core of the Rydberg atom, the contact point between the trajectory of the molecule and that sphere can be parametrised by two angles ϕ and θ in standard spherical coordinates. In addition to that, the velocity vector, which determines the direction of the trajectory, can rotate in the tangent plane to the sphere at the contact point which determines the angle χ.

In the following, we limit ourselves to a special case while generalisation to other cases is straight-forward. Namely, we assume the scattering plane to be the XZ plane of the coordinate system, i.e. we set the azimuthal angle $\phi = 0$ and the tangent angle $\chi = 0$. The trajectory of the molecule, as depicted in Fig. 6.4 (a), can then be written as

$$\boldsymbol{r}^{\vartheta}_{\text{mol}}(t) = \boldsymbol{v}_0 t + \boldsymbol{r}_0 = vt \begin{pmatrix} -\sin\vartheta \\ 0 \\ \cos\vartheta \end{pmatrix} + b \begin{pmatrix} \cos\vartheta \\ 0 \\ \sin\vartheta \end{pmatrix}, \tag{6.40}$$

where ϑ is the angle between $\boldsymbol{v}_0$ and the Z-axis[1] as shown in Fig. 6.4 (b). For $\vartheta = 0$, the molecule flies in Z-direction, i.e. parallel to the quantisation axis as shown in Fig. 6.4 (a), leading to

$$\boldsymbol{r}^{0}_{\text{mol}}(t) = vt\, \boldsymbol{e}_Z + b\, \boldsymbol{e}_X. \tag{6.41}$$

For $\vartheta = \pi/2$, it flies in $-X$-direction and the trajectory is perpendicular to the quantisation axis, i.e. $\boldsymbol{r}^{\pi/2}_{\text{mol}}(t) = (-vt, 0, b)^T$. Note that every angle ϑ corresponds to a different experimental setup. If the beam of molecules (or Rydberg atoms) is directed, the orientation of the trajectory can be controlled in the experiment and it is sufficient to consider one specific value of ϑ. If not, for instance when dealing with clouds of particles, averaging over some or all angles might be required.

We now turn to the internal degrees of freedom. They are described by the full Hamiltonian of Eq. (6.24) and treated quantum mechanically. The classical trajectory $\boldsymbol{r}_{\text{mol}}(t)$ of Eq. (6.41) is inserted into the different orders of the multipole expansion of the potential presented in Sec. 6.2.1. This effectively renders them time-dependent. For large distances, the dipole-multipole interaction is very small while it is strongest at $t = 0$, where the separation between the two particles is minimal. The Schrödinger equation under the full Hamiltonian is then solved numerically using the Newton propagator (cf. Sec. 3.1.2) as implemented in the QDYN library [62].

[1] In other words: ϑ is the polar angle θ in spherical coordinates for the special case of an azimuthal angle $\phi = 0$ and an tangent angle $\chi = 0$.

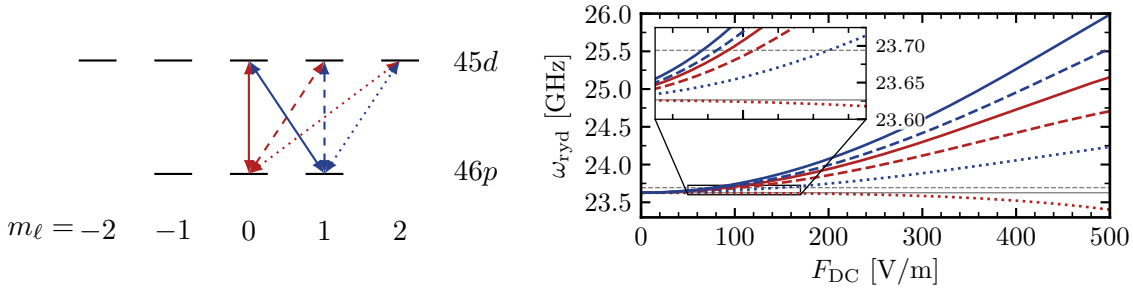

Figure 6.5: Hilbert space of the Rydberg atom at the chosen dipole transitions $46p$ to $45d$ (a) and their Stark splitting (b). The line style indicates the different transitions. Note that all arrows indicate dipole-allowed transitions except for the dotted red one which is dipole-forbidden. The solid, horizontal grey line in (b) indicates the transition frequency at zero field (23.626 GHz), the dashed line indicates the inversion splitting of ammonia for $J = K = 1$ ($\omega_{\mathrm{inv}} = 23.694\,\mathrm{GHz}$). The Stark map is symmetric in $\pm m_\ell$. The inset shows a zoom to $F_{\mathrm{DC}} = 50$ to $170\,\frac{\mathrm{V}}{\mathrm{m}}$ where the Rydberg transitions are in resonance with the ammonia inversion mode.

While ideally, we would assume the two particles to be infinitely far apart at the beginning and in the end of the scattering process, we have to assume finite values for the numerical simulation. More specifically, we choose the initial time of the process, $-t_0 < 0$, such that $\hat{V}_{\mathrm{int}}(-t_0)$ is negligible. The initial distance $|\boldsymbol{r}_{\mathrm{mol}}(-t_0)|$ should therefore be much larger than the impact parameter, $|\boldsymbol{r}_{\mathrm{mol}}(-t_0)| \gg b$, and the radius of the Rydberg atom, $|\boldsymbol{r}_{\mathrm{mol}}(-t_0)| \gg 100\,\mathrm{nm}$. In our simulations, we find a value of $|\boldsymbol{r}_{\mathrm{mol}}(-t_0)| = 2\,\mu\mathrm{m}$ to be suitable and determine t_0 from $t_0 \approx v/r_{\mathrm{mol}}(t_0)$. The final time is set to $+t_0$.

6.2.3 Calculation of the cross-section

Ultimately, we aim to study the influence of the scattering on the particle's internal degrees of freedom. If the two particles possess resonant transitions from their respective initial state, we expect them to exchange energy. The likelihood of a transition event to occur is described by the cross-section σ which, in classical terms, can be interpreted as the effective size of the scattering centre b^2. In the following, we present numerical calculations of the cross-section for the scattering between Rydberg atoms and polar molecules.

First, we identify suitable initial states of the Rydberg atom and molecule such that an energy exchange between them can occur. Regarding the molecule, we consider the inversion mode of ammonia which has a transition frequency around $\omega^0_{\mathrm{inv}} = 23.786\,\mathrm{GHz}$. Note that the exact inversion splitting ω_{inv} depends on J and K as given in Eq. (6.20). We consider a subspace with fixed values of J and K since transitions in J are highly off-resonant (and transitions in K are forbidden for oblate symmetric tops, cf. Eq. (6.23)). The molecular Hilbert space $|\nu^{\pm} JKM\rangle \equiv |\nu^{\pm} M\rangle_{JK}$ has a dimension of $2(2J+1)$ due to the degeneracy in M. We thus need to identify transitions in the Rydberg atom which are near-resonant to the selected inversion mode.

For clarity, we define the splitting between two Rydberg levels with energy E_0 and E_1 as

$$\omega_{\text{ryd}} = E_0 - E_1. \tag{6.42}$$

The detuning between molecular and Rydberg transitions is quantified by

$$\Delta = \omega_{\text{ryd}} - \omega_{\text{inv}}. \tag{6.43}$$

A suitable transition in the Rydberg atom is the dipole transition from $46p$ to $45d$ shown in Fig. 6.5 inspired by the experiment in [151]. At zero field, all transitions between the upper ($45d$ corresponding to E_0) and lower ($46p$ corresponding to E_1) states, as indicated by the arrows in (a), are degenerate with a frequency of $23.626\,\text{GHz}$. They are therefore close to resonance with the ammonia inversion mode (e.g. $\Delta = -68\,\text{MHz}$ for $J = K = 1$). Transitions to higher or lower Rydberg states are sufficiently detuned and can be neglected. In other words, it is sufficient to constrain our analysis to the subspace $46p$ to $45d$ and we introduce the notation

$$|\uparrow, m_\ell\rangle \equiv |45d, m_\ell\rangle \quad \text{with} \quad |m_\ell| \leq 2, \tag{6.44a}$$

$$|\downarrow, m_\ell\rangle \equiv |46p, m_\ell\rangle \quad \text{with} \quad |m_\ell| \leq 1. \tag{6.44b}$$

As the DC field is switched on, each state experiences a different Stark shift thus lifting the degeneracy between states with different $|m_\ell|$ values. As a result, the transition frequencies ω_{ryd} between the lower and upper manifold diverge as shown in panel (b). The Stark shift of the Rydberg states therefore tunes the energy mismatch Δ between the Rydberg atom and the molecule.

It is important to notice that the product Hilbert space can become very large when describing both particles. Each state of the Rydberg atom (molecule) consists of $2\ell+1$ ($2J+1$) sub-levels due to the projection quantum number m_ℓ (M). To reduce the numerical cost during the simulations, we remove states with only off-resonant transitions from the Hilbert space similarly to a RWA in light-matter interactions [9]. Taking the example of two two-level systems, the particles only interact significantly if one particle is in the lower state $|\downarrow\rangle$ and the other one in the upper state $|\uparrow\rangle$. Transitions from the initial states $|\uparrow\uparrow\rangle$ or $|\downarrow\downarrow\rangle$, on the other hand, are highly off-resonant and no energy transfer takes place. We therefore remove these states from the Hilbert space. In our model, neither the molecule nor the Rydberg atom are merely two-level systems. More specifically, we remove the product states $|\uparrow, m_\ell\rangle \otimes |\nu^- M\rangle_{JK}$ and $|\downarrow, m_\ell\rangle \otimes |\nu^+ M\rangle_{JK}$, as they correspond to both the Rydberg atom and the molecule being in the higher or lower energy level, respectively[1]. We have tested numerically that removal of these states does not affect the outcome of the simulations.

We now consider one exemplary scattering event to provide some intuition on the dynamics during the scattering process. We assume the molecule to be initially in the upper inversion state $|\nu^-, M = 0\rangle_{J=1,K=1}$ (the subscript is omitted in the following discussion for clarity). For $J = 1$

[1]Note that the symmetric inversion state $|\nu^+ M\rangle_{JK}$ has a lower energy than the antisymmetric state $|\nu^- M\rangle_{JK}$.

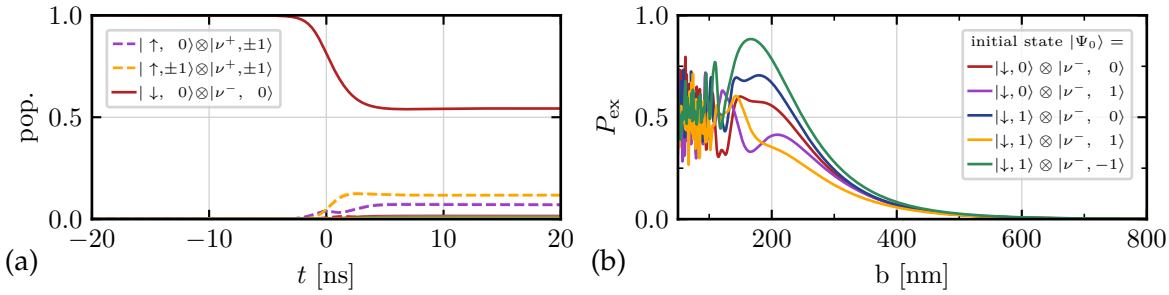

Figure 6.6: (a) Time evolution of the initial state $|\Psi_0\rangle = |\downarrow, m_\ell = 0\rangle \otimes |\nu^-, M = 0\rangle_{11}$ (solid red line) for $F_{\text{DC}} = 0\,\frac{\text{V}}{\text{cm}}$, $v = 100\,\frac{\text{m}}{\text{s}}$ and $b = 250\,\text{nm}$. The line colour indicates the population in different product states as given by the legend (the subscript 11 of the molecular states has been omitted for simplicity). Dashed lines indicate that the two particles exchanged excitation. The lines for positive and negative projection quantum numbers (as indicated by the $\pm$ sign) lie on top of each other. Other product states are populated with less than 2% at any time and are not specified in the legend. (b) Transition probability P_{ex} for different initial states $|\Psi_0\rangle$ as given by the legend as a function of the impact parameter. The remaining parameters are identical to (a).

and $K = 1$, the inversion splitting equals $\omega_{\text{inv}} = 23.694\,\text{GHz}$. Due to selection rules, we expect dipole-dipole interaction to be dominant but we consider all three orders of the multipole expansion in the simulations. We choose as an initial Rydberg state $|\downarrow, m_\ell = 0\rangle$ (using the definition of Eq. (6.44)). We do not employ a DC field, i.e. we set $F_{\text{DC}} = 0\,\frac{\text{V}}{\text{cm}}$, such that all Rydberg transitions are degenerate and equal to $23.626\,\text{GHz}$ (cf. Fig. 6.5 (b)). Moreover, we set the velocity to $v = 100\,\frac{\text{m}}{\text{s}}$ and the impact parameter to $b = 250\,\text{nm}$.

Figure 6.6 (a) shows the evolution of the populations as a function of time. It can be seen that at the end of the interaction, the two particles have exchanged roughly half of the excitation, as the population of the initial state (solid red line) has decreased to 54%. Conversely, the population of states where the Rydberg atom is in the excited and the molecule in the ground state (indicated by dashed lines) have increased. The molecular state $|\nu^+, M = 0\rangle$ is not populated significantly, since the transition $M = 0 \leftrightarrow M' = 0$ is forbidden (cf. Eq. (6.23)). Note that, since we have started in $m_\ell = M = 0$, the dynamics are symmetric with respect to the sign of m_ℓ and M. As a result, states for which both projection quantum numbers are inverted in sign (e.g. $|\uparrow, m_\ell = 0\rangle \otimes |\nu^+, M = 1\rangle$ and $|\uparrow, m_\ell = 0\rangle \otimes |\nu^+, M = -1\rangle$, purple lines) are populated almost equally, such that the corresponding two curves lie on top of each other. The state with negative sign has been plotted in a lighter shade of the same colour. Upon very close examination, the population differs between the two signs by maximally 0.5 percentage points around $1.3\,\text{ns}$ for the yellow curve, and by 0.3 percentage points around $6\,\text{ns}$ for the purple curve (not visible at this scale). The slight asymmetry is caused by higher order multipole contributions.

In order to calculate the cross-section of the process, it is not the time-resolved dynamics of a single scattering event but the final transition probability $P_{\text{ex}}^{\Psi_0}$ we require, where $|\Psi_0\rangle$ denotes the initial state. The transition probability can be defined as one minus the survival probability,

$P_{\text{ex}}^{\Psi_0} = 1 - P_0$ with $P_0 = |\langle\Psi_0|\hat{U}(\infty)\Psi_0\rangle|^2$ being the probability that the system is still in its initial state $|\Psi_0\rangle$ after the scattering process and $\hat{U}(t)$ the time-evolution operator. However, we aim to study whether the particles have exchanged their energy, i.e. if the molecule transitioned from one inversion state to the other, instead of just checking whether it has left its initial state. In case the molecule is initially in the upper inversion state $|\nu^- M\rangle$, the transition probability can be defined as

$$P_{\text{ex}}^{\Psi_0} = \sum_{M'} |\langle\nu^+ M'|U(\infty)\nu^- M\rangle|^2, \tag{6.45}$$

and equivalently, if the molecule is initially in the lower state $|\nu^+ M\rangle$. The transition probability could also be defined in terms of the Rydberg atom. However, since the combined system of Rydberg atom and molecule is closed and since we have removed states with only off-resonant transitions from the Hilbert space, the transition probability is equal for both particles. $P_{\text{ex}}^{\Psi_0}$ can then be interpreted as the probability that the particles have exchanged their excitation during the scattering process.

The transition probability $P_{\text{ex}}^{\Psi_0}$ of Eq. (6.45) depends implicitly both on internal and external parameters of the scattering process. External parameters refer to the classical scattering trajectory; namely the impact parameter b, the relative velocity v between the particles and possibly different orientations of the trajectory with respect to the quantisation axis. Internal parameters refer to the quantum state of both particles, such as their initial states and the detuning Δ between the relevant transitions.

To clarify the role of (some of) these parameters, we calculate the transition probability $P_{\text{ex}}^{\Psi_0}$ for different initial states and different impact parameters b. All other parameters are unchanged with respect to the single trajectory discussed above. Figure 6.6 (b) shows the transition probability for all possible initial states (as indicated by the line colour; the remaining combinations follow from symmetry by inverting the sign of both projection quantum numbers) for impact parameters from $b_{\text{min}} = 50\,\text{nm}$ to $b_{\text{max}} = 800\,\text{nm}$ in steps of $b_{\text{step}} = 1\,\text{nm}$. The shape of these curves is characteristic for the scattering process. For large impact parameters, the interaction between the two particles is very weak and no transition takes place. As b decreases and the two particles approach each other, the transition probability increases. At some critical value of the impact parameter, $P_{\text{ex}}^{\Psi_0}$ reaches its maximal value (here around $b = 180\,\text{nm}$). If the particles come even closer, the accumulated phase oscillates rapidly and the transition probability fluctuates around 50% for all initial states.

Finally, the cross-section can be calculated by averaging the transition probability over all possible trajectories of the molecule with respect to the quantisation axis. If we assume the molecule to fly in Z-direction ($\vartheta = 0$), as defined in Eq. (6.41), it is still not possible to control experimentally where in the XY-plane the molecule passes the Rydberg atom. Evaluation of the cross-section thus requires integration over b and the azimuthal angle ϕ in standard spherical

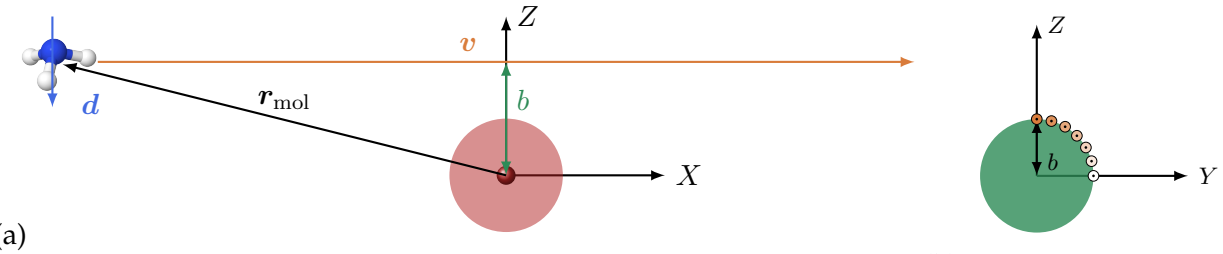

(a) (b)

Figure 6.7: (a) Same as Fig. 6.4 (a) but the molecule flying in X-direction. (b) Different possible angles $\tilde{\vartheta}$ between the trajectory and the Z-axis from $\tilde{\vartheta} = 0$ (orange, corresponding to the trajectory shown in (a)) to $\pi/2$ (white). The velocity vector points out of the plane of the page.

coordinates [45, 40]

$$\sigma_{\Psi_0} = \int_0^\infty b\, db \int_0^{2\pi} d\phi\, P_{\text{ex}}^{\Psi_0}(b, \phi). \tag{6.46}$$

Due to the cylindrical symmetry around the Z-axis, the integral over ϕ can be evaluated to

$$\sigma_{\Psi_0} = 2\pi \int_0^\infty b\, db\, P_{\text{ex}}^{\Psi_0}(b). \tag{6.47}$$

Note that for $\vartheta \neq 0$, the integral cannot be evaluated as easily. If, for example, the molecule flies in X-direction ($\vartheta = \pi/2$ in Eq. (6.40)) as shown in Fig. 6.7 (a), it can cross the atom anywhere in the YZ-plane as shown in Fig. 6.7 (b). The Rydberg orbital is in general not symmetric around the X-axis and the transition probability depends on the angle $\tilde{\vartheta}$ between the trajectory and the Z-axis in the YZ-plane[1] shown in Fig. 6.7 (b). To compute the cross-section, it is therefore required to integrate over $\tilde{\vartheta}$ instead of ϕ in Eq. (6.46).

When calculating the cross-section numerically, the integral over b in Eq. (6.47) has to be truncated. We choose the upper bound b_{max} such that the transition probability converges to zero and the lower bound b_{min} such that the rapid oscillations of the transition probability average out in the integral. The parameter range of b shown in Fig. 6.6 (b) would thus be suitable for the integration. Lastly, the state-dependent cross sections σ_{Ψ_0} can be averaged over all possible initial states to obtain the final cross-section σ. The value of σ then still depends on the relative velocity v and the amplitude of the DC field F_{DC}, which effectively determines the detuning between the particles. We study these dependencies thoroughly in the next section.

It shall finally be noted that which of the scattering parameters can be tuned and which ones must be averaged depends on the specific experimental realisation. For instance, we have assumed the molecule to fly in Z-direction which is not always adjustable. Moreover, in the experiment [151], for instance, it is not possible to select the initial state of the molecule, while the initial state of the Rydberg atom can be engineered to some degree. It would therefore be required to average over the molecular states but not over all Rydberg states.

[1] Analogous to ϑ, $\tilde{\vartheta}$ is the polar angle θ in spherical coordinates for an azimuthal angle $\phi = \pi/2$.

6.3 Electric field control of the scattering cross-sections

In this section, we utilise our model for simulating the scattering cross-section. We use the Stark effect to tune the energy mismatch Δ between Rydberg atom and molecule. The resulting electric field controlled cross-sections correspond to the signal measured in an experiment and provide insight into the dynamics during the scattering process. For simplicity, we assume the molecule to fly in Z-direction (cf. Eq. (6.41)) while generalisation to other orientations is straight-forward.

As discussed before, we consider the inversion mode of ammonia together with the subspace of the Rydberg atom's Hilbert space around the dipole transition $46p$ to $45d$ as presented in Fig. 6.5. We employ the notation for the Rydberg states defined in Eq. (6.44). The Rydberg atom can easily be prepared in either state in realistic experiments. As the DC field is switched on, the states experience different Stark shifts as shown in Fig. 6.5 (b). Since the Stark effect lifts the degeneracy between states with different values of $|m_\ell|$, the Rydberg atom possesses several resonance frequencies for each molecular inversion mode. Beyond that, the states get mixed by the field such that ℓ is not a good quantum number any more. However, since the considered states have a large quantum defect, they are well-separated from neighbouring states and their mixing is comparatively small (for instance as compared to states within the Stark manifold). We therefore still label the states by their ℓ value.

Regarding the molecule, we consider two different scenarios. In Sec. 6.3.1, we assume the initial state of the molecule to be within one subspace with fixed values of J and K. In Sec. 6.3.2, we consider a thermal ensemble of molecules, where multiple rotational states are populated initially according to the Maxwell-Boltzmann distribution.

6.3.1 State-selected molecules

We start by assuming that the rotational state of the molecule can be selected in the experiment, e.g. $|\nu^\pm, M\rangle_{J=1,K=1}$. For example, state-selective preparation of molecular states can be achieved using time-varying inhomogeneous electric field as shown for the upper inversion state $|\nu^-, |M|=1\rangle_{J=1,K=1}$ in Refs. [165, 166].

We follow the steps laid out in the previous section and calculate the state-dependent cross-sections numerically for all significant[1] initial states $|\downarrow, m_\ell\rangle \otimes |\nu^-, M=0\rangle_{K=1,J=1}$ using Eq. (6.47). We omit the subscript of the molecular state in the following discussion. We assume that the initial energy level of the Rydberg atom can be prepared selectively and therefore focus on the atom being initially in $46p$ while considering different values of m_ℓ. Consequently, it is sufficient to consider initial states of the molecule being in the upper inversion level, as energy exchange is highly off-resonant if both particles are in their lower energy level. All other parameters, i.e. the considered range of impact parameters and the time-grid, are given in Tab. A.9 in Appendix A.3.

[1] "Significant" refers to the states shown in Fig. 6.6 (b), since all other possible initial states follow by symmetry arguments.

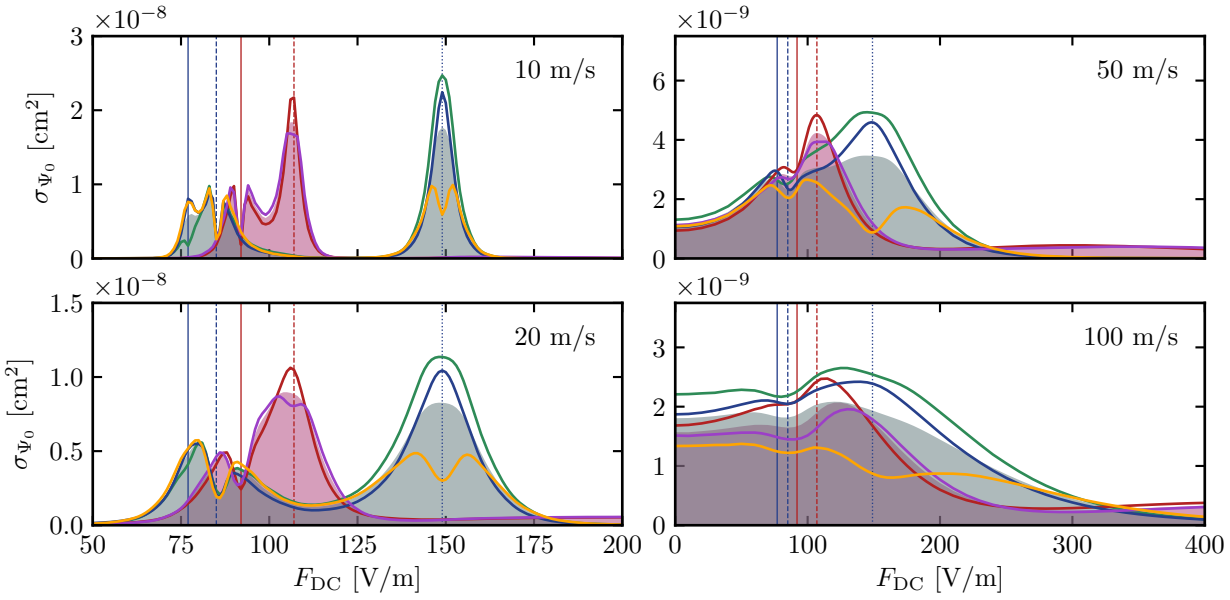

Figure 6.8: Cross-section for different initial states (solid lines, same colour code as in Fig. 6.6 (b)) as a function of the DC field F_{DC} for the $46p$ to $45d$-transition and four different velocities. The vertical lines indicate the resonances (same line style as in Fig. 6.5). The red shaded area indicates the cross-section averaged over all initial states with $m_\ell = 0$ corresponding to the red and purple lines, and the blue shaded area for $m_\ell = 1$ corresponding to the blue, green and yellow lines, respectively. Note the different scales of the x-axis in the left- and right-hand column. The scale of the y-axis changes by a factor of $\frac{1}{2}$ as the velocity increases.

Figure 6.8 shows the state-dependent cross-section for different initial states (indicated by the line colours) and four different velocities: 10, 20, 50 and 100 $\frac{\mathrm{m}}{\mathrm{s}}$. These range roughly between the lowest and highest relative velocity that are conceivable in experiments with cold atoms and molecules [167]. It can clearly be seen that the cross-sections are larger around the resonances indicated by vertical lines. The positions of the resonances correspond to the intersection between the field dependent Rydberg transition frequencies ω_{ryd} and the inversion splitting of ammonia in Fig. 6.5 (b). Moreover, it is visible on first sight that lines increase in width and decrease in amplitude as the velocity increases (note the changing scale of the x- and y-axis). The broader line width can be understood qualitatively as a decreased energy resolution as the particles move faster and is a direct consequence of the time-energy uncertainty relation. The peak value of the cross-section decreases with velocity since the particles are close to each other for a shorter amount of time, thus having less time to interact.

We now consider the case of $v = 10\ \frac{\mathrm{m}}{\mathrm{s}}$ in more detail, as the low velocity reveals the clearest line structure. It is noticeable that different initial states (i.e. lines with different colours) behave rather differently around the various resonances. Roughly speaking, states where the Rydberg atom is initially in $m_\ell = 0$ (red and purple line, red shade) are more affected by resonances relating to $46p, m_\ell = 0$ (red vertical lines), while states with the Rydberg atom initially in $m_\ell = 1$

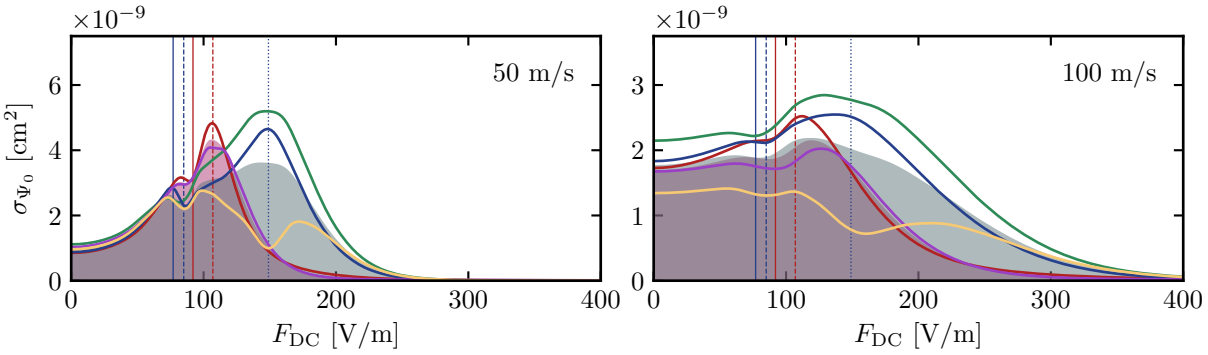

Figure 6.9: Same as Fig. 6.8 but when neglecting dipole-quadrupole and dipole-octupole contributions. The plots for $v = 10$ and $20\ \frac{\mathrm{m}}{\mathrm{s}}$ look qualitatively the same as shown in Fig. 6.8 and are therefore omitted.

(blue, green and yellow line, blue shade) are more affected by resonances relating to $46p, m_\ell = 1$ (blue vertical lines). This makes sense since the states which possess resonant transitions with the molecule are populated initially. However, even within a group of states, there are striking differences which cannot be explained as easily. When considering the right-most resonance (dotted blue vertical line), it is apparent that the blue and green line behave very similarly and show a clear resonance peak, while the yellow line shows a deep dip. We study this observation thoroughly in the next chapter using a simplified model in order to explain the line shape around the resonance.

Even in experiments where it is not possible to engineer the initial state of the molecule and the Rydberg atom precisely (i.e. to control m_ℓ and M), it is reasonable to assume that the initial state of the Rydberg atom can be prepared up to the sign of m_ℓ, i.e. $|{\downarrow}, |m_\ell|\rangle$. The energy splitting between $45d$ and $46p$ is sufficiently large to allow for selective excitation and the value of $|m_\ell|$ can be tuned by the polarisation of the excitation laser [151] (and equivalently for $|{\uparrow}, |m_\ell|\rangle$). Consequently, we average the state-dependent cross-sections accordingly, taking the weight of the different initial states into account. That is, all states shown in Fig. 6.8 except for $|{\downarrow}, m_\ell = 0\rangle \otimes |\nu^-, M = 0\rangle$ (red) have a weight of two, as the system is symmetric with respect to the magnetic quantum number. For instance, the initial states $|{\downarrow}, 0\rangle \otimes |\nu^-, \pm 1\rangle$ lead to the same results. The coloured shades thus indicate the cross-sections for the averaged initial states $|{\downarrow}, 0\rangle \otimes |\nu^-, M\rangle$ (red) and $|{\downarrow}, \pm 1\rangle \otimes |\nu^-, M\rangle$ (blue). At very low velocities, such as 10 and $20\ \frac{\mathrm{m}}{\mathrm{s}}$, the two different cases $|m_\ell| = 0$ and 1 can be distinguished very well. At higher velocities, the peaks broaden significantly which impedes the resolution of single transitions. However, until roughly $50\ \frac{\mathrm{m}}{\mathrm{s}}$, differences between the two cases can be resolved in particular around the two right-most transition (dashed red and dotted blue). At even higher velocities, such as $100\ \frac{\mathrm{m}}{\mathrm{s}}$, the two spectra look qualitatively almost the same and only differ in amplitude. We would thus expect that an experiment is able to distinguish the two initial Rydberg states for relative velocities up to $50\ \frac{\mathrm{m}}{\mathrm{s}}$. This is well within the limits of the current experimental capabilities [167].

Lastly, we investigate the influence of higher order multipole contributions, namely dipole-quadrupole and dipole-octupole interactions, on the electric field controlled cross-sections. To this end, we repeat the calculation without considering quadrupole and octupole contributions. For low velocities, $v < 50\,\frac{\mathrm{m}}{\mathrm{s}}$, the spectra do not change significantly. Only for higher velocities such as 50 and $100\,\frac{\mathrm{m}}{\mathrm{s}}$ do the two cases deviate as shown in Fig. 6.9. For high fields, the cross-sections of the $m_\ell = 0$ states goes down to zero when only the dipole-dipole interaction is considered (red shade on right-most edge in both panels in Fig. 6.9). When considering all three orders, on the other hand, they are non-vanishing (cf. Fig. 6.8). This can be explained as follows. As can be seen from the Stark map in Fig. 6.5 (b), the transition $46p, m_\ell = 0 \leftrightarrow 45d, m_\ell = 2$ (red dotted) experiences a weaker Stark shift than all the other levels. This transition is forbidden in the dipole case as $\Delta m_\ell = 2$ and forbidden in the quadrupole case as $\Delta\ell = 1$. However, in the presence of a strong electric field, the states do not only experience an energy shift but they also get mixed with adjacent states. When computing the expectation value of the angular quantum number of the field-dressed state closest to $45d, m_\ell = 2$, we obtain a value of $\langle\ell\rangle = 2.08$ at $F_{\mathrm{DC}} = 400\,\frac{\mathrm{V}}{\mathrm{m}}$. This value is larger than 2 which would have been the result for a pure d states. It can be deduced that a fraction of the state actually fulfils the $\Delta\ell = 2$ selection rule that is required for quadrupole transitions to occur from $46p, m_\ell = 0$. As the detuning of this transition from the molecular inversion splitting is comparatively small, high velocities with broad lines allow the transition to occur. Accordingly, the effect is more pronounced for $v = 100\,\frac{\mathrm{m}}{\mathrm{s}}$, as the lines are broader and the detuning less significant than for $50\,\frac{\mathrm{m}}{\mathrm{s}}$ or even lower velocities.

In summary, there are two competing effects which allow or prevent non-vanishing cross-sections at high fields: (1) the Stark effect mixes states with different ℓ values and enables quasi-forbidden transitions, and (2) the Stark shift increases the detuning and prevents transitions from occurring. At high fields around $400\,\frac{\mathrm{V}}{\mathrm{m}}$ and $v = 100\,\frac{\mathrm{m}}{\mathrm{s}}$, the two effects are balanced enough to allow for a transition, leading to the non-vanishing cross-section around $400\,\frac{\mathrm{V}}{\mathrm{m}}$ for $m_\ell = 0$. For $m_\ell = 1$, on the other hand, the cross section vanishes with and without higher-order contributions, as the only possible transition with $\Delta m_\ell = 2$, $46p, m_\ell = -1 \leftrightarrow 45d, m_\ell = 1$, is too far detuned (blue dashed line in Fig. 6.5, note that the Stark shift is independent of the sign of m_ℓ). The non-vanishing cross-section at large DC fields could be observed in an experiment by comparing the measurement results when starting with a Rydberg atom in $m_\ell = 0$ and 1, respectively.

6.3.2 Thermal ensemble of molecular states

So far, we have assumed the molecule to be in the rotational state $J = K = 1$. In the following, we estimate how the cross-section depends on the J and K value of the molecule. Most importantly, the inversion splitting of ammonia depends on J and K as given in Eq. (6.20). Since we expect energy transfer to occur only if the two transitions systems are approximately resonant, it is possible to reduce the relevant number of states. As can be seen from Fig. 6.3 (a), the only states

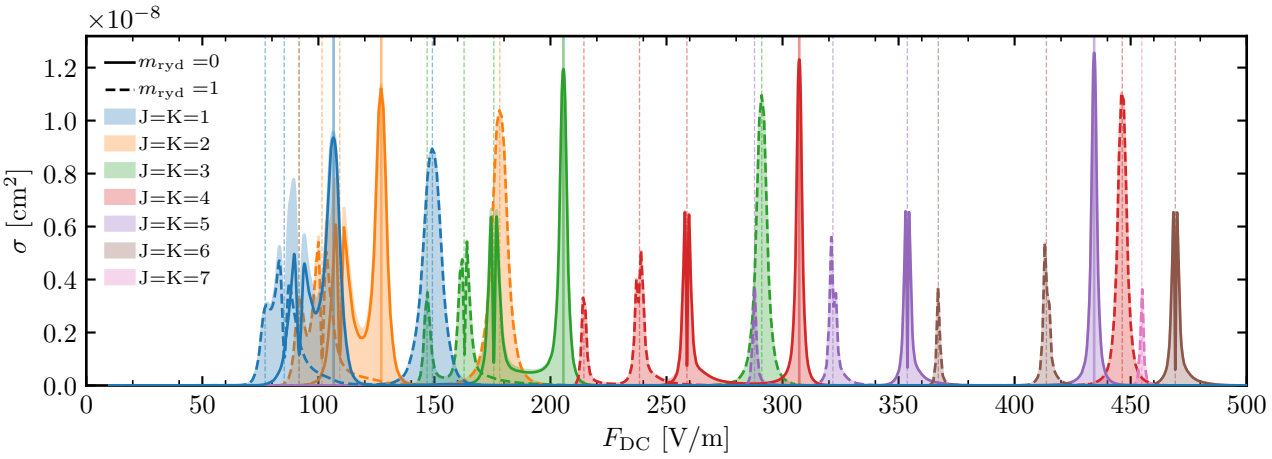

Figure 6.10: Cross-section as a function of the DC field F_{DC} for the $46p$ to $45d$-transition for different initial molecular states $|\nu^-, M\rangle_{KM}$ for $v = 10\,\frac{\mathrm{m}}{\mathrm{s}}$. The Rydberg atom is initially in $|\downarrow, m_\ell\rangle$. Solid lines show cross-sections averaged over all M values of the molecule for $m_\ell = 0$, dashed lines for $m_\ell = \pm 1$. The shaded regions indicate their sums. The resonances depend on the inversion splitting and are thus different for different values of J and K as indicated by their line colour.

which contribute to the cross-section for small J are the ones with $K = J$[1]. This assumption was confirmed by numerical tests with $K < J$. The Rydberg atom is still assumed to be initially in $|\downarrow, m_\ell\rangle$ and the velocity was chosen to be $v = 10\,\frac{\mathrm{m}}{\mathrm{s}}$. For simplicity, we assume a pure dipole-dipole interaction and neglect higher order multipole-contributions.

Figure 6.10 shows the cross-section of the dipole transition from $46p$ to $45d$ for initial molecular states $|\nu^- M\rangle_{JK}$ with different values of $J = K$. It is apparent from the figure that the density of resonances decreases towards higher field values. This is due to the Stark splitting of the Rydberg atom which increases the spacing between different transitions (cf. Fig. 6.5 (b), when the lines diverge towards high field strengths).

The dependence of the height and width of the peaks on J can be investigated most easily when comparing peaks corresponding to the same Rydberg transition. For instance, peaks indicated by the solid vertical lines (i.e. at 107, 127, 206, 307 and 434 $\frac{\mathrm{V}}{\mathrm{m}}$) correspond to resonances of the inversion mode for $J = K = 1 \ldots 5$, respectively, with the $46p, m_\ell = 0 \leftrightarrow 45d, m_\ell = 1$ transition. It can be seen that their height increases and their width decreases with J. This can be explained as follows. It can be shown by analytical approximations[2] [40] that the line width of a transition induced by dipole-dipole interaction scales as $1/\sqrt{d_{\mathrm{ryd}} d_{\mathrm{mol}}}$ with d_{ryd} and d_{mol} being the dipole matrix elements of the Rydberg atom and molecule, respectively. The matrix elements d_{mol} scale as $K/\sqrt{J(J+1)}$ (cf. Tab. 6.2) such that we expect the line width to scale as $\Delta_\sigma \sim \sqrt[4]{\frac{J+1}{J}}$ for $K = J$. In other words, the lines become more narrow as J increases. The maxi-

[1] "Small" refers to $J < 7$. For $J \geq 9$, the inversion mode of rotational states with $K = J - 1$ become resonant to the Rydberg transition. However, high rotational states only get populated at high temperatures such that their contribution is small and we neglect them.

[2] We elaborate these approximations in Sec. 7.2.4.

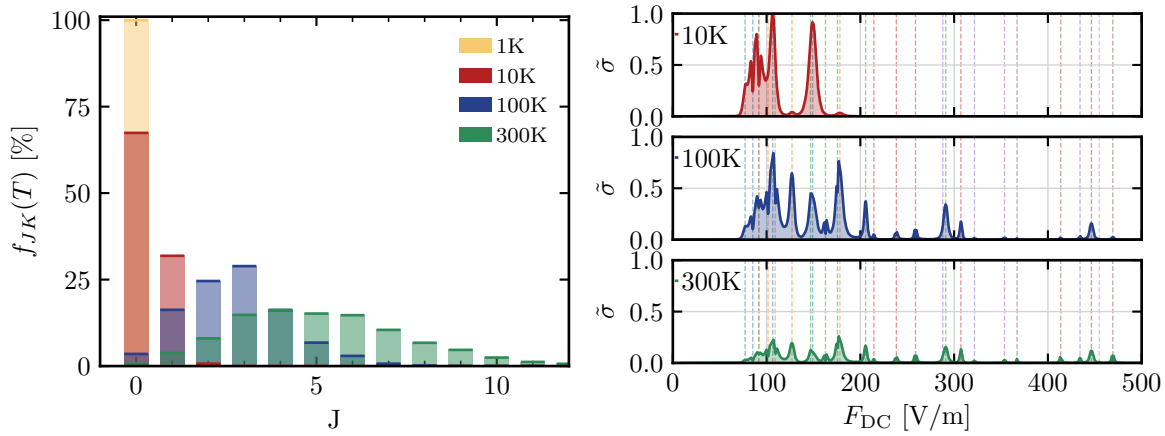

Figure 6.11: (a) Boltzmann distribution of the occupation of rotational eigenstates $|JK\rangle$ of the molecule for three different temperatures. (b) Thermally averaged cross-section as a function of the DC field F_{DC} for the $46p$ to $45d$-transition for three different temperatures at $v = 10\,\frac{\mathrm{m}}{\mathrm{s}}$. The y-axis was normalised to the maximal value of $\sigma_{\mathrm{max}} = 2.16 \cdot 10^{-10}\,\mathrm{cm}^2$, such that $\tilde{\sigma} = \sigma/\sigma_{\mathrm{max}}$. The vertical dashed lines show the resonances with the line colour as given in Fig. 6.10.

mal cross-section, on the other hand, is expected to scale as $d_{\mathrm{ryd}} d_{\mathrm{mol}}$ [40] which can be seen from the dipole-dipole interaction potential of Eq. (6.34). This causes the cross-section peaks to scale as $\max(\sigma) \sim \sqrt{\frac{J}{J+1}}$ for $K = J$; the height of the lines thus increases with J. These approximations match the observations in Fig. 6.10 perfectly.

One consequence of this observation is that most of the lines are sufficiently narrow and distant from each other to be properly resolved; the only exception being the area of high line density around $100\,\frac{\mathrm{V}}{\mathrm{m}}$. The situation is qualitatively similar for higher velocities. However, the lines broaden significantly for higher velocities as shown in Fig. 6.8. As a result, it might not be possible to distinguish as many resonances for high velocities. We provide a thorough discussion of the scaling of the transition lines with the velocity in Sec. 7.2.4.

If it is not possible to selectively prepare the initial state of the molecule in an experiment, the rotational states are likely to be populated thermally. The occupation of the molecular eigenstates $|\nu^{\pm} M\rangle_{JK}$ at a non-zero temperature is given by the Maxwell-Boltzmann distribution,

$$f_{JK}(T) = \frac{g}{N} e^{-\frac{E^{\mathrm{rot}}_{JK}}{k_B T}}, \tag{6.48}$$

see also Fig. 6.11 (a), with k_B being the Boltzmann constant, T the temperature, and E^{rot}_{JK} the energy of the rotational eigenstates as given in Eq. (6.12). N is a normalisation factor such that $\sum_{J=0}^{\infty} \sum_{K=0}^{J} f_{JK}(T) = 1$. Lastly, g is the statistical weight of the state $g = 2(2J+1)$, except for $K = 3n$ with $n \geq 1$ where $g = 4(2J+1)$, since these states have twice the statistical weight due to the three-fold symmetry axis of the molecule [38]. Figure 6.11 (b) shows the thermally averaged spectra for three different temperatures. Note that all initial Rydberg and molecular

states have been averaged. It can clearly be seen that even around room temperature, $T = 300\,\mathrm{K}$, it is possible to resolve most of the resonances and assign them to different initial molecular states. Given a measured spectrum, it would thus be possible to determine the composition of the initial molecular state from the resonances and their relative heights in the data. Note that we have assumed a constant relative velocity of $v = 10\,\frac{\mathrm{m}}{\mathrm{s}}$ between the two particles here. The situation would change drastically if also the velocity would be thermally distributed. At room temperature, the particles would possess a mean velocity of $600\,\frac{\mathrm{m}}{\mathrm{s}}$ which would broaden the lines massively and render the resolution of single resonances impossible.

6.4 Summary

We have provided in this chapter a model for simulating the scattering process between rubidium Rydberg atoms and ammonia molecules. While many studies to date approximate the interaction between the dipole moment of the molecule and the charge distribution of the Rydberg atom as a dipole-dipole interaction, we have expanded the interaction potential to third order, thus accounting for dipole-dipole, -quadrupole and -octupole contributions between the two particles. The relative motion has been assumed to be uniform and classical. We have focused on one exemplary orientation, namely the molecule moving along the direction of the quantisation axis, considering different relative velocities. However, generalisation to other orientations as specified by the experimental setup is straight-forward. We have calculated the cross-section of the scattering process numerically, considering as an example the $46p$ to $45d$ transition of the Rydberg atom coupled to the inversion mode of ammonia. The particles exchange energy if the transitions are in resonance predominantly due to the dipole-dipole interaction between them. We have shown that the cross-section can be controlled using the electric field by means of the Stark shift of the Rydberg energy levels. Effectively, the electric field thus tunes the energy mismatch between the particles.

We have studied two different scenarios corresponding to different experimental setups: state-selected molecules and a thermal ensemble of molecular states. In the first case, the cross-section peaks around the resonances as shown in Fig. 6.8; the plot serves as a prediction for the outcome of realistic experiments. We understood the occurrence and absence of peaks for different initial states by considering the Stark map of the transitions. Most importantly, we found that the initial state of the Rydberg atom, more specifically its initial magnetic quantum number m_ℓ, affects the cross-section significantly. Moreover, we found a strong broadening of the transitions with the relative velocity and estimated that resonances can be resolved up to values about $50\,\frac{\mathrm{m}}{\mathrm{s}}$ which is well within experimental capabilities. Lastly, we have identified and explained features of dipole-quadrupole transitions for high electric fields, thus demonstrating the importance of higher order multipole contributions for the cross-section.

In the second case, we have assumed the molecule to be initially in a thermal state which is composed of several rotational states with different J and K quantum numbers. Due to the

resonance conditions, we could restrict the number of relevant inversion modes to 7. We found that the resulting cross-sections (shown in Fig. 6.11) show a rich line structure. Most importantly, it is possible to resolve most of the resonances even at high temperatures of $300\,\mathrm{K}$. Since the final cross-sections depend on the composition of rotational states in the molecular ensemble, cross-sections measured in an experiment could be used to deduce the composition of the molecule's rotational state, i.e. the relative population of different $J = K$-states.

Despite having obtained first, valuable insights into the dynamics and having provided predictions for experiments, we have not been able to explain all observations. For instance, we could not explain which resonances lead to dips or peaks in the cross-sections as a function of the electric field for different initial states. We therefore turn to a more theoretical analysis of the different orders of the interaction potential in the next chapter. This will allow for a thorough understanding of the scattering process and the role of higher order multipole contributions.

7

MULTIPOLAR CHARACTER OF FÖRSTER RESONANCE ENERGY TRANSFER

In the previous chapter, we have studied the collision of two particles and found that they exchange energy without emitting radiation. This well-known process is called Förster resonance energy transfer (FRET) [41], sketched in Fig. 7.1. Typically, FRET is defined as the non-radiative transfer of energy from a donor to an acceptor mediated by the resonant dipole-dipole interaction between the two particles. It can be summarised as

$$D^* + A \to D + A^*, \tag{7.1}$$

where D denotes the donor, A the acceptor, and the asterisk the excitation. First experimental observations of this effect date back to 1922 [168] in the dissociation of hydrogen with mercury. The exchange of energy was found to be mediated by dipole-dipole coupling between the particles and Theodor Förster was the first to develop a successful theoretical treatment [169]. Today, FRET has found many applications, most prominently in molecular biology as a spectroscopic technique [41], for example using quantum dots for the study of biomolecular interactions [170].

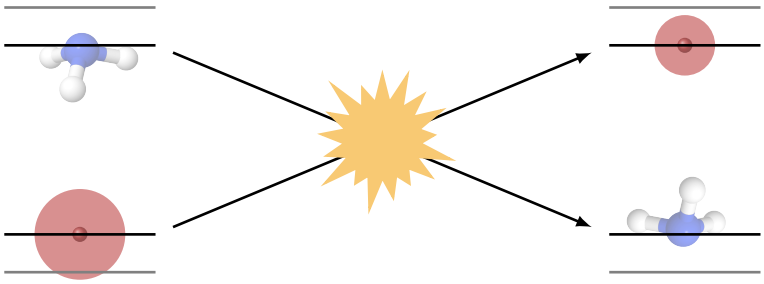

Figure 7.1: Sketch of the Förster resonance energy transfer (FRET) between a polar molecule (ammonia, blue) and a Rydberg atom (red), approximated by two-level systems. If the two systems are in resonance, they can exchange energy during the scattering process.

One excellent platform to observe, study and utilise FRET are Rydberg atoms due to their large dipole moments [171, 172]. For example, the strong coupling and Stark tunability make FRET an attractive tool for implementing quantum gates and for quantum simulation [173]. The basic prerequisite for the observation of FRET is the existence of resonant dipole transitions in the two particles. This cannot only be found in Rydberg-Rydberg systems, but also when a Rydberg atom interacts with a polar molecule [174] which is a particularly suitable system as particles possess large (transition) dipole moments. In the 1970s, first experiments of collisions between polar molecules and Rydberg atoms were conducted, demonstrating the conversion of rotational to electronic energy in collisions [175]. Later, experiments studied the collision of rubidium Rydberg atoms and ammonia molecules considering transitions between different inversion levels of ammonia [152, 153].

Moreover, FRET can serve as a mechanism for the non-destructive detection of polar molecules via Rydberg atoms [149, 40]. Methods for detecting polar molecules are rare and often limited to special molecular species, see Ref. [40] and references therein. The resonant interaction of FRET imprints a strong enough signature of the molecular state onto the Rydberg atom which can be utilised for its detection. In the spirit of an indirect measurement, similar as discussed in Chapter 5, the Rydberg atom serves as a meter for extracting information on the state of the molecule. As only the Rydberg atom is detected, the molecule itself will not be destroyed and can be used for further experiments.

All of the aforementioned studies have only considered the dipole-dipole interaction between two particles and also Förster's original theory explicitly relies on the electric dipole approximation. There are, however, cases when this approximation is not fit to describe the dynamics of a system adequately. When considering experiments with Rydberg atoms, for instance, the dipole approximation seems highly questionable as Rydberg orbitals can measure up to microns in diameter. As the reaction partners approach, the Rydberg electron's charge distribution can no longer be approximated as a dipole and higher-order terms of the multipole expansion are expected to become significant. The same is true for quantum dots, which have a finite size and are large as compared to e.g. the dye molecules they are supposed to detect [176, 177]. Only recently, the dipole-quadrupole interaction has been investigated for Rydberg atoms [178] where it has been found to allow for entanglement between electronic and rotational motion between two atoms. In quantum dots, dipole-quadrupole contributions have been found to be dominating over the dipole-dipole contributions in certain cases [176]. Another study on quantum dots considered all multipole moments and found that the multipole contributions were non-monotonous, indicating that any multipole expansion might be insufficient [177]. This suggests to inspect higher-order contributions in interactions between Rydberg atoms and polar molecules as well.

In this chapter, we continue the work presented in the previous chapter and study the multipolar character of FRET for the combined system of Rydberg atom and ammonia molecule. While inspired by the experiment of Ref. [151], our model is not limited to simulating the out-

come of experiments; it also provides a playground to systematically study the role of multipole contributions to FRET from a theoretical point of view. For instance, the state-dependence of the line shape of the cross-section as a function of the DC field for dipole-dipole interactions which we have observed in Sec. 6.3 is still not fully understood. Other, more general open questions relate to the significance of higher-order contributions, for instance in view of the particle distance which, in a scattering process, can be controlled indirectly via tuning their relative velocity. Moreover, higher-order multipole contributions could alter the line width, shape or position of transitions, or give rise to completely new peaks in the spectrum. Therefore, our goal is to estimate the influence and benefit of higher-order contributions; and determine when and under which conditions the dipole approximation breaks down

The remainder of this chapter is structured as follows. In Sec. 7.1, we investigate the scattering cross-section of a simplified model, namely two two-level-systems subject to dipole-dipole interaction. Afterwards, in Sec. 7.2, we perform a systematic study of the line shape of dipole, quadrupole and octupole transitions independently. Finally, in Sec. 7.3, we study the multipolar character of FRET at the example of a dipole-forbidden transition and investigate the corresponding cross-section as a function of the electric field.

7.1 Dipole-dipole interaction of two-level systems

In the previous chapter, we have studied the cross-section of the $46p$ to $45d$ transition of the Rydberg atom coupled to the inversion mode of ammonia. We have observed that the cross-section shows a complex structure of peaks and dips as a function of the electric field (cf. Fig. 6.8). In other words, we have seen that the efficiency of FRET depends strongly on the electric field and the initial states of both particles. While we have been able to relate the positions of the peaks to the resonances between the particles which occur at specific field values, the exact shape of the lines (peaks or dips) could not be understood yet.

In the following, we tackle this problem by considering a much simpler model system. Namely, we assume both the Rydberg atom and the molecule to be two-level systems. To this end, we select two states of the Hilbert spaces of each particle and study the dynamics during their collision. The dipole-dipole interaction potential from Eq. (6.34) can be written for two dipoles as

$$\hat{V}_1(t) = \frac{\hat{\boldsymbol{d}}_1 \cdot \hat{\boldsymbol{d}}_2}{r(t)^3} - \frac{3\Big(\hat{\boldsymbol{d}}_1 \cdot \boldsymbol{r}(t)\Big)\Big(\hat{\boldsymbol{d}}_2 \cdot \boldsymbol{r}(t)\Big)}{r(t)^5}, \tag{7.2}$$

where $\boldsymbol{r}(t)$ is the (classical) distance between the two particles and $\hat{\boldsymbol{d}}_i$ are their dipole moments. We neglect higher-order contributions in this section. The distance $\boldsymbol{r}(t)$ is time-dependent as the particles fly past each other. The trajectory can be parametrised as described in Sec. 6.2.2, where we have assumed the molecule to perform a uniform motion, i.e. to pass the Rydberg atom in a straight line with a constant relative velocity. Here, we assume the molecule to fly in z-direction, $\boldsymbol{v} = v\boldsymbol{e}_z$, as given by Eq. (6.41).

In order to evaluate the matrix elements of the potential in Eq. (7.2), we chose the spherical basis, $(\pm\boldsymbol{e}_x + i\boldsymbol{e}_y)$ and $\boldsymbol{e}_z$, to represent the operators. Due to the dipole section rules, transitions can only occur between states with $\Delta m = 0, \pm 1$ (cf. Eq. (6.33) for the Rydberg atom and Tab. 6.2 for the molecule). $\Delta m = 0$ corresponds to the matrix elements of the $\hat{z}$-operator and $\Delta m = \pm 1$ to $(\pm\hat{x} + i\hat{y})$. Due to the scalar products in Eq. (7.2), only three different kinds of transitions are allowed in the combined system as shown in Fig. 7.2 (a): linear flip-flop, $\Delta m_1 = \Delta m_2 = 0$ (blue), diagonal flip-flop, $\Delta m_1 = -\Delta m_2 = \pm 1$ (green) and criss-cross, $\Delta m_1 = \Delta m_2 = \pm 1$ (red). In the following, we discuss each case and the resulting dynamics separately.

7.1.1 Flip-flop transitions

We first consider the transition with $\Delta m_1 = \Delta m_2 = 0$ (blue), which we term the linear flip-flop transition. Due to the dipole selection rules, the only relevant components of the dipole moments are the ones in z-direction and we thus write $d_i^z = \langle\uparrow m_i|\hat{\boldsymbol{d}}_i \cdot \boldsymbol{e}_z|\downarrow m_i\rangle = \langle\downarrow m_i|\hat{\boldsymbol{d}}_i \cdot \boldsymbol{e}_z|\uparrow m_i\rangle$ with $i = 1, 2$ labelling the two dipoles. When inserting the trajectory of Eq. (6.41) into $\hat{V}_1(t)$ from Eq. (7.2), the dipole-dipole coupling strength

$$V_1(t) = \langle\downarrow m_1, \uparrow m_2|\hat{V}_1(t)|\uparrow m_1, \downarrow m_2\rangle = \langle\uparrow m_1, \downarrow m_2|\hat{V}_1(t)|\downarrow m_1, \uparrow m_2\rangle$$

takes the form

$$V_1(t) = \frac{d_1^z\, d_2^z}{\left(b^2 + (vt)^2\right)^{3/2}} - \frac{3\, d_1^z\, d_2^z\, (b\sin\vartheta + vt\cos\vartheta)^2}{\left(b^2 + (vt)^2\right)^{5/2}}. \tag{7.3}$$

The interaction strength is shown in Fig. 7.2 (b) for $\vartheta = 0$ ($\boldsymbol{v} \parallel \boldsymbol{e}_z$, first column) where we have assumed for simplicity $d_1^z = d_2^z = v = b = 1$. It can be seen that the interaction changes sign twice (note the weak local minimum around $t = \pm 1$) and takes its the peak value at $t = 0$ where the two particles are closest to each other. The time-evolution of the two dipoles is determined by the accumulated phase $\Phi(t)$ which, in the resonant case, can simply be written as

$$\Phi(t) = \int_{-\infty}^{t} V_1(t')dt', \tag{7.4}$$

shown in panel (c). Due to the time-dependence of the potential, the accumulated phase equals exactly zero at $t = 0$.

The consequence of this can be seen most easily when propagating the two two-level systems in time. To this end, we assume an initial state[1] $|\downarrow, m_1 = 1\rangle \otimes |\uparrow, m_2 = 1\rangle \equiv |\downarrow\uparrow\rangle$. Note that the grey dotted levels shown in Fig. 7.2 (a) are not taken into account in the simulations such that dipoles are perfect two-level systems. The time-dependent dynamics are shown in panel (d) for which we have assumed realistic parameters with dipole moments $d_1^z \approx 0.7\,\mathrm{D}$ (corresponding

[1]The opposite situation $|\uparrow, m_1 = 1\rangle \otimes |\downarrow, m_2 = 1\rangle$ leads to the same results.

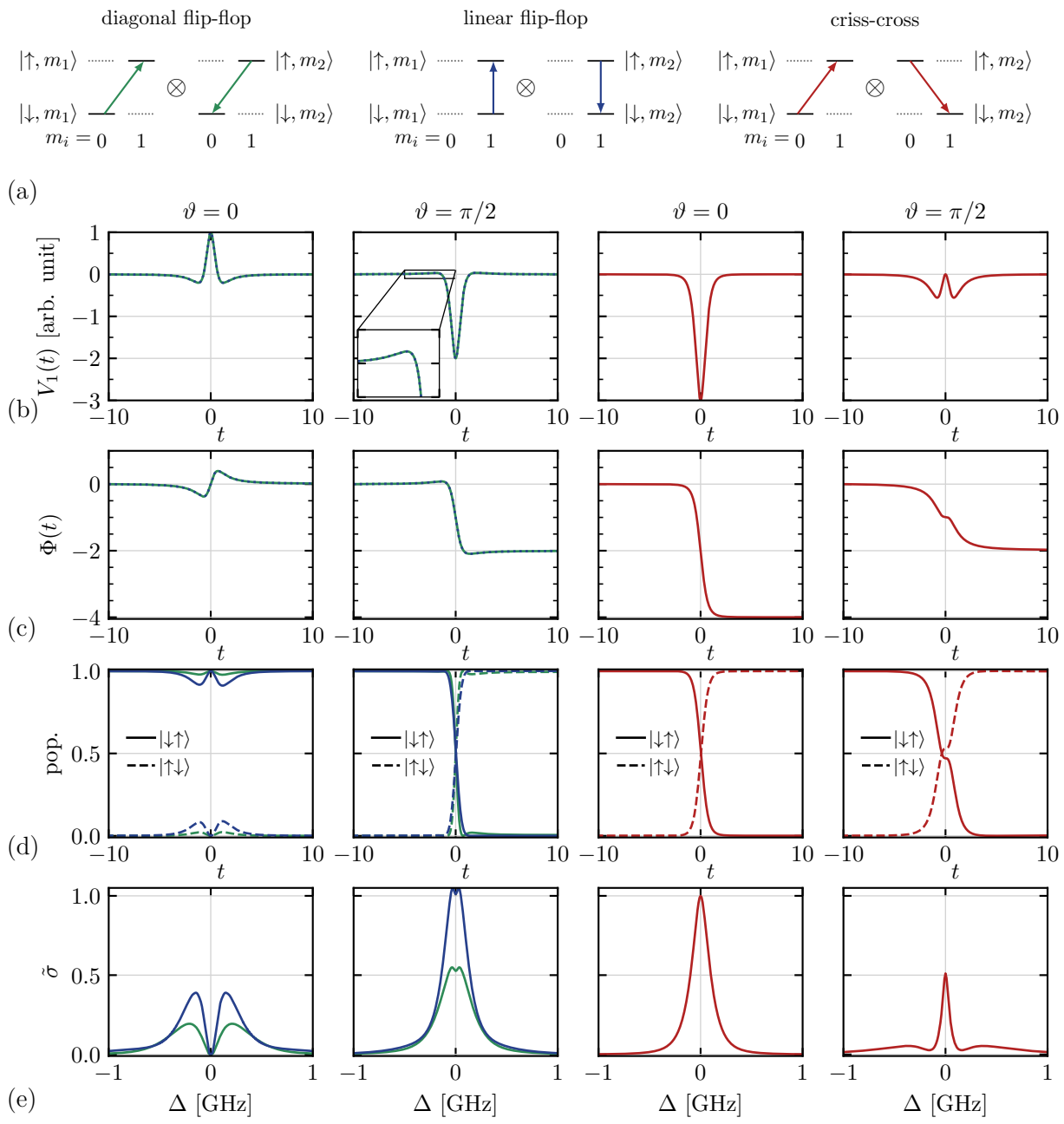

Figure 7.2: Allowed transitions in two two-level systems due to dipole-dipole coupling (a) and corresponding quantities of the scattering process (b-e). The two left-most columns correspond to flip-flop transitions (green and blue), and the two right-most to criss-cross transitions (red). The value of ϑ is given on top of each column. (b) shows the interaction strength $V_1(t)$ in arbitrary units and (c) its integrated value $\Phi(t)$. (d) shows an exemplary time propagation of the initial state $|\downarrow\uparrow\rangle$ under the potential $V_1(t)$ at resonance, $\Delta = 0$, for $v = 100\,\frac{\mathrm{m}}{\mathrm{s}}$ and $b = 160\,\mathrm{ns}$, except for the green and red lines for $\vartheta = \pi/2$ for which $b = 110\,\mathrm{ns}$. (e) shows the normalised cross-section $\tilde{\sigma}$ as a function of the detuning Δ between the two transitions with $\tilde{\sigma} = \sigma/\sigma_{\mathrm{max}}$ and $\sigma_{\mathrm{max}} = 2.733 \cdot 10^{-10}\,\mathrm{cm}^2$. No integration over ϕ was carried out. The data shown in (d+e) result from numerical simulations using realistic parameters, while (b+c) are plots of analytical formulas using arbitrarily chosen parameters.

to ammonia), $d_2^z \approx 3000\,\mathrm{D}$ (rubidium), $b = 160\,\mathrm{nm}$, and $v = 100\,\frac{\mathrm{m}}{\mathrm{s}}$. The figure shows that the two-level systems exchange about 10% of their excitation around $t = 1$, but return exactly to their initial state at $t = 0$. This is due to the accumulated phase being equal to 0 at $t = 0$. The dynamics are symmetric around $t = 0$, such that the systems return to their initial state for $t \to \infty$.

The cross-section of the process can be calculated as explained in Sec. 6.2.3 by integrating the transition probability over the impact parameter b where we have assumed values from $b = 50$ to $500\,\mathrm{nm}$ in steps of $10\,\mathrm{nm}$. We repeat this for different values of the detuning Δ between the two transitions. The result is shown in panel (e). Because the population always returns to its initial state when the two transitions are in resonance, the cross-section is zero at $\Delta = 0$. When introducing a non-zero detuning, on the other hand, the symmetry of the interaction potential is broken and a non-zero phase can be accumulated for $t \to \infty$ which ultimately results in a non-zero cross-section. Only for large values of the detuning does the cross-section vanish again as energy transfer becomes highly off-resonant.

The situation is very different when changing the orientation of the trajectory. As a second example, we consider $\vartheta = \pi/2$ which corresponds to the trajectory being perpendicular to the quantisation axis, $\boldsymbol{v} \perp \boldsymbol{e}_z$ (second column of Fig. 7.2). The peak value of the coupling strength in panel (b) at $t = 0$ is twice as strong as in the previous case and the local maximum around $t = \pm 1$ is less pronounced (see inset). As a result, the absolute value of the accumulated phase (c) is almost monotonically increasing. When evolving the system in time, the dipoles perform an almost perfect swap (d) which results in a large value of the cross-section at resonance (e).

It can be seen, however, that the cross-section increases slightly for small detuning. This can be explained as follows. The non-monotonicity of the phase Φ causes a small hump in the populations at the times where the potential takes its local maxima. The population overshoots the target, i.e. the initial state is completely depopulated shortly after $t = 0$ but gets slightly repopulated directly afterwards. Since the two-level systems are failing to perform a perfect swap, exchange efficiency is slightly less than 1 at the end of the interaction. A small detuning compensates for the overshooting and removes the humps from the population curves. As a result, the cross-section is slightly higher right next to the resonance, thus causing a small dip in the centre of the line.

Next, we consider the $\Delta m_1 = -\Delta m_2 = \pm 1$ transition, which we term the diagonal flip-flop transition (green lines in Fig. 7.2). Due to the dipole selection rules, only dipole moments in $\boldsymbol{e}_x$ and $\boldsymbol{e}_y$ directions contribute to these transitions. The corresponding matrix elements are $d_i^{\pm} = \langle \uparrow m_i \pm 1 | \hat{\boldsymbol{d}}_i^{\pm} \cdot (\pm \boldsymbol{e}_x + i \boldsymbol{e}_y) | \downarrow m_i \rangle$ with $i = 1, 2$. If the two matrix elements are of opposite sign, i.e. d_1^+ and d_2^- or vice versa, the resulting selection rule is $\Delta m_1 = -\Delta m_2 = \pm 1$. It is apparent from the figure that the diagonal flip-flop (green) leads to the same results as the linear flip-flop discussed above (blue). Only in the realistic simulations of the population dynamics and the cross-section (d+e) do the blue curves show a larger amplitude than the green ones because the matrix elements of the $\hat{z}$ operator are larger than those of the $\hat{x}/\hat{y}$-elements ($d_{\mathrm{mol}} \approx 0.5\,\mathrm{D}$, $d_{\mathrm{ryd}} \approx 2080\,\mathrm{D}$).

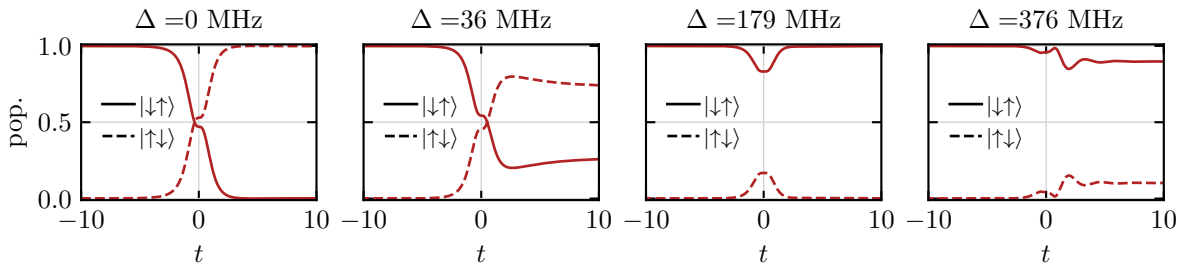

Figure 7.3: Time-evolution of the initial state $|\downarrow, m_1 = 0\rangle \otimes |\uparrow, m_2 = 0\rangle \equiv |\downarrow\uparrow\rangle$ which couples to $|\uparrow, m_1 = 1\rangle \otimes |\downarrow, m_2 = 1\rangle \equiv |\uparrow\downarrow\rangle$ (criss-cross transition) for $\vartheta = \pi/2$, $b = 110\,\mathrm{nm}$ and $v = 100\,\frac{\mathrm{m}}{\mathrm{s}}$. Same as right-most panel in Fig. 7.3 (d) but for different values of the detuning Δ. The first panel corresponds to resonance, the second one to a slight detuning, the third to the local minimum of the cross-section in Fig. 7.3 (d) (right-most panel), and the last one to the local maximum at larger detuning.

7.1.2 Criss-cross transitions

We obtain a significantly different scenario if the two matrix elements are of the same sign, e.g. d_1^+ and d_2^+. In this case, we obtain the selection rule $\Delta m_1 = \Delta m_2 = \pm 1$ (red curves in Fig. 7.2) which we term criss-cross transition. The dipole-dipole interaction strength $V_1(t)$ takes the form

$$V_1(t) = -\frac{3\, d_1^+\, d_2^+\, (b\cos\vartheta - vt\cos\vartheta)^2}{(b^2 + (vt)^2)^{5/2}}. \tag{7.5}$$

The case $\vartheta = 0$ is shown in the third column and shows similarities to the flip-flop transition for $\vartheta = \pi/2$ (second column). There is, however, an important difference. The time-dependent potential $V_1(t)$ does not possess local maxima (panel b) and therefore, the integrated phase $\Phi(t)$ (c) is monotonically decreasing[1]. For the time-evolution, we assume the initial state $|\downarrow, m_1 = 0\rangle \otimes |\uparrow, m_2 = 0\rangle \equiv |\downarrow\uparrow\rangle$ which couples to $|\uparrow, m_1 = 1\rangle \otimes |\downarrow, m_2 = 1\rangle \equiv |\uparrow\downarrow\rangle$. It can be seen (panel d) that the population curves do not overshoot the target due to the monotonicity of the accumulated phase. The maximal value of the cross-section can therefore be found at resonance (e) and any detuning decreases it. As such, this case is the most intuitive of all that have been discussed.

Lastly, we consider the criss-cross transition for $\vartheta = \pi/2$ (right-most column). The potential $V_1(t)$ is always non-positive and becomes zero at $t = 0$. As a result, the accumulated phase $\Phi(t)$ is monotonically decreasing and shows a saddle point at $t = 0$. This translates to a saddle point in the population transfer (d) which does not prevent an efficient population transfer. Consequently, the largest value of the cross-section can be found at resonance (e). Different from the case $\vartheta = 0$, however, the cross-section decreases quickly as the detuning increases. Most interestingly, the cross-section increases again after reaching a local minimum, resulting in broad "wings" in the spectrum. This can be understood by considering the time-dependent dynamics at different values of the detuning.

[1]The sign of Φ is of no significance.

Figure 7.3 shows the dynamics of a criss-cross transition for one fixed value of b and different detunings Δ between the transitions. While it is required to integrate over b to obtain the cross-section, the time-resolved dynamics provides qualitative insights which allow for understanding the shape of the cross-section. It can be seen that a small detuning of $\Delta = 36\,\mathrm{MHz}$ between the two transitions diminishes the population exchange as compared to the resonant case, $\Delta = 0$. The state $|\uparrow\downarrow\rangle$ (dashed line) is less populated than before at the end of the interaction, and the population even decreases after having reached a local maximum around $t = 2$. This rebound effect can be interpreted as the accumulated phase $\Phi(t)$ being "bend down" towards zero by the detuning. At the value of $\Delta = 179\,\mathrm{MHz}$, the exchange probability is zero and the cross-section reaches a local minimum (compare to right-most column in Fig. 7.2 (e)). This can be interpreted as the accumulated phase being bend down to zero at the end of the interaction. If the detuning is increased even more, however, $\Delta = 376\,\mathrm{MHz}$, the initial states accumulates a non-vanishing phase Φ at the end of the interaction, such that the exchange probability and the cross-section rise. This leads to the "wings" of the cross-section for large detuning. For even larger detuning the energy mismatch is too strong to allow for any transfer of excitation from one two-level system to the other.

In summary, we have studied three different transitions, the criss-cross and the linear and diagonal flip-flop, at two exemplary values of ϑ and found very different line shapes for the cross-section when tuning the energy mismatch Δ between the two systems. We have found that the line shapes can be directly related to the shape of the interaction strength $V_1(t)$. While the linear and diagonal flip-flop, corresponding to the selection rules $\Delta m_1 = -\Delta m_2 = 0, \pm 1$, lead to the same results, the criss-cross transition with $\Delta m_1 = \Delta m_2 = \pm 1$ produces significantly different line shapes. Conversely, the shape of a transition line allows for direct conclusions on which transitions take place in a scattering process. We can use these insights to analyse the shape of the cross-sections as a function of the electric field of the full model for Rydberg atom and molecule as we demonstrate in the following.

7.2 Cross-section line shapes for different order multipole contributions

After having studied the cross-section for the dipole-dipole transition in a simplified toy model in the previous section, we now turn to investigating all three orders of the multipole expansion derived in Sec. 6.2.1 for the full model of Rydberg atom and molecule. While in the previous chapter we have controlled the cross-section using an electric field via the Stark effect of the Rydberg atom, we now tune the inversion splitting ω_{inv} instead and keep the DC field F_{DC} constant. The advantage of this method is two-fold: Firstly, it allows for disentangling the effect of tuning the energy mismatch from Stark mixing. In Sec. 6.3, we have observed that quasi-forbidden transitions can be driven due to the Stark mixing of the initial or target state with high- or low-angular momentum states. By tuning the inversion splitting instead of the DC field amplitude

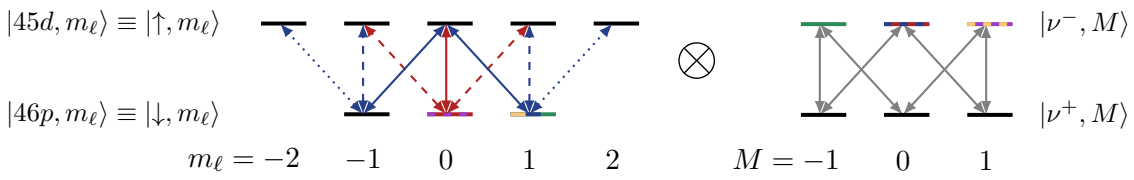

Figure 7.4: Hilbert space of the Rydberg atom (left) and the molecule (right, the index $J = K = 1$ has been omitted) considered to study the dipole-dipole interaction. The arrows indicate the dipole allowed transitions between the lower and upper manifolds. The line style for the Rydberg transitions is the same as in Fig. 6.5. The coloured levels indicate the relevant initial states; for instance, the red levels indicate the state $|\downarrow, 0\rangle \otimes |\nu^-, 0\rangle$ (same colour code as in Fig. 6.6 (b)).

(and setting $F_{\text{DC}} = 0$), we can study the influence of the detuning on the transition cross-section while excluding Stark mixing. Secondly, at zero DC field, all the Rydberg transitions are degenerate such that there is only a single resonance similar to the toy model studied above. As observed in the previous chapter, for instance in Fig. 6.8, the peaks at different resonances overlap which renders it complicated to determine the line width of the transition. However, note that for real ammonia molecules, this tunability is only possible to a certain extent. The inversion splitting depends on J and K (cf. Fig. 6.3) and is thus controllable only on a coarse grained scale by selecting J and K carefully. However, a change in J and K is also accompanied by a modified Hilbert space dimension and matrix elements. We disentangle this interdependence by tuning ω_{inv} for a given subspace of J and K directly.

This section is structured as follows. We study the role of different order multipole contributions for FRET systematically by considering the dipole-dipole, dipole-quadrupole and dipole-octupole interaction independently from each other in Sec. 7.2.1 to 7.2.3, respectively. In each section, we determine the maximal value $\max(\sigma)$ of the cross-section and the line width Δ_σ of the transition for different relative velocities v. We summarise our findings and compare them to analytical approximations in Sec. 7.2.4.

7.2.1 Dipole-dipole transitions

We now start by studying FRET between a rubidium Rydberg atom and ammonia when considering dipole-dipole interactions only. To this end, we consider the dipole transition $46p$ to $45d$ in the Rydberg atom (cf. Fig. 6.5) and restrict ourselves to the molecular inversion mode for $J = K = 1$. The molecule is thus described as a $2(2J + 1) = 6$-level system, $|\nu^\pm, M = 0, \pm 1\rangle_{J=1,K=1}$, degenerate in M. We omit the subscript in the following. The bipartite Hilbert space is depicted in Fig. 7.4. We utilise the same notation as in the previous chapter and label the Rydberg atom by $|\uparrow, m_\ell\rangle = |45d, m_\ell\rangle$ with $m_\ell = 0, \pm 1, \pm 2$ and $|\downarrow, m_\ell\rangle = |46p, m_\ell\rangle$ with $m_\ell = 0, \pm 1$. We assume the molecular inversion splitting ω_{inv} to be freely adjustable while the splitting between the energy levels in the Rydberg atom is given by the realistic model. The scattering is modelled as given in Sec. 6.2.2 with the trajectory from Eq. (6.40), where we assume the molecule to fly in z-direction

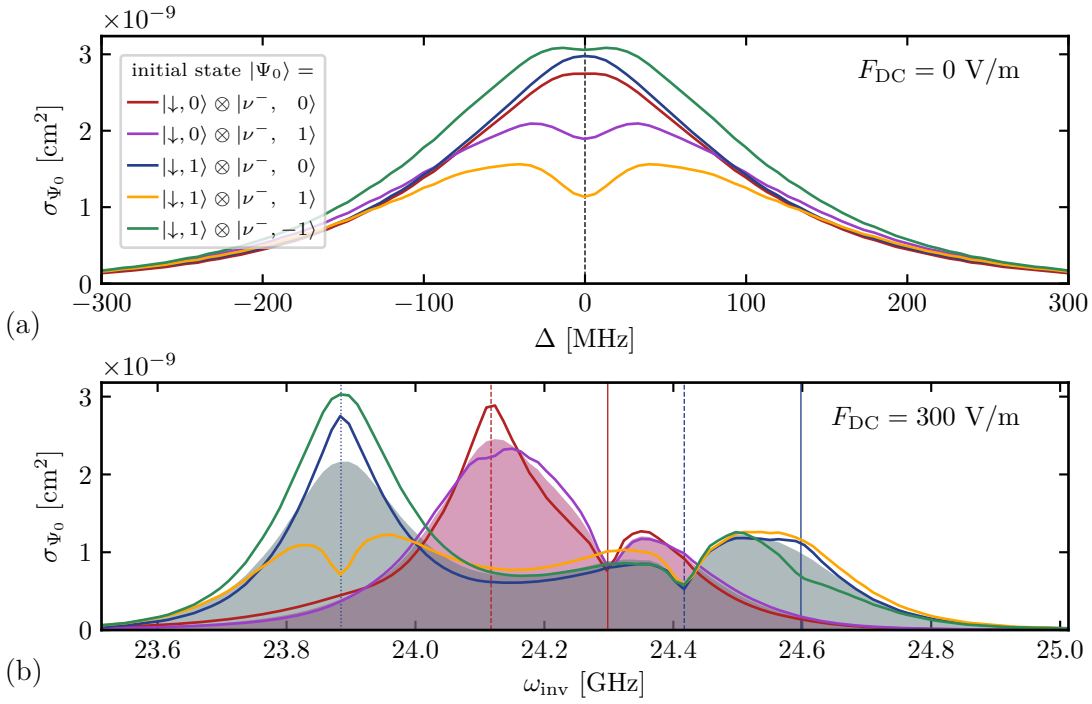

Figure 7.5: Cross-section for different initial states as indicated by the line colour for the $46p$ to $45d$-transition and two different DC fields F_{DC} at $v = 100\,\frac{\mathrm{m}}{\mathrm{s}}$. (a) shows the cross-section as a function of the detuning Δ of the molecular inversion frequency ω_{inv} from the Rydberg transition $\omega_{\mathrm{ryd}} = 23.626\,\mathrm{GHz}$. (b) refers to ω_{inv} as the Rydberg transitions are no longer degenerate; the vertical lines indicate the resonances (same line style as in Figs. 6.5 and 7.4).

(corresponding to $\vartheta = 0$ in Eq. (6.41); the following study can easily be generalised to other trajectories). The cross-section can then be calculated as described in Sec. 6.2.3 by integrating over the impact parameter b using Eq. (6.47). The range over which b was integrated numerically and the starting time t_0 of the time-evolution is given in Tab. A.11 in Appendix A.3 for different velocities.

Figure 7.5 (a) shows the cross-section σ_{Ψ_0} as a function of the detuning Δ (defined as the Rydberg transition frequency minus the inversion splitting of ammonia in Eq. (6.43)) for all relevant[1] initial states $|\downarrow, m_\ell\rangle \otimes |\nu^-, M\rangle$ for $v = 100\,\frac{\mathrm{m}}{\mathrm{s}}$ and $F_{\mathrm{DC}} = 0$ at which all Rydberg transitions are degenerate with $\omega_{\mathrm{ryd}} = 23.626\,\mathrm{GHz}$. The lines of all initial states are centred around the resonance and possess a width of a few hundred megahertz. However, the cross-section at resonance differs significantly depending on the initial state. This is because for every initial state, multiple different transitions are allowed. This has two implications. On the one hand, the amplitude of the matrix elements, which affects the height of the peaks, depends strongly on the transition. For the Rydberg atom, the solid red, dashed blue and dotted blue transitions in Fig. 7.4 are at least one order of magnitude stronger than all the others, for instance. On the other hand, the character of the transition – flip-flop or criss-cross – determines whether the cross-section shows a dip or peak at resonance as discussed in the previous section (cf. first and third column in Fig. 7.2).

[1] All other combinations follow from symmetry arguments.

The identification of the dominant transitions for each initial state, and thus the understanding of the line shape, is simpler when assuming a non-zero DC field. In this case, the Rydberg levels experience an individual Stark shift such that the lines split up into five individual ones (cf. Fig. 6.5 (b), the dotted red line of that figure does not play a role here as it is dipole forbidden). The resulting cross-section as a function of the inversion splitting is shown in Fig. 7.5 (b); the resonances are indicated by the vertical lines. The similarity of this figure to Fig. 6.8 (in particular around $v = 20\,\frac{\mathrm{m}}{\mathrm{s}}$), which presents the cross-section as a function of the DC field, is striking. However, the direction of the x-axes of the two figures is reversed. While larger DC fields induce a larger Rydberg frequency and larger *positive* detuning Δ (as defined in Eq. (6.43)), larger inversion frequencies cause a more *negative* detuning.

After inversion of the x-axis, the major difference between the two figures is the distance between the peaks. While it is possible to distinguish the different resonances at $v = 100\,\frac{\mathrm{m}}{\mathrm{s}}$ in Fig. 7.5 (b), this is not possible in Fig. 6.8. For $F_{\mathrm{DC}} = 300\,\frac{\mathrm{V}}{\mathrm{m}}$, as considered in Fig. 7.5 (b), the separation between different Rydberg transitions is of the order of $100\,\mathrm{MHz}$ due to the Stark shift as can be seen from the Stark map of Fig. 6.5. They can be brought in resonance with the inversion mode of ammonia by tuning ω_{inv} directly and the resonances are well-resolved at high velocities of $100\,\frac{\mathrm{m}}{\mathrm{s}}$. In Fig. 6.8, the inversion splitting is fixed and in resonance with the Rydberg transitions around DC fields of $100\,\frac{\mathrm{V}}{\mathrm{m}}$. At this lower field strength, the Rydberg transitions are much closer to each other and only separated by some tens of megaherz. Resolution of this separation can only be obtained for lower velocities around $20\,\frac{\mathrm{m}}{\mathrm{s}}$. Phrased differently, when controlling the cross-section using the Stark effect, we consider intersections of the Rydberg transitions in the Stark map with horizontal lines corresponding to one inversion mode; when controlling the cross-section via the inversion splitting, we consider intersections of the Stark map with vertical lines given by one value of the DC field. As a result, the outcome is qualitatively very similar and all insights acquired on the cross-section controlled by the inversion splitting gather in the following can be directly applied to the electric field controlled cross-section of Fig. 6.8.

We now consider the initial state $|\downarrow, 0\rangle \otimes |\nu^-, 0\rangle$ (red line) of Fig. 7.5 (b) in more detail. The peaks and dips in the cross-section are clearly related to the resonances corresponding to the Rydberg atom being in $46p, m_\ell = 0$ (vertical red lines), while being unaffected by the others (vertical blue lines). The strongest peak occurs at the $46p, m_\ell = 0 \leftrightarrow 45d, m_\ell = \pm 1$ transition (vertical red dashed line). As the Rydberg atom is initially in $m_\ell = 0$, it apparently performs a $\Delta m_\ell = \pm 1$ transition to $45d, m_\ell = \pm 1$. The shape of the peak clearly indicates a criss-cross transition (compare to third column in Fig. 7.2 (e)) as flip-flop transitions cause dips in the cross-section (first column in Fig. 7.2 (e)). From this, it can be followed that the molecule also performs a $\Delta M = \Delta m_\ell = \pm 1$ transition. In principle, a diagonal flip-flop transition with $\Delta M = -\Delta m_\ell = \pm 1$ would also be allowed by the dipole selection rules. However, since this transitions leads to a dip in the cross-section, it is overshadowed by the peak of the criss-cross transition. A linear flip-flop transition with $\Delta M = \Delta m_\ell = 0$, on the other hand, is forbidden by the molecular selection rule $M = 0 \not\leftrightarrow M' = 0$. As a result, the state-dependent cross-section shows a strong dip at the

$46p, m_\ell = 0 \leftrightarrow 45d, m_\ell = 0$ transition (vertical solid red line), which matches the expected line shape of the linear criss-cross transition. The initial state $|\downarrow, 0\rangle \otimes |\nu^-, 1\rangle$ (purple line) shows very similar results as $|\downarrow, 0\rangle \otimes |\nu^-, 0\rangle$ (red), since the Rydberg atom is initially in the same state.

The other three initial states correspond to the Rydberg atom being initially in $m_\ell = 1$ and thus relate to the resonances indicated by vertical blue lines. The cross-section of the initial state $|\downarrow, 1\rangle \otimes |\nu^-, 0\rangle$ (blue line) shows a strong peak at the $46p, m_\ell = \pm 1 \leftrightarrow 45d, m_\ell = \pm 2$ transition (vertical blue dotted line). This indicates a criss-cross transition with $\Delta M = \Delta m_\ell = 1$. The other diagonal transition, $46p, m_\ell = \pm 1 \leftrightarrow 45d, m_\ell = 0$ (vertical solid blue line), is of the same kind but less strong, as the corresponding Rydberg matrix elements are smaller. Finally, the linear flip-flop transition $46p, m_\ell = \pm 1 \leftrightarrow 45d, m_\ell = \pm 1$ (vertical dashed blue line) causes a deep dip in the spectrum. The initial state $|\downarrow, 1\rangle \otimes |\nu^-, -1\rangle$ (green line) shows a very similar behaviour to $|\downarrow, 1\rangle \otimes |\nu^-, 0\rangle$ (blue), since similar transitions are involved. Finally, the state $|\downarrow, 1\rangle \otimes |\nu^-, 1\rangle$ (yellow line) deviates from the described behaviour around the $46p, m_\ell = \pm 1 \leftrightarrow 45d, m_\ell = \pm 2$ transition (vertical dotted blue line). The molecule cannot undergo a $\Delta M = 1$ transition as the Hilbert space ends with $M = 1$. This results in the linear flip-flop transition $\Delta m_\ell = \Delta M = 1$ being forbidden. The option with $\Delta m_\ell = \Delta M = -1$ is allowed but the corresponding matrix elements of the Rydberg atom are small. Instead, the diagonal flip-flop with $\Delta m_\ell = -\Delta M = 1$ is the dominating transition, causing the strong dip in the spectrum.

The observed line shapes are thus in excellent agreement with our understanding of the dipole-dipole transitions acquired in Sec. 7.1 from studying two two-level systems. The cross-section depends strongly on the initial state the Rydberg atom and to a smaller degree on the initial state of the molecule. From studying the shape of the transition lines around the different resonances, we can deduce which transitions are the dominating ones, thus gaining understanding of the underlying dynamics. It shall lastly be noted that some differences between the complex system in Fig. 7.5 and the simplified model from the previous section occur. Most strikingly, the dips in the spectrum do not go all the way down to zero in the current case. The reason is that for multi-level systems, the dynamics cannot be limited to a single transition. For instance, we have discussed above that the initial state $|\downarrow, 1\rangle \otimes |\nu^-, 1\rangle$ (yellow state in Fig. 7.4) causes a dip at the $46p, m_\ell = \pm 1 \leftrightarrow 45d, m_\ell = \pm 2$ transition (vertical blue dotted line). In addition to that, a transition to $|\uparrow, 2\rangle \otimes |\nu^+, 0\rangle$ might occur (at the vertical blue dashed line) which is followed by a transition to $|\downarrow, 1\rangle \otimes |\nu^-, -1\rangle$ (green state). This state is connected to $|\uparrow, 1\rangle \otimes |\nu^-, -2\rangle$ via a criss-cross transition at the $46p, m_\ell = \pm 1 \leftrightarrow 45d, m_\ell = \pm 2$ transition (vertical blue dotted line). The resulting peak adds to the dip of the yellow line, rendering it less deep. All in all, we found that the study on the isolated transition in two-level systems of Sec. 7.1 allowed for understanding the intricate dynamics in the full system of a Rydberg atom and a molecule.

So far, we have considered a fixed relative velocity between the two particles of $v = 100\,\frac{\mathrm{m}}{\mathrm{s}}$. We now aim to investigate the influence of the velocity on the maximal cross-section and the width of the lines. For this purpose, we average the cross-section over all possible initial states and weigh them with the appropriate statistical weight (as explained in Sec. 6.3). The averaging

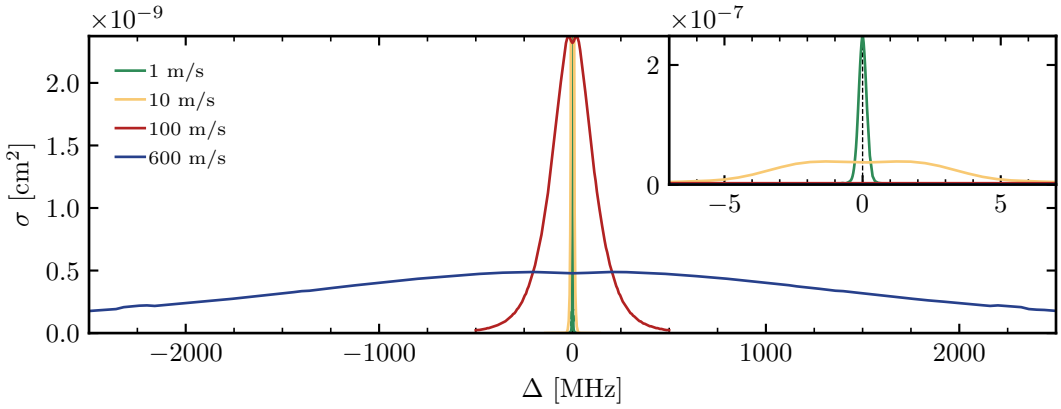

Figure 7.6: Cross-section averaged over all possible initial states for different velocities for the $46p$ to $45d$-transition for $F_{\mathrm{DC}} = 0$. The limit of the y-axis was set to the peak cross-section of $v = 100\,\frac{\mathrm{m}}{\mathrm{s}}$ ($1\,\frac{\mathrm{m}}{\mathrm{s}}$ in the inset) despite the peak values of lower velocities being higher as shown in the inset. Otherwise similar to Fig. 7.5.

is relevant to experiments without state selection with respect to m_ℓ or M. We determine the cross-section σ as a function of the detuning Δ of the Rydberg transition frequency from the inversion mode of ammonia for four different velocities: 1, 10, 100 and $600\,\frac{\mathrm{m}}{\mathrm{s}}$. While $600\,\frac{\mathrm{m}}{\mathrm{s}}$ corresponds to the average velocity at room temperature, $10\,\frac{\mathrm{m}}{\mathrm{s}}$ reflects the lowest velocity that can be reached in the experiment of Ref. [167]. The result for $F_{\mathrm{DC}} = 0$ is shown in Fig. 7.6. The figure reveals a strong decrease of the maximal cross-section $\max(\sigma)$ and an increase of the line width Δ_σ with the velocity. We determine both parameters quantitatively as follows. The height $\max(\sigma)$ simply corresponds to the maximal value of the cross-section. The line width Δ_σ can be determined as the full width of the peak at half maximum (FWHM). Other ways of characterising the shape of the line are possible. For instance, the height could be chosen at resonance (which is slightly smaller than $\max(\sigma)$ as the lines show small dips at resonance) or the shape could be fitted using a Gaussian or a Voigt profile (convolution of a Gaussian with a Lorentz distribution). All procedures lead to quantitatively very similar results which is why we employ the simpler method of taking the maximum and the FWHM in the following. Table 7.1 presents the determined height and widths of the lines for the dipole-dipole interaction. We investigate the scaling in more detail in Sec. 7.2.4.

We have already established that the cross-section as a function of the detuning presented in this section is directly related to the cross-section as a function of the electric field presented in Sec. 6.3.1. They merely present two different ways of tuning the energy mismatch between the transitions of Rydberg atoms and molecule. The results obtained in this section, such as the insights on the broadening of the lines with the velocity or the occurrence of dips and peaks in cross-section, can directly be applied to the outcome of experiments where the cross-section is controlled by tuning the electric field. We demonstrate this point by comparing the line width of the cross-section as a function of the detuning given in Tab. 7.1 to the line width shown in Fig. 6.8

v[m/s]	$\max(\sigma)$[cm^2]			Δ_σ[MHz]		
	dip.	quad.	oct.	dip.	quad.	oct.
1	$1.5 \cdot 10^{-7}$	$2.7 \cdot 10^{-8}$	$5.3 \cdot 10^{-9}$	0.42	0.96	1.28
10	$1.9 \cdot 10^{-8}$	$5.5 \cdot 10^{-9}$	$1.8 \cdot 10^{-9}$	8.8	20.8	20.8
100	$2.0 \cdot 10^{-9}$	$1.3 \cdot 10^{-9}$	$5.4 \cdot 10^{-10}$	260	440	360
600	$3.1 \cdot 10^{-10}$	$3.8 \cdot 10^{-10}$	$2.0 \cdot 10^{-10}$	3840	4800	3200

Table 7.1: Maximal value of the cross-section $\max(\sigma)$ and the width of the line at half maximum Δ_σ determined from the numerical simulations for dipole-dipole (dip.), dipole-quadrupole (quad.), and dipole-octupole (oct.) interactions for different velocities v.

where the electric field has been tuned. Consider the peak of the $46p, m_\ell = 1 \leftrightarrow 45d, m_\ell = 2$ transition in Fig. 6.8 (vertical blue dotted line) for $v = 10\,\frac{\mathrm{m}}{\mathrm{s}}$ which is a good example, since it is isolated from the remaining resonances. The peak is centred around $149\,\frac{\mathrm{V}}{\mathrm{m}}$ with a width of about $9\,\frac{\mathrm{V}}{\mathrm{m}}$ at half maximum. The Stark map of this transition (shown in Fig. 6.5 (b)) reveals a rise of the Stark shift from 64 to $72\,\mathrm{MHz}$ between 144 and $154\,\frac{\mathrm{V}}{\mathrm{m}}$. Tuning the electric field from 144 to $154\,\frac{\mathrm{V}}{\mathrm{m}}$ thus corresponds to tuning the Rydberg transition by $8\,\mathrm{MHz}$. This matches the value in Tab. 7.1, $8.8\,\mathrm{MHz}$, perfectly, given the rough approximation we have just conducted. This comparison could be repeated and refined for other transitions in the same fashion. However, as most transitions overlap for a non-zero DC field, it is difficult to determine the width of single transitions when tuning the DC field. In particular, it would be impossible to determine the line width of a single transition at high velocities of $100\,\frac{\mathrm{m}}{\mathrm{s}}$ or more using this method. This highlights the main advantage of tuning the energy mismatch at zero DC field instead, as it allows us to determine the line width and height for different initial states and velocities accurately.

7.2.2 Dipole-quadrupole transitions

We now go one step further and study the multipolar character of FRET. To this end, we consider another subspace of the Rydberg transition which displays quadrupole and octupole transitions. Namely, we chose $50p$ as an initial state as shown in Fig. 7.7. It is located in a distance of about $23\,\mathrm{GHz}$ above the $n = 47$ Stark manifold, which we denote by 47ℓ, containing states with $\ell \geq 3$. Quadrupole and higher transitions would thus be possible. The dipole transition to $49d$, on the other hand, is highly detuned from the ammonia inversion mode with a transition frequency of $18.142\,\mathrm{GHz}$. As we have to consider three significant Rydberg states, we label them for clarity in ascending order of energy (cf. Fig. 7.7),

$$|2, m_\ell\rangle \equiv |49d, m_\ell\rangle \quad \text{with} \quad |m_\ell| \leq 2, \tag{7.6a}$$

$$|1, m_\ell\rangle \equiv |50p, m_\ell\rangle \quad \text{with} \quad |m_\ell| \leq 1, \tag{7.6b}$$

$$|0, m_\ell\rangle \equiv |47f, m_\ell\rangle \quad \text{with} \quad |m_\ell| \leq 3. \tag{7.6c}$$

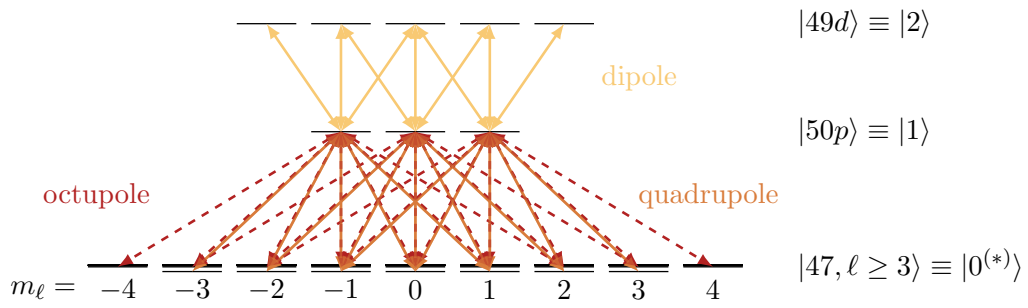

Figure 7.7: Hilbert space of Rydberg atom around $50p$ which has a dipole allowed transition (yellow) to the $49d$ state with 18.142 GHz, and quadrupole (orange) and octupole (dashed red) allowed transitions towards the 47ℓ manifold. The quadrupole transition couples $50p$ to the $47f$ state with a transition frequency of 23.490 GHz, and the octupole couples to $47g$ with 22.698 GHz.

As explained in Sec. 6.2.3 for the dipole transition from $46p$ to $45d$, we remove states with only off-resonant transitions from the Hilbert space to reduce the numerical cost during the simulations. We thus remove the states $|2\rangle \otimes |\nu^- M\rangle_{JK}$ and $|0\rangle \otimes |\nu^+ M\rangle_{JK}$ from the Hilbert space as they correspond to both particles being the highest and lowest energy state, respectively. Moreover, states with $\ell > 4$ can be neglected as only transitions with $\Delta\ell = 0, \ldots, 2$ are allowed when considering interactions up to second order in the multipole expansion. Note that we do not remove the state $|2, m_\ell\rangle$ entirely despite its large detuning Δ from the molecular transition as we found it to affect the dynamics as will be shown later.

We start by performing simulations under consideration of the first two orders of the multipole expansion, i.e. dipole-dipole and dipole-quadrupole contributions. As an initial Rydberg state, we choose one state of the $50p$ manifold, i.e. $|1, m_\ell\rangle$, and consider the average over Rydberg states with the same absolute value $|m_\ell|$ later. We expect quadrupole transitions to occur to $|0, m_\ell\rangle$ ($47f$) due to the $\Delta\ell = 2$ selection rule. Additionally, dipole transitions are allowed towards $|2, m_\ell\rangle$ ($49d$) with $\Delta\ell = 1$. We assume the molecule to be initially in $J = K = 1$, i.e. $|\nu^\pm, M\rangle$ with $M = 0, \pm 1$, just as before.

Since the initial state has both dipole and quadrupole allowed transitions, we can compare them directly by calculating the cross-section of two different transitions at otherwise equal circumstances. For the same reasons outlined above, we vary the inversion splitting ω_{inv} instead of the electric field. First, we scan the inversion splitting ω_{inv} around the quadrupole transition, $\omega_{\text{inv}} \sim 23.490\,\text{GHz}$, and consider the initial state of the molecule to be $|\nu^+, M\rangle$. As a result, the Rydberg atom transfers its excitation to the molecule by means of dipole-quadrupole coupling. Second, we scan the inversion frequency around the dipole transition, $\omega_{\text{inv}} \sim 18.142\,\text{GHz}$, and set the initial state of the molecule to $|\nu^-, M\rangle$, such that it transfers its excitation to the Rydberg atom by means of dipole-dipole coupling. The opposite choices, i.e. scanning the initial state $|1, m_\ell\rangle \otimes |\nu^+, M\rangle$ around 18.142 GHz or $|1, m_\ell\rangle \otimes |\nu^-, M\rangle$ around 23.490 GHz, do not allow for any energy transfer as they are highly off-resonant. Fig. 7.8 (a) shows the cross-section as a function of the inversion splitting for $v = 100\,\frac{\text{m}}{\text{s}}$; the parameters for the time-grid and the range of

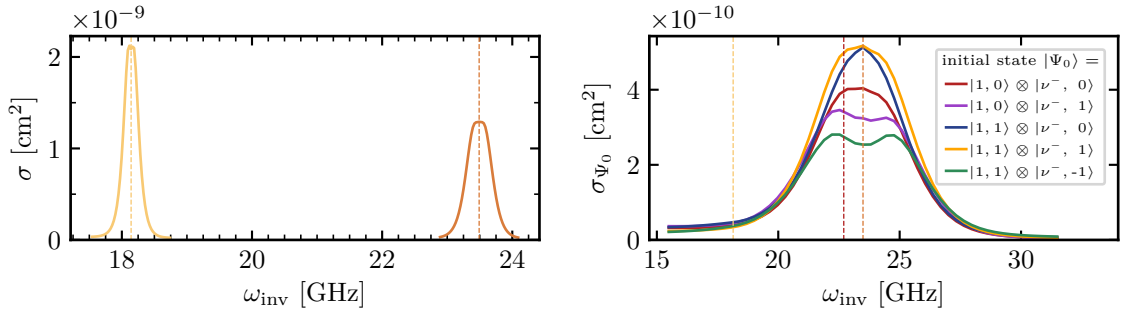

Figure 7.8: (a) Cross-section averaged over all possible initial states $|1, m_\ell\rangle \otimes |\nu^\pm M\rangle$ for $v = 100\,\frac{\mathrm{m}}{\mathrm{s}}$ as a function of the inversion frequency ω_{inv}. The yellow peak corresponds to the dipole transition $|1\rangle \leftrightarrow |2\rangle$ with the molecule being initially in $|\nu^-\rangle$, and the orange peak to the quadrupole transition $|1\rangle \leftrightarrow |0\rangle$ with the molecule initially in $|\nu^+\rangle$ using the labels defined in Eq. (7.6). (b) Cross-section for different initial states $|1, m_\ell\rangle \otimes |\nu^+ M\rangle$ for $v = 600\,\frac{\mathrm{m}}{\mathrm{s}}$. The vertical dashed lines indicate the resonances from $50p$ to $49d$ ($|1\rangle \leftrightarrow |0\rangle$, yellow), $47g$ (red) and $47f$ ($|1\rangle \leftrightarrow |2\rangle$, orange).

impact parameter are given in Tab. A.12 in Appendix A.3. The peaks corresponding to the two resonances are very pronounced and, most strikingly, the quadrupole peak is about half as high as the dipole peak, corroborating our conjecture that quadrupole contributions are relevant for the study of FRET.

To further study the dipole-quadrupole interaction, we calculate the cross-section as a function of the detuning between the Rydberg transition and the molecular inversion mode for four different velocities: 1, 10, 100 and 600 $\frac{\mathrm{m}}{\mathrm{s}}$, similar to the dipole-dipole case in Fig. 7.6. We focus on the quadrupole transition and thus assume an initial state of $|1, m_\ell\rangle \otimes |\nu^+, M\rangle$ (with different values of m_ℓ and M). The qualitative picture is very similar as for the dipole transition shown in Fig. 7.6 and we use the same procedure to extract the maximal value of the cross-section and the line width as before; the exact values of the line width and height are listed in Tab. 7.1. As an example, consider the case of $v = 600\,\frac{\mathrm{m}}{\mathrm{s}}$ in more detail, as shown in Fig. 7.8 (b). It can be seen that the cross-section is maximal around the resonance of the quadrupole transition (vertical orange line). There is no peak around the octupole transition (vertical red line) as we did not include dipole-octupole interactions. There is also no peak at the dipole transition (vertical yellow line) as the molecule is in the lower energy state and cannot provide energy to excite the Rydberg atom to $49p$. The shape of the individual lines depends on the specific initial state similarly as for the dipole-dipole case discussed above. Equivalently as conducted in Sec. 7.1 for the dipole-dipole case, it is possible to study the isolated transitions for the dipole-quadrupole case in order to understand the occurrence of peaks in dips in the cross-section. The strategy is completely analogous and will therefore not be discussed here in further detail.

Upon closer inspection, the cross-section in Fig. 7.8 (b) reveals an interesting feature: it is not symmetric with respect to $\Delta = 0$. This can most clearly be seen in σ approaching zero for $\Delta > 0$ but showing a significant offset for $\Delta < 0$. A non-vanishing cross-section at large detuning can in fact be explained by the presence of the dipole transition $|1\rangle \leftrightarrow |2\rangle$ with a resonance frequency of

18.142 GHz. As the molecule is initially in the lower inversion level $|\nu^+\rangle$, it cannot transfer energy to the Rydberg atom and cannot excite it from $|1\rangle$ to $|2\rangle$. However, the states $|1, m_\ell\rangle \otimes |\nu^-, M\rangle$ and $|2, m_\ell\rangle \otimes |\nu^+, M\rangle$ get strongly coupled if the inversion splitting of ammonia is around 18.142 GHz. In a process which resembles STIRAP, a strong dressing of the Rydberg states $|1\rangle$ and $|2\rangle$ induced by the inversion mode of ammonia allows for a population transfer from $|1\rangle$ to $|0\rangle$ despite the direct $|0\rangle \leftrightarrow |1\rangle$ transition being strongly detuned from the ammonia inversion. In the end of the interaction, some of the Rydberg atom's population is in $|0\rangle$ ($\sim 4\%$ for $b = 100\,\mathrm{nm}$) while the highest state $|2\rangle$ never gets populated. The upper inversion level of the molecule, on the other hand, is significantly populated when the two particles are closest ($\sim 20\%$) while equally only a small fraction survives at the end of the interaction (also $\sim 4\%$). For this effect to occur, the line of the transition has to be sufficiently broad to overlap with the resonance frequency of the dipole. As a result, the asymmetry only appears for very high velocities; the other lines at 1, 10, and 100 $\frac{\mathrm{m}}{\mathrm{s}}$ are symmetric around the resonance.

7.2.3 Dipole-octupole transition

We now employ the potential in the multipole expansion up to third order and thus include dipole-octupole terms into the simulations. We consider a similar part of the Rydberg Hilbert space as discussed above for the dipole-quadrupole interaction. However, due to the octupole selection rule $\Delta\ell = 3$, transitions from $50p$ to $47g$ with an energy splitting of 22.698 GHz are allowed. We thus have to include $47g$ into the simulations and denote it by

$$|0^*, m_\ell\rangle \equiv |47g, m_\ell\rangle \quad \text{with} \quad |m_\ell| \leq 4. \tag{7.7}$$

The following simulations were conducted by Cornelius Hoffmann as part of his Bachelor's thesis under my co-supervision [5]. Here, we give an overview of the main results. The cross-section when considering only dipole-octupole interactions (thus neglecting dipole-dipole and dipole-quadrupole interactions) has been calculated for different velocities equivalently to the dipole-dipole and -quadrupole case above. The initial state of the molecule is the same as before. The parameters of the simulation are listed in Tab. A.13 in Appendix A.3, the resulting line widths and heights in Tab. 7.1.

Since the transition frequencies of the quadrupole and octupole transitions are in close proximity, interesting features appear in the spectrum when considering all three orders of the multipole expansion in the calculation of the cross-section. To study the mutual influence of the quadrupole and octupole contributions, Fig. 7.9 shows the cross-section as a function of the detuning for different velocities for three different scenarios: considering all three orders of the multipole expansion (solid blue line), considering the dipole-octupole interaction only (red dotted lines), and considering only dipole-dipole and dipole-quadrupole interaction, thus neglecting the octupole terms (orange dashed lines). It can be seen that for none of the considered velocities, the blue line is merely the sum of the orange and red lines.

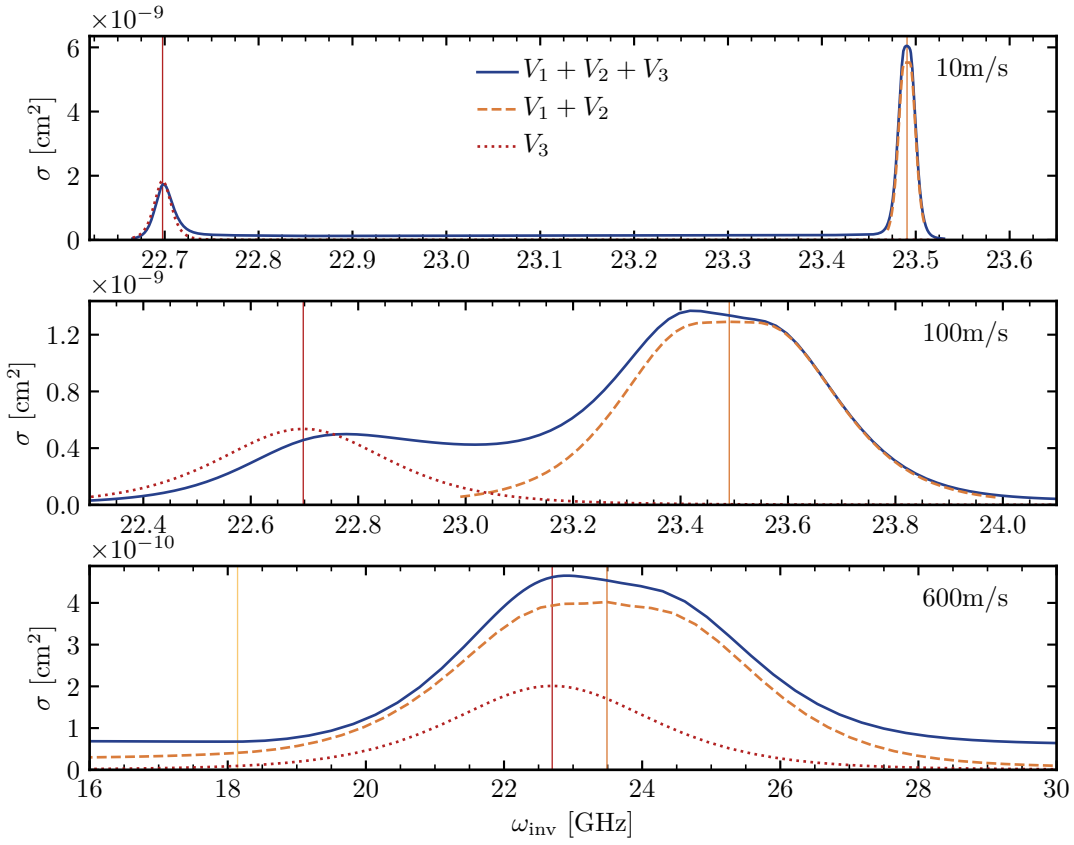

Figure 7.9: Cross-section averaged over all possible initial states $|1, m_\ell\rangle \otimes |\nu^+ M\rangle$ for three different velocities as a function of the inversion frequency ω_{inv} when considering only dipole-dipole and dipole-quadrupole interactions (orange dashed), only dipole-octupole interactions (red dotted), or all three orders together (blue solid). The vertical lines indicate the resonances $|1\rangle \leftrightarrow |2\rangle$ (dipole, yellow), $|1\rangle \leftrightarrow |0^*\rangle$ (octupole, red) and $|1\rangle \leftrightarrow |0\rangle$ (quadrupole, orange). Note the different scales of the x- and y-axis.

For $v = 10\,\frac{\text{m}}{\text{s}}$, the lines corresponding to the quadrupole and octupole transition of the Rydberg atom (vertical orange and red lines, respectively) are very narrow and thus do not overlap. However, it can be seen that the cross-section does not go to zero in between the two peaks when considering all three orders of the potential (blue) even though the independent contributions (orange and red) vanish. For $v = 100\,\frac{\text{m}}{\text{s}}$, the influence is even more striking. The peak of both the quadrupole and octupole contribution is shifted inwards when considering all three orders of the multipole expansion. Especially the quadrupole peak around the vertical orange line becomes strongly asymmetric and acquires a small hump left of the resonance. For even higher velocities, $v = 600\,\frac{\text{m}}{\text{s}}$, where the peaks of the quadrupole and octupole transitions strongly overlap, the quadrupole peak is the dominant contribution. The octupole terms modify the shape of the transition by introducing a small asymmetry and increasing the peak amplitude. Remarkably, the blue curve is much smaller than the sum of the orange and red curves. Moreover, the

cross-section does not vanish at large detuning when considering all three orders of the potential (blue). The orange line is identical to Fig. 7.8 (b) when averaging over the initial states; the cross-section is therefore non-vanishing for small inversion frequencies due to the dipole transition as discussed above. This, however, does not explain the comparatively large cross-section at strong detuning on both sides of the resonance. To this end, similar arguments as employed before are required: an increased set of accessible states due to the larger number of allowed transitions, and interference between different paths allowing to perform far off-resonant transitions. The thorough discussion of the dipole-octupole transition is content of the Bachelor thesis of Ref. [5].

7.2.4 Velocity-dependence of multipole transition line shapes

We now summarise the finding of the last section regarding the maximal cross-section $\max(\sigma)$ and the line width Δ_σ of the dipole-multipole transitions as a function of the detuning between the Rydberg and molecular transition. We first determine the scaling of both quantities with the velocity v by analytical approximations and compare them to our numerical simulations afterwards. These insights will shed light on the breakdown of the dipole approximation in FRET. The analytical derivations loosely follow the argument conducted in Ref. [40] for dipole transitions but we extend it to higher-order contributions.

For the following approximations, we assume for simplicity the Rydberg atom and molecule to consist of two energy levels $|\uparrow / \downarrow\rangle$ only. An energy transfer occurs only if one particle is in the ground state while the other one is in the excited state, i.e. $|\uparrow\rangle \otimes |\downarrow\rangle \equiv |\uparrow\downarrow\rangle$ or $|\downarrow\rangle \otimes |\uparrow\rangle \equiv |\downarrow\uparrow\rangle$. The other two combinations are off-resonant and can be neglected just as before. We write the Hamiltonian in the product basis $\{\ |\uparrow\downarrow\rangle,\ |\downarrow\uparrow\rangle\ \}$ as

$$\hat{H}_n = \begin{pmatrix} 0 & V_n(t) \\ V_n(t) & \Delta \end{pmatrix}, \tag{7.8}$$

where Δ is the energy mismatch between the two-level systems (cf. Eq. (6.43)). $V_n(t)$ is the n-th order multipole expansion term from Sec. 6.2.1 which scales as $r^{-(n+2)}$. The interaction is time-dependent as the distance between the particles changes over time. In case of resonance, $\Delta = 0$, their time-evolution can be solved easily and the states accumulate a relative phase of $\Phi(t)$ as given in Eq. (7.4).

The value of the cross-section at resonance can be approximated by considering the interaction strength between the two particles as follows. The interaction is strongest when the particles are closest to each other. They feel the interaction over a distance $r \sim b$ and thus interact approximately during a time $T \sim \frac{b}{v}$ assuming uniform motion. In order to achieve a significant transfer of excitation from one system to the other, the phase accumulated during this time has to be of the order of one, $\Phi \approx V_n T \sim 1$; too small phases lead to a negligible population transfer while too large phases induce fast oscillations which average out. Combining these equations results

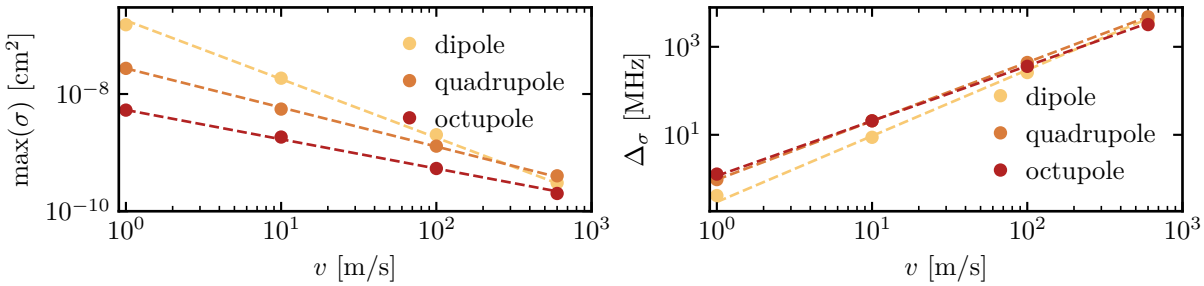

Figure 7.10: Maximal value of the cross-section, $\max(\sigma)$ and width of the line at half maximum Δ_σ as a function of the velocity v for dipole, quadrupole and octupole transitions. The points indicated the values extracted from the simulations (cf. Tab. 7.1), the dashed lines are fits of the expected scaling behaviour.

in an approximation for the critical value of b at which the accumulated phase is of order one,

$$\Phi = V_n T \sim \frac{1}{b^{n+2}} \frac{b}{v} = \frac{1}{v b^{n+1}} \sim 1$$
$$\Rightarrow b^* = v^{-1/(n+1)}.$$

Finally, we estimate that the scattering cross-section σ, which can be interpreted as the effective size of the scattering centre, is roughly of the size b^2. This leads us to the approximate scaling of the cross-section as,

$$\sigma \sim v^{-\frac{2}{n+1}}. \tag{7.9}$$

For a dipole transition in the Rydberg atom, $n = 1$, we thus expect a scaling of $1/v$; for a quadrupole $1/v^{2/3}$ and for a octupole $1/\sqrt{v}$. The proportionality factor depends on the specific transition that is considered and on the dipole matrix elements of both particles. For instance, we have seen in Sec. 7.1, that a diagonal flip-flop (dipole-dipole) transition together with $\vartheta = 0$ leads to a vanishing cross-section at resonance, meaning that the proportionality constant is zero in that case. The scaling of the cross-section with v, however, is the same for all transitions and orientations of the trajectory, as the dipole-multipole potential from Sec. 6.2.1 always scales as $r^{-(n+2)}$.

Figure 7.10 (a) shows the maximal cross-sections obtained from the simulations of the previous sections (given in Tab. 7.1) together with fits of Eq. (7.9). The exponent was set to the predicted value given by Eq. (7.9) and only the proportionality factor was fitted. It can be seen that all three orders follow the predicted scaling perfectly. The fits show a relative standard error of about 5%. As mentioned in Sec. 7.2.1, the fit does not depend strongly on whether we consider the maximal value of the cross-section, the cross-section at resonance, or the peak value of the cross-section when fitting it with a Gaussian or a Voigt profile, since we are averaging over multiple initial states.

In order to derive the scaling of the peak intensity of the cross-section with the velocity, we have assumed the mismatch between the two systems to be vanishing. However, we have clearly observed significant cross-sections for non-zero detuning in the previous simulation. As a result, the cross-section as a function of the detuning describes a peak with a specific width. This line width Δ_σ can be approximated as follows [40]. A non-adiabatic transition occurs at non-zero Δ if the coupling $V_n(t)$ (the off-diagonal elements in Eq. (7.8)) is roughly equal to the energy mismatch Δ (diagonal element). The transition occurs at a critical distance r^* between the particles which is defined by the point where $\Delta = V_n$ with $V_n \sim 1/(r^*)^{n+2}$. Solving for r^* yields $r^* \sim \Delta^{-1/(n+2)}$. The particles require a time of approximately $t \sim r^*/v$ to cover the critical distance. According to the Landau-Zener theory [179], a transition occurs if the accumulated phase Δt is larger than one, or in other words, if the transition rate v/r^* is larger than the energy mismatch Δ. Inserting the critical radius r^* into $\Delta_\sigma \sim v/r^*$ and solving for Δ_σ yields the scaling of the line width with the velocity,

$$\Delta_\sigma \sim v^{\frac{n+2}{n+1}}. \tag{7.10}$$

This results in $v^{3/2}$ for dipole, $v^{4/3}$ for quadrupole and $v^{5/4}$ for octupole transitions. Fig. 7.10 (b) shows the line width of the cross-sections obtained from the simulations of the previous sections as given in Tab. 7.1 together with a fit of the expected scaling behaviour. All three orders seem to follow the expected behaviour perfectly. The relative standard errors of the line width's fit vary between 0.5% for the quadrupole, 4% for the octupole, and 11% for the dipole. The deviations can be explained by the simplified analytical approximation. While we have assumed pure two-level systems in the derivations, the realistic model is more complex which affects the line shape and width and discussed in the previous sections.

On a more fundamental level, Fig. 7.10 gives an estimate of when the multipole expansion breaks down. It can be seen that for velocities $v > 100\,\frac{\mathrm{m}}{\mathrm{s}}$, the cross-sections of all three orders are of the same order of magnitude. For $600\,\frac{\mathrm{m}}{\mathrm{s}}$, the dipole peak is of even lower amplitude than the quadrupole one. As it is at the heart of the multipole expansion that higher-orders decrease in significance, the validity of the expansion clearly breaks down for high velocities of approximately $v > 100\,\frac{\mathrm{m}}{\mathrm{s}}$. Note that the velocity implicitly reflect the distance between the particles. For the calculation of the cross-section, we have to integrate the transition probability over the impact parameter (cf. Eq. (6.46)) and the transition probability takes a peak value close to one at some critical impact parameter b. This critical value decreases as the velocity increases. For $100\,\frac{\mathrm{m}}{\mathrm{s}}$, this value is approximately reached at $b = 200\,\mathrm{nm}$, which is about twice the radius of the Rydberg orbital. To predict the outcome of the scattering process accurately at room temperature, corresponding to a mean velocity of $600\,\frac{\mathrm{m}}{\mathrm{s}}$, for instance, it would thus be necessary to consider the full interaction potential. On the other hand, we have found that isolated transitions, such as the dipole transition from $46p$ to $45d$, which does not experience a strong mixing with other states and which is sufficiently detuned from other transitions, is not strongly affected by including

higher-order terms into the potential. We conclude that the multipole expansion still offers a viable approximation to the realistic behaviour for isolated transitions, i.e. those which do not experience a strong Stark mixing.

The systematic study of the line width and height of the cross-section as a function of the detuning between the Rydberg and molecular transition for different orders of the multipole expansion conducted in this chapter can be utilised to generate predictions for the outcome of experiments. For example, we can generalise the results of Sec. 6.3, where we have simulated the cross-section as a function of the electric field for the Rydberg transition $46p \leftrightarrow 45d$, to other cases. For dipole-dipole transitions, we can combine the scaling laws of Eqns. (7.9) and (7.10) with the scaling of the line width and height with K and J obtained in Sec. 6.3.2. We recall that we found the line width to scale as $\Delta_\sigma \sim 1/\sqrt{d_{\text{ryd}} d_{\text{mol}}}$ while the maximal cross-section scales as $\max(\sigma) \sim d_{\text{ryd}} d_{\text{mol}}$ with $d_{\text{mol}} \sim K/\sqrt{J(J+1)}$. The scaling of the cross-section of dipole-dipole transitions and $J = K$ can thus be summarised as

$$\Delta_\sigma \sim v^{3/2} \frac{\sqrt[4]{J(J+1)}}{\sqrt{K}}, \qquad \max(\sigma) \sim \frac{1}{v} \frac{K}{\sqrt{J(J+1)}}. \tag{7.11}$$

Using these, it is possible to estimate by how much transition lines broaden or narrow when changing the velocity v, the K or J value. In other words, they allows for predicting cross-sections at essentially arbitrary velocities without performing additional simulations.

Consider for example the cross-sections for a thermal ensemble of molecules presented in Figs. 6.10 and 6.11. In that case, the cross-section was determined at a fixed relative velocity of $v = 10\,\frac{\text{m}}{\text{s}}$. We conclude from Fig. 6.10 that it should still be possible to resolve most of the resonances if the lines are no more than twice or thrice as broad, corresponding to velocities of about $20\,\frac{\text{m}}{\text{s}}$ (compare as an example the cross-sections of $v = 10\,\frac{\text{m}}{\text{s}}$ and $20\,\frac{\text{m}}{\text{s}}$ for $J = K = 1$ in Fig. 6.8). As the resonances are further separated for higher values of J and K, individual peaks might be well-isolated for velocities up to $50\,\frac{\text{m}}{\text{s}}$. Beyond that, most of the lines overlap strongly and it will most likely not be possible any more to resolve single resonances from the cross-sections. This qualitative discussion can be refined by changing the width and height of the resonance peaks using the exact scaling laws of Eq. (7.11). Our thorough analysis thus provides the necessary tools for approximating the cross-section as a function of the DC field without performing additional numerical simulations.

7.3 Electric field control of a quadrupole transition

In the previous section, we have studied the cross-section as a function of the inversion splitting of ammonia in order to systematically investigate the scaling of the transition line width and height with the relative velocity between the two particles. Now, we return to controlling the cross-section via the electric field, which serves as a prediction for the outcome of realistic experiments. The goal is to study the multipolar character of FRET at the example of the $50p$ to

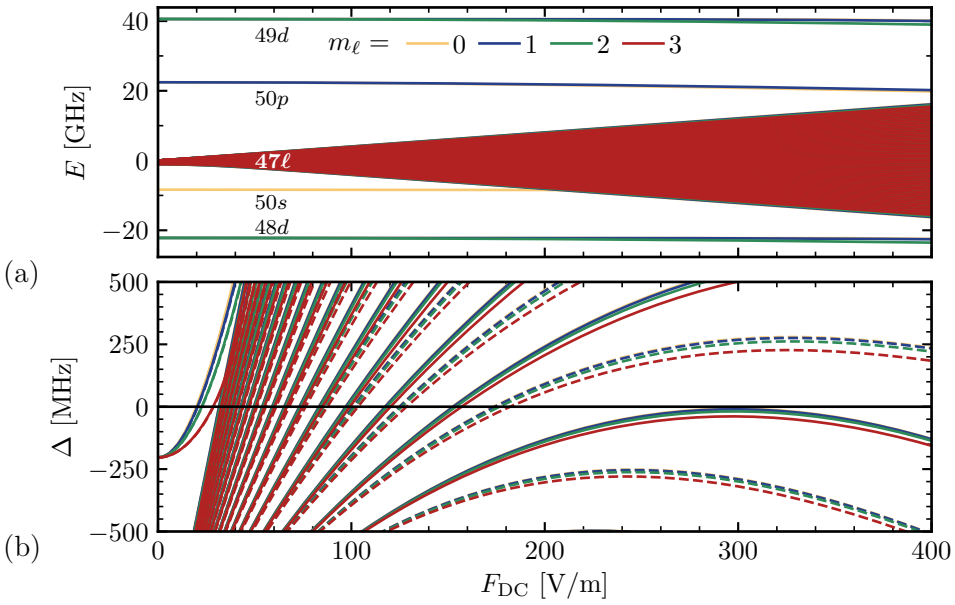

Figure 7.11: Stark map of the Hilbert space of the Rydberg atom shown in Fig. 7.7 for $m_\ell \leq 3$ as indicated by the line colour. (a) shows the absolute energies E where the zero of energy was set to the circular state of the $n = 47$ manifold. (b) shows the detuning Δ of the Rydberg transition frequencies from the to the molecular inversion mode for $J = K = 1$. The dashed lines assume the reference state $50p$, $m_\ell = 0$ and the solid lines $m_\ell = 1$.

47ℓ Rydberg transition, similarly as conducted in Sec. 6.3 for the dipole transition. Most importantly, we can use our insights about the cross-section from the previous section to understand the electric field controlled cross-section of higher order multipole transitions more easily.

We expect the difference between the electric field controlled and the inversion frequency controlled cross-section to be more substantial in the present case, as compared to the dipole transition from $46p$ to $45d$ from Sec. 6.3 and 7.2.1, for the following reason: Tuning the inversion splitting had the advantage of disentangling the tunability of the energy mismatch between the Rydberg and molecular transition from Stark mixing of the Rydberg atom. However, when considering the Rydberg transition $50p$ to 47ℓ (cf. Fig. 7.7), the influence of Stark mixing is immense as 47ℓ constitutes the Stark manifold once an electric field is established. Figure 7.11 (a) displays the Stark map of the Rydberg subspace from 47ℓ to $49d$. It can be seen that the Stark shift of the states within the Stark manifold (47ℓ) is about one order of magnitude larger than the shift of states with a large quantum defect (e.g. $50p$ and $49d$). In addition to that, the states in the Stark manifold mix strongly such that ℓ is not a good quantum number any more. As a result, there is not "one" f (or g) state any more – once the DC field is employed, almost all states have a certain amount of f (or g) character mixed in. When tuning the cross-section by the electric field, instead of by the inversion splitting, it can therefore be expected that many quadrupole transitions occur from $50p$ to states within the Stark manifold which have a fraction of $\ell = 3$ mixed in. Dipole transitions, on the other hand, are highly unlikely as states $\ell = 2$ (such as $49d$) are strongly

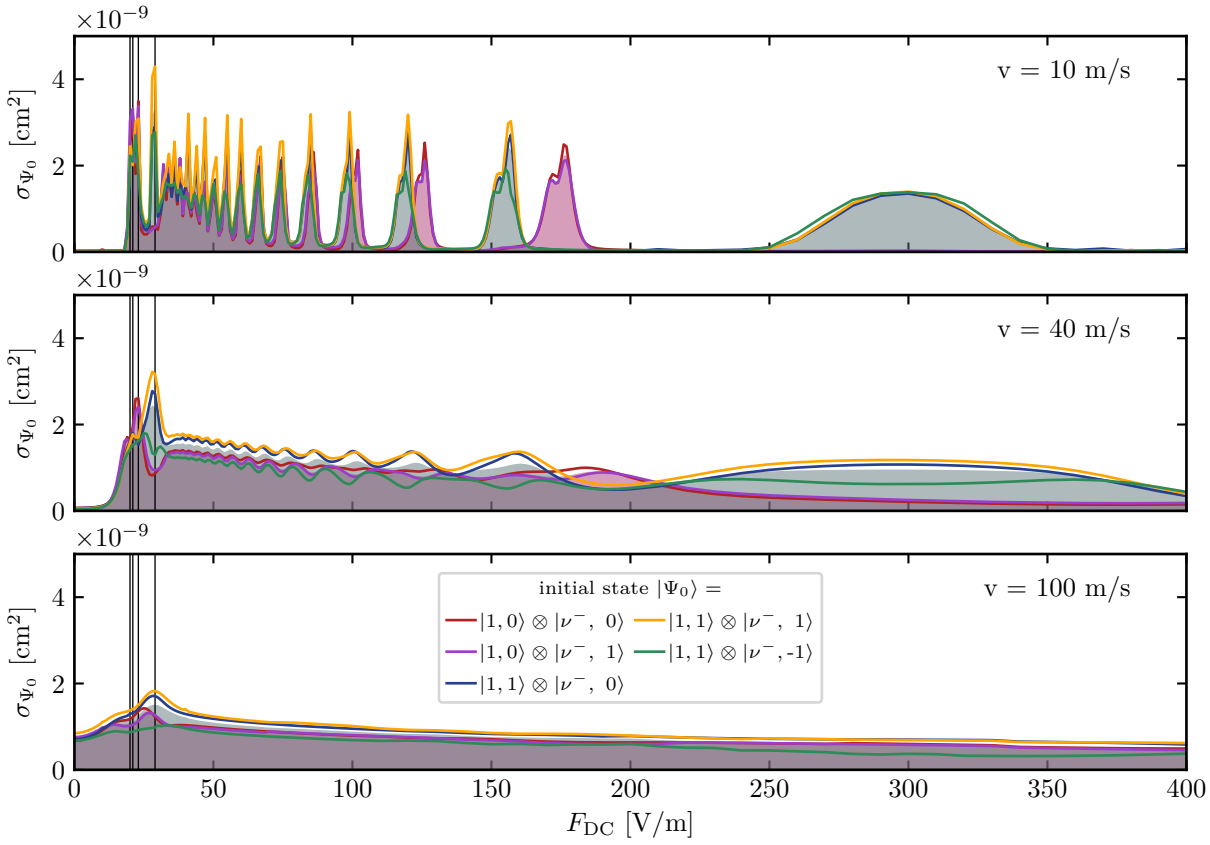

Figure 7.12: Cross-section for different initial states (solid lines) as a function of the DC field F_{DC} for the $50p$ to 47ℓ-transition for three different velocities. The vertical lines indicate the resonances of the $50p$ to $47f$ Rydberg transition with the $J = K = 1$ inversion mode of ammonia. The red shaded area indicates the cross-section averaged over all initial states with $m_\ell = 0$ corresponding to the red and purple lines, and the blue shaded area for $m_\ell = 1$ corresponding to the blue, green and yellow lines, respectively.

detuned from the transition frequency of the inversion mode. We thus expect this transition to be dominated by dipole-quadrupole interactions. In this section, we therefore study the electric field controlled cross-section when considering the Rydberg transition $50p$ to 47ℓ and all three orders of the multipole expansion.

We assume the Rydberg atom to be initially in $50p$ and the molecule to be in the lower inversion state with $J = K = 1$, i.e. $|50p, m_\ell\rangle \otimes |\nu^+ M\rangle_{K=1,J=1}$. During the simulations, we consider all states within 47ℓ with $\ell = 3 \ldots 46$ (instead of limiting the number of states by using the selection rules as has been done in Sec. 7.2.2 and 7.2.3), as they all get mixed by the Stark effect. Note that this increases the size of the Hilbert space immensely and renders the numerical simulations more expensive. All other parameters are given in Tab. A.10 in Appendix A.3. Figure 7.12 shows the cross-section as a function of the DC field strength for three different velocities. We only investigate the cross-section up to fields of $F_{\mathrm{DC}} = 400\ \frac{\mathrm{V}}{\mathrm{m}}$ as for higher fields, the reference state $50p$

gets significantly mixed with the Stark manifold and a clear addressing would be complicated (see Stark map in Fig. 7.11). Already at first glance, the spectrum of this transition looks much richer than the one of the dipole transition discussed in Sec. 6.3. The reason is the aforementioned mixing of the states due to the Stark effect.

To gain further insight, we start by discussing the lowest velocity, $v = 10\,\frac{\mathrm{m}}{\mathrm{s}}$, in more detail. The spectrum reveals a regular peak structure which can in fact be attributed to the structure of the Stark manifold: Figure 7.11 (b) shows the detuning Δ (cf. Eq. (6.43)) of the Rydberg transitions $\omega_{\mathrm{ryd}} = E_0 - E_1$ (as defined in Eq. (6.42) with $50p$ corresponding to E_0 and 47ℓ to E_1) from the molecular inversion mode with $J = K = 1$. By comparing Fig. 7.11 (b) to Fig. 7.12 at $v = 10\,\frac{\mathrm{m}}{\mathrm{s}}$, it can clearly be seen that each peak in the cross-section corresponds to the inversion mode matching one Rydberg transition from $50p$ to a state within the Stark manifold. For instance, around $300\,\frac{\mathrm{V}}{\mathrm{m}}$, we observe an isolated, broad peak when the Rydberg atom is initially in $50p, m_\ell = 1$ which corresponds to a transition to the DC dressed states which touch on the resonance at the same field strength (solid lines in the Stark map). The strong peaks around $25\,\frac{\mathrm{V}}{\mathrm{m}}$ (indicated by the vertical black lines) corresponds to the resonance of $50p$ to $47f$ transition[1] with the inversion mode. Measurement of the cross-section as a function of the electric field thus allows for direct conclusions about the Hilbert space of the Rydberg atom and observation of the Stark manifold.

When considering other velocities, it can be seen that the pattern of the Stark manifold can be observed for velocities up to about $40\,\frac{\mathrm{m}}{\mathrm{s}}$. At higher velocities, the peaks get too broad to resolve individual transitions and no substructure can be resolved in the spectrum except for the initial resonance to $47f$ (indicated by the vertical black lines). For even higher velocities, $600\,\frac{\mathrm{m}}{\mathrm{s}}$, not even the main resonance is resolved any more and the cross-section appears almost completely flat (data not shown).

In order to estimate which contributions of the multipole expansion play a major role, we repeat the simulations with only selected contributions to the interaction potential at velocities of $100\,\frac{\mathrm{m}}{\mathrm{s}}$. We start by considering only dipole-dipole interactions and investigate both possibilities of the molecule being initially in the upper or lower inversion state. The resulting transfer probabilities are vanishingly small and the cross-sections three to six orders of magnitudes smaller (data not shown). The dipole-quadrupole interaction is thus the dominating contribution for the spectrum shown in Fig. 7.12 and no transitions to the higher lying state $49d$ take place. This is not surprising as it high highly detuned with $\omega_{\mathrm{ryd}} = 18.142\,\mathrm{GHz}$. Moreover, initial states where the molecule is in the upper state do not play a major role for any order of the multipole expansion and we find deviations of maximally 1% when neglecting them.

When truncating the multipole expansion after the second order, i.e. when neglecting the dipole-octupole interaction, the spectrum looks almost identical to the one presented in Fig. 7.12. The only difference is a minor offset: the curves without the dipole-octupole interaction have a minimally smaller amplitude. This difference is not even visible on the scale of the plot shown

[1] To be exact, ℓ is not a good quantum number at non-vanishing DC field. We label by $47f$ the state with the largest overlap with the state $|n = 47, \ell = 3\rangle$ in the spherical basis.

above. We conclude that the dipole-quadrupole interaction is dominating this process and transitions mostly occur from $50p$ to $47f$ due to the $\Delta\ell = 2$ selection rule of quadrupole transitions. In principle, octupole transitions with $\Delta\ell = 3$ from $50p$ to $47g$ are also allowed. However, $47g$ already joins the Stark manifold at very small DC fields and therefore gets strongly mixed with other states. This decreases the transition probability as every DC dressed state has only a small fraction of the g-state mixed in. Due to this and the lower amplitude of octupole transitions in general, they do not contribute significantly to the spectrum in Fig. 7.12.

If the goal is to observe an isolated octupole transition, equivalently to having observed an isolated quadrupole transition above, one could change the initial state to be a d state below the Stark manifold. Fig. 7.11 shows that the state $48d$ is located $25.4\,\mathrm{GHz}$ below the Stark manifold. This transition frequency, however, is detuned by about $2\,\mathrm{GHz}$ from the ammonia inversion mode for $J = K = 1$. By moving to lower principal quantum numbers, the transition frequency can be reduced and the two particles can again be brought into resonance.

Lastly, we discuss the influence of the admixture of higher rotational states, $J, K > 1$, onto the spectrum of this transition. Most of the arguments from Sec. 6.3.2 on the dipole transition $46p$ to $45d$ can be applied to this case in a similar fashion. Some differences must be considered. Firstly and most importantly, the $50p$ to 47ℓ-transition has a richer spectrum with more narrowly spaced lines as we are driving transitions into the Stark manifold. Most of the resonances might therefore be placed very closely to each other, rendering it more difficult to distinguish them. Secondly, the quadrupole and octupole lines are broader as the dipole ones which lowers the velocity at which they might be distinguished. This has been shown in Fig. 7.10 (b). Thirdly, the scaling of the line width and height with J and K for a fixed velocity has to be reconsidered when assuming dipole-quadrupole or dipole-octupole interactions as given in Eqns. (6.37) and (6.38). While the scaling of the interaction strength with the dipole element of the Rydberg atoms changes as compared with dipole-dipole coupling, the interaction strength still scales linearly with the dipole moment of the molecule in higher orders of the multipole expansion. As a result, the line width and height scale the same way with K and J as for the dipole-dipole interaction (cf. Eq. (7.11)).

Taking these points together, the only lines which might be possible to resolve when including higher rotational states in Fig. 7.12 are the ones at fields higher than $100\,\frac{\mathrm{V}}{\mathrm{m}}$ as they are fairly well separated. This prediction can be tested by determining the resonances between the Rydberg transitions and the inversion mode of ammonia for higher values of J and K, and plotting them into Fig. 7.12. The width of the peaks can be approximated by assuming the scaling laws derived above. As discussed in Sec. 6.3.2 for the dipole transition, it would be possible to determine the population of different rotational states in a molecular ensemble by comparing the spectroscopic measurements of an experiment to the simulated spectra. The Rydberg atom would thus serve as a probe of measuring the population of different J and K states of the molecule.

7.4 Summary

In this chapter, we have presented a thorough analysis of different order multipole contributions to the Förster resonance energy transfer (FRET) between Rydberg atoms and ammonia molecules. We have studied the dipole-dipole interaction considering two states in each system only, and were able to explain the complex structure of peaks and dips in the electric field controlled cross-section by means of the interaction potential. We found that the initial states of the systems and the orientation of the trajectory strongly affect the line shape of the cross-section. Our observations could be tested experimentally by preparing the Rydberg atoms in different $|m_\ell|$ levels before scattering them off molecules and determining the spectrum afterwards.

Afterwards, we have studied different orders of the multipole expansion independently and determined the scaling of the resulting maximal cross-section and its line width with the relative velocity between the two particles. We have found a scaling of both quantities with the relative velocity of the particles which is in excellent agreement with an analytical approximation as shown in Fig. 7.10. Using these data, we have estimated the breakdown of the dipole approximation to occur at a relative velocity between the two particles of $100\,\frac{\mathrm{m}}{\mathrm{s}}$ which can be interpreted as a distance of about $200\,\mathrm{nm}$ between them. Moreover, we have observed interference of higher-order contributions giving rise to features in the cross-section as a function of the inversion splitting of ammonia which cannot be explained when considering different orders independently. We attribute those effects to an increased set of accessible states due to the larger number of allowed transitions, and interference between different paths which allow for driving off-resonant transitions. Lastly, we have investigated a dipole-forbidden transition in the Rydberg atom and found strong signatures of FRET, thus highlighting the importance of dipole-quadrupole interactions. The cross-section has been tuned as a function of the electric field and displayed a rich structure of peaks which reflects the structure of the Rydberg atom's Stark manifold. The simulations serve as a direct prediction for the outcome of experiments, when recording the state of the Rydberg atoms after their collision with ammonia molecules when tuning the electric field.

Beyond studying the breakdown of the multipole expansion, the thorough investigation of the transition lines allows for predicting the spectrum of the cross-section for different initial states or velocities without performing additional simulations. Conversely, the shape of a experimentally measured spectrum allows for drawing conclusions about the state of the molecule. On the one hand, FRET transfers population in the Rydberg atom to another energy level; detection of the atom in this state is thus a clear indicator for the presence and density of molecules. On the other hand, the peak structure of the cross-section as a function of the DC field serves as an indicator for which rotational levels $|JK\rangle$ of the molecule are populated, and their relative hight reveals the population of these levels. The Rydberg atom thus acts as a sensor providing information about the molecular state which is the first step towards a non-destructive measurement of polar molecules as proposed recently [40].

All of our simulations can be generalised to other initial states, transitions or even atomic or molecular species easily. The main requirement is the existence of a (near-)resonant transition in two particles with large dipole (or n-pole) matrix elements. The striking advantage of utilising Rydberg atoms for FRET is, in addition to large dipole moments, their rich spectrum which allows for tuning the transition frequencies by choosing the principal quantum number n in addition to a fine-tuning using the Stark effect. This allows for combining them with essentially arbitrary molecular transitions in the MW-range. Moreover, the simulations can be adapted to various experimental conditions, such as thermally distributed velocities or trajectories with arbitrary or undetermined orientations. The most important consequence of increasing the number of parameters over which to average is an increased computation time. In some cases, however, a few sampling points are sufficient to estimate the effect of an average. For instance, three to four sampling points for the velocity v are sufficient to reveal the general scaling behaviour of the cross-section. If the velocity is not selected accurately but, for instance, given by a Gaussian distribution, the only effect that is to be expected is a broadening of the lines.

As mentioned above, several features that have been found in the simulations could be compared directly to the outcome of experiments. It would be most insightful to study the predicted features related to higher-order effects, such as the non-vanishing cross-section for large detuning (cf. Fig. 6.8) or quadrupole transitions into the Stark manifold (cf. Fig. 7.12). As a next step regarding the simulations, it would be interesting to study the final state of the molecule after the interaction. One question would be if it is possible to selectively prepare states in molecules by means of their interaction with Rydberg atoms; one example being the orientation of a molecular ensemble along the quantisation axis. The preparation of the Rydberg atoms in well-chosen initial states offers a degree of freedom in this scenario.

The simulated cross-sections as a function of the DC field could be compared to spectroscopic measurements of experiments to gauge the accuracy of the model. If deviations between the theoretical predictions and the experimental measurements were detected, there are several options to improve and generalise the model. For instance, the simple approximation of a classical trajectory and the molecule being in uniform motion could be lifted and replaced by a more involved simulation of the particles' motion. This might be necessary especially for experiments with very low relative velocities between the two particles, as we assumed the change in internal energy caused by the collision to be small compared to the kinetic energy of the particles. Also, the multipole expansion of the interaction potential could be replaced by numerically solving the Schrödinger equation under the full interaction potential. This would increase the cost of the numerical simulations significantly but also increase the accuracy of the simulations. More precisely, it would be possible to simulate the cross-section for arbitrary velocities and also if higher order multipole transitions are involved. In summary, the model we have presented and studied in the last two chapters serves as a starting point and playground for investigating the multipolar character of FRET and collisions between Rydberg atoms and polar molecules.

8

SUMMARY AND OUTLOOK

In this thesis, I have presented multiple ways of using Rydberg atoms in different fields of quantum technology. I have developed new ways to employ Rydberg atoms in novel settings, improve established methods, use them as ancillas for the study of open quantum system dynamics, and study their interaction with other particles. All of these projects are linked in their central endeavour: controlling Rydberg atoms for quantum technologies. To this end, I went from quantum metrology to quantum sensing; from isolated, single Rydberg atoms – both alkali and alkaline-earth – over light-matter interaction and open quantum system dynamics, to the scattering process between Rydberg atoms and molecules. All these results show both the versatility of Rydberg atoms as well as the employed methods.

Fast Navigation in the Stark manifold

I have started by studying single alkali Rydberg atoms and their control using electromagnetic radiation. The accurate preparation of specific target states is a vital task for essentially every quantum technology. The difficulty often lies in the required accuracy, speed or even sheer possibility to prepare the desired states. In Chapter 3, I have demonstrated by means of two selected examples that all of these problems can be tackled using optimal control theory. I have started by deriving optimised RF pulse shapes for preparing circular states of Rydberg atoms both fast and accurately under experimental constraints on pulse amplitude and bandwidth. In collaboration with experimentalists from Laboratoire Kastler Brossel (LKB) at Collège de France, Paris, we showed that the circularisation can be performed within $\sim 100\,\mathrm{ns}$ with an excellent fidelity of 99% in the simulations and 96% in the experiment. This is a great improvement in speed, as compared to adiabatic methods which take a few microseconds, and in fidelity, as compared to a simple π-pulse with 80% efficiency. Beyond merely improving existing protocols, we have also shown that optimal control theory can be used to prepare non-trivial superposition states for which no intuitive preparation method was known beforehand. We have demonstrated the preparation of a Schrödinger-cat like state, i.e. a superposition of two states at opposite poles of the Bloch sphere, within $150\,\mathrm{ns}$ with a fidelity of 99% in the simulations and 93% in the experiment.

The results of that chapter serve as a proof-of-principle for the preparation of almost arbitrary states in the Stark manifold of Rydberg atoms using optimal control theory. Most importantly, the method can be generalised to an essentially arbitrary number of control pulses with arbitrary polarisation. The method is moreover not limited to a small subspace of the Stark manifold, as we have used in our examples, but can be extended to controlling the dynamics within the full Stark manifold. One interesting application would be the preparation of a superposition of opposite circular states (i.e. circular states with $|m_\ell = n-1\rangle$ and $|m_\ell = -n+1\rangle$) using RF pulses only [58, 1]; or similarly the preparation of a superposition between states on the upper and lower edge of the Stark manifold (i.e. between extremal elliptic states with $|m_\ell = 0, \mu = -n+1\rangle$ and $|m_\ell = 0, \mu = n-1\rangle$). While the former would serve as an excellent sensor for magnetic fields [58], the latter would do the same for electric fields [47]. Also a combination of optimal control theory with quantum Zeno dynamics seems interesting, as MW pulses can be used to truncate the Hilbert space [180], thus enabling new control strategies which would have been challenging otherwise due to the high symmetry within the Stark manifold. All in all, our study paves the way for preparing highly complex, non-classical states of Rydberg atoms under experimental conditions, which can advance many fields of quantum technology.

Improved modelling of alkaline-earth atoms

Afterwards, we have extended our model from alkali to alkaline-earth atoms. The second valence electron will leave the ionic core optically active and will thus further increase the versatility of Rydberg atoms for quantum technologies. In order to apply optimal control theory to alkaline-earth atoms efficiently, an accurate model is a major requirement. In Chapter 4, we have therefore studied Stark maps of strontium to improve the modelling of alkaline-earth atoms. We have started from the single-active electron (SAE) model proposed in literature and found significant discrepancies between experimental and simulated data. Based on the acquired insights and physical understanding, we have developed an improved model which reproduces the experimental data with high fidelity. First tests suggest that fast and accurate circularisation of strontium using optimal control is possible under experimental conditions, albeit more challenging than for rubidium.

Optimal control of alkaline-earth atoms would prove useful in many fields of quantum technology as the existence of two valence electrons opens the possibility to combine different tasks: while the inner electron can be used to trap, cool or image the atom, the outer electron can be used for quantum technology applications. One very promising example are Rydberg atom quantum simulators which can be used to study many-body physics [94]. A major prerequisite for this technology is the accurate trapping of atoms in a lattice as demonstrated for alkali Rydberg atoms in low-angular-momentum states in three dimensions using ponderomotive bottle beam traps [101]. Low-angular momentum Rydberg states, however, possess a comparatively short lifetime in the $100\,\mu\mathrm{s}$ range, thus significantly limiting the time during which the simulator

can perform simulations. Circular Rydberg atoms, on the other hand, have much longer intrinsic lifetime around $50\,\mathrm{ms}$ for $n = 50$. While trapping of circular states of alkali atoms has been demonstrated in two-dimensions [181], their control is generally more challenging as they are impervious to visible light. Strontium atoms in circular states could solve these problems by providing an optical transition of the core electron and the remarkable properties of circular Rydberg atoms (like a long lifetime) at the same time. While the preparation of circular Rydberg states of strontium has already been demonstrated in the experiment [182], the current fidelity is limited to about 85% which is not sufficient for quantum simulation. The presented work thus paves the way for fast an accurate circularisation of strontium Rydberg atoms and, ultimately, optical manipulation of circular Rydberg atoms.

Quantum simulation of open quantum systems

In the previous two projects, the Rydberg atoms have been assumed to be free of dissipation. This was possible as the total duration of the experiment was much shorter than the excited state's lifetime. The fast protocol times achieved via optimal control allow for the preparation of even intricate superpositions faster than decoherence could destroy them. In addition to that, the carefully engineered control pulses with limited bandwidth and amplitude proved to be very stable against other sources of noise, such as field fluctuations. However, it is not always possible to avoid decoherence on the relevant time scales. It is therefore of utmost importance for the engineering of quantum technologies, which require highest precisions, to study open quantum systems. Quantum simulation, itself one pillar of quantum technology, provides a suitable tool for this objective. In Chapter 5, I have therefore presented a quantum simulator for open quantum system dynamics in which dissipation strength and non-Markovianity can be tuned independently from each other. In the Markovian limit, the dynamics of the open quantum system can be described by a Lindblad master equation.

The proposed simulator uses the quantum Zeno effect to enable the controlled, experimental study of dissipation, memory effects, and their interplay in open quantum system dynamics. In particular, it will allow for classifying the role of memory effects for the controllability of open quantum systems [30]. In more detail, it is constructive to combine two experimental protocols: a specific control protocol (to prepare a desired state or implement a quantum gate) and the measurement-based open system simulator. Changing the type and strength of dissipation in the open system simulator will allow for assessment whether or not, and how well, the control protocol's figure of merit can be optimised. In the same spirit, such a combination of quantum control and tunable dissipation allows for investigating how memory effects alter control strategies for open quantum systems and their relevance for applications in quantum technology.

Multipolar character of FRET in the scattering of Rydberg atoms and polar molecules

The quantum simulator capitalises on the strong interaction between Rydberg atoms and light caused by their large dipole moment. For the same reason, Rydberg atoms are ideal for combination with other systems. These so-called quantum hybrid systems hold great interest for quantum technologies as they promise to unify the advantages of their constituents. When combining Rydberg atoms with molecules, for instance, the high level of control achievable for atoms can be transferred to molecules. As a concrete example, the strong dipole-dipole coupling between Rydberg atoms and polar molecules can be exploited for a novel, non-destructive detection method of the latter where the Rydberg atoms serve as meters. To this end, I have studied the scattering process between the two species in Chapter 6. I have modelled the scattering process from first principles assuming their interaction to be that of a dipole (the molecule) with a charge distribution (the Rydberg electron) and expanded the potential up to third order, thus accounting for dipole-dipole, -quadrupole and -octupole contributions. I have calculated the cross-section of the scattering process numerically and presented predictions for the outcome of realistic experiments. Moreover, the measured spectrum was found to provide information on the composition of the rotational states of the molecule.

If the particles possess a resonant transition, they exchange energy without emitting radiation in a process known as Förster resonance energy transfer (FRET). FRET is usually treated in the dipole-dipole approximation which is expected to break down if the size of one of the particles becomes comparable to their separation. In Chapter 7, I have studied the first three orders of the multipole expansion independently and investigated their influence on FRET. This allows for understanding the state-dependence of the cross-section around the resonances between the Rydberg transitions and the inversion mode of ammonia. Different orders of the multipole expansion were found to interfere causing, for instance, non-vanishing cross-sections for large detuning of the particles' transitions. Furthermore, I compared the scaling of the maximal cross-section and the transition line width of the cross-section as a function of the detuning to analytical approximations and found an excellent agreement. This allows for estimating the breakdown of the dipole-dipole approximation at relative velocities of approximately $v > 100\,\frac{\mathrm{m}}{\mathrm{s}}$ due to the large size of the Rydberg orbitals. Lastly, the cross-section of a dipole-quadrupole transition in the Rydberg atom was simulated as a function of the DC field, revealing strong signatures of the Stark manifold which can be resolved until velocities of approximately $40\,\frac{\mathrm{m}}{\mathrm{s}}$.

The results of these two chapters can easily be generalised to other atomic or molecular species and promise advances in predominantly two directions: the development of a non-destructive detection method of polar molecules via Rydberg atoms, and the systematic study of the multipolar character of FRET. In combination, several interesting question arise: What spectroscopic possibilities open up in detection methods when the full interaction potential (i.e. higher order multipole contributions) is taken into account? What role does the angular dependence, i.e. the orientation of the trajectory, play? Can the final state of the molecular ensemble

be engineered? The presented work has only scratched the surface of these questions but the model allows for investigating them in detail. FRET is the basis for prominent spectroscopic techniques for molecular systems and regularly employed with quantum dots [41, 170]. The benefit of improving the understanding of this method and exploiting its full potential is therefore formidable.

Control of Rydberg atoms for quantum technologies

Lastly, let us take a step back and consider the results of this thesis in a bigger context. I have presented methods for controlling the dynamics in high-dimensional Hilbert spaces, optimising unknown model parameters, simulating an environment, truncating Hilbert spaces, simulate scattering and study resonant energy transfer. While all projects involved Rydberg atoms, generalisations to other systems is straight-forward in all cases, as the Hamiltonian can easily be adjusted or replaced in theoretical simulations. I have thus presented a comprehensive toolbox for controlling and simulating quantum dynamics. Of course, all these efforts were supported by prior work in the group and the QDYN library [62].

Quantum technology has received major public attention due to immense public funding programs or investments by multinational companies, such as Google, IBM and Intel [15]. Quantum control cuts every pillar of quantum technology as laid out in the Quantum Technologies Roadmap of the European Community [15]. In this thesis, I have specifically addressed two of these pillars – quantum metrology and simulation – and presented great achievements. However, fast and accurate control, as demonstrated in Chapter 3, is a vital task for all areas of quantum technology, including quantum computing, which is without question the most prominent effort and challenge the community aims to achieve. The results on navigating the Stark manifold of Rydberg atoms serve as a clear example of how to tackle this challenge. Beyond this, improving the convergence between theory and experiment is one of the main obstacles for realising quantum technology [15]. Our joined work with experimentalists from the LKB demonstrates the great performance of optimised pulse shapes in an experiment. The insights gained in the process will most certainly be valuable when moving to different applications in other experimental platforms. The Roadmap further names the study of fidelity limits in the presence of noise in the Markovian and non-Markovian regime as a major challenge – a study which is clearly facilitated by the proposed quantum simulator. Its great versatility allows for exploring the influence of different kinds of environments in various experimental platforms. The combination of the quantum simulator with selected control schemes allows for investigating the detriments and perhaps even benefits of an environment with given properties. In conclusion, the study of quantum control can bring the whole field of quantum technology forward as “it is control that turns scientific knowledge into technology” [27].

A

PARAMETERS OF THE SIMULATION

In the following, we present all the parameters we used for the theoretical simulations of Rydberg atoms and their interaction with molecules. We start by listing the model parameters for describing rubidium atoms in Sec. A.1, followed by the parameters for strontium in Sec. A.2. In Sec. A.3, we list the parameters employed for simulating the scattering trajectories of rubidium and ammonia.

A.1 Rubidium

We assume experiments with the alkali atom ^{85}Rb which have a nuclear charge of $Z = 37$ and a dipole polarisability of $\alpha_c = 9.0760$ [183]. Furthermore, we have assumed the following quantum defects as listed in [52].

L	J	δ_0	δ_2	
0 (s)	$1/2$	3.131145	0.195	[184]
1 (p)	$1/2$	2.65486	0.280	[184]
	$3/2$	2.64165	0.318	[184]
2 (d)	$3/2$	1.34807	-0.603	[184]
	$5/2$	1.34642	-0.545	[184]
3 (f)	$5/2$	0.0165192	-0.085	[185]
	$7/2$	0.0165437	-0.086	[185]
4 (g)	$7/2, 9/2$	0.004	0	[186]
5 (h)	$9/2, 11/2$	0.001	0	[186]
6 (i)	$11/2, 13/2$	0.0006	0	[186]
7 (j)	$13/2, 15/2$	0.0003	0	[186]

Table A.1: Quantum defects of rubidium.

A.2 Strontium

In our simulation with alkali-earth atoms, we now consider strontium atoms. We start by listing the employed quantum defects in Sec. A.2.1, followed by the parameters for the single-active electron (SAE) model in Sec. A.2.2. Afterwards, we list the experimental data points which we have used to perform the fit of the model parameters at zero DC field in Sec. A.2.3. Finally, in Sec. A.2.4, we present a summary of the optimised model parameters.

A.2.1 Quantum defects

In the following tables, we list the quantum defects for the singlets ($S = 0$) and triplets ($S = 1$) separately. The reference is [114] unless noted otherwise. The values in the tables are the initial ones we used before performing any optimisation and which have been used to generate Fig. 4.1.

L	δ_0	δ_2	δ_4
0 (s)	3.26896	-0.138	0.9
1 (p)	2.7295	-4.67	-157
2 (d)	2.3807	-39.41	-1090
3 (f)	0.08707 [115]	-2	0 [115]
4 (g)	0.038 [115]		
5 (h)	0.0134759 [115]		

Table A.2: Quantum defects of the strontium singlets.

L	J	δ_0	δ_2	δ_4
0 (s)		3.371	0.5	
1 (p)	$L-1$	2.8866	0.44	-1.9
	L	2.8824	0.407	1.3
	$L+1$	2.8719	0.446	-1.9
2 (d)	$L-1$	2.658	3	-8800
	L	2.636	-1	-9800
	$L+1$	2.63	-42.3	-18000
3 (f)		0.111867 [115]	-2.2 [115]	120
4 (g)		0.03844 [115]		
5 (h)		0.0134759[115]		

Table A.3: Quantum defects of the strontium triplets.

A.2.2 SAE parameters

In our simulations, we have employ the ℓ-dependent potential in the SAE approximation [32] as given in Eq. (4.4) with the effective charge from Eq. (4.5) where $Z = 38$. We employed modified polarisability from Eq. (4.6) with $\alpha_c = 7.5$. The parameters have been taken from [32] and take the following values:

$\ell =$	0	1	2	$\geq$3
α_1^ℓ	3.36124	3.28205	2.155	2.1547
α_2^ℓ	1.3337	1.24035	1.4545	1.14099
α_3^ℓ	5.94337	3.78861	4.5111	2.1987
r_c^ℓ	1.59	1.58	1.57	1.56

Table A.4: SAE model parameters of strontium.

A.2.3 Experimental data at zero field

In the following, we list the experimental data at zero DC field as recorded by our experimental collaborators [115], which we have used in Sec. 4.2.2 to fit optimise the model parameters. The following three tables give the position of the $\ell = 3$, 4 and 5 levels separately.

n	s	j	E [MHz]
48	1	2	-217966.3301
48	1	3	-217928.4631
48	1	4	-217880.4551
48	0	3	-216395.7901
49	0	3	-158400.9931
50	1	3	-105210.2536
50	1	4	-105167.8101
50	0	3	-103856.7001
51	0	3	-52494.51309
52	1	3	-5264.001086
52	1	4	-5226.288086
52	0	3	-4071.646086
53	0	3	41631.86691
54	0	3	84816.08591

Table A.5: Experimentally determined position of the energy levels of $\ell = 3$ (f) at zero DC field where the zero of energy was set to the centre of the $n = 52$ manifold.

n	s	j	E [MHz]
49	1	3	-155727.8551
49	1	4	-155721.4251
49	1	5	-155703.7251
49	0	4	-155683.5201
51	1	4	-50116.23589
51	0	4	-50082.61309
53	1	4	43752.30091
53	0	4	43782.27891

Table A.6: Experimentally determined position of the energy levels of $\ell = 4$ (g) at zero DC field where the zero of energy was set to the centre of the $n = 52$ manifold.

n	E [MHz]
48	-212054.4201
48	-212049.4601
50	-100009.2621
52	-653.6000865
52	-649.5700865
54	87869.36191
54	87872.92591

Table A.7: Experimentally determined position of the energy levels of $\ell = 5$ (h) at zero DC field where the zero of energy was set to the centre of the $n = 52$ manifold. Note that the labels singlet and triplets are not longer valid for h states

A.2.4 Summary of the optimised model parameters

In this section, we briefly summarise the optimised parameters of the modified SAE model derived in Sec. 4.2.2. We optimised the states with $3 \leq \ell \leq 5$ (f, g, and h) and found the following parameters.

ℓ	n	δ_0^1	δ_2^1	δ_0^3	δ_2^3
3 (f)	$\left\{\begin{matrix}48,50,52\\50,52\end{matrix}\right\}$	0.087369	-1.549	$\left\{\begin{matrix}0.1110\\0.1097\end{matrix}\right\}$	$\left\{\begin{matrix}2.63\\5.95\end{matrix}\right\}$
4 (g)	48	0.0383956461906433	0	0.0388678805351258	0
5 (h)	48,52,54	0.013975	-0.158	δ_0^1	0

ℓ	n	Ω_{nL} [MHz]	$\omega_{n\ell}$ [MHz]
3 (f)	48,50,52	$10^{5.826}\, n^{-3}$	0
4 (g)	48	-0.0195797509096735	2.7204884613256435
5 (h)	48,52,54	0	$10^{4.703}\, n^{-3}$

Table A.8: Optimised quantum defects (upper panel) and spin-orbit couplings (lower panel) for the f to h states. $\delta_{0,2}^1$ and $\delta_{0,2}^3$ denote the zero-th and second order quantum defects (subscript 0 or 2) for singlets and triplets (superscript 1 or 3). The n-column denotes the n-values that were considered during the fit. The only exception are the quantum defects for the singlets for which the value $n = 48, \ldots, 54$ were taken into account. For the quantum defect of the f triplets, two different fits are presented considering different n-values (indicated by the curly brackets).

A.3 Scattering

As explained in Sec. 6.2.2 of Chapter 6, the calculation of the cross-section requires first, the propagation of the combined system from some initial time $-t_0$ to some final time t_0 which we assume to be $t_0 \approx v/r_{\text{mol}}(t_0)$. Second, the transition probability has to be integrated over the impact parameter, which is discretised from b_{min} to b_{max} in steps of b_{step}. In the following, we list the parameters that have been used to generate the figures in Chapter 6 and 7.

v[m/s]	t_0[ns]	b_{start}[nm]	b_{stop}[nm]	b_{step}[nm]
10	200	200	2000	10
20	100	100	1000	6
50	40	100	1000	6
100	20	50	1000	5

Table A.9: Parameters for the determination of the cross-section in Fig. 6.8 for the $46p$ to $45d$-transition. For each velocity, the considered grid of the impact parameter is given, determined by b_{start} and b_{stop} and b_{step}. The time-propagation was conducted from $-t_0$ to t_0.

v[m/s]	t_0[ns]	b_{start}[nm]	b_{stop}[nm]	b_{step}[nm]
10	200	60	700	20
40	50	60	600	20
100	20	50	400	10

Table A.10: Parameters for the determination of the cross-section in Fig. 7.12 for the $50p$ to 47ℓ-transition. Otherwise same as Tab. A.9.

v[m/s]	t_0[ns]	b_{start}[nm]	b_{stop}[nm]	b_{step}[nm]	$\max(\sigma)$[cm^2]	Δ_σ[MHz]
1	2000	500	5500	50	$1.5 \cdot 10^{-7}$	0.42
10	200	200	2000	20	$1.9 \cdot 10^{-8}$	8.8
100	20	50	800	10	$2.0 \cdot 10^{-9}$	260
600	3	50	300	5	$3.1 \cdot 10^{-10}$	3840

Table A.11: Parameters for the determination of the dipole line shape in Sec. 7.2.1. For each velocity, the considered grid of the impact parameter is given, determined by b_{start} and b_{stop} and b_{step}. The time-propagation was conducted from $-t_0$ to t_0. The resulting maximal value of the cross-section $\max(\sigma)$ and the width of the line at half maximum Δ_σ were determined from the simulations.

v[m/s]	t_0[ns]	b_{start}[nm]	b_{stop}[nm]	b_{step}[nm]	$\max(\sigma)$[cm^2]	Δ_σ[MHz]
1	2000	200	2000	100	$2.7 \cdot 10^{-8}$	0.96
10	200	200	1000	50	$5.5 \cdot 10^{-9}$	20.8
100	20	50	500	10	$1.3 \cdot 10^{-9}$	440
600	3	10	250	10	$3.8 \cdot 10^{-10}$	4800

Table A.12: Same as Tab. A.11 but for the quadrupole transitions in Sec. 7.2.2.

v[m/s]	t_0[ns]	b_{start}[nm]	b_{stop}[nm]	b_{step}[nm]	$\max(\sigma)$[cm^2]	Δ_σ[MHz]
1	2000	50	1000	50	$5.3 \cdot 10^{-9}$	1.28
10	200	50	550	25	$1.8 \cdot 10^{-9}$	20.8
100	20	50	500	10	$5.4 \cdot 10^{-10}$	360
600	3	30	400	10	$2.0 \cdot 10^{-10}$	3200

Table A.13: Same as Tab. A.11 but for the octupole transitions in Sec. 7.2.3.

B

SPHERICAL TENSORS

In this appendix, we summarise the most important relations for spherical tensors up to rank $k = 3$ which are used to calculate the matrix element of Rydberg atoms. The tensors of rank 1, Sec. B.1, can be used to evaluate the dipole matrix elements which are necessary to determine the coupling between Rydberg atoms and external fields, or to evaluate the dipole-dipole coupling between Rydberg atoms and molecules. Higher order tensors serve to calculate higher order multipole elements to investigate the multipolar character of FRET.

B.1 Dipole

To give a complete overview, we also repeat the most important relations for spherical tensors of rank $k = 1$ here. The components are defined as [45]

$$T_0^{(1)} = z, \tag{B.1a}$$

$$T_{\pm1}^{(1)} = \mp\frac{1}{\sqrt{2}}(x \pm iy), \tag{B.1b}$$

and they are proportional to spherical harmonics with $\ell = 1$,

$$T_q^{(1)} = \sqrt{\frac{4\pi}{3}} r Y_1^m. \tag{B.2}$$

From the properties of the spherical harmonics (cf. Eq. (2.18)), we can deduce the dipole selection rules $\Delta\ell = \pm1$ and $\Delta m = 0, \pm1$. By inverting the system of equations in Eq. (B.1), we can compute

the transformation from spherical to Cartesian components as

$$\begin{aligned} x &= \frac{1}{\sqrt{2}}\left(T^{(1)}_{-1} - T^{(1)}_{1}\right), \\ y &= \frac{i}{\sqrt{2}}\left(T^{(1)}_{-1} + T^{(1)}_{1}\right), \\ z &= T^{(1)}_{0} \end{aligned} \tag{B.3}$$

which allows to calculate the matrix elements of the Cartesian components x, y and z.

The angular part of the dipole matrix elements , $\left\langle \ell m \left| \frac{\hat{\mathbf{r}}}{r} \right| \ell' m' \right\rangle$ as given in Eq. (2.11), can most easily be evaluated by first rewriting the Cartesian coordinates into spherical ones,

$$\begin{aligned} x \pm iy &= r \sin\vartheta e^{\pm i\varphi}, \\ z &= r\cos\vartheta. \end{aligned}$$

It is then possible to evaluate the overlap integrals as (taking for example the $\hat{z}$ element)

$$\left\langle \ell' m' \left| \frac{\hat{z}}{r} \right| \ell m \right\rangle = \int \sin\vartheta d\vartheta \int d\varphi \, (Y^m_\ell)^*(\vartheta,\varphi) \, \cos\vartheta \, Y^m_\ell(\vartheta,\varphi). \tag{B.4}$$

The non-vanishing elements of the dipole operator in the spherical basis can be derived analytically to be [43]

$$\left\langle \ell m \left| \frac{\hat{z}}{r} \right| \ell+1, m \right\rangle = \sqrt{\frac{(\ell+1-m)(\ell+1+m)}{(2\ell+1)(2\ell+3)}}, \tag{B.5a}$$

$$\left\langle \ell m \left| \frac{\hat{z}}{r} \right| \ell-1, m \right\rangle = \sqrt{\frac{(\ell-m)(\ell+m)}{(2\ell+1)(2\ell-1)}}, \tag{B.5b}$$

$$\left\langle \ell m \left| \frac{\hat{x} \pm i\hat{y}}{r} \right| \ell+1, m\pm 1 \right\rangle = \pm\sqrt{\frac{(\ell\pm m+2)(\ell\pm m+1)}{(2\ell+1)(2\ell+3)}}, \tag{B.5c}$$

$$\left\langle \ell m \left| \frac{\hat{x} \pm i\hat{y}}{r} \right| \ell-1, m\pm 1 \right\rangle = \mp\sqrt{\frac{(\ell\mp m)(\ell\mp m-1)}{(2\ell+1)(2\ell-1)}}, \tag{B.5d}$$

from which we can read the well-known dipole transition selection rules $\Delta\ell = \pm 1$ and $\Delta m = 0, \pm 1$. Alternatively, the full matrix elements (i.e. including the radial part) can also be evaluated in the parabolic basis to [49, 52]

$$\langle n m_1 m_2 \,|\, \hat{z} \,|\, n m_1 m_2 \rangle = \frac{3n}{2Z}(m_1 - m_2), \tag{B.6a}$$

$$\langle n m_1 \pm 1 m_2 \,|\, \hat{x} \pm i\hat{y} \,|\, n m_1 m_2 \rangle = \frac{3n}{2Z}\sqrt{(n \pm 2m_1 + 1)(n \mp 2m_1 - 1)}, \tag{B.6b}$$

$$\langle n m_1 m_2 \pm 1 \,|\, \hat{x} \pm i\hat{y} \,|\, n m_1 m_2 \rangle = -\frac{3n}{2Z}\sqrt{(n \pm 2m_2 + 1)(n \mp 2m_2 - 1)}. \tag{B.6c}$$

B.2 Quadrupole

To compute the spherical components of a symmetric matrix in Cartesian coordinates, $(x_i x_j)_{x_i,x_j=x,y,z}$, we can use the relation Eq. (2.15) to construct the tensor product of two spherical tensors of rank 1 (cf. Eq. (B.1)). The only non-vanishing elements are [46]

$$T_0^{(0)} = -\frac{1}{\sqrt{3}}\left(x^2+y^2+z^2\right), \tag{B.7a}$$

$$T_0^{(2)} = \frac{1}{\sqrt{6}}\left(2z^2-x^2-y^2\right), \tag{B.7b}$$

$$T_{\pm1}^{(2)} = \mp xz - iyz, \tag{B.7c}$$

$$T_{\pm2}^{(2)} = \frac{1}{2}\left(x^2-y^2\pm 2ixy\right). \tag{B.7d}$$

By comparing them to the spherical harmonics, we can deduce the relation

$$T_0^{(0)} = -\sqrt{\frac{4\pi}{3}} r^2 Y_0^0, \tag{B.8}$$

$$T_q^{(2)} = \sqrt{\frac{8\pi}{15}} r^2 Y_2^m. \tag{B.9}$$

By inverting the system of equations in Eq. (B.7), we can compute the transformation from spherical to Cartesian components as [46]

$$\begin{aligned}
xx &= -\frac{1}{\sqrt{3}}T_0^{(0)} - \frac{1}{\sqrt{6}}T_0^{(2)} + \frac{1}{2}\left(T_2^{(2)}+T_{-2}^{(2)}\right),\\
xy &= -\frac{i}{2}\left(T_2^{(2)}-T_{-2}^{(2)}\right),\\
xz &= \frac{1}{2}\left(T_{-1}^{(2)}-T_1^{(2)}\right),\\
yy &= -\frac{1}{\sqrt{3}}T_0^{(0)} - \frac{1}{\sqrt{6}}T_0^{(2)} - \frac{1}{2}\left(T_2^{(2)}+T_{-2}^{(2)}\right),\\
yz &= \frac{i}{2}\left(T_2^{(2)}+T_{-2}^{(2)}\right),\\
zz &= -\frac{1}{\sqrt{3}}T_0^{(0)} + \sqrt{\frac{2}{3}}T_0^{(2)}
\end{aligned} \tag{B.10}$$

with $xy = yx$ and so forth due to the symmetry of the matrix. Note that the spherical tensor of rank 0 is required for the transformation because the tensor $(x_i x_j)_{x_i,x_j=x,y,z}$ is not traceless. From the transformation and the properties of the spherical tensors, we can deduce the quadrupole selection rules as explained in the main text just after Eq. (2.18). The result is $\Delta m = 0, \pm 1, \pm 2$ and $\Delta \ell = 0, \pm 2$.

The matrix element of zz, for instance, can be calculated as

$$\begin{aligned}
\left\langle \ell m \left| \frac{zz}{r^2} \right| \ell' m' \right\rangle &= \left\langle \ell m \left| \left(-\frac{1}{\sqrt{3}} T_0^{(0)} + \sqrt{\frac{2}{6}} T_0^{(2)} \right) / r^2 \right| \ell' m' \right\rangle \\
&= \left\langle \ell m \left| \left(\frac{1}{\sqrt{3}} \sqrt{\frac{4\pi}{3}} r^2 Y_0^0 + \sqrt{\frac{2}{3}} \sqrt{\frac{8\pi}{15}} r^2 Y_2^0 \right) / r^2 \right| \ell' m' \right\rangle \\
&= \left\langle \ell m \left| \sqrt{\frac{4\pi}{9}} Y_0^0 + \sqrt{\frac{16\pi}{45}} Y_2^0 \right| \ell' m' \right\rangle \\
&= \sqrt{\frac{4\pi}{9}} \left\langle \ell m \left| Y_0^0 \right| \ell' m' \right\rangle + \sqrt{\frac{16\pi}{45}} \left\langle \ell m \left| Y_2^0 \right| \ell' m' \right\rangle .
\end{aligned}$$

The matrix elements of spherical harmonics can then be calculated using Eq. (2.18).

B.3 Octupole

We repeat same procedure for the next order, $(x_i x_j x_k)_{x_i,x_j,x_k=x,y,z}$ with 27 components. The number of distinct elements is given by the urn problem in statistics where we draw $k = 3$ times out of an urn with $n = 3$ elements while putting the elements back in the urn after being drawn and neglecting the order of the elements,

$$N = \binom{n+k-1}{k} = 10. \tag{B.11}$$

To compute the spherical components of the tensor of rank 3, we use Eq. (2.15) with tensors of ranks $k_1 = 1$ and $k_2 = 2$. We obtain[1]

$$T_0^{(1)} = -\sqrt{\frac{4}{15}} z r^2, \tag{B.12a}$$

$$T_{\pm 1}^{(1)} = \pm \sqrt{\frac{4}{15}} \frac{1}{\sqrt{2}} (x \pm iy) r^2, \tag{B.12b}$$

$$T_0^{(3)} = \frac{1}{\sqrt{10}} \left(2z^3 - 3x^2 z - 3y^2 z \right), \tag{B.12c}$$

$$T_{\pm 1}^{(3)} = \frac{1}{2} \sqrt{\frac{3}{10}} \left(\pm x^3 + i x^2 y \pm x y^2 + i y^3 \right) - \sqrt{\frac{6}{5}} \left(\pm x z^2 + i y z^2 \right), \tag{B.12d}$$

$$T_{\pm 2}^{(3)} = \sqrt{\frac{3}{4}} \left(x^2 z \pm 2ixyz - y^2 z \right), \tag{B.12e}$$

$$T_{\pm 3}^{(3)} = \frac{1}{2\sqrt{2}} \left(\mp x^3 - 3ix^2 y \pm 3xy^2 + iy^3 \right) \tag{B.12f}$$

[1] The following relations were derived in collaboration with Cornelius Hoffmann [5].

By comparing them to the spherical harmonics, we can deduce the relation

$$T_q^{(1)} = -\sqrt{\frac{16\pi}{45}} r^3 Y_1^m, \tag{B.13}$$

$$T_q^{(3)} = \sqrt{\frac{8\pi}{35}} r^3 Y_3^m. \tag{B.14}$$

By inverting the system of equations in Eq. (B.12), we can compute the transformation from spherical to Cartesian components as

$$\begin{aligned}
x^3 &= \frac{3}{5\sqrt{2}}(T_{-1}^{(1)} - T_1^{(1)}) - \frac{\sqrt{\frac{3}{10}}}{2}(T_{-1}^{(3)} - T_1^{(3)}) + \frac{1}{2\sqrt{2}}(T_{-3}^{(3)} - T_3^{(3)}) \\
x^2 y &= \frac{i}{5\sqrt{2}}(T_{-1}^{(1)} + T_1^{(1)}) - \frac{i}{2\sqrt{30}}(T_{-1}^{(3)} + T_1^{(3)}) + \frac{i}{2\sqrt{2}}(T_{-3}^{(3)} + T_3^{(3)}) \\
x^2 z &= \frac{1}{5}T_0^{(1)} - \frac{1}{\sqrt{10}}T_0^{(3)} + \frac{1}{2\sqrt{3}}(T_{-2}^{(3)} + T_2^{(3)}) \\
xy^2 &= +\frac{1}{5\sqrt{2}}(T_{-1}^{(1)} - T_1^{(1)}) - \frac{1}{2\sqrt{30}}(T_{-1}^{(3)} - T_1^{(3)}) - \frac{1}{2\sqrt{2}}(T_{-3}^{(3)} - T_3^{(3)}) \\
xyz &= \frac{i}{2\sqrt{3}}(T_{-2}^{(3)} - T_2^{(3)}) \\
xz^2 &= \frac{1}{5\sqrt{2}}(T_{-1}^{(1)} - T_1^{(1)}) + \sqrt{\frac{2}{15}}(T_{-1}^{(3)} - T_1^{(3)}) \\
y^3 &= \frac{3i}{5\sqrt{2}}(T_{-1}^{(1)} + T_1^{(1)}) - \frac{1}{2}i\sqrt{\frac{3}{10}}(T_{-1}^{(3)} + T_1^{(3)}) - \frac{i}{2\sqrt{2}}(T_{-3}^{(3)} + T_3^{(3)}) \\
y^2 z &= \frac{1}{5}T_0^{(1)} - \frac{1}{\sqrt{10}}T_0^{(3)} - \frac{1}{2\sqrt{3}}(T_{-2}^{(3)} + T_2^{(3)}) \\
yz^2 &= \frac{i}{5\sqrt{2}}(T_{-1}^{(1)} + T_1^{(1)}) + i\sqrt{\frac{2}{15}}(T_{-1}^{(3)} + T_1^{(3)}) \\
z^3 &= \frac{3}{5}T_0^{(1)} + \sqrt{\frac{2}{5}}T_0^{(3)}
\end{aligned} \tag{B.15}$$

with $xxy = xyx = yxx$ and so forth due to the symmetry of the matrix. The tensor $Q^{(2)} = (x_i x_j x_k)_{x_i,x_j,x_k=x,y,z}$ is not traceless and the trace

$$\mathrm{Tr}\left\{Q^{(2)}\right\} = \left(\sum_{i,j=x,y,z} Q_{i,j,k}^{(2)} \delta_{i,j}\right)_k \tag{B.16}$$

is of rank 1. Therefore, the spherical tensor of rank 1 is needed for the transformation in Eq. (B.15). From this transformation and the properties of the spherical tensors, we can deduce the quadrupole selection rules as explained in the main text just after Eq. (2.18). The result is $\Delta m = 0, \ldots, \pm 3$ and $\Delta \ell = \pm 1, \pm 3$.

C

TECHNICAL DETAILS REGARDING STRONTIUM

This appendix is dedicated to technical details regarding the modelling of strontium in Chapter 4. We first give details on the evaluation of the matrix elements of $\hat{\boldsymbol{l}}_1 \cdot \hat{\boldsymbol{s}}_1$ which is the basis for the j_1-coupling. Afterwards, we elaborate on the attempted optimisation of the radial part in App. C.2. Lastly, in App. C.3, we show and discuss the Stark map around the 50^3F triplets in order to estimate the effectiveness of our model regarding triplet states.

C.1 Calculating the matrix elements of $\hat{\boldsymbol{l}}_1 \cdot \hat{\boldsymbol{s}}_1$

A spin-orbit coupling which is proportional to $\hat{\boldsymbol{l}}_1 \cdot \hat{\boldsymbol{s}}_1$, as given in Eq. (4.24), describes the coupling of the outer electron's spin to its orbital angular momentum. The difficulty in evaluating the matrix elements lies in the choice of basis. While we have chosen the LS basis $|JM_JLS\rangle$ as the computational basis, the matrix elements of $\hat{\boldsymbol{l}}_1 \cdot \hat{\boldsymbol{s}}_1$ can only be evaluated in the uncoupled basis. The main task is thus to calculate the transformation from the coupled to the uncoupled basis which describes the two electrons independently, which we will present in the following.

We first recall that upper case operators refer to the two-electron system and lower case operators to single electrons. We label the inner electron with an index 2 and the outer electron with an index 1. We furthermore assume the inner electron to be in the ground state, $\ell_2 = m_{\ell_2} = 0$. Since we are dealing with electrons, we have $s_1 = s_2 = \frac{1}{2}$ and $m_{s_1} = m_{s_2} = \pm\frac{1}{2}$. The first step of the basis transformation is to uncouple the total angular momentum $\hat{\boldsymbol{J}}$ to the orbital angular momentum $\hat{\boldsymbol{L}}$ and the spin $\hat{\boldsymbol{S}}$, or in other words, to go from the $|JM_JLS\rangle$ to the $|LM_LSM_S\rangle$ basis. This works equivalently to Eq. (4.26) and can be written as

$$|JM_J\rangle = \sum_{M_LM_S} C^{JM_J}_{LM_LSM_S} |LM_LSM_S\rangle \,, \tag{C.1}$$

where $C^{JM_J}_{LM_LSM_S}$ is a Clebsch-Gordan coefficient.

Next, we have to uncouple $\hat{\boldsymbol{L}}$ to $\hat{\boldsymbol{l}}_1$ and $\hat{\boldsymbol{l}}_2$, and $\hat{\boldsymbol{S}}$ to $\hat{\boldsymbol{s}}_1$ and $\hat{\boldsymbol{s}}_2$, i.e. go to the uncoupled basis $|\ell s m_\ell m_s\rangle_1 \otimes |\ell s m_\ell m_s\rangle_2 = |\ell_1 s_1 m_{\ell_1} m_{s_1}, \ell_2 s_2 m_{\ell_2} m_{s_2}\rangle = |\ell_1 \ell_2 m_{\ell_1} m_{\ell_2}\rangle \otimes |s_1 s_2 m_{s_1} m_{s_2}\rangle$,

$$|LM_L\rangle = \sum_{m_{\ell_1} m_{\ell_2}} C^{LM_L}_{\ell_1 m_{\ell_1} \ell_2 m_{\ell_2}} |\ell_1 m_{\ell_1} \ell_2 m_{\ell_2}\rangle \tag{C.2a}$$

$$|SM_S\rangle = \sum_{m_{s_1} m_{s_2}} C^{SM_S}_{s_1 m_{s_1} s_2 m_{s_2}} |s_1 m_{s_1} s_2 m_{s_2}\rangle . \tag{C.2b}$$

The assumption that the inner electron is in the ground state leaves only one option in Eq. (C.2a), $L = \ell_1$ and $M_L = m_{\ell_1}$, such that all but one Clebsch-Gordan coefficients are vanishing. Plugging Eq. (C.2) into Eq. (C.1) results in

$$|JM_J LS\rangle = \sum_{M_L M_S} \sum_{m_{s_1} m_{s_2}} C^{JM_J}_{LM_L SM_S} C^{SM_S}_{s_1 m_{s_1} s_2 m_{s_2}} |\ell_1 m_{\ell_1} s_1 m_{s_1}\rangle \otimes |\ell_2 m_{\ell_2} s_2 m_{s_2}\rangle . \tag{C.3}$$

Next, we couple $\hat{\boldsymbol{l}}_1 + \hat{\boldsymbol{s}}_1 = \hat{\boldsymbol{j}}_1$,

$$|\ell_1 m_{\ell_1} s_1 m_{s_1}\rangle = \sum_{j_1 m_{j_1}} C^{j_1 m_{j_1}}_{\ell_1 m_{\ell_1} s_1 m_{s_1}} |j_1 m_{j_1} \ell_1 s_1\rangle . \tag{C.4}$$

and insert this into Eq. (C.3),

$$|JM_J LS\rangle = \sum_{M_L M_S} \sum_{m_{s_1} m_{s_2}} \sum_{j_1 m_{j_1}} C^{JM_J}_{LM_L SM_S} C^{SM_S}_{s_1 m_{s_1} s_2 m_{s_2}} C^{j_1 m_{j_1}}_{\ell_1 m_{\ell_1} s_1 m_{s_1}} |j_1 m_{j_1} \ell_1 s_1\rangle |\ell_2 m_{\ell_2} s_2 m_{s_2}\rangle . \tag{C.5}$$

In order to calculate a matrix elements between two states, we have to repeat these steps for the second state $|J' M'_J L' S'\rangle$. The matrix element between them is then given by

$$\begin{aligned} a \langle J' M'_J L' S' | \hat{\boldsymbol{l}}_1 \cdot \hat{\boldsymbol{s}}_1 | JM_J LS\rangle = \frac{a}{2} \sum_{j_1 m_{j_1}} \Big(j_1(j_1+1) - \ell_1(\ell_1+1) - s_1(s_1+1) \Big) C^{j_1 m_{j_1}}_{\ell_1 m_{\ell_1} s_1 m_{s_1}} \\ \sum_{M'_L M'_S} \sum_{m'_{s_1} m'_{s_2}} \sum_{M_L M_S} \sum_{m_{s_1} m_{s_2}} C^{JM_J}_{LM_L SM_S} C^{J' M'_J}_{L' M'_L S' M'_S} C^{SM_S}_{s_1 m_{s_1} s_2 m_{s_2}} C^{S' M'_S}_{s'_1 m'_{s_1} s'_2 m'_{s_2}} \\ \langle j_1 m_{j_1} l'_1 s'_1 | j_1 m_{j_1} l_1 s_1\rangle \langle l'_2 m'_{l_2} s'_2 m'_{s_2} | l_2 m_{l_2} s_2 m_{s_2}\rangle , \end{aligned} \tag{C.6}$$

where a is a constant. This expression can be simplified by considering the physics of the problem. We know that for electrons $s_1 = s_2 = s'_1 = s'_2 = \frac{1}{2}$. The first scalar product therefore leads to the selection rule $L = l_1 = l'_1 = L'$ as we assumed $\ell_2 = m_{\ell_2} = 0$. This assumption naturally leads to $\ell_2 = \ell'_2$ and $m_{\ell_2} = m'_{\ell_2}$. We could furthermore couple the second angular momentum to $\hat{\boldsymbol{j}}_2 = \hat{\boldsymbol{l}}_2 + \hat{\boldsymbol{s}}_2$ and afterwards couple both angular momenta together, $\hat{\boldsymbol{J}} = \hat{\boldsymbol{j}}_1 + \hat{\boldsymbol{j}}_2$. This would still allows us to calculate the expectation value of $\hat{\boldsymbol{l}}_1 \cdot \hat{\boldsymbol{s}}_1$. In the basis $|JM_J j_1 j_2\rangle$ we see directly that $J = J'$ and $M_J = M'_J$. Lastly, we have to check if $m_{s_2} = m'_{s_2}$ to determine the value of the second scalar product. We know that $m_{j_1} + m_{j_2} = M_J = M'_J = m'_{j_1} + m'_{j_2} = m_{j_1} + m'_{j_2}$ from which

follows $m_{j_2} = m'_{j_2}$. From $m_{\ell_2} = 0$ follows that $m_{s_2} = m_{j_2}$. When combining both, we see that $m_{s_2} = m_{j_2} = m'_{j_2} = m'_{s_2}$. The second scalar product is therefore always equal to one. Next, we investigate the range of the double sums. Since M_L and M_S are linked, the corresponding sum runs from $M_S = -S, \ldots, S$ with M_L being fully determined by $M_L = M_J - M_S$. The sum over m_{s_1} only runs over the two values $m_{s_1} = \pm\frac{1}{2}$ with m_{s_2} being determined by $m_{s_2} = M_S - m_{s_1}$. The same applies to the primed state. Combining everything, we can write Eq. (C.6) as

$$a \langle JM_J LS' | \hat{l}_1 \cdot \hat{s}_1 | JM_J LS \rangle \equiv \frac{a}{2} \sum_{j_1} C(j_1) \Big(j_1(j_1+1) - \ell_1(\ell_1+1) - s_1(s_1+1) \Big), \tag{C.7a}$$

$$C(j_1) = \sum_{m_{j_1}} C^{j_1 m_{j_1}}_{\ell_1 m_{\ell_1} s_1 m_{s_1}} \sum_{M'_S} \sum_{m'_{s_1}} \sum_{M_S} \sum_{m_{s_1}} C^{JM_J}_{LM_L SM_S} C^{JM_J}_{LM'_L S'M'_S} C^{SM_S}_{s_1 m_{s_1} s_2 m_{s_2}} C^{S'M'_S}_{s_1 m'_{s_1} s_2 m'_{s_2}}. \tag{C.7b}$$

If we further set $\omega_{n\ell} = \frac{a}{2}$, we arrive at the expression given in Eq. (4.29). The constant a can be identified with the radial part and the pre-factors given in Eq. (4.24), $a = \frac{\alpha^2 Z}{2} \langle \hat{\boldsymbol{r}}^{-3} \rangle$ where α is the fine-structure constant.

C.2 Optimisation of the radial part

To further improve the agreement between theoretical simulations and experiment for the Stark map from $50^1F_3, m_j = 2$ to $49g$ for $m_j = 1, \ldots, 3$ discussed in Sec. 4.2.3, we have tried to not only optimise the exchange energy and spin-orbit coupling, which influence the energies at zero DC field, but also the radial part of the matrix elements directly. The idea behind this is motivated by multichannel quantum defect theory (MQDT) which considers linear combinations of scattering channels. If the approximation of the inner electron being the ground state does not hold, the outer electron will equally be influenced by it. As a result, the potential seen be the single active electron will be modified and the radial matrix elements will be different. Our approach is thus to optimise the radial matrix elements

$$R_{nj\ell s, n'j'\ell's'} = \left\langle nj\ell s \,\middle|\, \hat{\boldsymbol{z}} \,\middle|\, n'j'\ell's' \right\rangle \tag{C.8}$$

directly. Note that the matrix elements depend on j and s as the quantum defects change the energy of the respective eigenstates at zero field. The radial matrix elements do not depend on the DC field but they are used to calculate the Stark map at different DC fields as given in Eq. (4.25). At zero field, on the other hand, the matrix elements do not play a role but the position of the energy levels is fully determined by the quantum defects (and the spin-orbit couplings $\omega_{n\ell}$ and Ω_{nL} in our extended model).

The optimisation procedure is as follows: instead of evaluating the fidelity of the simulations at zero DC field, we consider experimental points at higher DC field. As a first test, we start with a comparatively low value of $50.4\,\frac{\mathrm{V}}{\mathrm{m}}$. We match the theoretical Stark lines of the Stark map shown in Fig. 4.8 (b) to the corresponding experimental data point manually, resulting in 11 experimental

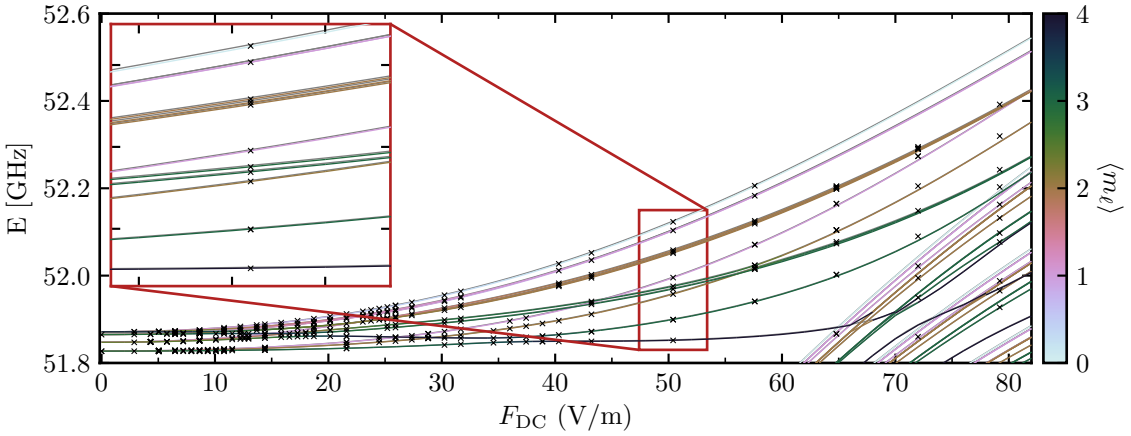

Figure C.1: Stark map from $50^1F_3, m_j = 2$ to 50^3F for $m_j = 0, \ldots, 4$ before (grey lines in the background) and after (coloured lines) the radial optimisation using the points at $50.4\,\frac{\mathrm{V}}{\mathrm{m}}$. The inset shows a zoom as indicated by the red rectangle. The line colour indicates the expectation value of m_ℓ, the grey crosses indicate the experimental measurements. The grey lines show the same Stark map as Fig. 4.8 (b).

points we optimise at the same time. We then optimise all radial elements that couple to $49g$ or $50f$ which fulfil $n = 48, 49, 50$ and $\ell = 2, \ldots, 5$. In total, that leaves 176 matrix elements. We have stopped the optimisation after about 3400 iterations when the error has dropped from $35\,\mathrm{MHz}^2$ to $1.25\,\mathrm{MHz}^2$. The result of the optimisation is shown in Fig. C.1. It can be seen that the optimisation was successful as the coloured lines, which represent the optimised Stark map, match the experimental measurements better as the grey ones indicating the old Stark map (note in particular the highest line in the inset). Upon investigation of the optimised matrix element, we find only about two dozen parameters which have been changes significantly.

The Stark maps shows, however, that theory and experiment still deviate significantly at higher field strengths. We therefore proceed by optimising two field strengths at the same time, namely 50.4 and $72\,\frac{\mathrm{V}}{\mathrm{m}}$ which adds another 7 points to the optimisation. We have stopped the optimisation after 2700 iterations when the error has dropped from $308\,\mathrm{MHz}^2$ to $160\,\mathrm{MHz}^2$. The result of the optimisation is shown in Fig. C.2. It can be seen that the points around $72\,\frac{\mathrm{V}}{\mathrm{m}}$ improve at the expense of those at $50.4\,\frac{\mathrm{V}}{\mathrm{m}}$ (see e.g. the pink line in the middle of the insets). Moreover, the overall increase of fidelity was less striking as before. This can clearly be attributed to the increased difficulty of the optimisation due to the higher number of sampling points and the overall very large number of optimisation parameters.

We have tried different methods to improve the fidelity of the optimisation. We assume the major problem to be the large number of optimisation parameters as parameter optimisation is usually conducted with a handful of parameters only. The first approach was thus to include only those matrix elements in the parameter optimisation which have changed significantly in a previous optimisation attempt. However, we could not identify a small number of "necessary" matrix elements that needed optimisation as the significantly optimised matrix elements change

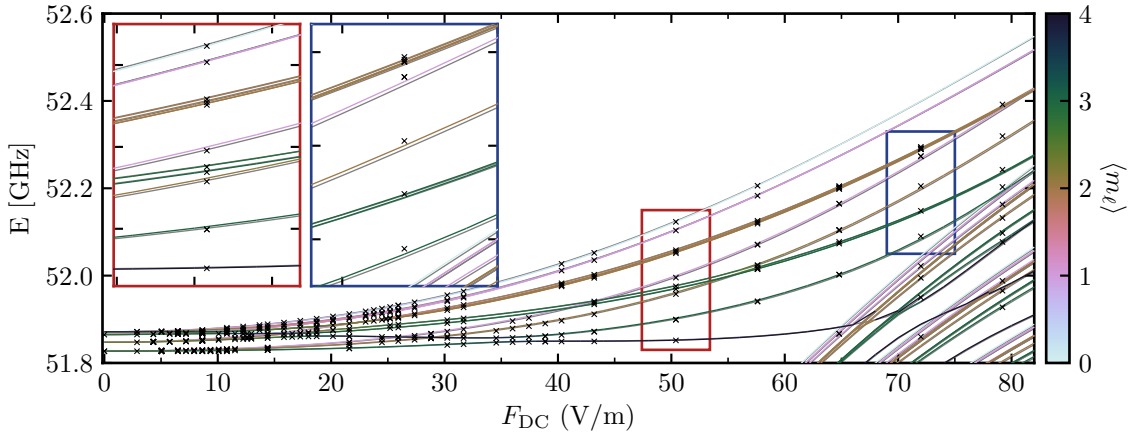

Figure C.2: Same as Fig. C.1 but after optimisation using the points at 50.4 and $72\,\frac{\mathrm{V}}{\mathrm{m}}$. The insets show a zoom as indicated by the coloured rectangles.

depending on the initial parameters and the pre-selection that was performed. Moreover, we have tried to scale the experimental points to account for a possible malcalibrated DC field, or to omit the exchange energy in the potential of Numerov, as the singlets and triplets should see the same core potential. The latter approach reduces the number of matrix elements as they no longer depend on j and s, $R_{n\ell,n'\ell'}$. However, all these approaches did not prove to be fruitful.

In order to reduce the number of optimisation parameters more systematically, we have changed the approach. Instead of optimising all radial matrix elements in Eq. (C.8) directly, we scale the radial wavefunction of each state with a factor,

$$\tilde{R}_{nj\ell s,n'j'\ell's'} = \left\langle nj\ell s \,\middle|\, \epsilon_{nj\ell s}\hat{\boldsymbol{z}}\epsilon_{n'j'\ell's'} \,\middle|\, n'j'\ell's' \right\rangle , \tag{C.9}$$

such that each state always experiences the same correction. This reduces the number of optimisation parameters to 48. The correction factors were limited to values between 0 and 2. Using this method, we could achieve much lower errors of $7\,\mathrm{MHz}^2$ (with an initial error of $308\,\mathrm{MHz}^2$) which is much lower than before. The result is shown in Fig. C.3. It can be seen that the agreement between theory and experiment as increased significantly at the selected DC fields of 50.4 and $72\,\frac{\mathrm{V}}{\mathrm{m}}$ (red and blue inset, respectively). On the other hand, the agreement decreases within the Stark manifold (green inset) as we did not include those points into the optimisation. We have tried to remove more and more parameters from the optimisation to distil the relevant scaling factors that are necessary to improve the optimisation without destroying the match of the Stark manifold but did not find promising results. The optimisation was significantly less successful when including the points in the Stark manifold into the optimisation and we always lose fidelity at higher fields where we did not include the points into the optimisation.

We conclude that the optimisation of the radial part, may it be directly (cf. Eq. (C.8)) or through state-dependent scaling factors (cf. Eq. (C.9)), does not lead to fruitful results. The main

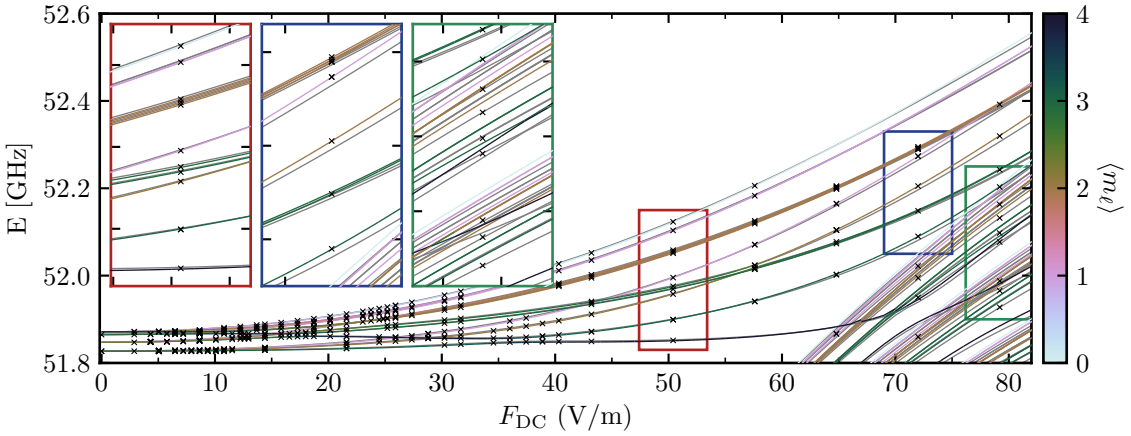

Figure C.3: Same as Fig. C.1 but after optimisation using the points at 50.4 and 72 $\frac{\mathrm{V}}{\mathrm{m}}$ using Eq. (C.9). The insets show a zoom as indicated by the coloured rectangles.

problem seemed to be the large number of optimisation parameters when optimising the matrix elements directly which lead to slow or no convergence of the optimisation within a few thousand iterations. When reducing the number of parameters by using state-dependent optimisation parameters, on the other hand, we could improve the fidelity at the field that has been considered during the optimisation, but lost at higher fields. In both cases, the optimised parameters did not allow for any fruitful insights which matrix elements needed optimisation. It might be possible to improve the optimisation if more experimental data was available, especially at much higher fields when the g state has joined the Stark manifold and thus follows a smooth line similar to rubidium or hydrogen. It might also be beneficial if we had access to absolute energies since all the considered Stark maps show the transition frequencies between two states such that their values depends on two states. If absolute energies were available it would be possible to optimise both states independently, hence deducing which of the two states leads to the deviation in the Stark map.

In order to estimate if further optimisation is even necessary for our goal of controlling the dynamics within the Stark manifold, we test the influence of the radial optimisation on an exemplary propagation. In the main text, we have made the conjecture that we merely fail to reproduce the correct curvature of quantum defects states (here the g-state) when joining the Stark manifold. When propagating states in the Stark manifold, however, the DC fields chosen in the experiment are usually higher, around 100 $\frac{\mathrm{V}}{\mathrm{m}}$, where the g-state is already part of the Stark manifold (cf. Fig. 4.10 (b)). Thus, it is likely that no fine-tuning of the Hamiltonian is necessary for the control of quantum dynamics. To test this, we compare two cases: a Hamiltonian with the optimised parameters presented in Sec. 4.2.2 and the radially optimised Hamiltonian from this section. We have chosen one radially optimised Hamiltonian for which the fidelity has increased after the optimisation while leaving the States within the Stark manifold mostly intact. We compare the Hamiltonians for both cases at a DC field of 110 $\frac{\mathrm{V}}{\mathrm{m}}$. We find that the singlets

in the Stark manifold are not significantly affected by the radial optimisation. Only the triplets and the low-angular-momentum states with a significant quantum defect are slightly modified. For the f states, we find a deviation of around $60\,\mathrm{MHz}$ between the two models. For the g state, the mismatch is slightly smaller. On average, the difference between the two models is around a few $100\,\mathrm{kHz}$. To estimate the influence of these deviations, we perform a circularisation using a π-pulse similarly as explained in Sec. 4.3. We take the initial state to be the lowest singlet of the $m_j = m_\ell = 2$ ladder. Due to selection rules, the propagation does not change the spin quantum number of the state. The population will therefore stay within the subspace of singlet states (and triplet states which are significantly mixed with singlets). As the singlets are only marginally affected by the radial optimisation, the populations during the circularisation differ on average by about 10^{-4} between the two Hamiltonians. As this is below the sensitivity of the experiment, we conclude that the optimisation of the radial part does not affect the dynamics in the Stark manifold significantly and a further optimisation does not seem necessary.

C.3 Stark map around 50f triplets

To test the optimised model parameters obtained in Sec. 4.2.3 and prove that they do not only reproduce the considered Stark map around $49g$, we calculate the Stark map of an additional transition and compare them to experimental data. Here, we present the data for the transition from the reference state $50^1F, m = 2$ towards the 50^3F triplets. The simulated Stark map and the corresponding measurements are shown in Fig. C.4. This map illustrates clearly that at high DC fields, states with the same m_ℓ quantum number tend to cluster together. The plots the simula-

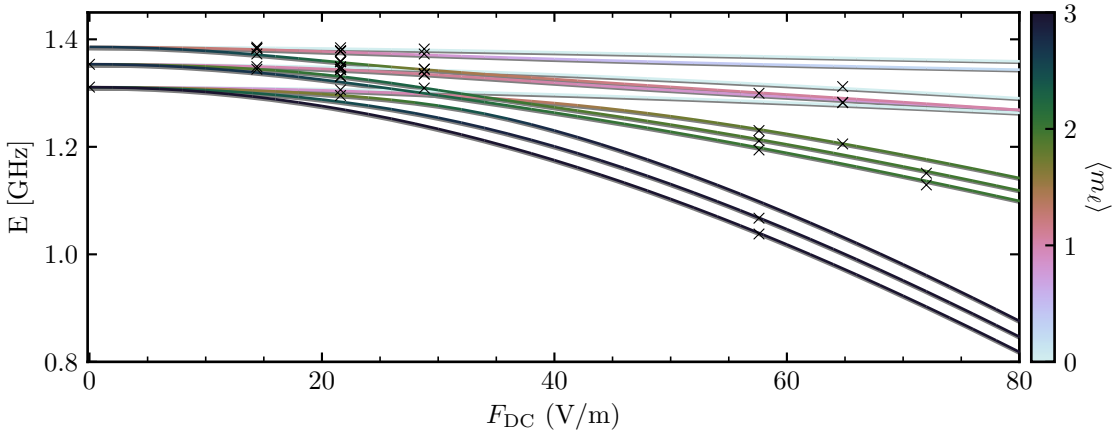

Figure C.4: Stark map from $50^1F_3, m_j = 2$ to 50^3F for $m_j = 0, \ldots, 4$ using the optimised parameters. The line colour indicates the expectation value of m_ℓ, the crosses indicate the experimental measurements. The coloured lines show the simulations when having fitted the F-states $n = 50, 52$ (lower number in Tab. 4.2), the grey lines in the background indicate the fit for $n = 48, 50, 52$ (upper number).

tions for two different initial sets of parameters. The coloured lines correspond to simulations when when considering only $n = 50, 52$ for fitting the triplet states (lower number in Tab. 4.2) which we assume to deliver better results when considering 50^3F states. As a comparison, we have plotted the simulations with the fit of $n = 48, 50, 52$ (upper number) using grey lines in the background. The deviation is hardly visible. However, upon close inspection it can be seen that the grey lines show slightly lower transition frequencies than the coloured ones. In particular, the points at zero field match the coloured lines much better (zoom not shown). The overall agreement between simulation and experiment is very good and we conclude, that our model can also reproduce the Stark map of triplet states. In order to improve the agreement further, as slight deviations are visible at higher fields, more experimental data is required. These deviations can be attributed to the large errors when fitting the quantum defects of triplet states (cf. Fig. 4.5 (b)) that have been discussed in the main text extensively.

REFERENCES

[1] S. Patsch, *Optimal control of Stark manifolds in Rydberg atoms: Creation of a superposition of opposite circular states*, Masterarbeit, Universität Kassel, 2016

[2] S. Patsch, *Herleitung einer Lindblad-Mastergleichung für die Quanten-Zeno-Dynamik von Photonen in einer Cavity*, Bachelorarbeit, Universität Kassel, 2014

[3] A. Larrouy, *Manipulation of Rydberg atoms using quantum optimal control*, PhD thesis, Université Pierre et Marie Curie - Paris VI, 2020

[4] C. Oglialoro, *Berechnung und Analyse der Quadrupolübergangselemente von Rydberg-Atomen*, Bachelorarbeit, Universität Kassel, 2020

[5] C. Hoffmann, *Oktupolwechselwirkung zwischen Rydberg-Atomen und polaren Molekülen*, Bachelorarbeit (in prepraration), Freie Universität Berlin, 2022

[6] S. Gleyzes, S. Kuhr, C. Guerlin, J. Bernu, S. Deléglise, U. B. Hoff, M. Brune, J. M. Raimond, and S. Haroche, *Quantum jumps of light recording the birth and death of a photon in a cavity*, Nature **446**, 297 (2007)

[7] S. Haroche, *Controlling Photons in a Box and Exploring the Quantum to Classical Boundary*, Reviews of Modern Physics **85**, 1083 (2013)

[8] T. F. Gallagher, *Rydberg atoms*, Cambridge Monographs on Atomic, Molecular, and Chemical Physics, Cambridge University Press, Cambridge, 1994

[9] S. Haroche and J.-M. Raimond, *Exploring the Quantum. Atoms, Cavities, and Photons*, Oxford University Press, New York, 2006

[10] M. Brune, E. Hagley, J. Dreyer, X. Maître, A. Maali, C. Wunderlich, J.-M. Raimond, and S. Haroche, *Observing the Progressive Decoherence of the "Meter" in a Quantum Measurement*, Physical Review Letters **77**, 4887 (1996)

[11] G. Nogues, A. Rauschenbeutel, S. Osnaghi, M. Brune, J.-M. Raimond, and S. Haroche, *Seeing a single photon without destroying it*, Nature **400**, 239 (1999)

[12] O. Firstenberg, C. S. Adams, and S. Hofferberth, *Nonlinear quantum optics mediated by Rydberg interactions*, Journal of Physics B **49**, 152003 (2016)

[13] F. Ripka, H. Kübler, R. Löw, and T. Pfau, *A room-temperature single-photon source based on strongly interacting Rydberg atoms*, Science **362**, 446 (2018)

[14] M. A. Nielsen and I. L. Chuang, *Quantum Computation and Quantum Information*, Cambridge University Press, 10th edition, 2010

[15] A. Acín, I. Bloch, H. Buhrman, T. Calarco, C. Eichler, J. Eisert, D. Esteve, N. Gisin, S. J. Glaser, F. Jelezko, S. Kuhr, M. Lewenstein, M. F. Riedel, P. O. Schmidt, R. Thew, A. Wallraff, I. Walmsley, and F. K. Wilhelm, *The quantum technologies roadmap: a European community view*, New Journal of Physics **20**, 080201 (2018)

[16] R. Feynman, *Simulating Physics with Computers*, International Journal of Theoretical Physics **21**, 467 (1982)

[17] C. S. Adams, J. D. Pritchard, and J. P. Shaffer, *Rydberg atom quantum technologies*, Journal of Physics B **53**, 012002 (2020)

[18] N. Šibalić and C. S. Adams, Rydberg Physics, in *Rydberg Physics*, pages 1–27, IOP Publishing, 2018

[19] R. G. Hulet and D. Kleppner, *Rydberg Atoms in "Circular" States*, Physical Review Letters **51**, 1430 (1983)

[20] A. Browaeys and T. Lahaye, *Many-body physics with individually controlled Rydberg atoms*, Nature Physics **16**, 132 (2020)

[21] H. Bernien, S. Schwartz, A. Keesling, H. Levine, A. Omran, H. Pichler, S. Choi, A. S. Zibrov, M. Endres, M. Greiner, V. Vuletic, and M. D. Lukin, *Probing many-body dynamics on a 51-atom quantum simulator*, Nature **551**, 579 (2017)

[22] D. Barredo, V. Lienhard, S. de Léséleuc, T. Lahaye, and A. Browaeys, *Synthetic three-dimensional atomic structures assembled atom by atom*, Nature **561**, 79 (2018)

[23] C. L. Degen, F. Reinhard, and P. Cappellaro, *Quantum Sensing*, Reviews of Modern Physics **89**, 035002 (2017)

[24] V. Giovannetti, S. Lloyd, and L. Maccone, *Quantum Metrology*, Physical Review Letters **96**, 010401 (2006)

[25] V. Giovannetti, S. Lloyd, and L. Maccone, *Advances in Quantum Metrology*, Nature Photonics **5**, 222 (2011)

[26] J. Ma, X. Wang, C. P. Sun, and F. Nori, *Quantum spin squeezing*, Physics Reports **509**, 89 (2011)

[27] S. J. Glaser, U. Boscain, T. Calarco, C. P. Koch, W. Köckenberger, R. Kosloff, I. Kuprov, B. Luy, S. Schirmer, T. Schulte-Herbrüggen, D. Sugny, and F. K. Wilhelm, *Training Schrödinger's cat: quantum optimal control - Strategic report on current status, visions and goals for research in Europe*, The European Physical Journal D **69**, 279 (2015)

[28] P. Brumer and M. Shapiro, *Principles and Applications of the Quantum Control of Molecular Processes*, John Wiley and Sons Ltd., 2003

[29] T. Caneva, M. Murphy, T. Calarco, R. Fazio, S. Montangero, V. Giovannetti, and G. E. Santoro, *Optimal control at the quantum speed limit*, Physical Review Letters **103**, 240501 (2009)

[30] C. P. Koch, *Controlling open quantum systems: Tools, achievements, and limitations*, Journal of Physics: Condensed Matter **28**, 213001 (2016)

[31] F. B. Dunning, T. C. Killian, S. Yoshida, and J. Burgdörfer, *Recent advances in Rydberg physics using alkaline-earth atoms*, Journal of Physics B **49**, 112003 (2016)

[32] M. Hiller, S. Yoshida, J. Burgdörfer, S. Ye, X. Zhang, and F. B. Dunning, *Characterizing high-n quasi-one-dimensional strontium Rydberg atoms*, Physical Review A **89**, 023426 (2014)

[33] H.-P. Breuer and F. Petruccione, *Theory of open quantum systems*, Oxford University Press, New York, 2002

[34] I. M. Georgescu, S. Ashhab, and F. Nori, *Quantum simulation*, Reviews of Modern Physics **86**, 153 (2014)

[35] H.-P. Breuer, E.-M. Laine, J. Piilo, and B. Vacchini, *Colloquium: Non-Markovian dynamics in open quantum systems*, Reviews of Modern Physics **88**, 021002 (2016)

[36] H. M. Wiseman and G. J. Milburn, *Quantum Measurement and Control*, Cambridge University Press, 2010

[37] H. W. Kroto, *Molecular Rotation Spectra*, John Wiley and Sons Ltd., New York, 1975

[38] C. H. Townes and A. L. Schawlow, *Microwave Spectroscopy*, Dover Publications, Inc., New York, 1975

[39] O. Dulieu, M. Raoult, and E. Tiemann, *Cold molecules: A chemistry kitchen for physicists?*, Journal of Physics B **39**, 11 (2006)

[40] M. Zeppenfeld, *Nondestructive detection of polar molecules via Rydberg atoms*, EPL (Europhysics Letters) **118**, 13002 (2017)

[41] D. L. Andrews, D. S. Bradshaw, R. Dinshaw, and G. D. Scholes, *Resonance Energy Transfer*, Photonics: Scientific Foundations, Technology and Applications **4**, 101 (2015)

[42] T. Fließbach, *Theoretische Quantenmechanik*, volume III of *Lehrbuch zur Theoretischen Physik*, Spektrum Akademischer Verlag, Heidelberg, 7. edition, 2005

[43] H. A. Bethe and E. E. Salpeter, *Quantum Mechanics of One- and Two-Electron Atoms*, Plenum Publishing Corporation, New York, plenum/ros edition, 1977

[44] B. V. Numerov, *A method of extrapolation of perturbations*, Monthly Notices of the Royal Astronomical Society **54**, 592 (1924)

[45] J. J. Sakurai and J. Napolitano, *Modern quantum mechanics*, Pearson Education, San Francisco, 2nd edition, 2011

[46] J. Kranendonk, *Solid Hydrogen*, Springer US, 1983

[47] A. Facon, *Chats de Schrödinger d'un atome de Rydberg pour la métrologie quantique*, PhD thesis, Université Pierre et Marie Curie - Paris VI, France, 2015

[48] W. Greiner and B. Müller, *Quantenmechanik Symmetrien*, Verlag Europa-Lehrmittel, Haan-Gruiten, 5. edition, 2014

[49] M. J. Englefield, *Group Theory and the Coulomb Problem*, Wiley-Interscience, 1972

[50] H. J. Silverstone, *Perturbation theory of the Stark effect in hydrogen to arbitrarily high order*, Physical Review A **18**, 1853 (1977)

[51] J.-C. Gay, D. Delande, and A. Bommier, *Atomic quantum states with maximum localization on classical elliptical orbits*, Physical Review A **39**, 6587 (1989)

[52] A. Signoles, *Manipulation cohérent d'états de Rydberg elliptique par dynamique Zénon quantique*, PhD thesis, Université Pierre et Marie Curie - Paris VI, France, 2014

[53] F. T. Arecchi, E. Courtens, R. Gilmore, and H. Thomas, *Atomic Coherent States in Quantum Optics*, Physical Review A **6**, 2211 (1972)

[54] K. Husimi, *Some Formal Properties of the Density Matrix*, Proceedings of the Physico-Mathematical Society of Japan. 3rd Series **22**, 264 (1940)

[55] G. S. Agarwal, *State reconstruction for a collection of two-level systems*, Physical Review A **57**, 671 (1998)

[56] J.-M. Raimond, M. Brune, and S. Haroche, *Colloquium: Manipulating quantum entanglement with atoms and photons in a cavity*, Reviews of Modern Physics **73**, 565 (2001)

[57] A. Ramos, K. Moore, and G. Raithel, *Measuring the Rydberg constant using circular Rydberg atoms in an intensity-modulated optical lattice*, Physical Review A **96**, 032513 (2017)

[58] E. K. Dietsche, A. Larrouy, S. Haroche, J. M. Raimond, M. Brune, and S. Gleyzes, *High-sensitivity magnetometry with a single atom in a superposition of two circular Rydberg states*, Nature Physics **15**, 326 (2019)

[59] A. Facon, E.-K. Dietsche, D. Grosso, S. Haroche, J.-M. Raimond, M. Brune, and S. Gleyzes, *A sensitive electrometer based on a Rydberg atom in a Schrödinger-cat state*, Nature **535**, 262 (2016)

[60] S. Patsch, D. M. Reich, J.-M. Raimond, M. Brune, S. Gleyzes, and C. P. Koch, *Fast and accurate circularization of a Rydberg atom*, Physical Review A **97**, 053418 (2018)

[61] A. Larrouy, S. Patsch, R. Richaud, J.-M. Raimond, M. Brune, C. P. Koch, and S. Gleyzes, *Fast Navigation in a Large Hilbert Space Using Quantum Optimal Control*, Physical Review X **10**, 021058 (2020)

[62] *QDYN library*, `https://www.qdyn-library.net/`

[63] S. A. Bhatti, C. L. Cromer, and W. E. Cooke, *Analysis of the Rydberg character of the* $5d7d\,^1D_2$ *state of barium*, Physical Review A **24**, 161 (1981)

[64] M. L. Zimmerman, M. G. Littman, M. M. Kash, and D. Kleppner, *Stark structure of the Rydberg states of alkali-metal atoms*, Physical Review A **20**, 2251 (1979)

[65] M. Goerz, *Optimizing Robust Quantum Gates in Open Quantum Systems*, PhD thesis, Universität Kassel, 2015

[66] H. Tal-Ezer and R. Kosloff, *An accurate and efficient scheme for propagating the time dependent Schrödinger equation*, The Journal of Chemical Physics **81**, 3967 (1984)

[67] R. Kosloff, *Time-Dependent Quantum-Mechanical Methods for Molecular Dynamics*, The Journal of Physical Chemistry **92**, 2087 (1988)

[68] A. Gil, J. Segura, and N. Temme, *Numerical Methods for Special Functions*, Society for Industrial and Applied Mathematics, Philadelphia, 2007

[69] E. H. Dowell and S. E. Widnall, *Quarterly of Applied Mathematics*, volume 9, 1966

[70] M. Berman, R. Kosloff, and H. Tal-Ezer, *Solution of the time-dependent Liouville-von Neumann equation: Dissipative evolution*, Journal of Physics A: Mathematical and General **25**, 1283 (1992)

[71] R. Kosloff, *Propagation Methods for Quantum Molecular Dynamics*, Annual Review of Physical Chemistry **45**, 145 (1994)

[72] D. D'Allesandro, *Introduction to Quantum Control and Dynamics*, Chapman & Hall/CRC, Boca Raton, Florida, 2008

[73] J. P. Palao and R. Kosloff, *Optimal control theory for unitary transformations*, Physical Review A **68**, 062308 (2003)

[74] D. M. Reich, M. Ndong, and C. P. Koch, *Monotonically convergent optimization in quantum control using Krotovs method*, Journal of Chemical Physics **136**, 104103 (2012)

[75] J. A. Nelder and R. Mead, *A Simplex Method for Function Minimization*, The Computer Journal **7**, 308 (1965)

[76] T. Caneva, T. Calarco, and S. Montangero, *Chopped random-basis quantum optimization*, Physical Review A **84**, 22326 (2011)

[77] D. E. Goldberg, *Genetic Algorithms in Search, Optimization and Machine Learning*, Addison-Wesley Longman Publishing Co., Inc. Boston, 1989

[78] N. Khaneja, T. Reiss, C. Kehlet, T. Schulte-Herbrüggen, and S. J. Glaser, *Optimal control of coupled spin dynamics: design of NMR pulse sequences by gradient ascent algorithms*, Journal of Magnetic Resonance **172**, 296 (2005)

[79] A. Konnov and V. Krotov, *On global Methods of successive Improvement of Controlled Processes*, Automation and Remote Control **60**, 1427 (1999)

[80] J. Somlói, V. A. Kazakov, and D. J. Tannor, *Controlled dissociation of I_2 via optical transitions between the X and B electronic states*, Chemical Physics **172**, 85 (1993)

[81] S. E. Sklarz and D. J. Tannor, *Loading a Bose-Einstein Condensate onto an Optical Lattice: an Application of Optimal Control Theory to The Non Linear Schroedinger Equation*, Physical Review A **66**, 053619 (2002)

[82] A. Signoles, E.-K. Dietsche, A. Facon, D. Grosso, S. Haroche, J.-M. Raimond, M. Brune, and S. Gleyzes, *Coherent transfer between low-angular momentum and circular Rydberg states*, Physical Review Letters **118**, 253603 (2017)

[83] P. Nussenzveig, F. Bernardot, M. Brune, J. Hare, J. M. Raimond, S. Haroche, and G. W., *Preparation of high-principal-quantum-number "circular" states of rubidium*, Physical Review A **48**, 3991 (1993)

[84] C. Gollub, M. Kowalewski, and R. De Vivie-Riedle, *Monotonic convergent optimal control theory with strict limitations on the spectrum of optimized laser fields*, Physical Review Letters **101**, 073002 (2008)

[85] M. Schröder and A. Brown, *Generalized filtering of laser fields in optimal control theory: Application to symmetry filtering of quantum gate operations*, New Journal of Physics **11**, 105031 (2009)

[86] M. Lapert, R. Tehini, G. Turinici, and D. Sugny, *Monotonically convergent optimal control theory of quantum systems with spectral constraints on the control field*, Physical Review A **79**, 063411 (2009)

[87] V. Giovannetti, S. Lloyd, and L. Maccone, *Quantum limits to dynamical evolution*, Physical Review A **67**, 052109 (2003)

[88] M. H. Goerz, T. Calarco, and C. P. Koch, *The quantum speed limit of optimal controlled phasegates for trapped neutral atoms*, Journal of Physics B , 44 (2011)

[89] M. J. Holland and K. Burnett, *Interferometric detection of optical phase shifts at the Heisenberg limit*, Physical Review Letters **71**, 1355 (1993)

[90] M. Kitagawa and M. Ueda, *Squeezed spin states*, Physical Review A **47**, 5138 (1993)

[91] W. Muessel, H. Strobel, D. Linnemann, D. B. Hume, and M. K. Oberthaler, *Scalable Spin Squeezing for Quantum-Enhanced Magnetometry with Bose-Einstein Condensates*, Physical Review Letters , 113 (2014)

[92] T. Xia, X. L. Zhang, and M. Saffman, *Analysis of a controlled phase gate using circular Rydberg states*, Physical Review A **88**, 062337 (2013)

[93] S. R. Cohen and J. D. Thompson, *Quantum Computing with Circular Rydberg Atoms*, Physical Review X Quantum **2**, 030322 (2021)

[94] T. L. Nguyen, J.-M. Raimond, C. Sayrin, R. Cortinas, T. Cantat-Moltrecht, F. Assemat, I. Dotsenko, S. Gleyzes, S. Haroche, G. Roux, T. Jolicoeur, and M. Brune, *Towards quantum simulation with circular Rydberg atoms*, Physical Review X **8**, 011032 (2018)

[95] D. Maxwell, D. J. Szwer, D. Paredes-Barato, H. Busche, J. D. Pritchard, A. Gauguet, M. P. A. Jones, and C. S. Adams, *Microwave control of the interaction between two optical photons*, Physical Review A **89**, 043827 (2014)

[96] Y.-G. Liu, K. Xia, and S.-L. Zhu, *Efficient microwave-to-optical single-photon conversion with a single flying circular Rydberg atom*, Optics Express **29**, 9942 (2021)

[97] M. M. Aliyu, A. Ulugöl, G. Abumwis, and S. Wüster, *Transport on flexible Rydberg aggregates using circular states*, Physical Review A **98**, 043602 (2018)

[98] J. Huang, X. Qin, H. Zhong, Y. Ke, and C. Lee, *Quantum metrology with spin cat states under dissipation*, Scientific Reports **5**, 17894 (2015)

[99] K. C. Younge, B. Knuffman, S. E. Anderson, and G. Raithel, *State-Dependent Energy Shifts of Rydberg Atoms in a Ponderomotive Optical Lattice*, Physical Review Letters **104**, 173001 (2010)

[100] T. Pohl, H. R. Sadeghpour, and P. Schmelcher, *Cold and ultracold Rydberg atoms in strong magnetic fields*, Physics Reports **484**, 181 (2009)

[101] D. Barredo, V. Lienhard, P. Scholl, S. De Léséleuc, T. Boulier, A. Browaeys, and T. Lahaye, *Three-Dimensional Trapping of Individual Rydberg Atoms in Ponderomotive Bottle Beam Traps*, Physical Review Letters **124**, 023201 (2020)

[102] J. Millen, *A cold strontium Rydberg gas*, PhD thesis, Durham University, 2011

[103] A. A. Budini, *Stochastic representation of a class of non-Markovian completely positive evolutions*, Physical Review A **69**, 042107 (2004)

[104] R. Mukherjee, J. Millen, R. Nath, M. P. Jones, and T. Pohl, *Many-body physics with alkaline-earth Rydberg lattices*, Journal of Physics B **44**, 18 (2011)

[105] W. E. Cooke, T. F. Gallagher, S. A. Edelstein, and R. M. Hill, *Doubly Excited Autoionizing Rydberg States of Sr*, Physical Review Letters **40**, 178 (1978)

[106] P. McQuillen, X. Zhang, T. Strickler, F. B. Dunning, and T. C. Killian, *Imaging the evolution of an ultracold strontium Rydberg gas*, Physical Review A **87**, 013407 (2013)

[107] J. Millen, G. Lochead, and M. P. Jones, *Two-electron excitation of an interacting cold Rydberg gas*, Physical Review Letters **105**, 213004 (2010)

[108] I. C. Percival, *Planetary Atoms*, Proceedings of the Royal Society of London A **353**, 289 (1977)

[109] G. Tanner, K. Richter, and J. M. Rost, *The theory of two-electron atoms: Between ground state and complete fragmentation*, Reviews of Modern Physics **72**, 497 (2000)

[110] S. Ye, X. Zhang, T. C. Killian, F. B. Dunning, M. Hiller, S. Yoshida, S. Nagele, and J. Burgdörfer, *Production of very-high-n strontium Rydberg atoms*, Physical Review A **88**, 043430 (2013)

[111] P. A. M. Dirac, *The Principles of Quantum Mechanics*, Oxford University Press, Oxford, fourth edition, 1958

[112] M. Aymar, C. H. Greene, and E. Luc-Koenig, *Multichannel Rydberg spectroscopy of complex atoms*, Reviews of Modern Physics **68**, 1015 (1996)

[113] M. Weissbluth, *Atoms and Molecules*, Academic Press, Inc. Ltd., London, student edition, 1978

[114] C. L. Vaillant, M. P. Jones, and R. M. Potvliege, *Long-range Rydberg-Rydberg interactions in calcium, strontium and ytterbium*, Journal of Physics B **45**, 13 (2012)

[115] S. Gleyzes, Laboratoire Kastler Brossel, Collège de France, Paris, France, private communication

[116] T. Rowan, *Functional Stability Analysis of Numerical Algorithms*, PhD thesis, Department of Computer Sciences, University of Texas at Austin, 1990

[117] Steven G. Johnson, *The NLopt nonlinear-optimization package*, `http://github.com/stevengj/nlopt`

[118] C. R. Harris, K. J. Millman, S. J. van der Walt, R. Gommers, P. Virtanen, D. Cournapeau, E. Wieser, J. Taylor, S. Berg, N. J. Smith, R. Kern, M. Picus, S. Hoyer, M. H. van Kerkwijk, M. Brett, A. Haldane, J. F. del Río, M. Wiebe, P. Peterson, P. Gérard-Marchant, K. Sheppard, T. Reddy, W. Weckesser, H. Abbasi, C. Gohlke, and T. E. Oliphant, *Array programming with NumPy*, Nature **585**, 357 (2020)

[119] Á. Rivas, S. F. Huelga, and M. B. Plenio, *Quantum non-Markovianity: characterization, quantification and detection*, Reports on Progress in Physics **77**, 094001 (2014)

[120] U. Weiss, *Quantum dissipative systems*, World Scientific, 4th edition, 2012

[121] I. de Vega and D. Alonso, *Dynamics of non-Markovian open quantum systems*, Reviews of Modern Physics **89**, 015001 (2017)

[122] B. Bylicka, D. Chruściński, and S. Maniscalco, *Non-Markovianity and reservoir memory of quantum channels: A quantum information theory perspective*, Scientific Reports **4**, 5720 (2014)

[123] D. M. Reich, N. Katz, and C. P. Koch, *Exploiting Non-Markovianity for Quantum Control*, Scientific Reports **5**, 12430 (2015)

[124] C. Li, G. Guo, and J. Piilo, *Non-Markovian quantum dynamics : What is it good for ?*, EPL (Europhysics Letters) **128**, 30001 (2019)

[125] S. Maniscalco, J. Piilo, F. Petruccione, and A. Messina, *Simulating open quantum systems with trapped ions*, Acta Physica Hungarica Series B, Quantum Electronics **23**, 67 (2005)

[126] J. T. Barreiro, M. Müller, P. Schindler, D. Nigg, T. Monz, M. Chwalla, M. Hennrich, C. F. Roos, P. Zoller, and R. Blatt, *An open-system quantum simulator with trapped ions*, Nature **470**, 486 (2011)

[127] S. Patsch, S. Maniscalco, and C. P. Koch, *Quantum simulation of non-Markovianity using the quantum Zeno effect*, Physical Review Research **2**, 023133 (2020)

[128] V. B. Braginsky and F. Y. Khalili, *Quantum nondemolition measurements: the route from toys to tools*, Reviews of Modern Physics **68** (1996)

[129] P. Facchi, V. Gorini, G. Marmo, S. Pascazio, and E. C. Sudarshan, *Quantum Zeno dynamics*, Physics Letters, Section A: General, Atomic and Solid State Physics **275**, 12 (2000)

[130] P. Facchi and S. Pascazio, *Quantum Zeno Subspaces*, Physical Review Letters **89**, 080401 (2002)

[131] P. Facchi and S. Pascazio, *Quantum Zeno dynamics: mathematical and physical aspects*, Journal of Physics A **41**, 493001 (2008)

[132] S. Wißmann, A. Karlsson, E.-M. Laine, J. Piilo, and H.-P. Breuer, *Optimal state pairs for non-Markovian quantum dynamics*, Physical Review A **86**, 062108 (2012)

[133] S. Lorenzo, F. Plastina, and M. Paternostro, *Geometrical characterization of non-Markovianity*, Physical Review A **88**, 020102 (2013)

[134] Á. Rivas, S. F. Huelga, and M. B. Plenio, *Entanglement and non-Markovianity of quantum evolutions*, Physical Review Letters **105**, 050403 (2010)

[135] M. J. Hall, J. D. Cresser, L. Li, and E. Andersson, *Canonical form of master equations and characterization of non-Markovianity*, Physical Review A **89**, 042120 (2014)

[136] F. Ciccarello, G. M. Palma, and V. Giovannetti, *Collision-model-based approach to non-Markovian quantum dynamics*, Physical Review A **87**, 040103 (2013)

[137] B. Vacchini, *Non-Markovian master equations from piecewise dynamics*, Physical Review A **87**, 030101(R) (2013)

[138] J. M. Raimond, P. Facchi, B. Peaudecerf, S. Pascazio, C. Sayrin, I. Dotsenko, S. Gleyzes, M. Brune, and S. Haroche, *Quantum Zeno dynamics of a field in a cavity*, Physical Review A **86**, 32120 (2012)

[139] F. Assemat, D. Grosso, A. Signoles, A. Facon, I. Dotsenko, S. Haroche, J. M. Raimond, M. Brune, and S. Gleyzes, *Quantum Rabi Oscillations in Coherent and in Mesoscopic Cat Field States*, Physical Review Letters **123**, 143605 (2019)

[140] P. Facchi and S. Pascazio, *Kick and fix: the roots of quantum control*, Proceedings of 11th Italian Quantum Information Science conference **12**, 30 (2019)

[141] F. Lucas, *Adaptive resummation of Markovian quantum dynamics*, PhD thesis, Universität Duisburg-Essen, 2014

[142] E. L. Hahn, *Spin Echoes*, Physical Review **80**, 580 (1950)

[143] A. Blais, R. S. Huang, A. Wallraff, S. M. Girvin, and R. J. Schoelkopf, *Cavity quantum electrodynamics for superconducting electrical circuits: An architecture for quantum computation*, Physical Review A **69**, 062320 (2004)

[144] D. Kienzler, H.-Y. Lo, B. Keitch, L. de Clercq, F. Leupold, F. Lindenfelser, M. Marinelli, V. Negnevitsky, and J. P. Home, *Quantum harmonic oscillator state synthesis by reservoir engineering*, Science **347**, 53 (2015)

[145] F. Schäfer, I. Herrera, S. Cherukattil, C. Lovecchio, F. S. Cataliotti, F. Caruso, and A. Smerzi, *Experimental realization of quantum zeno dynamics*, Nature Communications **5**, 3194 (2014)

[146] B. Zhao, A. W. Glaetzle, G. Pupillo, and P. Zoller, *Atomic Rydberg Reservoirs for Polar Molecules*, Physical Review Letters **108**, 193007 (2012)

[147] S. D. Huber and H. P. Büchler, *Dipole-Interaction-Mediated Laser Cooling of Polar Molecules to Ultracold Temperatures*, Physical Review Letters **108**, 193006 (2012)

[148] E. Kuznetsova, S. T. Rittenhouse, I. I. Beterov, M. O. Scully, S. F. Yelin, and H. R. Sadeghpour, *Effective spin-spin interactions in bilayers of Rydberg atoms and polar molecules*, Physical Review A **98**, 043609 (2018)

[149] E. Kuznetsova, S. T. Rittenhouse, H. R. Sadeghpour, and S. F. Yelin, *Rydberg-atom-mediated nondestructive readout of collective rotational states in polar-molecule arrays*, Physical Review A **94**, 032325 (2016)

[150] E. Kuznetsova, S. T. Rittenhouse, H. R. Sadeghpour, and S. F. Yelin, *Rydberg atom mediated polar molecule interactions: a tool for molecular-state conditional quantum gates and individual addressability*, Physical Chemistry Chemical Physics **13**, 17115 (2011)

[151] F. Jarisch and M. Zeppenfeld, *State resolved investigation of Förster resonant energy transfer in collisions between polar molecules and Rydberg atoms*, New Journal of Physics **20**, 113044 (2018)

[152] L. Petitjean, F. Gounand, and P. R. Fournier, *Collisions of rubidium Rydberg-state atoms with ammonia*, Physical Review A **33**, 143 (1986)

[153] X. Ling, M. T. Frey, K. A. Smith, and F. B. Dunning, *The role of inversion transitions in K(150p)/NH3, ND3 collisions*, The Journal of Chemical Physics **98**, 2486 (1993)

[154] R. V. Krems, *Molecules in Electromagnetic Fields*, John Wiley and Sons Ltd., New York, 2019

[155] C. Sommer, *Construction and Operation of a Cryogenic Source for Cold Polar Molecules*, PhD thesis, Max-Planck-Institut für Quantenoptik, Garching and Physik Department, Technische Universität München, 2011

[156] M. Born and R. Oppenheimer, *Zur Quantentheorie der Molekeln*, Annalen der Physik **389**, 457 (1927)

[157] C. Eckart, *Some Studies Concerning Rotating Axes and Polyatomic Molecules*, Physical Review **47**, 552 (1935)

[158] F. Jarisch, *Förster Resonance Energy Transfer between Rubidium Rydberg States and Ammonia*, Masterarbeit, Technische Universität München, 2017

[159] S. Green, *Energy transfer in $NH_3 - He$ collisions*, Journal of Chemical Physics **73**, 2740 (1980)

[160] D. K. Coles, W. E. Good, J. K. Bragg, and A. H. Sharbaugh, *The stark effect of the ammonia inversion spectrum*, Physical Review **82**, 877 (1951)

[161] J. M. Jauch, *The hyperfine structure and the Stark effect of the ammonia inversion spectrum*, Physical Review **72**, 715 (1947)

[162] A. Rauk, L. C. Allen, and K. Mislow, *Pyramidal Inversion*, Angewandte Chemie International Edition **9**, 400 (1970)

[163] J. W. Simmons and W. Gordy, *Structure of the Inversion Spectrum of Ammonia*, Physical Review **73**, 713 (1948)

[164] D. J. Griffiths, *Introduction to electrodynamics*, Prentice-Hall, Inc., New Jersey, 3rd edition, 1999

[165] L. Petitjean, F. Gounand, and P. R. Fournier, *Collisions of rubidium Rydberg-state atoms with ammonia*, Physical Review A **33**, 143 (1986)

[166] H. L. Bethlem, F. M. Crompvoets, R. T. Jongma, S. Y. van de Meerakker, and G. Meijer, *Deceleration and trapping of ammonia using time-varying electric fields*, Physical Review A **65**, 053416 (2002)

[167] M. Zeppenfeld, Max-Planck-Institut für Quantenoptik, Garching, *private communication*

[168] G. Carlo and J. Franck, *Über Zerlegung von Wasserstoffmolekülen durch angeregte Quecksilberatome*, Zeitschrift für Physik **11**, 161 (1922)

[169] T. Förster, *Zwischenmolekulare Energiewanderung und Fluoreszenz*, Annalen der Physik **437**, 55 (1948)

[170] M. Cardoso Dos Santos, W. R. Algar, I. L. Medintz, and N. Hildebrandt, *Quantum dots for Förster Resonance Energy Transfer (FRET)*, Trends in Analytical Chemistry **125**, 115819 (2020)

[171] K. A. Safinya, J. F. Delpech, F. Gounand, W. Sandner, and T. F. Gallagher, *Resonant Rydberg-Atom-Rydberg-Atom Collisions*, Physical Review Letters **47**, 405 (1981)

[172] S. Ravets, H. Labuhn, D. Barredo, L. Béguin, T. Lahaye, and A. Browaeys, *Coherent dipole-dipole coupling between two single Rydberg atoms at an electrically-tuned Förster resonance*, Nature Physics **10**, 914 (2014)

[173] R. Faoro, B. Pelle, and A. Zuliani, *Few-body interactions in frozen Rydberg gases*, European Physical Journal: Special Topics **225**, 2935 (2016)

[174] R. F. Stebbings and F. B. Dunning, *Rydberg States of Atoms and Molecules*, Cambridge University Press, New York, 2011

[175] K. A. Smith, F. G. Kellert, R. D. Rundel, F. B. Dunning, and R. F. Stebbings, *Discrete Energy Transfer in Collisions of* $\mathrm{Xe(nf)}$ *Rydberg Atoms with* $N\mathrm{H_3}$ *Molecules*, Physical Review Letters **40**, 1362 (1978)

[176] R. Baer and E. Rabani, *Theory of resonance energy transfer involving nanocrystals: The role of high multipoles*, The Journal of Chemical Physics **128**, 184710 (2008)

[177] G. Gil, S. Corni, A. Delgado, A. Bertoni, and G. Goldoni, *Excitation energy-transfer in functionalized nanoparticles: Going beyond the Förster approach*, Journal of Chemical Physics **144** (2016)

[178] J. Deiglmayr, H. Saßmannshausen, P. Pillet, and F. Merkt, *Observation of dipole-quadrupole interaction in an ultracold gas of rydberg atoms*, Physical Review Letters **113**, 193001 (2014)

[179] C. Zener and R. H. Fowler, *Non-adiabatic crossing of energy levels*, Proceedings of the Royal Society of London. Series A, Containing Papers of a Mathematical and Physical Character **137**, 696 (1932)

[180] A. Signoles, A. Facon, D. Grosso, I. Dotsenko, S. Haroche, J.-M. Raimond, M. Brune, and S. Gleyzes, *Confined quantum Zeno dynamics of a watched atomic arrow*, Nature Physics **10**, 715 (2014)

[181] R. G. Cortiñas, M. Favier, B. Ravon, P. Méhaignerie, Y. Machu, J. M. Raimond, C. Sayrin, and M. Brune, *Laser Trapping of Circular Rydberg Atoms*, Physical Review Letters **124**, 123201 (2020)

[182] R. C. Teixeira, A. Larrouy, A. Muni, L. Lachaud, J. M. Raimond, S. Gleyzes, and M. Brune, *Preparation of Long-Lived, Non-Autoionizing Circular Rydberg States of Strontium*, Physical Review Letters **125**, 263001 (2020)

[183] M. Marinescu, H. R. Sadeghpour, and A. Dalgarno, *Dispersion coefficients for alkali-metal dimers*, Physical Review A **49**, 982 (1994)

[184] D. Meschede, *Centimeter-wave spectroscopy of highly excited rubidium atoms*, Journal of the Optical Society of America B **4**, 413 (1987)

[185] J. Han, Y. Jamil, D. V. L. Norum, P. J. Tanner, and T. F. Gallagher, *Rb nf quantum defects from millimeter-wave spectroscopy of cold ^{85}Rb Rydberg atoms*, Physical Review A **74**, 054502 (2006)

[186] P. Nussenzveig, *Mesures de champs au niveau du photon par interférométrie atomique*, PhD thesis, Université Pierre et Marie Curie - Paris VI, France, 1994

Declaration of Authorship

I declare to the Freie Universität Berlin that I have completed the submitted dissertation independently and without the use of sources and aids other than those indicated. The present thesis is free of plagiarism. I have marked as such all statements that are taken literally or in content from other writings. This dissertation has not been submitted in the same or similar form in any previous doctoral procedure. I agree to have my thesis examined by a plagiarism examination software.

Berlin, 8 October 2021

Sabrina Patsch